UBITRON DEVICE RESEARCH

SAIC Final Report No. SAIC-97/1073

Submitted to:

Vacuum Electronics Branch, Code 6840
Electronics Science and Technology Division
Naval Research Laboratory
Washington, D.C. 20375

Submitted by:

Applied Physics Operation
Science Applications International Corporation
1710 Goodridge Drive
McLean, VA 22102
(703) 734-5840

December 1997

CONTENTS

I. INTRODUCTION

The research performed on this contract covers a broad range of topics related to coherent radiation sources. In general, the research can be divided into two broad categories: theoretical research into innovative concepts in the physics of ubitrons (or free-electron lasers) and helix traveling wave tubes, and in the application of this theory to the support of the experimental ubitron program in the Vacuum Electronics Branch of the Electronics Science and Technology Division at the Naval Research Laboratory (NRL). The work on this program was conducted by the Principal Investigator, Dr. H.P. Freund at a level of effort of 1 Manyear per calendar year during the contract period.

The general theory research covers a wide range of topics of interest. In regard to ubitron/free-electron laser research, work has covered a wide variety of topics. Nonlinear analyses and simulation codes have been developed (1) for short wavelength free-electron lasers driven by planar wigglers using a superposition of Gauss-Hermite optical modes, (2) for the CHI wiggler ubitron using the modes of a coaxial waveguide, and (3) for a corrugated waveguide in conjunctino with a helical wiggler. Thus, the ubitron work has spanned vitually the entire range of wiggler geometries either in use at the prtesent time or under development. The helix traveling wave tube work has includsed both linear analyses and nonlinear simulations for sheath helix geometry.

The theory support for the ubitron program in Code 6840 covers two distinct experiments. The first experiment is that of a fundamental harmonic ubitron using a helical wiggler and an axial guide field. Extensive theoretical capability to analyze this configuration has been developed over the course of this and preceding contacts with Code 6840 at NRL, and the simulation codes developed were employed to analyze the results of this experiment. Gratifyingly, good agreement has been found between the experiment and the theory. The second experiment employs a planar wiggler and operated at higher harmonics of the resonance frequency. Once again, good agreement has been found between simulation and the experiment.

The organization of this final report is as follows. A description of the general theory developed under the contract is given in Section. II. A discussion of the theoretical support provided for the ubitron experiments is given in Section III. A summary is given in Section IV. The text of the report will not be very detailed in that figures and drawings illustrating the results of the work will not be given in the body of the report. These are shown instead in the papers published during the contract period, and copies of all papers published in refereed journals for this research is given in Appendices following the text of the report.

II. GENERAL THEORY

The general theory developed under the contract can be classified into two parts corresponding to ubitrons/free-electron lasers and helix traveling wave tubes (TWTs). Each of these categories will be discussed separately.

The ubitron/FEL work principally includes slow-time-scale nonlinear formulations and simulation codes of (1) short wavelength devices using planar wigglers where the electromagnetic mode structure is represented as a superposition of Gauss-Hermite modes, (2) helical wiggler/axial guide field configurations describing either smooth-bore or corrugated cylindrical waveguides, and (3) the Coaxial Hybrid Iron (CHI) wiggler design which uses a coaxial mode structure as well. Additional work has been done on electron trajectories in a self-consistent wiggler model as a means of studying the effects of wiggler

errors, and on the compilation of an annual status report on long wavelength ubitrons/FELs.

The work on short wavelength FELs was motivated by the potential interest in infrared FELs. In this regard a simulation code (named MEDUSA) was developed which treats planar wiggler geometry and uses a superposition of the Gauss-Hermite modes for the electromagnetic fields. This work was published in two stages in the Physical Review and in Nuclear Instruments and Methods in Physics Research, and are reproduced in Appenndices I and II. The code MEDUSA has generated interest outside the Naval Research Laboratory, and has been released (with approval of NRL) to a number of researchers outsaide NRL.

A nonlinear formulation and simulation code has been developed for the CHI wiggler model which makes use of the modes in a coaxial waveguide. The basic theory for this model has been published in Nuclear Instruments and Methods in Physics Research, and is reproduced in Appendix III. This model has been used in the design of an experiment being performed in Code 6840 at NRL, which will be discussed in Sec. III. However, it has also been used in design studies for a far-infrared CHI-wiggler FEL, which has been published in Nuclear Instruments and Methods in Physics Research and is reproduced in Appendix IV. In addition, the model has also been used to generate adesign study of a CHI-wiggler based free-electron maser for use in cyclotron heating of magnetically confined thermonuclear fusion reactors. This work has been published in the Physics of Plasmas and in Nuclear Instuments and Methods in Physics Research, and is reproduced in Appendices V and VI.

Due to ongoing interest in reducing the voltage requirements in ubitrons, a theory was developed for treating corrugated waveguide geometries. The motivation here was to employ the slow-wave structure as a method of dispersion control to reduce the electron energies requires for high frequency resonance in free-electron masers. To this end, a nonlinear slow-time-scale formulation and simulation code was developed to treat a helical wiggler/axial guide field configuration in conjunction with a corrugated cylindrical waveguide.This research was published in Nuclear Instruments and Methods in Physics Research, and is reproduced in Appendix VII.

An earlier simulation code (ARACHNE) which treats a helical wiggler/axial guide field geometry for the modes in a smooth-bore cylindrical waveguide has also been used to study the usefulness of an annular electron beam. Impressively high growth rates and efficiencies were found, which suggests that this configuration his potentially interesting for future applications. The work has been published in Nuclear Instruments and Methods in Physics Research, and is reproduced in Appendix VIII.

Another ubitron/FEL research project was performed in collaboration with L.H. Yu at Brookhaven National Laboratory. This study dealt with electron trajectories in a self-consistent wiggler model into which random errors can be introduced. The orbits in such a wiggler with imperfections was compared with the orbits for a sinusiodal wiggler model with corresponding amplitude errors, and good agreement was found. The discrepancies between the two wiggler models were attributed to the inclusion of phase as well as amplitude fluctuations in the seelf-consistent wiggler model. This work was published in Nuclear Instruments and Methods in Physics Research, and is reproduced in Appendix IX.

An effort was also undertaken to compile annual status reports of long wavelength FEL experiments. These were published in Nuclear Instruments and Methods in Physics Research, and are reproduced in Appendices X-XII.

Tunring now to the helix TWT work, we note that there were five publications in this subject area during the contract period. The principal activity was directed toward the development of a 2-1/2 dimensional time domain simulation code for a sheath helix TWT (named GATOR); however, some work was also devoted to the derivation of a linear stability theory of the sheath helix with dielectric loading.

GATOR is a time-domain simulation of the interaction in a sheath helix which treats tapered helices with both dielectric and vane loading, and is capable of dealing with multiple frequencies and backward waves. Here, the electromagnetic fields are treated by a superposition of the modes in a vacuum sheath helix in which the amplitudes and phases of the modes are assumed to vary in z and t. The equations governing the evolution of the amplitudes and pahses are obtained by a method analogous to the derivation of Poynting's equation. The partial differential equations which result are solved on a grid in z for each time step in terms of the microscopic source currents. These equations are solved in conjunction wit the Lorentz force equations for an ensemble of electrons using a leap-frog method, and the source currents are obtained at each time step by mapping teh individual electron contributions to the nearest neighbor grid points. Both AC and DC space-charge forces are also included in the formalism. The publications describing the development of GATOR are reproduced in Appendices XIII-XV.

Finally, the linear theory was primarily performed in order to develop the mode structure for GATOR as well as to have a theory against which to check the predictions of GATOR in the exponentially growing regime. This theory dealt with a solid or annular electron beam prpagating through a sheath helix with a dielectric load. The work was published in the IEEE Transactions on Plasma Devices, and is reproduced in Appendix XVI. Note that another linear anlaysis describing both helix TWTs and FELs was published in Nuclear Instruments and Methods in Physics Research. This comaprison was intended to study the predicted scaling of the growth rates to confirm whether the well-known scaling laws from the Pierce Theory in the ballistic and space-charge dominated regime were valid. It was found that the Pierce analysis is primarily valid only when the interaction was relatively narrow band, and the scaling laws could differ significantly for sufficiently broad bandwidth interactions. This work was published in Nuclear Instruments and Methods in Physics Research, and is reproduced in Appendix XVII.

Theoretical analyses have also been conducted to study (1) the effect of nonlinear dielectric elements in helix traveling wave tubes, and (2) shot noise in gyroklystrons. These studies have not yet appeared in the refereed literature, but preprints of submitted papers are provided in Appendices XVIII and XIX.

III. THEORETICAL SUPPORT

Theoretical support was provided during the contract period for the Ku-Band ubitron and the Ka-Band CHI wiggler ubitron amplifier programs in Code 6840 at NRL.

The Ku-Band amplifier program employed a conventional helical wiggler/axial guide magnetic field configuration, and achieved an average power of 36 W with peak powers reaching 4 MW. The nonlinear theory was performed with the ARACHNE code, which was in substantial agreement with the experiment in regard to both output powers and beam transmission. The latter point is significant for this experiment as substantial amounts of current was lost to the waveguide walls during the course of the interaction. This work was published in Nuclear Instruments and Methods in Physics Research, and is reproduced in Appendix XX.

The support for the Ka-Band CHI wiggler amplifier program is ongoing since the experiment has not yet become operational. Hence, the primary support thus far is in the design of the experiment. In this regard, two papers have been published in Nuclear Instruments and Methods in Physics Research (see Appendices XXI and XXII) dealing with performance calculations and wiggler characterization respectively.

Theoretical support has also been provided for helix TWTs using the CHRISTINE simulation code, which is a one-dimensional parametric model of a sheath helix TWT. A paper has been written in collaboration with the staff at Nortthrop-Grumman Corp. and submitted for publication to the IEEE Transaction on Plasma Science (see Appendix XXIII).

IV. SUMMARY AND DISCUSSION

The preceding contents of the final report represent the technical work performed under this contract, and the 20 Appendices include the refereed papers published during the contract term. However, this does not include a list of contributed papers presented at conferences (which may be published in such non-archival formats as conference proceedings). In this regard, more than 60 contributed papers were presented at a variety of professional conferences. In addition, Dr Freund has seen publication of both the first and second editions of his book "Principles of Free-electron Lasers" coauthored with T.M. Antonsen, Jr., and is a coholder of a patent on the CHI wiggler design.

APPENDIX I

Nonlinear Theory of Short Wavelength Free-Electron Lasers

H.P. Freund
Phys. Rev. E, 5401 (1995)

Nonlinear theory of short-wavelength free-electron lasers

H. P. Freund
Science Applications International Corporation, McLean, Virginia 22102
(Received 11 May 1995)

The nonlinear evolution of free-electron laser (FEL) amplifiers is studied for infrared and shorter wavelengths. The configuration of interest consists in the propagation of an energetic electron beam through a drift tube in the presence of a periodic wiggler magnetic field with planar symmetry. A three-dimensional formulation is derived in which the electromagnetic field is represented as an expansion of Gaussian optical modes. Since the wiggler model is characterized by planar symmetry, the Gauss-Hermite modes are used for this purpose. A set of nonlinear differential equations is derived for the evolution of the amplitude and phase of each mode, and they are solved simultaneously in conjunction with the three-dimensional Lorentz force equations for an ensemble of electrons in the presence of the magneto-static wiggler, self-electric and self-magnetic fields due to the charge and current distributions of the beam, and the electromagnetic fields. It is important to note that no wiggler average is used in the integration of the electron trajectories. This permits the self-consistent modeling of effects associated with (1) the injection of the beam into the wiggler, (2) emittance growth due to inhomogeneities in the wiggler and radiation fields as well as due to the self-fields, (3) the effect of wiggler imperfections, and (4) betatron oscillations. The optical guiding of the radiation field is implicitly included in the formulation. This approach has important practical advantages in analyzing FELs, since it is necessary only to characterize the beam upon injection into the wiggler, and the subsequent evolution is treated self-consistently. Numerical simulations are performed for two examples corresponding to an infrared FEL at wavelengths near 3.5 μm, and an x-ray FEL operating in the neighborhood of 1.4 Å wavelengths corresponding to the proposed linear coherent light source (LCLS) at the Stanford Linear Accelerator Center. Results for both cases indicate that the more severe limiting factor on the performance of the FEL is the beam emittance. For the infrared example, the transition to the thermal regime occurs for an axial energy spread of $\Delta\gamma_z/\gamma_0 \approx 0.19\%$, and optimal performance is obtained for $\Delta\gamma_z/\gamma_0 < 0.1\%$ and γ is the relativistic factor. This restriction is more severe for the LCLS parameters, for which the thermal transition is found for $\Delta\gamma_z/\gamma_0 \approx 0.05\%$ and optimal performance requires $\Delta\gamma_z/\gamma_0 \leq 0.01\%$. Wiggler imperfections are found to be a much less important constraint on FEL design. Simulations indicate that there is no coherent "walkoff" of the beam from the symmetry axis due to wiggler imperfections, and that the radiation field is sufficiently guided by the interaction that no severe degradation is found in the extraction efficiency or growth rate for moderate levels of wiggler fluctuations.

PACS number(s): 41.60.Cr, 41.60.−m, 41.50.+h, 52.75.Ms

I. INTRODUCTION

The free-electron laser (FEL) has been demonstrated to operate at spectral ranges from the microwave through the ultraviolet [1–16] using a wide variety of accelerators, including modulators, pulse line accelerators, electrostatic accelerators, induction and rf linacs, and storage rings. The fundamental physics of the interaction relies upon stimulated scattering due to the ponderomotive potential created of the beating of a periodic magnetostatic wiggler and the radiation field in the presence of an energetic electron beam [17]. Wiggler magnets have been built with helical, planar, and azimuthal symmetry and FELs have been configured as master oscillator power amplifiers (MOPAs), oscillators, and super-radiant amplifiers. The term *super-radiant amplifier* was originally used to denote a device in which the radiation grows from noise in a single pass through the wiggler; however, the term self-amplified spontaneous emission (SASE) has recently become more widely used for this class of device.

MOPAs and SASE devices have typically been employed longer (millimeter and submillimeter) wavelengths using high-current but relatively low-energy electron beams. In this parameter regime, the FEL grain is sufficiently high to drive the signal to saturation in a single pass. In contrast, short-wavelength FELs (defined herein as near-infrared wavelengths and below) have required higher-energy beams. Since the currents available from most accelerators capable of producing the necessary energies were not high enough to yield single-pass gains suitable for amplifier operation, these FELs have typically been configured as oscillators. However, recently rf linac designs have been proposed in which the peak currents are high enough to make amplifier operation possible. The purpose of this paper is to address a range of important issues relevant to short-wavelength FEL amplifiers.

In this paper, a three-dimensional nonlinear formulation of the interaction in short-wavelength FELs is described and applied to the study of several devices of current interest in the infrared and x-ray spectra. The technique employed is similar to a formulation developed

previously [18–20] that was applied to long-waveguide FELs. The fundamental technique is based upon a representation of the electromagnetic field as a superposition of vacuum modes. The long-wavelength formulation was tailored to treat the modes in both cylindrical and rectangular waveguides. For the present case of short-wavelength FELs, Gaussian optical modes will be used. Nonlinear equations governing the evolution of the amplitude and phase of each mode are derived by taking an average of Maxwell's equations over the wave period. This eliminates the fast time- and space-scale variation from the equations, which greatly reduces the computational requirements. These equations are integrated simultaneously with the three-dimensional Lorentz force equations for an ensemble of electrons subject to the total aggregate of static and fluctuating fields. This includes the magnetostatic wiggler, the electromagnetic radiation fields, and the static self-electric and self-magnetic fields produced by the bulk charge and current densities of the beam [21]. However, collective Raman effects associated with the fluctuating fields of the beam space-charge waves are neglected in the analysis because the frequencies of interest are much higher than the beam plasma frequency.

It is important to emphasize that no average is performed over the Lorentz force equations. This permits the simulation of the entire wealth of three-dimensional phenomena in the FEL including, but not limited to, emittance growth in the injection of the beam into the wiggler and during the course of the interaction, the effect of transverse inhomogeneities in the fields which manifests as an effective energy spread leading to resonance broadening and betatron oscillations, optical guiding of the radiation field by the beam, and the self-consistent modeling of wiggler imperfections.

Two wiggler models are used, both of which have planar symmetry. The reason for this is that most of the short-wavelength FELs, as well as the undulators used in synchrotron light sources, are planar designs. In view of this wiggler symmetry, the preferred choice for the optical modes are the Gauss-Hermite modes. It should be observed in this regard that the drift tube in which the electron beam propagates also constitutes a waveguide, and that Gaussian modes do not rigorously satisfy the boundary condition on the drift tube wall. As a result, it is implicitly assumed that the spot size of the Gaussian radiation beam is much less than the radius of the drift tube. Furthermore, since the radiation is guided by the beam, it is also assumed that the beam radius is much smaller than the drift tube radius.

The organization of the paper is as follows. The general mathematical formulation is described in Sec. II. This includes the wiggler geometry, the Gauss-Hermite modes, the dynamical equations for the amplitudes and phases of the Gaussian modes, and the electron dynamics. Two numerical examples are discussed in Sec. III. The first is an infrared FEL operating at a wavelength of about 3.5 μm. The second is relevant to an x-ray FEL design which is under consideration at the Stanford Linear Accelerator Center (SLAC) [22] which is referred to as the Linear Coherent Light Source (LCLS) utilizing the SLAC linac. This is a 15-GeV design which is intended to operate at wavelengths ranging from 1 to 4 Å. In both cases, issues relating to the extraction efficiency, the sensitivity to beam emittance, the mode spectrum, and the effect of wiggler imperfection are examined. A summary and discussion is given in Sec. IV.

II. MATHEMATICAL FORMULATION

The physical configuration of interest is one in which an energetic electron beam propagates through a circular drift tube in the presence of a planar wiggler magnetic field. Since we are interested in radiation in the infrared spectrum and still shorter wavelengths, the electromagnetic field is expressed in terms of Gaussian optical modes. Furthermore, because the wiggler has a planar symmetry, it is most convenient to employ a superposition of Gauss-Hermite modes. The electron dynamics are treated using the full three-dimensional Lorentz force equations with these magnetostatic and electromagnetic fields. In addition, collective effects arising from the bulk self-electric and self-magnetic fields due to the charge and current distribution of the beam are included as well under the assumption of a circular pencil beam geometry. However, since the wavelength of interest is less than or of the order of several micrometers, the collective Raman effects due to the beam space-charge waves are neglected.

A. Wiggler geometry

Two different models of the wiggler field are used. One model is based upon a planar wiggler generated by a magnet stack with parabolically shaped pole faces [1], and has the form

$$\mathbf{B}_w(\mathbf{x})=B_w(z)\left\{\cos k_w z\left[\hat{\mathbf{e}}_x \sinh\left[\frac{k_w x}{\sqrt{2}}\right]\sinh\left[\frac{k_w y}{\sqrt{2}}\right]+\hat{\mathbf{e}}_y \cosh\left[\frac{k_w x}{\sqrt{2}}\right]\cosh\left[\frac{k_w y}{\sqrt{2}}\right]\right]\right.$$
$$\left.-\sqrt{2}\hat{\mathbf{e}}_z \sin k_w z \cosh\left[\frac{k_w x}{\sqrt{2}}\right]\sinh\left[\frac{k_w y}{\sqrt{2}}\right]\right\}, \quad (1)$$

where B_w denotes the wiggler amplitude and $k_w \equiv 2\pi/\lambda_w$ denotes the wiggler wave number corresponding to the wiggler period λ_w. This type of wiggler provides enhanced focusing of the electron beam in the plane transverse to the direction of bulk electron flow. The other wiggler model is one in which focusing in the direction of the wiggler-induced transverse oscillation is described by a polynomial increase in wiggler amplitude.

This is the x direction for the present choice of wiggler geometry, and the components of the field are represented as

$$B_{w,x}(\mathbf{x})=\left[\left[\sin k_w z-\frac{\cos k_w z}{k_w}\frac{d}{dz}\right]B_w(z)\right]\times\left[\sinh k_w y-\frac{Y(k_w y)}{2k_w^2}\frac{d^2}{dx^2}\right]\frac{1}{k_w}\frac{d}{dx}X(x)\,, \tag{2}$$

$$B_{w,y}(\mathbf{x})=\left[\left[\sin k_w z-\frac{\cos k_w z}{k_w}\frac{d}{dz}\right]B_w(z)\right]\times\left[\cosh k_w y-\frac{k_w y\sinh k_w y}{2k_w^2}\frac{d^2}{dx^2}\right]X(x)\,, \tag{3}$$

$$B_{w,z}(\mathbf{x})=B_w(z)\cos k_w z\left[\sinh k_w y-\frac{Y(k_w y)}{k_w^2}\right]\times\left[1+\frac{1}{k_w^2}\frac{d^2}{dx^2}\right]\frac{d^2}{dx^2}X(x)\,, \tag{4}$$

where $Y(k_w y)\equiv k_w y\cosh k_w y-\sinh k_w y$, and

$$X(x)\equiv 1+\frac{1}{2}\left[\frac{x}{\alpha_x}\right]^{2m} \tag{5}$$

describes the enhanced focusing in terms of two free parameters: the order of the polynomial m and the scale length α_x. Observe that in the limit in which the wiggler amplitude is constant and $X(x)\to 1$ (i.e., when $\alpha_x\to\infty$), then this wiggler reduces to the well-known three-dimensional form of a flat pole face wiggler $\mathbf{B}_w(\mathbf{x})\to B_w[\hat{e}_y\sin k_w z\cosh k_w y+\hat{e}_z\cos k_w z\sinh k_w y]$.

The wiggler amplitudes in each case are permitted to vary with axial position in order to model such effects as (1) the adiabatic injection of the beam into the wiggler, (2) efficiency enhancement using a tapered wiggler amplitude, and (3) the inclusion of imperfections in the wiggler. As such, we can write the amplitude as a superposition of systematic and random components

$$B_w(z)=B_w^{(s)}(z)+\Delta B_w(z)\,, \tag{6}$$

where the systematic $B_w^{(s)}$ describes the adiabatic entry taper as well as the uniform amplitude and systematic taper for efficiency enhancement, and the random component ΔB_w can either be chosen using a random number generator or the measured imperfections from an actual wiggler magnet.

We choose a systematic amplitude variation of the form

$$B_w^{(s)}(z)=\begin{cases}B_w\sin^2\left[\dfrac{k_w z}{4N_w}\right], & 0\le z\le N_w\lambda_w\\ B_w, & N_w\lambda_w<z\le z_0\\ B_w[1+k_w\varepsilon_w(z-z_0)], & z_0<z\,,\end{cases} \tag{7}$$

where B_w denotes the uniform wiggler amplitude, N_w is the length of the adiabatic entry taper in wiggler periods, z_0 is the start of the downstream amplitude taper for efficiency enhancement, and ε_w represents the slope of the taper.

The random component of the amplitude is determined by specifying the magnitude of the amplitude variations at periodic intervals of a wiggler period $\Delta z=\lambda_w/N_p$, and then mapping the amplitude between these points in a continuous fashion. Thus we choose a sequence of wiggler imperfections, $\Delta B_n=\Delta B_w(n\Delta z)$ either from a random number generator or from the measured variations in a specific wiggler magnet. The only restriction placed on this sequence is that $\Delta B_w=0$ over the entry taper region in order to ensure a positive definite amplitude. The variation in $\Delta B_w(z)$ between these points [i.e., $n\Delta z\le z\le(n+1)\Delta z$] is given by

$$\Delta B_w(n\Delta z+\delta z)=\Delta B_n+[\Delta B_{n+1}-\Delta B_n]\sin^2\left[\frac{\pi}{2}\frac{\delta z}{\Delta z}\right], \tag{8}$$

where $0\le\delta z\le\Delta z$. This method for the treatment of wiggler imperfections has been previously applied to long-wavelength FELs in which the electromagnetic fields are confined in a waveguide [23,24].

Free-electron lasers have been constructed using both wiggler types. The first design using parabolic pole faces was constructed by Phillips [1], and the second wiggler type has been used in a harmonic FEL experiment at the Naval Research Laboratory [25]. Both field types provide enhanced focusing which is necessary for the propagation of intense beams. It is important to note, however, that while the parabolic pole face model in Eq. (1) is curl- and divergence-free in the case of a uniform amplitude, the curl and divergence do not vanish identically when the amplitude is allowed to vary in z. This simply means that the fringing fields associated with variations in the amplitude are not included in the model. Since it is important to ensure that the wiggler model be self-consistent in order for the theory to be valid, and since the curl and divergence are proportional to the slope of the amplitude, we must restrict the use of this model to cases where the amplitude changes slowly with axial position. In contrast, both the divergence and the z component of the curl of the second wiggler model can be shown to be divergence-free for any smooth variation in the amplitude. In addition, while the transverse components of the curl do not vanish identically, they are small for most cases of interest.

B. Electromagnetic fields

The electromagnetic fields are represented in terms of the Gauss-Hermite optical modes. This constitutes a complete basis set which is consistent with the planar symmetry imposed by the wiggler geometry. It should be noted, however, that Gaussian optical modes must be

used with some caution because the drift tube in which the electron beam propagates also constitutes a waveguide, and the Gaussian modes do not rigorously satisfy the boundary conditions on the drift tube wall. As a result, the analysis must be restricted to cases where the radiation spot size is much smaller than the radius of the drift tube. Since the radiation will be guided by the interaction with the electron beam, this condition is equivalent to the requirement that the electron beam radius be much less than the drift tube radius.

The vector potential of the Gauss-Hermite modes can be expressed as [26]

$$\delta \mathbf{A}(\mathbf{x},t)=\sum_{l,n=0}^{\infty}\delta A_{l,n}(z)\frac{w_0}{w}\exp(-r^2/w^2)H_n\left[\frac{\sqrt{2}y}{w}\right]$$
$$\times\left\{H_l\left[\frac{\sqrt{2}x}{w}\right]\hat{\mathbf{e}}_x\sin\varphi_{l,n}-\frac{\sqrt{2}}{k_{l,n}w}\hat{\mathbf{e}}_z\left[\frac{\sqrt{2}x}{w}\frac{z}{z_0}H_l\left[\frac{\sqrt{2}x}{w}\right]\sin\varphi_{l,n}\right.\right.$$
$$\left.\left.+\left[\frac{\sqrt{2}x}{w}H_l\left[\frac{\sqrt{2}x}{w}\right]-H_l'\left[\frac{\sqrt{2}x}{w}\right]\right]\cos\varphi_{l,n}\right]\right\}, \tag{9}$$

where H_n denotes the Hermite polynomials, w_0 denotes the spot size at the radiation waist, and for frequency and wave number $(\omega,k_{l,n})$ the phase is given by

$$\varphi_{l,n}=\int_0^z dz' k_{l,n}(z')+\frac{k_0 r}{2R}$$
$$-(l+n+1)\tan^{-1}\left[\frac{z}{z_0}\right]-\omega t\ . \tag{10}$$

In addition, $k_0\equiv\omega/c$ is the free-space wavelength, $w^2\equiv w_0^2(1+z^2/z_0^2)$, $R(z)\equiv z(1+z_0^2/z^2)$, and $z_0\equiv k_0 w_0^2/2$ is the Rayleigh length. Observe that the amplitude and wave number of each mode is allowed to vary slowly in z to describe the growth of the wave as well as the dielectric effect of the beam on the dispersion. The Poynting flux for each mode can be written as

$$P_{l,n}=\frac{2^{l+n}l!n!}{16}\omega k_{l,n}w_0^2\delta A_{l,n}^2\ . \tag{11}$$

It should be remarked that this representation is correct to first order in $(k_{l,n}w)^{-1}\approx\lambda/w$, where λ denotes the wavelength; hence, this representation is valid only as long as the spot size is much greater than the wavelength. Observe as well that these modes approximate TEM modes only as long as $\lambda\ll w$. For all cases of interest in this paper, this inequality is satisfied, and it will prove convenient to use the TEM approximation for the field.

C. Dynamical equations

The dynamical equations which govern the evolution of the amplitude and wave number of each mode are found by substitution of the mode representation (9) into Maxwell's equations after averaging the equations over a wave period and orthogonalization in the transverse mode structure. The procedure is formally equivalent to that described for long-wavelength FELs [18–20], and results in equations of the form

$$\left[\frac{d^2}{dz^2}+\left[\frac{\omega^2}{c^2}-k_{l,n}^2\right]\right]\delta a_{l,n}=\frac{4\omega_b^2}{c^2}\frac{1}{2^{l+n}l!n!}\frac{w_0}{w}\left\langle\frac{v_x}{|v_z|}\exp(-r^2/w^2)H_l\left[\frac{\sqrt{2}x}{w}\right]H_n\left[\frac{\sqrt{2}y}{w}\right]\sin\varphi_{l,n}\right\rangle, \tag{12}$$

and

$$2k_{l,n}^{1/2}\frac{d}{dz}(k_{l,n}^{1/2}\delta a_{l,n})=\frac{4\omega_b^2}{c^2}\frac{1}{2^{l+n}l!n!}\frac{w_0}{w}\left\langle\frac{v_x}{|v_z|}\exp(-r^2/w^2)H_l\left[\frac{\sqrt{2}x}{w}\right]H_n\left[\frac{\sqrt{2}y}{w}\right]\cos\varphi_{l,n}\right\rangle, \tag{13}$$

where $\delta a_{l,n}\equiv e\delta A_{l,n}/m_e c^2$, ω_b is the beam plasma frequency, $\mathbf{v}$ is the instantaneous electron velocity, e and m_e are the electronic charge and rest mass, and c is the speed of light *in vacuo*.

The averaging operator in Eqs. (12) and (13) is defined over an ensemble of electrons injected into the wiggler within one wave period. The initial momentum space distribution is chosen to be monoenergetic but with a pitch-angle spread. This can be thought of as having a zero energy spread but a nonzero emittance. The specific form of the distribution is

$$F_0(\mathbf{p}_0)=A\exp[-(p_{z0}-p_0)^2/\Delta p_z^2]$$
$$\times\delta[p_0^2-p_{\perp 0}^2-p_{z0}^2]H(p_{z0})\ , \tag{14}$$

where the subscript 0 denotes initial quantities (i.e., upon entry to the wiggler at $z=0$), p_0 and Δp_z denote the initial bulk momentum and momentum spread, respectively,

H is the Heaviside function, and the normalization constant is

$$A \equiv \left[\pi \int_0^{p_0} dp_{z0} \exp[-(p_{z0}-p_0)^2/\Delta p_z^2] \right]^{-1} \tag{15}$$

Note that while this distribution is monoenergetic, there is an axial energy spread which is given by

$$\frac{\Delta\gamma_z}{\gamma_0} = 1 - \left[1 + 2(\gamma_0^2 - 1)\frac{\Delta p_z}{p_0} \right]^{-1/2} , \tag{16}$$

where $\gamma_0 \equiv (1+p_0^2/m_e^2c^2)^{1/2}$. The averaging operator takes the form

$$\langle(\cdots)\rangle \equiv \frac{A}{4\pi^2 w_0^2} \int_0^{2\pi} d\phi_0 \int_0^{p_0} dp_{z0} \beta_{z0} \exp[-(p_{z0}-p_0)^2/\Delta p_z^2] \int\int_{A_b} dx_0 dy_0 \sigma_\perp(x_0,y_0) \int_{-\pi}^{\pi} d\psi_0 \sigma_\parallel(\psi_0)(\cdots) , \tag{17}$$

where A_b denotes the initial cross sectional area of the beam, $\phi_0 \equiv \tan^{-1}(p_{y0}/p_{x0})$, $\beta_{z0} \equiv v_{z0}/c$, ψ_0 ($\equiv -\omega t_0$, where t_0 is the injection time) is the initial ponderomotive phase, and $\sigma_\parallel(\psi_0)$ and $\sigma_\perp(x_0,y_0)$ describe the initial beam distributions in phase and cross section.

D. Electron dynamics

These equations for the amplitude and phase of each of the Gauss-Hermite modes [(12) and (13)] are integrated simultaneously with the three-dimensional Lorentz force equations for an ensemble of electrons. As such, the procedure is capable of treating the self-consistent injection of the beam into the wiggler, emittance growth due to the inhomogeneities in the wiggler and radiation fields, betatron oscillations, and optical guiding of the radiation to list a few of the three-dimensional effects inherent in the interaction. Since this is an amplifier model, the Lorentz force equations are integrated in z and are of the form

$$v_z \frac{d}{dz}\mathbf{p} = -e(\mathbf{E}^{(s)}+\delta\mathbf{E}) - \frac{e}{c}\mathbf{v}\times(\mathbf{B}_w+\mathbf{B}^{(s)}+\delta\mathbf{B}) , \tag{18}$$

where $\mathbf{B}_w$ is the wiggler field, $\delta\mathbf{E}$ and $\delta\mathbf{B}$ are the electromagnetic fields associated with the total vector potential (9),

$$\delta\mathbf{E} = -\frac{1}{c}\frac{\partial}{\partial t}\delta\mathbf{A} \tag{19}$$

and

$$\delta\mathbf{B} = \nabla\times\delta\mathbf{A} . \tag{20}$$

In addition, $\mathbf{E}^{(s)}$ and $\mathbf{B}^{(s)}$ represent the self-electric and self-magnetic fields associated with the bulk charge and current distribution of the beam.

The technique used in the treatment of the self-electric and -magnetic fields has been described previously [21] and has been shown to give good agreement with a collective FEL experiment [27]. Under the assumption of a flat-top density profile the self-fields can be expressed as

$$\mathbf{E}^{(s)} = -\frac{m_e}{2e}\omega_b^2[(x-\langle x\rangle)\hat{\mathbf{e}}_x + (y-\langle y\rangle)\hat{\mathbf{e}}_y] \tag{21}$$

and

$$\mathbf{B}^{(s)} = -\frac{m_e}{2e}\omega_b^2\langle\beta_z\rangle[(y-\langle y\rangle)\hat{\mathbf{e}}_x - (x-\langle x\rangle)\hat{\mathbf{e}}_y] , \tag{22}$$

where $\langle x\rangle$ and $\langle y\rangle$ specify the beam centroid, the $\langle\beta_z\rangle$ is the average axial beam velocity. In order to make use of this approach, these average beam quantities must be determined at each point in the integration prior to the calculation of the self-fields. In addition, the beam initialization must include the space-charge depression in electron energy across the beam profile. This energy variation takes the form

$$\gamma(r) = \gamma_0 + \frac{\omega_b^2}{4c^2}(r^2 - R_b^2) \tag{23}$$

for an initial beam radius R_b, and results in an energy spread which may be expressed as

$$\frac{\Delta\gamma_{\text{self}}}{\gamma_0} \approx 5.88\times10^{-5}\frac{I_b}{\sqrt{\gamma_0^2-1}} , \tag{24}$$

where the beam current I_b is in A. It should be noted that this represents a coherent energy spread across the beam and is not the same as a thermal energy spread.

It should be remarked here that, in contrast to Maxwell's equations, there is no necessity to average the orbit equations. Recall that the amplifier model used is based upon the propagation of a single frequency wave, and that the interaction is resonant at the frequency where the bulk velocity of the electron beam is in synchronism with the phase velocity of the ponderomotive wave, i.e., $v_b \approx \omega/(k+k_w)$. Since the electromagnetic field in the Lorentz force equations is evaluated along the electron trajectory, the bulk phase (apart from the components which describe diffraction) varies as $\varphi = kz - \omega t$. Substitution of $z = z_0 + \omega t/(k+k_w)$ in this expression for the phase yields $\varphi \approx kz_0 - ck_w t$ under the assumption that $k \approx \omega/c >> k_w$. As a result, the contributions due to the electromagnetic fields in the Lorentz force equations vary on the scale length of the wiggler period, and the integration step need only be small enough to resolve this spatial scale.

III. NUMERICAL ANALYSIS

The set of coupled nonlinear differential equations for the amplitudes and phases of the Gauss-Hermite modes (12) and (13) are solved numerically in conjunction with the Lorentz force equations (18) for an ensemble of electrons. In general, Eqs. (13) and (14) are second order in the amplitude and phase, but it will prove numerically

convenient in many cases to neglect the second derivatives of the amplitude and phase, and to integrate the resulting first-order equations. The error associated with this approximation is, typically, small while the numerical stability is much improved. The algorithm employed for this purpose is a fourth-order Runge-Kutta-Gill technique, and the particle averages are carried out using a Gaussian quadrature technique in each of the degrees of freedom $(x_0, y_0, \psi_0, \phi_0, p_{z0})$. For cases discussed in this paper, a choice of 1000 particles was found to be adequate when $\Delta\gamma_z = 0$, which is increased to 9600 particles otherwise. The number of Gauss-Hermite modes necessary to describe the evolution of the electromagnetic field depends upon the detailed parameters of each particular example. Diffraction over the Rayleigh length is countered by optical guiding due to the beam, and the detailed balance depends upon the Rayleigh length, the growth rate, and the evolution of the beam envelope in the wiggler. As a result, the specific number of modes used in each case is determined by an empirical procedure in which successive simulation runs are made with increasing number of modes until convergence of the saturation power and saturation length are achieved.

The initial conditions are chosen to model the injection of a solid axisymmetric and monoenergetic electron beam with a uniform cross section. As mentioned previously, there is a coherent variation in the kinetic energy across the beam which is countered by a similar variation in the potential energy due to the self-electric field. The Gauss-Hermite modes are initially assumed to be at the free-space wavelength and it is assumed that the radiation waist is located at $z = 0$ with a spot size equal to the beam radius, although this can be altered to model the injection of power in a given mode with a different spot size. The initial power levels in each mode can be arbitrarily selected to describe the injection of a specific pulse or of noise. For each case discussed in this paper, however, it is assumed that the total initial power is in the lowest-order mode, and all higher-order modes grow from zero power due to the interaction with the electron beam.

It should be remarked that no attempt is made to "match" the beam upon entry to the wiggler in the sense that the beam emittance and radius are selected in order to ensure that the beam envelope remains constant. In the opinion of the author, this is a pointless and counterproductive procedure both from an experimental and theoretical standpoint. Radiation growth in a FEL is a microscopic process in which resonant electrons interact with the radiation field, and give rise to both amplification and refractive guiding of the wave. The interaction is extremely sensitive to the axial energy spread (or emittance) of the beam, and even a small axial energy spread can result in a substantial reduction in the peak extraction efficiency. In contrast, efforts to "match" the beam are motivated by the desire to achieve a uniform beam envelope in the hope that this will yield an improved overlap between the electron beam and the radiation field or, in other words, to maximize the filling-factor and the growth rate. However, the overlap between the beam and the radiation is a macroscopic process depending upon the growth and refractive guiding determined by the microscopic interaction. Hence, it is more important to minimize the emittance in a FEL than it is to match the electron beam to achieve a uniform envelope. Variations in the beam centroid due to the wiggler motion and the beam envelope due to betatron oscillations will merely result in guiding of the signal, while an enhanced emittance which may be necessary to match the beam will certainly result in a degradation in the extracted power. The most important consideration in the design of a FEL, therefore, is to minimize the emittance.

Two cases will be examined in this paper. The first is an infrared FEL operating at wavelengths in the neighborhood of 3.5 μm, and the second is an x-ray FEL operating at wavelengths near 1.4 Å. It will be assumed in both cases that the injected signal is at a power level of 10 kW. While this may be unrealistic if actual devices in these spectral ranges are operated in SASE mode, the analysis will still serve to determine essential characteristics of the interaction such as the extraction efficiency, sensitivity to emittance, mode character, and the effects of wiggler imperfections.

For convenience, the simulation will be referred to as MEDUSA.

A. Infrared FEL

In treating the infrared FEL, it is assumed that a 30-MeV/100-A electron beam with an initial radius of 0.0525 cm propagates through the drift tube in the presence of a planar wiggler with an amplitude of 5.2 kG, a period of 1.8 cm, and an entry taper region which is 10 wiggler periods in length. The specific radius of the drift tube is not important as long as it is much greater than the beam radius. In this case, the second wiggler model [(2)–(5)] is used with a choice of $m = 2$ and $\alpha_x = 0.2$ cm, and it should be noted that the detailed results will vary somewhat with these parameters. The initial spot size is assumed to be equal to the beam radius ($w_0 = 0.0525$ cm) and that an initial power of 10 kW is injected into the TEM_{00} mode. Note that while the Gauss-Hermite modes are only approximately TEM modes in the limit in which $\lambda \ll w_0$ and R_b, it is convenient to refer to them with this notation.

The first issue to be addressed is the growth of the signal for an ideal beam in which $\Delta\gamma_z = 0$ and the mode spectrum which results therefrom. The results from MEDUSA for the choice of $\lambda = 3.505$ μm are shown in Fig. 1, illustrating the evolution of the power versus axial position for the total signal and for the TEM_{00} mode. It is clear from the figure that the total signal grows in an approximately exponential fashion until saturation is reached at a power level of approximately 8.9 MW at $z/\lambda_w \approx 199$. This represents an efficiency of approximately 0.27% and an average growth rate for all modes of $|\mathrm{Im}k_j|/k_w \approx 2.69 \times 10^{-3}$. It is also clear from the figure that while the TEM_{00} mode was the dominant mode upon injection of the signal, higher-order modes grow rapidly. At saturation, the TEM_{00} mode power is 1.69 MW, which accounts for only 19% of the total power.

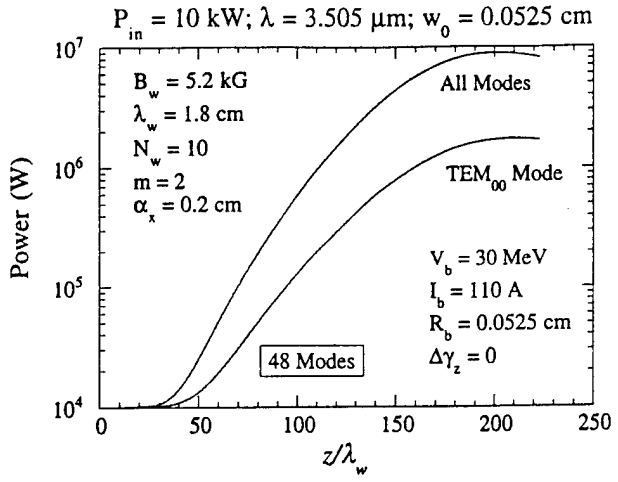

FIG. 1. Evolution of the power versus axial distance for an ideal beam.

The growth of higher-order modes depends upon specific details of the beam radius, wiggler amplitude (and, hence, the beam displacement for the midplane), and the radiation spot size and Rayleigh length. It is found that for the fundamental resonance represented by this case that the only TEM_{ln} modes which grow are those for which both l and n are even, and the ones which grow most rapidly are those where either l or n are zero. While the TEM_{00} mode represents less than half the total power at saturation, it is still the dominant mode. The TEM_{02} and TEM_{20} modes are the next highest at power levels approximately 45% that of the TEM_{00} mode. The power decreases rapidly for higher-order modes; however, some 48 modes must be retained in order for the mode superposition to converge to within better than 1% accuracy. This is illustrated in Fig. 2, in which the relative mode amplitudes (normalized to the power in the TEM_{00} mode) are shown at saturation. As shown in the figure, the bulk of the power is contained within five modes (the TEM_{00}, TEM_{02}, TEM_{20}, and TEM_{04}, and TEM_{40}), but substantial amounts of power are found in the tail of the superposition.

The even modes are seen to interact preferentially at the fundamental resonance; however, this does not mean that odd modes do not interact. It is expected that the even modes will also be preferentially amplified by interactions at odd harmonics, the odd modes will yield amplification at even harmonics by a periodic position interaction. This has been demonstrated at microwave frequencies in both theory and experiment at the Naval Research Laboratory [28], and in theory at infrared wavelengths at Los Alamos National Laboratory [29]. Harmonic interactions, however, will be discussed in a future paper.

The broad mode spectrum is not an artifact of the initial "top-hat" radial density profile. A parabolic density profile has also been used and, for a fixed total current, yielded a result which differed from the top-hat distribution by only a few percent. The principal reason for this is that the radial distribution describes only the initial state of the beam. The subsequent beam evolution is governed by the three-dimensional wiggler, radiation, and self-fields and the radial profile of the beam is quickly distorted from the initial state.

The importance of self-fields on the interaction can be illustrated by examining the resonant spectrum. The efficiency is plotted as a function of wavelength in Fig. 3 for an ideal beam subject to both the inclusion and neglect of the self-fields. The resonant interaction is seen to extend from a wavelength of approximately 3.47 μm through 3.52 μm with the peak efficiency found at the longer wavelengths. The effect of the self-fields for this case is to uniformly reduce the efficiency. At 3.5 μm, the efficiency drops from 0.30% without the self-fields to 0.27% with the self-fields which represents a 10% drop in efficiency. A similar decrease due to the self-fields is also found in the average growth rate as shown in Fig. 4. Here, the average growth rate at 3.505 μm decreases from $|\mathrm{Im}k|/k_w \approx 2.82\times10^{-3}$ without the self-fields to 2.69×10^{-3} with the inclusion of the self-fields. Note that this 10% drop in the efficiency is associated with a

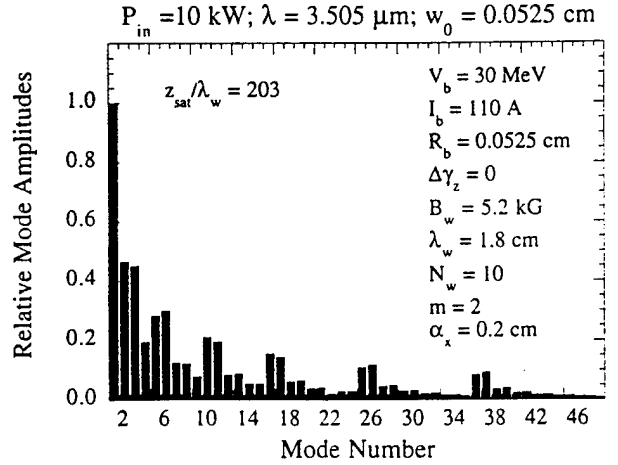

FIG. 2. Relative mode amplitudes at saturation as normalized to the power in the TEM_{00} mode.

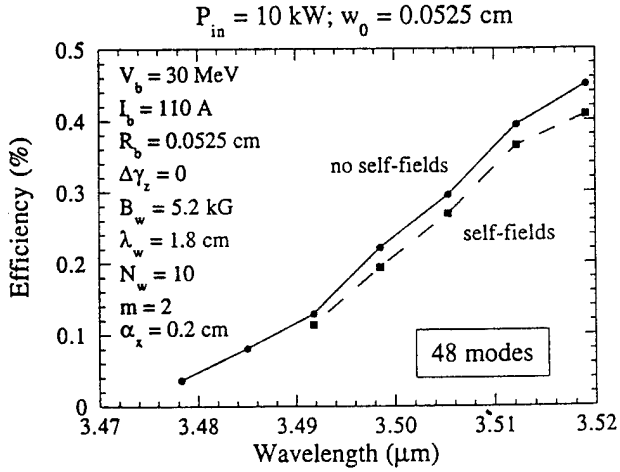

FIG. 3. Plot of the efficiency versus wavelength both with and without the self-fields.

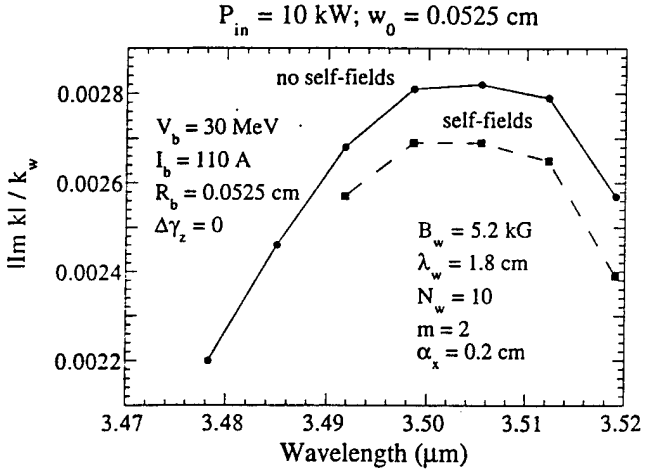

FIG. 4. Plot of the average growth rate versus wavelength with and without the self-fields.

coherent energy drop across the beam of only $\Delta\gamma_{self}/\gamma_0 \approx 0.01\%$. It should also be noted that one-dimensional phase trapping estimates of the efficiency [17] yield a value of 0.42% for the maximum efficiency, which is close to that shown in the figure.

The effect of the axial energy spread on the interaction is severe. In view of the FEL resonance condition, the transition to the thermal regime occurs for $\Delta v_z/v_0 \approx |\mathrm{Im}k|/[\mathrm{Re}k + k_w] \approx 5.24\times10^{-7}$ since $|\mathrm{Im}k|/k_w \approx 0.002\,69$ at a wavelength of 3.505 μm. This corresponds to an axial energy spread (16) of $\Delta\gamma_z/\gamma_0 \approx 0.19\%$. The variation in the efficiency and average growth rate with increases in the axial energy spread ($\Delta\gamma_z/\gamma_0$) is shown in Fig. 5 at a wavelength of 3.505 μm and subject to the inclusion of the self-fields over the range of axial energy spreads up to the thermal transition. It is clear from the figure that the interaction strength decreases rapidly with increases in the axial energy spread. The efficiency decreases by more than half as the energy spread increases to 0.2%, and the average growth rate also drops a significant amount from 2.69×10^{-3} to 1.86×10^{-3}. It is clear, therefore, that an experiment in this regime will require the axial energy spread to be held to less than 0.1% to realize optimal performance.

The effect of wiggler imperfections has been studied by this non-orbit-averaged approach for long-wavelength interactions in which the transverse mode pattern of the radiation is governed by the waveguide [23,24]. In such cases, the effect of wiggler imperfections was found to be small. Typically, root mean square (rms) wiggler imperfection levels of as much as a few percent were found to have negligible impact on the extraction efficiency and growth rate in a long-wavelength FEL. However, it has been suggested that this might not be the case for short-wavelength FELs. The speculation is that in the short-wavelength regime wiggler imperfections might cause the electron beam to walk off from the radiation spot thus resulting in a degradation in the efficiency and growth rate.

In order to address this speculation, we now consider the effect of the random contribution to the wiggler amplitude defined in Eqs. (6) and (8) and generate a sequence of random periodic fluctuations in the wiggler amplitude $\{\Delta B_n\}$ with a period of $\lambda_w/2$ (i.e., $N_p=2$ in the notation described in Sec. II). The effect of these wiggler imperfection distributions is studied statistically for ensembles of random sequences at fixed rms values. Typically, it is found that, at a given rms level, the ensemble averages require consideration of 35 different random sequences for the average efficiency to converge to within 1%. In order to isolate the effect of the wiggler imperfections, all such simulations are performed under the assumption of an ideal beam (i.e., $\Delta\gamma_l=0$).

MEDUSA indicates that, as in the case of the long-wavelength FELs studied previously [23,24], the effects of wiggler imperfections are also small for this infrared wavelength example. The variation in the ensemble-averaged efficiency with increases in $(\Delta B_w/B_w)_{rms}$ is shown in Fig. 6 for parameters consistent with the case shown in Fig. 1. The error bars in the figure denote the standard deviations. It is clear from the figure that the average efficiency is remarkably insensitive to the wiggler imperfections even for rms fluctuation levels as high as

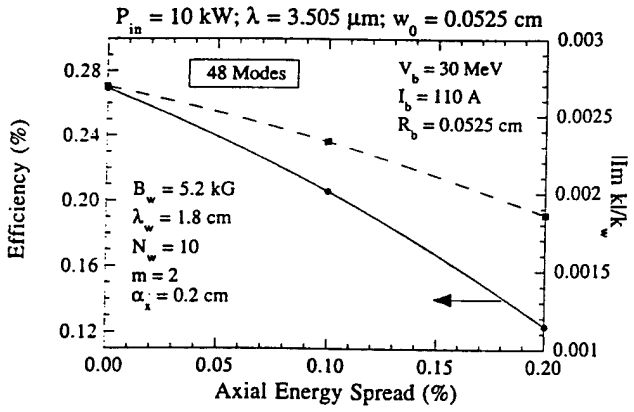

FIG. 5. Variation in the efficiency and average growth rate with axial energy spread.

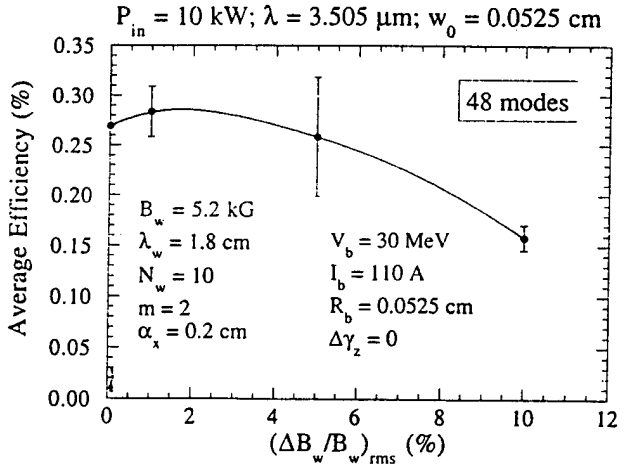

FIG. 6. Variation in the ensemble-averaged efficiency for $N_p=2$.

10%. Over this range of fluctuations, the efficiency drops by slightly less than half from 0.27% to 0.14%. More significantly, the ensemble-averaged efficiency actually increases slightly as $(\Delta B_w/B_w)_{rms}$ increases up to 2%, and drops only to 0.26% for $(\Delta B_w/B_w)_{rms}=5\%$. The reason for the small increase in the efficiency at low values of $(\Delta B_w/B_w)_{rms}$ is that the only constraint placed upon the random sequence is that of the rms fluctuation level. The average value of the wiggler fluctuation $\langle B_w \rangle$ is not constrained. Hence, what has happened is that the average value of the wiggler amplitude has increased slightly over the 5.2 kG of the uniform B_w, and this has resulted in a slight increase in the efficiency. However, this does not alter the conclusion that the interaction is relatively insensitive to imperfections in the wiggler field.

In order to explain why the effect is so small, we turn to a detailed consideration of the orbit dynamics due to the wiggler imperfections. Figure 7 shows the motion of the beam center $\langle x \rangle$ versus axial position for an ideal wiggler [i.e., $(\Delta B_w/B_w)_{rms}=0$] during the interaction shown in Fig. 1. The figure shows the spinning up of the beam in the entry taper region and the bulk wiggler-induced oscillation. The figure also shows that the beam motion is not regular but is substantially perturbed. In order to explain this, note that the beam centroid describes an average over the entire beam cross section. Electrons injected near the axis of symmetry execute an extremely regular trajectory showing largely the effects of the bulk wiggler oscillation. However, the off-axis electrons undergo substantial betatron motion under the action of both the wiggler and the radiation field. Note also that the initial beam radius $R_b \approx 0.03\lambda_w$ is substantially larger than the magnitude of the perturbations of the beam centroid; hence, these perturbations are relatively small in comparison with the scalloping of the beam envelope.

The motion of the beam center shown for the ideal wiggler is now compared with that found for the case of $(\Delta B_w/B_w)_{rms}=5\%$. The specific random sequence examined is one which gave an efficiency close to the ensemble average, and is shown in Fig. 8. A comparison of the amplification of the radiation for the ideal wiggler and for this choice of wiggler imperfections is shown in Fig. 9. It is evident that the total extracted power drops from 8.9 MW for the ideal wiggler to approximately 8.7 MW for this choice of wiggler imperfections. The motion of the beam center in the wiggler-plane corresponding to the interaction in this particular choice of wiggler imperfections is shown in Fig. 10. It is clear from the figure that while the specific motion of the beam center has changed from that shown in Fig. 7 for an ideal wiggler, the qualitative character of the motion has not. The electron beam is kicked off-axis many times during the course of the interaction as in the case of the ideal wiggler. In this case, these perturbations are due both to the large amplitude radiation field and the wiggler imperfections. Indeed, the combined effects of the large amplitude radiation field and the wiggler imperfections in this case has led to a much smaller maximum displacement from the symmetry plane than was found in Fig. 7 for the ideal wiggler. However, there is still no coherent walk off of the beam, and while the beam may be displaced in one direction from the symmetry plane at one point in the in-

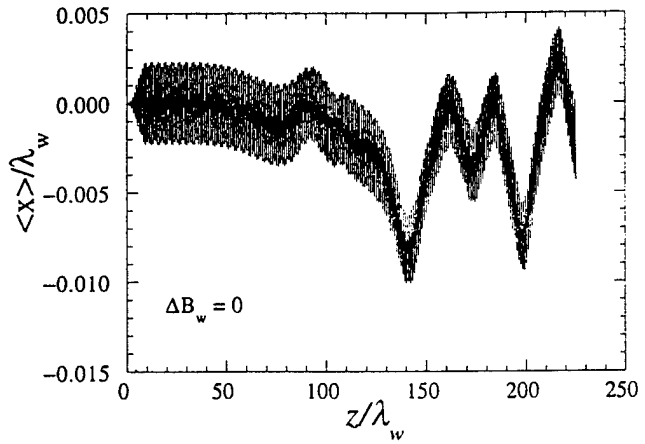

FIG. 7. Motion of the beam center versus axial position in an ideal wiggler.

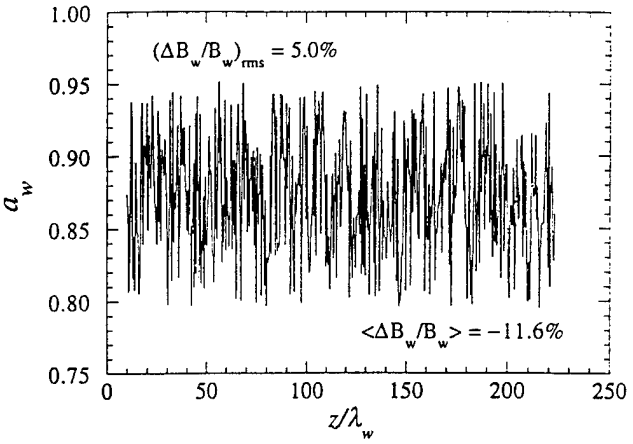

FIG. 8. Plot of the wiggler parameter for a specific random sequence.

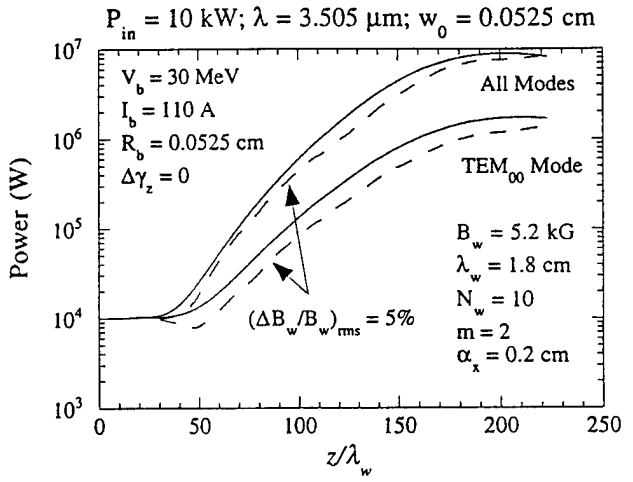

FIG. 9. Evolution of the power for an ideal wiggler (solid line) and for the random wiggler variations (dashed line) shown in Fig. 8.

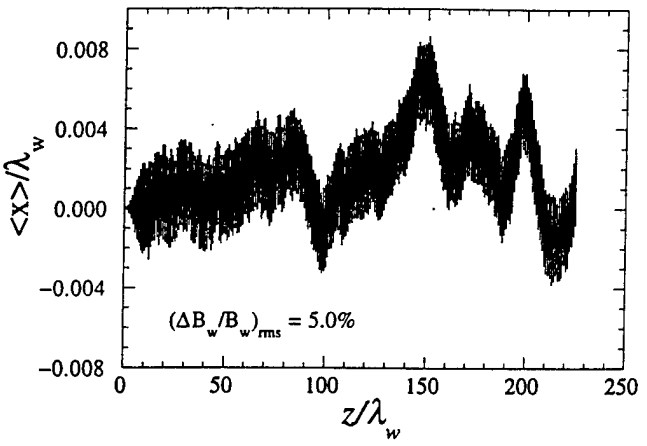

FIG. 10. Motion of the beam center versus axial position subject to wiggler imperfections.

teraction, it is displaced in the opposite direction at another point. The net result is that the beam center has returned to a point near the symmetry plane at the end of the interaction region.

The conclusions to be drawn from these results are twofold. In the first place, it does not appear that there is any serious walk off of the beam. The beam displacement from the symmetry plane can be relatively large even in the absence of wiggler imperfections when the radiation amplitude becomes large, but the effect of wiggler imperfections does not magnify this effect and can even counter it. Thus, MEDUSA does not predict any cumulative walkoff of the beam due to the wiggler imperfections. In the second place, the speculation that wiggler imperfections might result in a severe degradation in the gain and efficiency are exaggerated. The radiation is guided by the interaction. Displacements of the beam from the symmetry plane can result in the presence of a large component of higher-order modes which might negatively impact the ultimate use of the FEL; however, as attested by the fact that the maximum efficiency found from one-dimensional phase trapping arguments is close to that found by MEDUSA, the ultimate extracted power is not seriously affected. In general, therefore, the effect of wiggler imperfections is not severe, and is much less important a constraint on FEL design than the emittance of the electron beam.

B. X-ray FEL

The x-ray FEL parameters under study here correspond to the proposed LCLS at SLAC. Due to the lack of sources to drive a MOPA in this spectral band, the device would operate in the SASE mode using the SLAC linac at an energy of 15 GeV. The beam pulses would be compressed in the axial direction to achieve a peak current of 5 kA, and would have a radial extent of only 16 μm. The proposed wiggler would achieve a 16-kG amplitude at a period of 2.7 cm, and it is assumed for this study that the entry taper region is 10 wiggler periods in length. This implies a resonant wavelength in the neighborhood of 1.4 Å. As in the infrared example discussed previously, it shall also be assumed that the initial power is 10 kW in the TEM_{00} mode, and that the initial spot size matches the beam radius at 16 μm. The parabolic pole face wiggler (1) is used to study the interaction for an ideal wiggler, and the second wiggler (2) is to examine the effect of wiggler imperfections.

The issue of quantum mechanical effects should be discussed for this configuration if only for the purpose of dismissing them. Quantum mechanical effects can be neglected if the spreading of the electron wave packet over the length of the wiggler is less than the radiation wavelength. This can be formulated as [17,30]

$$\Delta z = \frac{\lambda_c L}{\gamma_0 \gamma_w} \ll \lambda \,, \tag{25}$$

where Δz denotes the spreading of the electron wave packet, $\lambda_c \equiv h/m_e c$ is the Compton wavelength, and L is the length of the wiggler. For the parameters of interest to the LCLS, the spreading of the wave packet over a wiggler length of 30 m is $\Delta z \approx 9.2\times 10^{-4}$ Å, which is approximately three orders of magnitude less than the 1.4-Å wavelength. At this length of wiggler, therefore, quantum mechanical effects can be neglected from the treatment. However, this is the closest that any operational or proposed FEL has approached to the regime where quantum mechanical effects are important, and if a wiggler of 100 m or more in length were required, then quantum mechanical effects might become important. Finally, another requirement for the neglect of quantum mechanical effects is that the electron recoil on emission of a photon is small. This can be formulated by the requirement that the frequency downshift in the emitted photon due to the electron recoil is less than the gain linewidth, and results in a criterion identical to (25).

First consider the interaction for the TEM_{00} mode alone. The spectrum is shown in Fig. 11 in which we plot the extraction efficiency versus wavelength for an ideal beam and both with and without the self-fields. As shown in the figure, the efficiency subject to the inclusion of the self-fields peaks at 0.97% at a wavelength of ap-

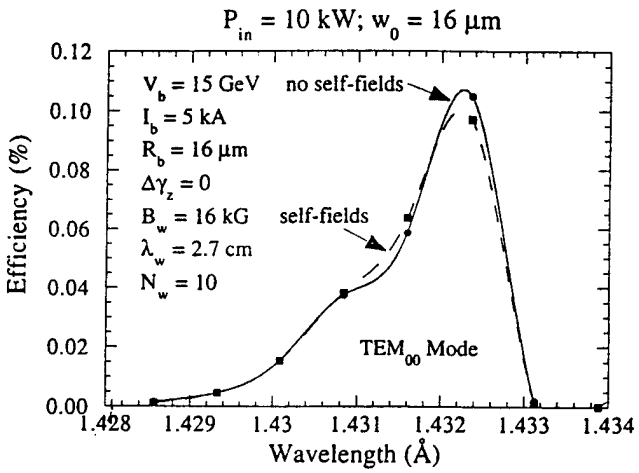

FIG. 11. Efficiency versus wavelength for single mode propagation.

proximately 1.4323 Å. The effect of the self-fields is small, but results in a decrease in the peak efficiency of approximately 7.5%. In contrast to the results for the infrared example, the effect of self-fields can result in slight enhancements in the efficiency in narrow parts of the spectrum.

In this example, it is found that adequate convergence of the mode superposition is achieved using 38 modes. A plot of the power as a function of axial position is shown in Fig. 12 for an ideal beam at a wavelength of 1.4323 Å. The interaction saturates at a power of approximately 98 GW for an efficiency of 0.13% over an interaction length of 30 m. This contrasts with a saturated power level of about 73 GW over a saturation length of 52 m, which is found using the TEM_{00} mode alone. As a consequence, as in the infrared example, while the TEM_{00} mode is dominant, it constitutes only about 27% of the total power at saturation. The relative mode amplitudes at saturation are shown in Fig. 13 and are normalized to the power in the TEM_{00} mode. It is clear that, as in the infrared example, the dominant modes are the TEM_{00}, TEM_{02}, TEM_{20}, TEM_{04}, and TEM_{40}, but substantial amounts of power are contained in the higher-order modes.

As might be expected, the interaction for the x-ray FEL is more sensitive to the axial energy spread than the infrared case. The average growth rate associated with the interaction in Fig. 12 is $|\mathrm{Im}k|/k_w \approx 1.15\times10^{-3}$, which implies that the transition to the thermal regime is found for $\Delta\gamma_z/\gamma_0 \approx 0.05\%$. A plot of the variation in the extraction efficiency and the saturation length at a wavelength of 1.4323 Å spanning the thermal transition regime is shown in Fig. 14. As shown in the figure, the extraction efficiency drops by more than half as the axial energy spread increases to 0.1%, and by 39% at the thermal transition. The growth rate also decreases, and the saturation length increases from about 30 m for an ideal beam to 39 m at the high end of this range. As such, it is necessary to keep the beam emittance as small as possible to remain far below the thermal transition for optimal performance, and the achievement of near-peak

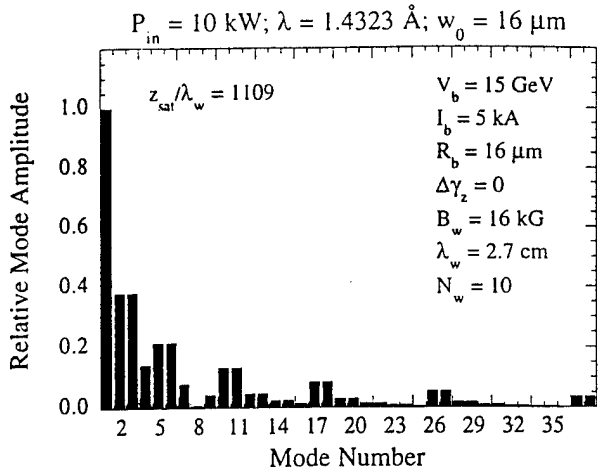

FIG. 13. Relative mode amplitudes at saturation as normalized to the power in the TEM_{00} mode.

efficiencies requires that $\Delta\gamma_z/\gamma_0 \leq 0.015\%$.

The effect of wiggler imperfections on the LCLS design is studied using the second wiggler model (2). The identical beam ($V_b=15$ GeV, $I_b=5$ kA, $R_b=16$ μm), wiggler ($B_w=16$ kG, $\lambda_w=2.7$ cm, $N_w=10$), and radiation ($P_{in}=10$ kW, $\lambda=1.4323$ Å, $w_0=16$ μm, 38 modes) parameters are used for this purpose as were used previously with the parabolic pole face wiggler model, except that we also assume that $m=2$ and $\alpha_x=0.1$ cm for the second wiggler model. The evolution of the power with axial position for an ideal wiggler is shown in Fig. 15 for purposes of comparison. As is evident in the figure, the power saturates at approximately 97 GW over a length of 30 m for an overall extraction efficiency of about 0.13%. This is very close to the results found for the parabolic pole face wiggler (97 MW over a saturation length of 30 m).

The motion of the beam center in the x direction (the direction of the principal wiggler-induced transverse velocity) is shown in Fig. 16 for the ideal wiggler case corresponding to that shown in Fig. 15. In contrast to the re-

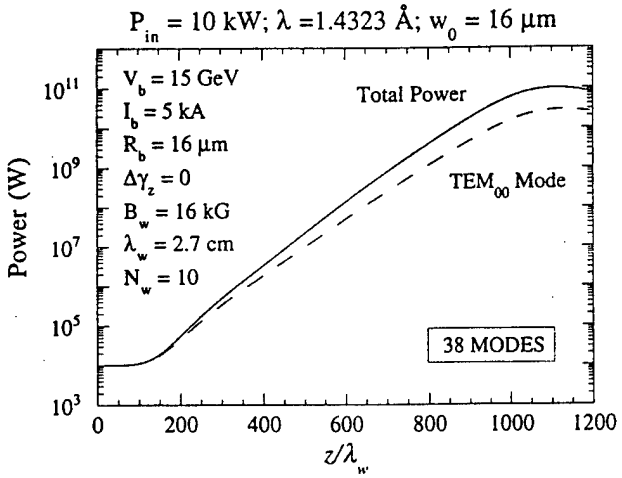

FIG. 12. Evolution of the power versus axial position.

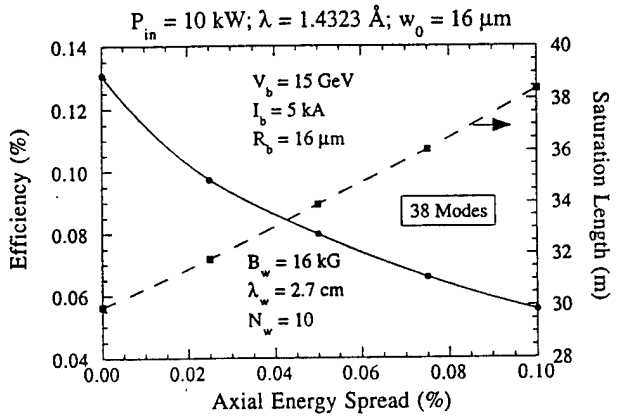

FIG. 14. Variation in the efficiency and saturation length versus axial energy spread.

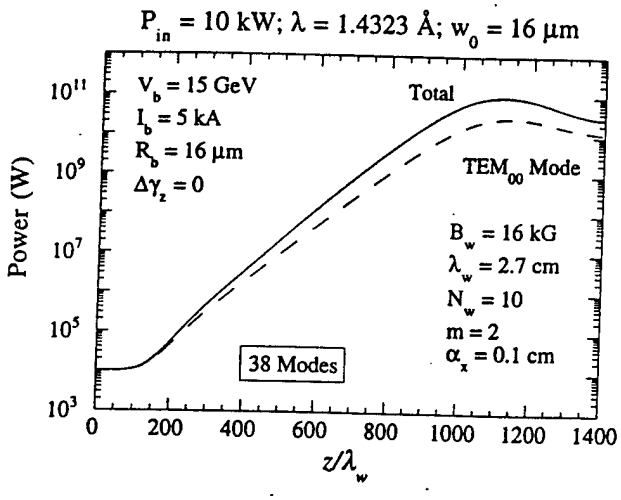

FIG. 15. Evolution of the power versus axial position for the LCLS parameters in an ideal wiggler using the second wiggler model. The solid (dashed) line denotes the total (TEM_{00} mode) power.

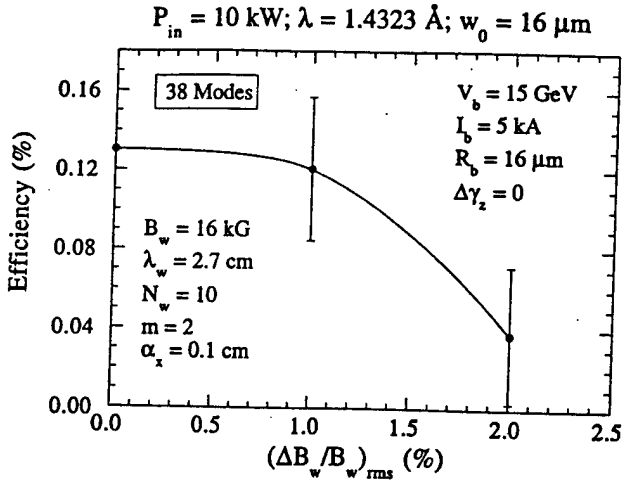

FIG. 17. Variation in the ensemble-averaged efficiency for $N_p=2$.

sults found for the 30-MeV beam and 3.5-μm radiation (see Fig. 7), the wiggler motion for the LCLS parameters in the absence of wiggler imperfections is extremely uniform. There is very little wandering of the beam center due to the high-amplitude radiation field, and the beam exhibits the bulk wiggler motion as well as the expected betatron oscillations. This is due to the increased "stiffness" of the 15-GeV beam, and accounts for the fewer number of modes needed relative to the infrared example.

The effect of wiggler imperfections for LCLS parameters is greater than for the infrared example, but still not severe. In studying the effect of wiggler imperfections, it is assumed, as in the preceding example, that the random wiggler amplitude variations occur every half wiggler period (i.e., $N_p=2$). The variation in the efficiency with increasing values of $(\Delta B_w/B_w)_{rms}$ is shown in Fig. 17. As in the preceding example, the dots in the figure represent the ensemble average over 35 randomly chosen amplitude fluctuation distributions, and the "error bars" denote the standard deviations. It is clear from the figure that the efficiency remains relatively unaffected by the wiggler imperfections for $(\Delta B_w/B_w)_{rms} \leq 1\%$, and decreases rapidly thereafter. The efficiency for the ideal wiggler in this case is 0.13%, which decreases to 0.12% for $(\Delta B_w/B_w)_{rms}=1\%$. This represents a negligible degradation in the interaction efficiency, and it is reasonable to conclude that the LCLS will operate up to nearly optimum efficiencies as long as the rms wiggler imperfections are kept to within this limit.

However, the LCLS parameters do exhibit a greater sensitivity to wiggler imperfections than was found for the preceding infrared wavelength FEL example. This is expected due to the narrower radius of the 15-GeV beam. In general, the smaller the beam radius, the more difficult it is for the interaction to guide the radiation. However, this is offset in the present case by the greater stiffness of the 15-GeV beam, which requires a relatively large level of wiggler imperfections to cause any appreciable beam deflection.

In order to illustrate the effect of the wiggler imperfections, we turn to a more detailed consideration of the orbit dynamics for a specific choice of wiggler imperfections. For this purpose, we compare the motion of the beam center for an ideal wiggler shown in Fig. 16 with the corresponding motion for $(\Delta B_w/B_w)_{rms}=1\%$ and the specific random sequence which resulted in an efficiency of 0.12% (i.e., which was chosen to the ensemble average). The variation in the wiggler parameter a_w for this case is shown in Fig. 18, and the motion of the beam center for this choice is shown in Fig. 19. It is clear from Fig. 19 that the variation in the beam center is relatively slow for this case, and that there is no coherent walkoff of the beam.

In this example, the beam is able to guide the radiation, and although the maximum displacement of the beam center relative to that found for an ideal wiggler is approximately 50% that of the maximum bulk wiggler-

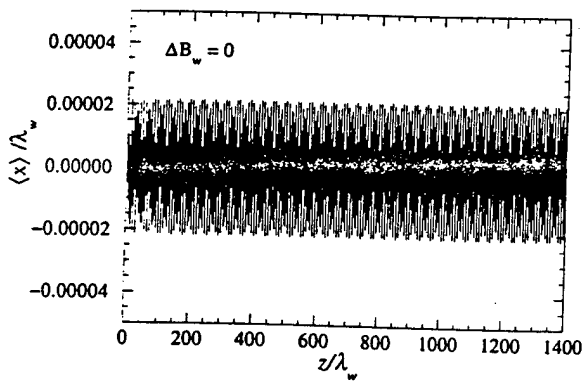

FIG. 16. Motion of the beam center versus axial position in an ideal wiggler for the LCLS parameters.

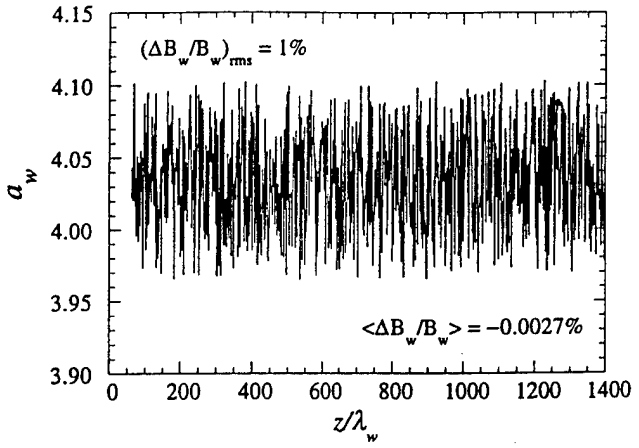

FIG. 18. Plot of the wiggler parameter for a specific random sequence.

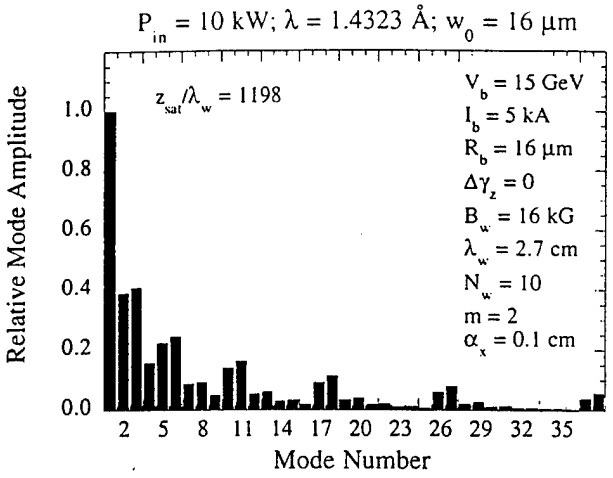

FIG. 20. Relative mode amplitudes at saturation normalized to the TEM_{00} mode subject to the wiggler imperfections shown in Fig. 18.

induced oscillation (at $z/\lambda_w \approx 150$), there is little degradation in the interaction efficiency. In order to illustrate the effect of the optical guiding, consider the relative mode amplitudes at saturation. The relative mode spectrum for this case as shown in Fig. 20. A comparison of the mode amplitudes shown in Fig. 20 with those shown in Fig. 13 for the ideal wiggler indicates a somewhat larger amount of power in the higher-order modes. This reflects the fact that the beam sweeps out a greater cross sectional area for this case than for the ideal wiggler, which implies that the radiation has been guided during the course of the interaction.

The overall conclusion from this study of the effects of beam energy spread and wiggler imperfections for the LCLS parameters is that optimal performance requires that the axial energy spread be kept small enough that $\Delta\gamma_z/\gamma_0 \leq 0.01\%$ and that the rms wiggler tolerances be kept to $(\Delta B_w/B_w)_{rms} \leq 1\%$. In general, the conclusion formed on the basis of both the infrared and x-ray examples studied here is that the electron beam quality imposes a more severe constraint on the interaction than does the wiggler quality.

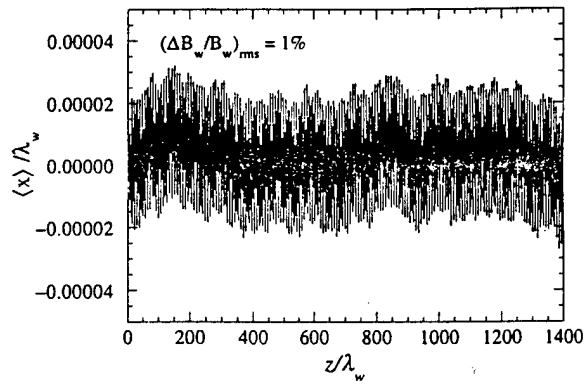

FIG. 19. Motion of the beam center versus axial position subject to wiggler imperfections.

IV. SUMMARY AND DISCUSSION

In this paper, a three-dimensional nonlinear formulation of the interaction in short-wavelength FELs is presented and used to evaluate the performance of several tentative experimental designs. For this purpose, the analysis is based upon a representation of the electromagnetic field as a superposition of the Gauss-Hermite optical modes which is appropriate for the planar wiggler configuration which is also assumed. Note that the Gauss-Laguerre modes would form the appropriate basis for a helical wiggler configuration. A set of coupled nonlinear differential equations is derived for the evolution of the amplitude and phase of each mode which is then integrated in conjunction with the three-dimensional Lorentz force equations for an ensemble of electrons.

It is important to emphasize that no wiggler average is performed on the Lorentz force equations, and that the orbits are integrated in the complete field structure including the magnetostatic wiggler, the electromagnetic fields, and the self-electric and self-magnetic fields formed by the bulk charge and current densities of the beam. As a result, it is necessary only to specify the characteristics of the beam upon entry to the wiggler and the emittance growth and evolution of the electron beam due to such effects as (1) the injection of the beam into the wiggler, (2) transverse inhomogeneities of the wiggler field (including betatron oscillations), (3) the interaction with the electromagnetic field, (4) the self-electric and self-magnetic fields of the beam, and (5) wiggler imperfections are implicitly included in the treatment.

It should be remarked in regard to the modeling of wiggler imperfections that all that is necessary is to specify the variation in the wiggler field amplitude as a function of axial position, and the simulation will self-consistently describe the response of the electron beam. Because of this, it is possible to model the imperfections of any specific wiggler magnet, although this was not attempted in the present work.

No attempt has been made to match the beam into the wiggler in the sense that the beam emittance and radius are selected to ensure that the beam envelope remains constant. In the opinion of the author, this is a pointless and counterproductive procedure both from an experimental and theoretical standpoint. Radiation growth is a microscopic process in which resonant electrons interact with the radiation field, and give rise to both amplification and refractive guiding of the wave. The interaction is extremely sensitive to the emittance of the beam, and even a small axial energy spread can result in a substantial reduction in the peak extraction efficiency. Efforts to match the beam are motivated by the desire to achieve a uniform beam envelope in the hope that this will yield an improved overlap between the electron beam and the radiation field or, in other words, to maximize the filling factor and the growth rate. However, the overlap between the beam and the radiation is a macroscopic process depending upon the growth and refractive guiding determined by the microscopic interaction. Hence, it is more important to minimize the emittance in a FEL than it is to match the electron beam to achieve a uniform envelope. Variations in the beam centroid due to the wiggler motion and the beam envelope due to betatron oscillations will merely result in guiding of the signal, while an enhanced emittance which may be necessary to match the beam will certainly result in a degradation in the extracted power. The most important consideration in the design of a FEL, therefore, is to minimize the emittance.

In general, the conclusion formed on the basis of both the infrared and x-ray examples studied here is that the electron beam quality must be kept small enough that the interaction is far from the transition to the regime where thermal effects become important. However, the interaction was found to be relatively insensitive to wiggler imperfections. In this regard, it should be emphasized that no coherent walkoff of the beam has been detected in simulation, and that the optical guiding of the radiation field is able to counter much of the jitter of the beam. Hence, it is found that electron beam quality imposes a much more severe constraint on the interaction than does the wiggler quality.

ACKNOWLEDGMENTS

The author would like to acknowledge ongoing discussions with Dr. S. Krinsky and Dr. L. H. Yu at Brookhaven National Laboratory and Dr. R. Tatchyn and Dr. Whittum at the Stanford Linear Accelerator Center. This work was supported by the Office of Naval Research. The computational work was supported in part by a grant of HPC time from the DoD HPC Shared Resource Center CEWES on a Cray C90 and a Y-MP, and in part by a grant of HPC time from the DoD HPC Center NAVO on a Cray C90.

[1] R. M. Phillips, IRE Trans. Electron Dev. ED-7, 231 (1960).
[2] L. R. Elias, W. M. Fairbank, J. M. J. Madey, G. J. Ramian, H. A. Schwettman, and T. I. Smith, Phys. Rev. Lett. **36**, 717 (1976).
[3] K. L. Felch, L. Vallier, J. M. Buzzi, P. Drossart, H. Boehmer, H. J. Doucet, B. Etlicher, and C. Rouillé, IEEE J. Quantum Electron. **QE-17**, 1354 (1981).
[4] R. K. Parker, R. H. Jackson, S. H. Gold, H. P. Freund, V. L. Granatstein, P. C. Efthimion, M. Herndon, and A. K. Kinkead, Phys. Rev. Lett. **48**, 238 (1982).
[5] M. Billardon, P. Ellaume, J. M. Ortega, C. Bazin, M. Bergher, M. Velghe, D. A. G. Deacon, and Y. Petroff, Phys. Rev. Lett. **51**, 1652 (1983).
[6] R. W. Warren, B. E. Newnam, J. G. Winston, W. E. Stein, L. M. Young, and C. A. Brau, IEEE J. Quantum Electron. **QE-19**, 391 (1983).
[7] J. Fajans, G. Bekefi, Y. Z. Yin, and B. Lax, Phys. Rev. Lett. **53**, 246 (1984).
[8] J. M. Slater, T. Churchill, D. C. Quimby, K. E. Robinson, D. Shemwell, A. Valla, A. A. Vetter, J. Adamski, W. Gallagher, R. Kennedy, B. Robinson, D. Shoffstall, E. Tyson, and A. Yeremian, Nucl. Instrum. Methods Phys. Res. Sect. A **250**, 228 (1986).
[9] J. C. Goldstein, B. E. Newnam, R. W. Warren, and R. L. Sheffield, Nucl. Instrum. Methods Phys. Res. Sect. A **250**, 4 (1986).
[10] J. Masud, T. C. Marshall, S. P. Schlesinger, and F. G. Yee, Phys. Rev. Lett. **56**, 1567 (1986).
[11] T. J. Orzechowski, B. R. Anderson, J. C. Clark, W. M. Fawley, A. C. Paul, D. Prosnitz, E. T. Scharlemann, S. M. Yarema, D. B. Hopkins, A. M. Sessler, and J. Wurtele, Phys. Rev. Lett. **57**, 2172 (1986).
[12] L. R. Elias, IEEE J. Quantum Electron. **QE-23**, 1470 (1987).
[13] T. I. Smith, H. A. Schwettman, R. Rohatgi, Y. Lapierre, and J. Edighoffer, Nucl. Instrum. Methods Phys. Res. Sect. A **259**, 1 (1987).
[14] V. N. Litvinenko and V. N. Vinokurov, Nucl. Instrum. Methods Phys. Res. Sect. A **304**, 66 (1991).
[15] J. M. Ortega, M. Bergher, R. Chaput, A. Dael, M. Velghe, Y. Petroff, J. C. Bourdon, R. Belbeoch, P. Brunet, Y. Dabin, B. Mouton, J. P. Perrine, E. Plouvier, R. Pointal, M. Renard, M. Roch, J. Rodier, P. Roudier, Y. Thiery, P. Bourgeous, P. Carlos, C. Hezard, J. Fagot, J. L. Fallou, P. Garganne, J. C. Malglaive, and D. T. Tran, Nucl. Instrum. Methods Phys. Res. Sect. A **285**, 97 (1989).
[16] D. A. Jaroszynzki, R. J. Bakker, A. F. G. van der Meer, M. Oepts, and P. W. van Amersfoort, Phys. Rev. Lett. **71**, 3798 (1993).
[17] H. P. Freund and T. M. Antonsen, Jr., *Principles of Free-electron Lasers* (Chapman & Hall, London, 1992).
[18] H. P. Freund and T. M. Antonsen, Jr., *Principles of Free-electron Lasers* (Ref. [17]), Chap. 5.
[19] A. K. Ganguly and H. P. Freund, Phys. Rev. A **32**, 2275 (1985).
[20] H. P. Freund, Phys. Rev. A **37**, 3371 (1988).
[21] H. P. Freund, R. H. Jackson, and D. E. Pershing, Phys.

Fluids B 5, 2318 (1993).
[22] H. Winick, K. Bane, R. Boyce, G. Loew, H. D. Nuhn, J. Paterson, P. Pianetta, T. Raubenheimer, J. Seeman, R. Tatchyn, V. Vylet, C. Pellegrini, J. Rosenzweig, G. Travish, D. Prosnitz, E. T. Scharlemann, K. Halbach, K. J. Kim, and M. Xie, in *Proceedings of the 1993 IEEE Particle Accelerator Conference* (IEEE, Piscataway, NJ, 1993), p. 1445.
[23] H. P. Freund and R. H. Jackson, Phys. Rev. A **45**, 7488 (1992).
[24] H. P. Freund and R. H. Jackson, Nucl. Instrum. Methods Phys. Res. Sect. A **331**, 461 (1993).
[25] H. Bluem, R. H. Jackson, H. P. Freund, D. E. Pershing, and V. L. Granatstein, Phys. Rev. Lett. **67**, 824 (1991).
[26] D. Marcuse, *Light Transmission Optics* (Van Nostrand, New York, 1982), Chap. 6.
[27] D. E. Pershing, R. D. Seeley, R. H. Jackson, and H. P. Freund, Nucl. Instrum. Methods Phys. Res. Sect. A **358**, 104 (1995).
[28] H. Bluem, R. H. Jackson, H. P. Freund, D. E. Pershing, and V. L. Granatstein, Phys. Rev. Lett. **67**, 824 (1991).
[29] M. J. Schmitt and B. D. McVey, Nucl. Instrum. Methods Phys. Res. Sect. A **304**, 571 (1991).
[30] C. A. Brau, *Free-Electron Lasers* (Academic, Boston, 1990).

APPENDIX II

Non-Wiggler-Averaged Theory of Short Wavelength Free-Electron Lasers

H.P. Freund
Nucl. Instrum. Meth. A375, 284 (1995)

ELSEVIER

INSTRUMENTS & METHODS IN PHYSICS RESEARCH Section A

Non-wiggler-averaged theory of short wavelength free-electron lasers

H.P. Freund[1]

Naval Research Laboratory, Washington, DC 20375, USA

Abstract

Short wavelength free-electron lasers are studied using a 3D nonlinear simulation using a superposition of Gauss–Hermite modes. The differential equations governing each mode are solved along with the 3D Lorentz force equations (no wiggler average is used) for an ensemble of electrons. This permits the self-consistent modeling of (1) beam injection, (2) emittance growth, (3) wiggler imperfections and (4) beatatron oscillations. Simulations are performed for a 1.4 Å FEL. Results indicate that beam emittance is the crucial limiting factor requiring $\Delta\gamma_z/\gamma_0 \leq 0.01\%$. The radiation is sufficiently guided that no severe degradation is found in the efficiency for moderate levels of wiggler fluctuations.

1. Introduction

The free-electron laser (FEL) has operated from the microwave through the ultraviolet spectra, and relies upon stimulated scattering due to the ponderomotive potential created of the beating of the wiggler and the radiation fields [1]. FELs have been configured as master oscillator power amplifiers, oscillators, and super-radiant amplifiers. The term *super-radiant amplifier* was originally used for a device in which the radiation grows from noise in a single pass through the wiggler; however, the term Self-Amplified Spontaneous Emission (SASE) has come into wide use.

In this paper, a 3D slow-time-scale nonlinear formulation of the interaction based on the Gauss–Hermite modes for short wavelength (near infrared wavelengths and below) FELs is described and applied to study an X-ray FEL. The differential equations governing each mode are integrated simultaneously with the 3D Lorentz force equations for an ensemble of electrons subject to the wiggler, electromagnetic, and static self-fields of the beam [2,3]. Collective Raman effects due to the beam space-charge waves are neglected.

It is important to emphasize that there is no average of the Lorentz force equations. This permits the simulation of the entire wealth of 3D phenomena including emittance growth in the injection of the beam into the wiggler and during the course of the interaction, the effect of transverse inhomogeneities in the fields which manifests as an effective energy spread leading to resonance broadening and betatron oscillations, optical guiding of the radiation field by the beam, and the self-consistent modeling of wiggler imperfections.

2. The mathematical formulation

The configuration of interest is that of a planar wiggler, and the electromagnetic field is expressed in terms of the Gauss–Hermite modes. The planar wiggler model used is

$$B_{w,x}(x) = \left[\left(\sin k_w z - \frac{\cos k_w z}{k_w}\frac{d}{dz}\right)B_w(z)\right] \times \left[\sinh k_w y - \frac{Y(k_w y)}{2k_w^2}\frac{d^2}{dx^2}\right]\frac{1}{k_w}\frac{d}{dx}X(x), \quad (1)$$

$$B_{w,y}(x) = \left[\left(\sin k_w z - \frac{\cos k_w z}{k_w}\frac{d}{dz}\right)B_w(z)\right] \times \left[\cosh k_w y - \frac{k_w y \sinh k_w y}{2k_w^2}\frac{d^2}{dx^2}\right]X(x), \quad (2)$$

$$B_{w,z}(x) = B_w(z)\cos k_w z\left[\sinh k_w y - \frac{Y(k_w y)}{2k_w^2} \times \left(1 + \frac{1}{k_w^2}\frac{d^2}{dx^2}\right)\frac{d^2}{dx^2}\right]X(x), \quad (3)$$

where B_w is the wiggler amplitude, $k_w \equiv 2\pi/\lambda_w$ is the wavenumber for period λ_w, $Y(k_w y) \equiv k_w y \cosh k_w y - \sinh k_w y$, and $X(x) \equiv 1 + (x/\alpha_x)^{2m}/2$ for order m and scale length α_x. This field satisfies $\nabla \cdot B_w = (\nabla \times B_w)_z = 0$, while $(\nabla \times B_w)_\perp$ is small.

The wiggler amplitude models adiabatic beam injection

[1] Permanent address: Science Applications International Corp., McLean, VA 22102.

0168-9002/96/$15.00
SDI 0168-9002(95)01352-0

and wiggler imperfections, and we write $B_w(z) = B_w^{(s)}(z) + \Delta B_w(z)$, where $B_w^{(s)}$ describes the entry taper and the uniform region, and the random component ΔB_w can either be chosen using a random number generator or the measured imperfections from an actual wiggler. We choose

$$B_w^{(s)}(z) = \begin{cases} B_w \sin^2\left(\dfrac{k_w z}{4N_w}\right); & 0 \le z \le N_w \lambda_w \\ B_w \quad ; & N_w \lambda_w < z \end{cases}, \tag{4}$$

where B_w is the uniform amplitude, and N_w defines the entry taper length. The random component ΔB_w is determined at regular intervals $\Delta z = \lambda_w / N_p$, and continuously mapped between these points. A sequence $\Delta B_n = \Delta B_w(n\,\Delta z)$ is chosen subject to the restriction that $\Delta B_w = 0$ for $z \le N_w \lambda_w$ to ensure a positive definite amplitude. The variation in $\Delta B_w(z)$ between these points [i.e., $n\,\Delta z \le z \le (n+1)\,\Delta z$] is [4]

$$\Delta B_w(n\,\Delta z + \delta z) = \Delta B_n + [\Delta B_{n+1} - \Delta B_n] \sin^2\left(\frac{\pi}{2}\frac{\delta z}{\Delta z}\right), \tag{5}$$

where $0 \le \delta z \le \Delta z$.

The electromagnetic field is represented by the Gauss–Hermite modes. These can be represented as TEM modes when the wavelength is much less than the spot size. Under this assumption, the vector potential is [5]

$$\delta A(x,t) = \sum_{l,n=0}^{\infty} \delta A_{l,n}(z) \frac{w_0}{w} \exp(-r^2/w^2) H_n\left(\frac{\sqrt{2}y}{w}\right) \times H_l\left(\frac{\sqrt{2}x}{w}\right) \hat{e}_z \sin\varphi_{l,n}, \tag{6}$$

where H_n denote the Hermite polynomials, w_0 is the spot size at the waist, and for frequency and wavenumber $(\omega, k_{l,n})$ the phase is

$$\varphi_{l,n} = \int_0^z dz'\, k_{l,n}(z') + \frac{k_0 r}{2R} - (l+n+1) \times \tan^{-1}\left(\frac{z}{z_0}\right) - \omega t. \tag{7}$$

In addition, $k_0 \equiv \omega/c$, $w^2 \equiv w_0^2(1 + z^2/z_0^2)$, $R(z) \equiv z(1 + z_0^2/z^2)$, and $z_0 \equiv k_0 w_0^2/2$ is the Rayleigh length. The dynamical equations which govern the evolution of each mode are [6]

$$\left[\frac{d^2}{dz^2} + \left(\frac{\omega^2}{c^2} - k_{l,n}^2\right)\right] \delta a_{l,n} = \frac{4\omega_b^2}{c^2} \frac{1}{2^{l+n} l! n!} \frac{w_0}{w} \times \left\langle \frac{v_x}{|v_z|} \exp(-r^2/w^2) H_l\left(\frac{\sqrt{2}x}{w}\right) H_n\left(\frac{\sqrt{2}y}{w}\right) \sin\varphi_{l,n} \right\rangle, \tag{8}$$

and

$$2k_{l,n}^{1/2} \frac{d}{dz}(k_{l,n}^{1/2}\,\delta a_{l,n}) = \frac{4\omega_b^2}{c^2} \frac{1}{2^{l+n} l! n!} \frac{w_0}{w} \times \left\langle \frac{v_x}{|v_z|} \exp(-r^2/w^2) H_l\left(\frac{\sqrt{2}x}{w}\right) H_n\left(\frac{\sqrt{2}y}{w}\right) \cos\varphi_{l,n} \right\rangle, \tag{9}$$

where $\delta a_{l,n} \equiv e\,\delta A_{l,n}/m_e c^2$, ω_b is the plasma frequency, v is the velocity, e and m_e are the electronic charge and rest mass, and c is the speed of light. The average is defined for a monoenergetic initial electron distribution with a pitch angle spread, and is

$$\langle(\cdots)\rangle \equiv \frac{A}{4\pi^2 w_0^2} \int_0^{2\pi} d\phi_0 \int_0^{p_0} dp_{z0}\, \beta_{z0} \exp[-(p_{z0} - p_0)^2/\Delta p_z^2] \times \int_{A_b} \int dx_0\, dy_0\, \sigma_\perp(x_0, y_0) \int_{-\pi}^{\pi} d\psi_0 \sigma_\parallel(\psi_0)(\cdots), \tag{10}$$

where p_0 and Δp_z denote the initial momentum and momentum spread, A_b is the initial beam area, $\varphi_0 \equiv \tan^{-1}(p_{y0}/p_{x0})$, $\beta_{z0} \equiv v_{z0}/c$, ψ_0 is the initial ponderomotive phase, $\sigma_\parallel(\psi_0)$ and $\sigma_\perp(x_0, y_0)$ describe the initial distributions in phase and cross section, and

$$A \equiv \left[\pi \int_0^{p_0} dp_{z0} \exp[-(p_{z0} - p_0)^2/\Delta p_z^2]\right]^{-1}. \tag{11}$$

While this describes a monoenergetic beam, there is an axial energy spread given by

$$\frac{\Delta\gamma_z}{\gamma_0} = 1 - \left[1 + 2(\gamma_0^2 - 1)\frac{\Delta p_z}{p_0}\right]^{-1/2}, \tag{12}$$

where $\gamma_0 \equiv (1 + p_0^2/m_e^2 c^2)^{1/2}$.

The Lorentz force equations are integrated in z and are of the form

$$v_z \frac{d}{dz} p = -e(E^{(s)} + \delta E) - \frac{e}{c} v \times (B_w + B^{(s)} + \delta B), \tag{13}$$

where B_w is the wiggler, δE and δB are the electromagnetic fields, and $E^{(s)}$ and $B^{(s)}$ are the self-electric and -magnetic fields of the beam which are expressed as [3]

$$E^{(s)} = -\frac{m_e}{2e} \omega_b^2 [(x - \langle x\rangle)\hat{e}_x + (y - \langle y\rangle)\hat{e}_y], \tag{14}$$

and

$$B^{(s)} = -\frac{m_e}{2e} \omega_b^2 \langle\beta_z\rangle [(y - \langle y\rangle)\hat{e}_x - (x - \langle x\rangle)\hat{e}_y], \tag{15}$$

where $\langle x\rangle$ and $\langle y\rangle$ specify the beam centroid, and $\langle\beta_z\rangle$ is the average axial velocity. Beam initialization includes the

space-charge depression of $\gamma(r) = \gamma_0 + \omega_b^2(r^2 - R_b^2)/4c^2$ for an initial radius R_b.

3. The numerical analysis

The dynamical equations are solved numerically, and the number of modes is found empirically by successive simulations with increasing numbers of modes until convergence is achieved. The Gauss–Hermite modes are initially at the free-space wavelength and the radiation waist is located at $z = 0$ with a spot size equal to the beam radius. All power is assumed to start in the lowest order mode, and higher order modes grow from zero.

No attempt is made to "match" the beam into the wiggler by selecting the emittance and radius so that the beam envelope remains constant. In the opinion of the author, this is counterproductive. The interaction is microscopic and gives rise to both amplification and guiding, and even a small emittance causes a substantial reduction in the peak efficiency. Efforts to "match" the beam are motivated by a desire to improve the overlap between the beam and the radiation to maximize the filling-factor and the growth rate. However, this overlap describes a macroscopic process depending upon growth and guiding by the microscopic interaction, and it is more important to minimize the emittance than it is to achieve a uniform envelope. Variations in the beam centroid and the beam envelope merely result in guiding of the signal, while an enhanced emittance which may be necessary to "match" the beam will certainly result in a degradation in the extracted power.

An X-ray FEL example is considered corresponding to the proposed linear coherent light source at SLAC [7]. This operates in the SASE mode at a 15 GeV energy, a 5 kA peak current, and a 16 μm beam radius. The wiggler has a 16 kG amplitude, a period of 2.7 cm, and it is assumed that $N_w = 10$, $m = 2$ and $\alpha_x = 0.1$ cm. The resonant wavelength is 1.4323 Å, and an initial power of 10 kW in the TEM_{00} mode is assumed. Convergence is found including the lowest order 38 TEM_{ln} modes (for l and n even). The odd modes do not interact at the fundamental resonance.

The evolution of the power versus z is shown in Fig. 1 for an ideal beam (zero emittance) and wiggler. The saturated power is ≈97 GW after 30 m for an efficiency of about 0.13%. The effect of emittance is shown in Fig. 2 where the efficiency is plotted versus the initial axial energy spread. Optimum performance requires that $\Delta\gamma_z/\gamma_0 \leq 0.01\%$.

In studying the effect of wiggler imperfections, it is assumed that $N_p = 2$. The variation in the efficiency versus $(\Delta B_w/B_w)_{rms}$ is shown in Fig. 3. The dots represent the ensemble average over 35 randomly chosen sequences, and the "error bars" denote the standard deviations.

Now consider the orbit dynamics for the orbit for $(\Delta B_w/B_w)_{rms} = 1\%$ and the specific random sequence which

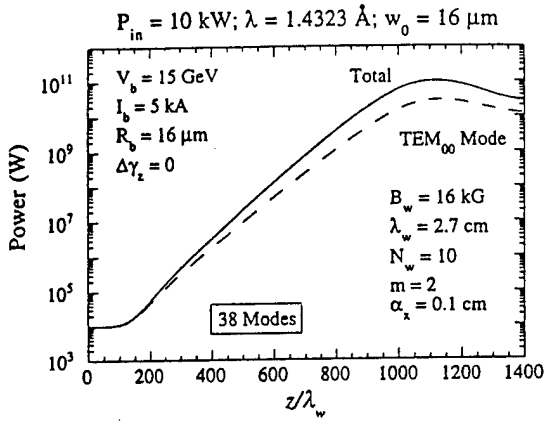

Fig. 1. Evolution of the power versus axial position for an ideal wiggler.

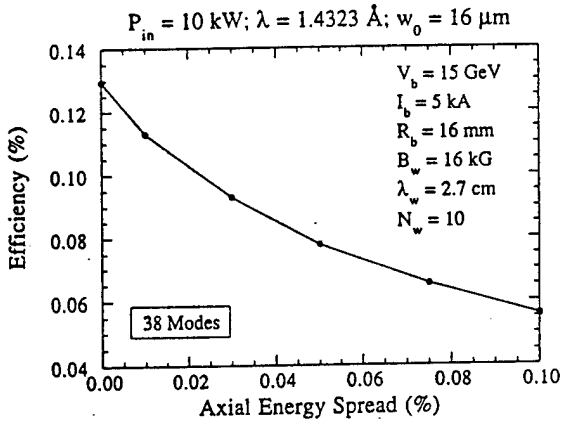

Fig. 2. Variation in the efficiency as a function of axial energy spread.

resulted in an efficiency of 0.12% (i.e., ≈the ensemble average). The variation in the wiggler parameter a_w for this case is shown in Fig. 4, and the motion of the beam center

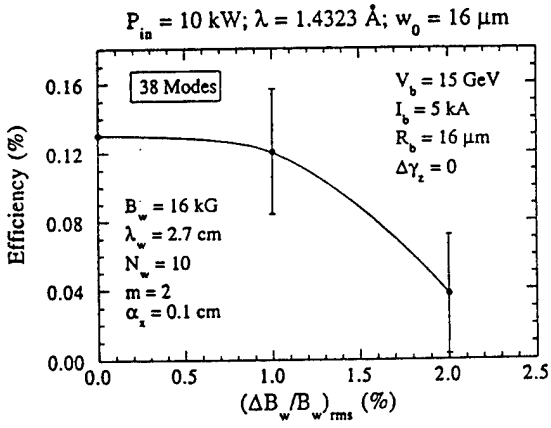

Fig. 3. Variation in the ensemble-averaged efficiency for $N_p = 2$.

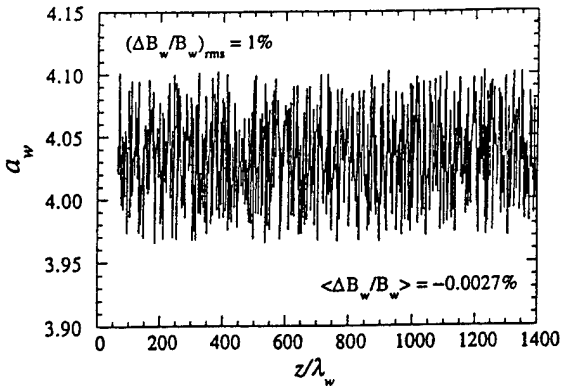

Fig. 4. Plot of the wiggler parameter for a specific random sequence.

is shown in Fig. 5. Note that the variation in the beam center is relatively slow, and there is no coherent walk-off of the beam.

4. Summary and discussion

In this paper, a 3D nonlinear formulation of the interaction in short wavelength FELs is presented based upon a representation of the electromagnetic field as a superposition of the Gauss–Hermite optical modes. A set of coupled nonlinear differential equations is derived for the evolution of each mode which is integrated in conjunction with the 3D Lorentz force equations for an ensemble of electrons. It is important to emphasize that no wiggler-average is performed on the Lorentz force equations. As a result, emittance growth and evolution of the electron beam due to (1) beam injection, (2) transverse wiggler inhomogeneities, (3) the interaction with the electromagnetic field, (4) the self-electric and -magnetic fields of the beam, and (5) wiggler imperfections are implicitly included.

The overall conclusion from this study of the effects of beam energy spread and wiggler imperfections for the LCLS parameters is that the electron beam quality imposes a more severe constraint on the interaction than does the wiggler quality.

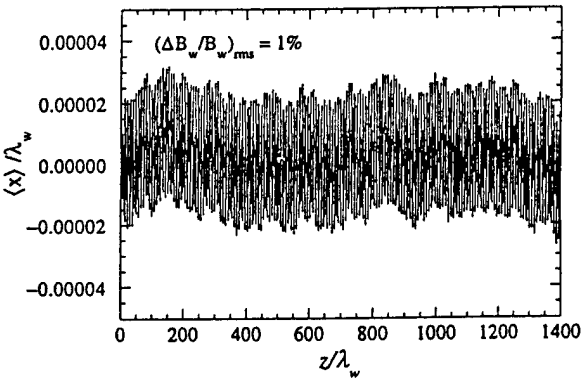

Fig. 5. Motion of the beam center versus axial position subject to wiggler imperfections.

Acknowledgements

The author acknowledges ongoing discussions with Drs. S. Krinsky, L.H. Yu, R. Tatchyn, and D. Whittum. This work was supported by the ONR. Computational work was supported by grants of HPC time from the DoD HPC Shared Resource Center CEWES on a Cray C90 and a Y-MP and the DoD HPC Center NAVO on a Cray C90.

References

[1] H.P. Freund and T.M. Antonsen, Jr., Principles of Free-Electron Lasers (Chapman & Hall, London, 1992).
[2] Ibid., chap. 5.
[3] H.P. Freund, R.H. Jackson and D.E. Pershing, Phys. Fluids B 5 (1993) 2318.
[4] H.P. Freund and R.H. Jackson, Phys. Rev. A 45 (1992) 7488.
[5] D. Marcuse, Light Transmission Optics (Van Nostrand, New York, 1982) chap. 6.
[6] H.P. Freund, Phys. Rev. E 52 (1995) 5401.
[7] H. Winick et al., Proc. 1993 IEEE Particle Accelerator Conf., IEEE Cat. No. 93CH3279-7, p. 1445.

APPENDIX III

Theory of the Free-Electron Laser Based upon a Coaxial Hybrid Wiggler

H.P. Freund, R.H. Jackson, D.E. Pershing, and J.M. Taccetti

Nucl. Instrum. Meth. **A358**, 139 (1995)

ELSEVIER

Nuclear Instruments and Methods in Physics Research A 358 (1995) 139–142

NUCLEAR INSTRUMENTS & METHODS IN PHYSICS RESEARCH Section A

Theory of the free-electron laser based upon a coaxial hybrid wiggler

H.P. Freund *,[1], R.H. Jackson, D.E. Pershing [2], J.M. Taccetti [3]

Naval Research Laboratory, Washington, DC 20375, USA

Abstract

A 3D nonlinear FEL formulation based upon a Coaxial Hybrid Iron (CHI) wiggler is described. The CHI wiggler is created by insertion of a central rod and an outer ring (composed of alternating ferrite and nonferrite spacers) along the axis of a solenoidal. Relatively high field strengths can be achieved with the CHI wiggler at shorter wiggler periods than is possible in many other conventional wiggler designs. The formulation is a slow-time-scale analysis of the interaction of an annular electron beam with the CHI wiggler in a coaxial waveguide. Simulations are presented for W-band operation. The results indicate that operation over a wide bandwidth is practical, and that the uniform- and tapered-wiggler bandwidths are comparable.

1. Introduction

The FEL wavelength depends upon the beam energy and the wiggler parameters as $\lambda \approx (1 + a_w^2)\lambda_w/2\gamma_0^2$, where λ_w is the wiggler period, γ_0 is the bulk relativistic factor, and $a_w \approx 0.0934 B_w \lambda_w$ for an rms wiggler amplitude B_w in kG and λ_w in cm. In the exponential Compton regime, both the gain and efficiency scale as $a_w^{2/3}/\gamma_0$. Hence, the wavelength, gain, and efficiency of the interaction all decrease as the beam energy increases for fixed wiggler parameters. A great deal of effort has been devoted to the design of short period wigglers to operate at short wavelengths with low beam energies. However, this is a self-defeating process since reductions in λ_w often result in reductions in B_w as well with a deleterious impact on the efficiency and gain.

We analyze an FEL based upon a Coaxial Hybrid Iron (CHI) wiggler [1] which is a configuration where a central rod and a coaxial ring of alternating ferrite and nonferrite spacers are inserted into a solenoid. The ferrite (nonferrite) spacers on the central rod are aligned opposite to the nonferrite (ferrite) spacers on the outer ring (see Fig. 1). This produces an azimuthally symmetric field where the amplitude can be increased by increasing the strength of the solenoid. Since the radial component of the field has a minimum at the center of the gap, the field focuses the beam against self-field induced spreading. In addition, the CHI wiggler results in an azimuthal bulk transverse velocity; hence, the interaction is strongest for waves with an azimuthal component.

The ease of construction of this design permits the development of wigglers with extremely short periods by the simple expedient of using thin spacers. In most wiggler designs this is offset by the fact that shorter periods typically result in lower amplitudes and increased field gradients. This is not necessarily the case for the CHI wiggler since high amplitudes can be achieved by using a stronger solenoid. Note also that the gyroresonance between the periodic and axial components can enhance the FEL interaction as well [2].

2. The general formulation

In a source-free region the divergence and curl of the magnetic field vanish, and the field of the CHI wiggler is found by solution of Laplace's equation $\nabla^2 B(r, z) = 0$ for appropriate boundary conditions. We assume that the ferrite spacers result in a step function in the axial field at $r = R_{in}$ and R_{out} such that $B_z(R_{in}, z) = B_{in}$ and $B_z(R_{out}, z) = B_{out}$ along the surface of the dielectric and zero along the surface of the ferrite. Each wiggler period corresponds to the combined length of two spacers, and we

* Corresponding author. Tel. +1 703 734 5840, fax +1 703 821 1134, e-mail: freund@mmace.nrl.navy.mil.

[1] Permanent address: Science Applications International Corp., McLean, VA 22102, USA.

[2] Permanent address: Mission Research Corp., Newington, VA 22122, USA.

[3] Permanent address: University of Maryland, College Park, MD 20742, USA.

SSDI 0168-9002(94)01473-6

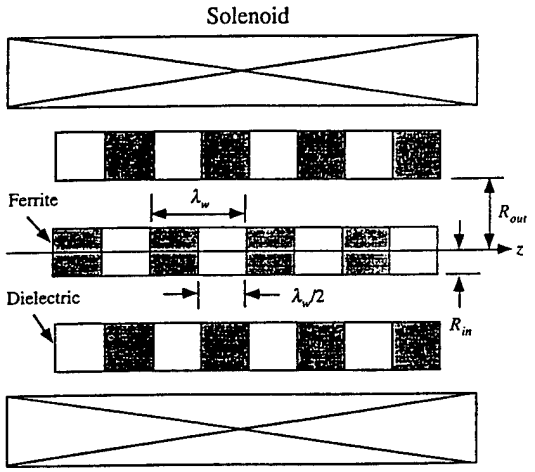

Fig. 1. Schematic illustration of the CHI wiggler configuration.

assume that the length of each spacer is $\lambda_w/2$. The solution which results is [3]

$$B_z(r, z) = B_0 + B_w \sum_{n=1}^{\infty} \cos(nk_w z) \times \frac{[S_n I_0(nk_w r) - T_n K_0(nk_w r)]}{G(nk_w R_{out}, nk_w R_{in})}, \quad (1)$$

and

$$B_r(r, z) = B_w \sum_{n=1}^{\infty} \sin(nk_w z) \times \frac{[S_n I_1(nk_w r) + T_n K_1(nk_w r)]}{G(nk_w R_{out}, nk_w R_{in})}, \quad (2)$$

where $B_w \equiv 2B_0$, $G(\xi, \zeta) \equiv I_0(\xi)K_0(\zeta) - I_0(\zeta)K_0(\xi)$,

$$S_n \equiv \left(\frac{2}{n\pi}\right) \sin\left(\frac{n\pi}{2}\right)\left[K_0(nk_w R_{in}) + K_0(nk_w R_{out})\right] \quad (3)$$

and

$$T_n \equiv \left(\frac{2}{n\pi}\right) \sin\left(\frac{n\pi}{2}\right)\left[I_0(nk_w R_{in}) + I_0(nk_w R_{out})\right]. \quad (4)$$

This is in agreement with the results of the Poisson/Superfish family of magnetics codes [4].

Now consider the dynamical equations which govern the electromagnetic fields and the electron beam. Consider propagation in a coaxial waveguide with inner and outer radii a and b. The neglect of space-charge effects is valid as long as $\omega_b/ck_w < \gamma_z^3 v_w^2/8\gamma_0 c^2$, where ω_b is the ambient plasma frequency, v_w is the bulk transverse wiggler velocity, and $\gamma_z = (1 - v_\parallel^2/c^2)^{-1/2}$ for a bulk streaming velocity $v_\parallel$. Space-charge effects can also be neglected if (1) the wavelength is less than the Debye length and the space-charge waves are subject to strong Landau damping, or (2) the bandwidth of the interaction is greater than the plasma frequency [5].

The boundary conditions at the walls of the coaxial waveguide are satisfied by a superposition of the TE, TM, and TEM modes of the waveguide. We limit the discussion here to the TE modes As such, the vector potential can be expressed as

$$\delta A(x, t) = \sum_{\substack{l=0 \\ m=1}}^{\infty} \delta A_{lm}(z)\left[\frac{l}{\kappa_{lm} r} Z_l(\kappa_{lm} r)\hat{e}_r \sin \alpha_{lm} + Z_l'(\kappa_{lm} r)\hat{e}_\theta \cos \alpha_{lm}\right], \quad (5)$$

where for angular frequency ω and wavenumber k_{lm}

$$\alpha_{lm} \equiv \int_0^z dz'\, k_{lm}(z') + l\theta - \omega t, \quad (6)$$

and $\omega^2 = c^2 k_{lm}^2 + c^2 \kappa_{lm}^2$ for a given cutoff κ_{lm}. The cutoffs are given by solution of the dispersion equation $J_l'(\kappa_{lm} a)Y_l'(\kappa_{lm} b) = J_l'(\kappa_{lm} b)Y_l'(\kappa_{lm} a)$, where J_l and Y_l denote the regular Bessel and Neumann functions of order l. The radial polarization functions are $Z_l(\kappa_{lm} r) \equiv J_l(\kappa_{lm} r) + \Delta_{lm} Y_l(\kappa_{lm} r)$, where $\Delta_{lm} \equiv -J_l'(\kappa_{lm} b)/Y_l'(\kappa_{lm} b)$.

The dynamical equations have been described in detail [2] and the results for the TE modes are

$$\left[\frac{d^2}{dz^2} + \left(\frac{\omega^2}{c^2} - k_{lm}^2 - \kappa_{lm}^2\right)\right]\delta a_{lm} = \frac{\omega_b^2}{c^2} H_{lm}\left\langle \frac{v_r}{|v_z|}\frac{l}{\kappa_{lm} r} Z_l(\kappa_{lm} r) \sin \alpha_{lm} + \frac{v_\theta}{|v_z|} Z_l'(\kappa_{lm} r) \cos \alpha_{lm}\right\rangle, \quad (7)$$

$$2k_{lm}^{1/2}\frac{d}{dz}\left(k_{lm}^{1/2}\delta a_{lm}\right) = \frac{\omega_b^2}{c^2} H_{lm}\left\langle \frac{v_r}{|v_z|}\frac{l}{\kappa_{lm} r} Z_l(\kappa_{lm} r) \cos \alpha_{lm} - \frac{v_\theta}{|v_z|} Z_l'(\kappa_{lm} r) \sin \alpha_{lm}\right\rangle, \quad (8)$$

where $\delta a_{lm} \equiv e\delta A_{lm}/m_e c^2$ is the normalized amplitude of the modes, and

$$H_{lm} \equiv \frac{2\kappa_{lm}^2(b^2 - a^2)}{(\kappa_{lm}^2 b^2 - l^2)Z_l^2(\kappa_{lm} b) - (\kappa_{lm}^2 a^2 - l^2)Z_l^2(\kappa_{lm} a)} \quad (9)$$

The electron beam is assumed to be monoenergetic with an axial energy spread determined by an initial (i.e., at $z = 0$) pitch angle spread, and the averaging operator is

$$\langle(\cdots)\rangle \equiv \frac{A}{4\pi A_g}\int_0^{2\pi} d\phi_0 \int_0^{p_0} dp_{z0}\ \beta_{z0} \times \exp\left[-(p_{z0}-p_0)^2/\Delta p_z^2\right] \times \int_{A_g}\int dx_0\, dy_0\ \sigma_\perp(x_0, y_0) \times \int_{-\pi}^{\pi} d\psi_0\ \sigma_\parallel(\psi_0)(\cdots), \quad (10)$$

where $A_g \equiv \pi(b^2 - a^2)$ is the area of the waveguide, $\beta_{z0} \equiv v_{z0}/c$ for the initial axial velocity v_{z0}, $\phi_0 \equiv \tan^{-1}(p_{y0}/p_{x0})$, (p_{x0}, p_{y0}, p_{z0}) denote the initial beam momenta, p_0 and Δp_z denote the initial total momentum of the beam and axial momentum spread respectively, ψ_0 ($\equiv -\omega t_0$, where t_0 is the time at which the particle crosses the $z = 0$ plane) is the initial ponderomotive phase, $\sigma_\perp$ and $\sigma_\parallel$ are the initial distributions of the beam in cross-section and phase, and

$$A \equiv \left[\pi\int_0^{p_0} dp_{z0}\ \exp\left[-(p_{z0}-p_0)^2/\Delta p_z^2\right]\right]^{-1} \quad (11)$$

is a constant. This results in an axial energy spread

$$\frac{\Delta\gamma_z}{\gamma_0} = 1 - \left[1 + 2\left(\gamma_0^2 - 1\right)\frac{\Delta p_z}{p_0}\right]^{-1/2}. \quad (12)$$

The equations for the fields are solved simultaneously with the orbit equations for an ensemble of electrons. We integrate the complete 3D Lorentz force equations

$$v_z \frac{d}{dz}p = -e\delta E - \frac{e}{c}v \times (B_{ext} + \delta B), \quad (13)$$

for each electron, where B_{ext} is the magnetostatic field due to the CHI wiggler, and δE and δB denote the aggregate electromagnetic fields for all the wave modes. By specifying the initial beam conditions and integrating the Lorentz force equations, we model the injection of the beam into the wiggler by means of a tapered wiggler amplitude. This describes any increase in the effective beam emittance in a self-consistent way. In addition, we also consider amplitude tapering for the purpose of efficiency enhancement. In order to describe these effects, we assume that the overall coefficient of the periodic component of the field varies as

$$B_w = \begin{cases} 2B_0 \sin^2\left(\dfrac{k_w z}{4N_w}\right); & z \le N_w\lambda_w, \\ 2B_0; & N_w\lambda_w < z \le z_0, \\ 2B_0\left[1 + k_w\epsilon_w(z - z_0)\right]; & z > z_0, \end{cases} \quad (14)$$

where N_w denotes the number of wiggler periods in the entry taper region, and ϵ_w is the normalized slope of the taper for purposes of efficiency enhancement.

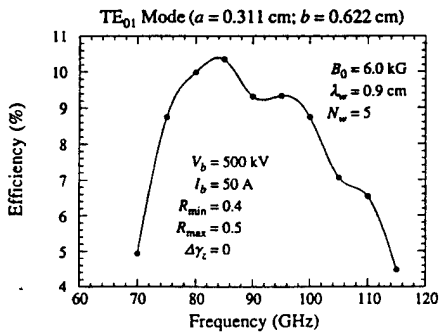

Fig. 2. Variation of the efficiency with frequency in the W-band.

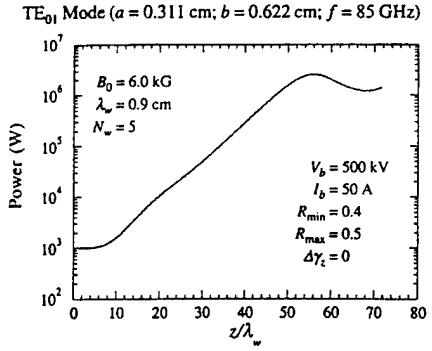

Fig. 3. Evolution of the power with axial position at 80 GHz.

3. Numerical analysis

The dynamical equations are solved for an amplifier configuration in which several modes may propagate at a fixed frequency ω. The initial conditions on the fields are chosen to model the injection of an arbitrary power level for each mode. The initial wavenumbers are chosen by the vacuum state, and the growth rates are initially zero since the amplitude of the periodic component of the CHI wiggler is also initially zero. The initial state of the beam models the injection of a continuous, axisymmetric beam

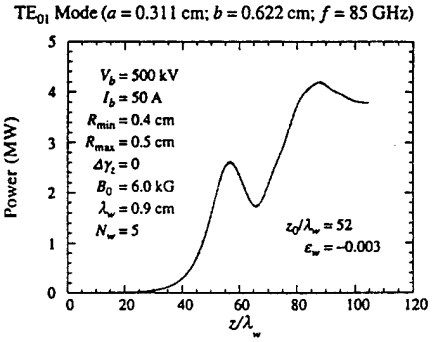

Fig. 4. Evolution of the power with axial distance for an optimized taper at 85 GHz.

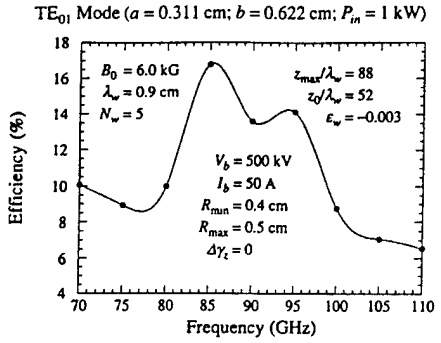

Fig. 5. Variation in the efficiency as a function of frequency in the W-band.

with a uniform density and annular cross-section. For convenience, we choose $R_{in} = a$ and $R_{out} = b$. While we shall be concerned with the fundamental resonance in this paper, both the first and third spatial harmonics of the CHI wiggler are included.

We consider W-band (80–100 GHz) operation and assume the beam has an energy of 500 keV, a current of 50 A, and inner and outer radii of 0.4 cm and 0.5 cm. The CHI wiggler has $B_0 = 6.0$ kG with a period of 0.9 cm and $N_w = 5$ and inner and outer radii of 0.311 cm and 0.622 cm respectively. The mode of interest is the TE_{01} mode with a drive power of 1 kW. Amplification is found over a frequency band from ≈ 70 to 115 GHz although the peak efficiencies are found from 80 to 100 GHz. This is illustrated in Fig. 2 in which we plot the saturation efficiency versus frequency for an ideal beam with $\Delta\gamma_z = 0$. As is evident, the maximum efficiency is approximately 10.3% at 85 GHz for an output power of almost 2.6 MW. However, the efficiency varies relatively little over the entire W-band and the interaction bandwidth is about 33%.

The evolution of the power is shown in Fig. 3 for the case of the peak efficiency at 85 GHz, and exponential growth is evident from the end of the entry taper region to the saturation point at $z/\lambda_w \approx 56$ for an interaction length of 50 cm. The decline in efficiency with increases in the initial axial energy spread is relatively benign, and decreases by less than a factor of two as the energy spread increases to somewhat beyond $\Delta\gamma_z/\gamma_0 \approx 1.25\%$. Thus, good operational efficiencies are expected for axial energy spreads less than 0.5%.

The performance of a tapered wiggler amplifier is sensitive to both the start-taper point and the slope of the taper. Optimization of the efficiency for operation at 80 GHz indicates that peak efficiency is found for a start-taper point at $z_0/\lambda_w \approx 52$ and a slope of $\epsilon_w \approx -0.003$. The evolution of the power versus distance for this case is shown in Fig. 4. It is evident that the output power peaks at approximately 4.2 MW over a total length of 88 wiggler periods. This translates into a total wiggler length of only 79 cm including the entry taper region.

The variation in the power versus frequency over the W-band is shown in Fig. 5 for parameters that optimize the device for operation at 80 GHz (i.e., $z_0/\lambda_w = 52$, $\epsilon_w = -0.003$, and a total length of 88 wiggler periods). As shown, the curve of the efficiency versus frequency is double-peaked. The larger peak is, as might be expected, at 85 GHz and the secondary peak is at the upper end of the W-band at 95 GHz representing an output power of about 3.5 MW. Hence, we conclude that it is possible to design a W-band MW amplifier using the CHI wiggler.

4. Summary and discussion

We have presented an analytical description of an FEL based upon the CHI wiggler. The nonlinear simulation is a slow-time-scale model for the self-consistent evolution of the modes of a coaxial waveguide with the trajectories of an ensemble of electrons [2]. We emphasize that no wiggler-period-average is applied to smooth the orbital dynamics. Hence, we treat the full particle dynamics and model the injection of the beam into the wiggler.

Specific examples have been discussed for W-band operation with uniform and tapered wigglers. Operation over a wide bandwidth is found to be practical for CHI wiggler-based FELs for both the uniform and tapered-wiggler examples. It is of interest that the bandwidth of the interaction for a tapered wiggler is found to be large. This contrasts with the commonly accepted belief that tapered-wiggler interaction results in a narrow bandwidth. Note that this conclusion is not confined to the CHI wiggler [5].

Our overall conclusion is that the CHI wiggler represents a design in which the limitations of conventional wigglers to reach high field strengths at short wiggler periods are overcome to some degree. The CHI wiggler, therefore, permits the construction of high frequency FELs at relatively low beam voltages.

Acknowledgement

This work was supported by the Office of Naval Research.

References

[1] R.H. Jackson, H.P. Freund, D.E. Pershing and J.M. Taccetti, Nucl. Instr. and Meth. A 341 (1994) 454.
[2] H.P. Freund and T.M. Antonsen, Jr., Principles of Free-electron Lasers (Chapman & Hall, London, 1992).
[3] H.P. Freund, R.H. Jackson, D.E. Pershing and J.M. Taccetti, Phys. Plasmas 1 (1994) 1046.
[3] A.M. Winslow, J. Comp. Phys. 2 (1967) 149.
[4] H.P. Freund, Nucl. Instr. and Meth. A 331 (1993) 496.
[5] B. Levush, H.P. Freund and T.M. Antonsen, Jr., Nucl. Instr. and Meth. A 341 (1994) 234.

APPENDIX IV

Design of a Far-Infrared CHI Wiggler Free-Electron Laser

K.H. Jackson, M. Blank, H.P. Freund, D.E. Pershing,
and J.M. Taccetti
Nucl. Instrum. Meth. **A375**, 226 (1996)

Nuclear Instruments and Methods in Physics Research A 375 (1996) 226–229

NUCLEAR INSTRUMENTS & METHODS IN PHYSICS RESEARCH Section A

ELSEVIER

Design of a far-infrared CHI wiggler free-electron laser

R.H. Jackson, M. Blank*, H.P. Freund[1], D.E. Pershing[2], J.M. Tacetti[3]

Naval Research Laboratory, Washington, DC 20375, USA

Abstract

The preliminary design of a voltage tunable far-infrared free-electron laser with a Coaxial Hybrid Iron (CHI) wiggler is presented. The CHI wiggler consists of a central rod and an outer ring of alternating ferromagnetic and non-ferromagnetic spacers. A period wiggler field is produced when the CHI structure is immersed in an axial magnetic field. The design under investigation makes use of a 1 MV/1 A annular electron beam interacting with the TE_{01} coaxial waveguide mode at approximately 1 THz ($\lambda = 300$ μm). The nominal wiggler period is 0.5 cm and the inner and outer waveguide radii are 0.4 and 0.8 cm respectively. An axial guide field of 5–10 kG is used. The device performance is modeled with a slow-time-scale nonlinear code, and self-fields and axial velocity spread are included in the model. Simulation results show output powers above 2 kW at frequencies from 850 GHz to 1040 GHz can be achieved for voltages ranging from 0.93 to 1.07 MV.

1. Introduction

The free-electron laser (FEL) has demonstrated operation over virtually the entire electromagnetic spectrum. In the exponential Compton regime, both the gain and saturation efficiency scale as $a_w^{2/3}/\gamma_0$ where $a_w \approx 0.0934 B_w \lambda_w$ for an rms wiggler amplitude B_w in kG and a wiggler period in cm. Hence, the gain and efficiency both decrease as the energy increases. A great deal of effort has been devoted, therefore, to the design of short period wigglers to operate at short wavelengths with low energies. However, this is often self-defeating since reductions in λ_w often result in corresponding reductions in B_w and a deleterious impact on the efficiency and gain.

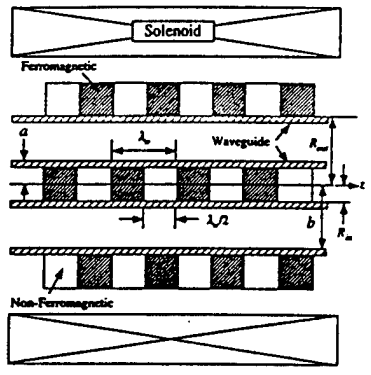

Fig. 1. Schematic representation of the CHI wiggler.

In this paper, we analyze the performance of a far-infrared FEL amplifier based upon the coaxial hybrid iron (CHI) wiggler [1–3] using a 3-D nonlinear slow-time-scale simulation. As shown schematically In Fig. 1, this wiggler design is based upon a configuration in which a central rod and a coaxial ring of alternating ferrite and dielectric spacers is inserted into a solenoidal magnetic field. Further, in this design the ferromagnetic (non-ferromagnetic) spacers on the central rod are aligned opposite to the non-ferromagnetic (ferromagnetic) spacers on the outer ring (i.e. a one half-period shift.) This produces an azimuthally symmetric period in which the amplitude can be increased by the relatively simple expedient of increasing the solenoidal field. The radial component of the field has a minimum at the center of the gap which provides enhanced beam focusing. This configuration permits the design of a relatively high amplitude but short period wiggler field.

2. The general formalism

The physical configuration is that of an annular electron beam propagating through a coaxial system which includes both coaxial waveguides and coaxial wiggler structures.

* Corresponding author.Tel. +1 202 767 6656, Fax +1 202 767 1280, e-mail blank@mmace.nrl.navy.mil.

[1] Permanent address: Science Applications International Corp., McLean, VA 22102, USA.

[2] Permanent address: Mission Research Corp., Newington, VA 22122, USA.

[3] Permanent address: University of Maryland College Park, MD 20742, USA.

PII S0168-9002(96)00140-4

An analytic solution for the CHI wiggler field can be shown to be [1–3]

$$B_z(r,z) = B_{0,\mathrm{ext}} + B_0 + B_w \sum_{n=1}^{\infty} \cos(nk_w z) \frac{[S_n I_0(nk_w r) - T_n K_0(nk_w r)]}{G(nk_w R_{\mathrm{out}}, nk_w R_{\mathrm{in}})}, \quad (1)$$

and

$$B_r(r,z) = B_w \sum_{n=1}^{\infty} \sin(nk_w z) \frac{[S_n I_1(nk_w r) + T_n K_1(nk_w r)]}{G(nk_w R_{\mathrm{out}}, nk_w R_{\mathrm{in}})}, \quad (2)$$

where $B_w \equiv 2B_0$, $G(\xi,\zeta) \equiv I_0(\xi)K_0(\zeta) - I_0(\zeta)K_0(\xi)$,

$$S_n \equiv \left(\frac{2}{n\pi}\right) \sin\left(\frac{n\pi}{2}\right)[K_0(nk_w R_{\mathrm{in}}) + K_0(nk_w R_{\mathrm{out}})], \quad (3)$$

and

$$T_n \equiv \left(\frac{2}{n\pi}\right) \sin\left(\frac{n\pi}{2}\right)[I_0(nk_w R_{\mathrm{in}}) + I_0(nk_w R_{\mathrm{out}})]. \quad (4)$$

Here B_0 and $B_{0,\mathrm{ext}}$ both relate to the external solenoidal field. The former value B_0 denotes the solenoidal field strength up to the saturation value of the ferromagnetic spacers. In contrast, $B_{0,\mathrm{ext}}$ denotes the remainder of the field in excess of the saturation level. Thus, $B_{0,\mathrm{ext}} = 0$ if the ferromagnetic spacers are not driven to saturation. This solution is in substantial agreement with the numerical results for the field obtained with the Poisson/Superfish family of magnetics codes.

A detailed discussion of the mathematical formulation and the simulation is given in Ref. [2] and we give only a brief description here. The radiation field is written as a superposition of the transverse electric (TE), transverse magnetic (TM), and transverse electric and magnetic (TEM) modes of the waveguide. We limit the discussion here to the TE modes. As such, the vector potential can be expressed as [2]

$$\delta A(x,t) = \sum_{\substack{l=0 \\ m=1}}^{\infty} \delta A_{lm}(z) \times \left[\frac{l}{\kappa_{lm} r} Z_l(\kappa_{lm} r)\hat{e}_r \sin\alpha_{lm} + Z_l'(\kappa_{lm} r)\hat{e}_\theta \cos\alpha_{lm}\right], \quad (5)$$

where the phase for angular frequency ω and wavenumber k_{lm} is

$$\alpha_{lm} \equiv \int_0^z \mathrm{d}z'\, k_{lm}(z') + l\theta - \omega t, \quad (7)$$

where $\omega^2 = c^2 k_{lm}^2 + c^2 \kappa_{lm}^2$ for a given cutoff κ_{lm}. The cutoffs are given by solution of the dispersion equation $J_l'(\kappa_{lm} a) Y_l'(\kappa_{lm} b) = J_l'(\kappa_{lm} b) Y_l'(\kappa_{lm} a)$, where J_l and Y_l denote the regular Bessel and Neumann functions, and $Z_l(\kappa_{lm} r) \equiv J_l(\kappa_{lm} r) + \Delta_{lm} Y_l(\kappa_{lm} r)$, where $\Delta_{lm} \equiv -J_l'(\kappa_{lm} b)/Y_l'(\kappa_{lm} b)$.

The dynamical equations for the modes in coaxial waveguides have been described in detail elsewhere [2], and the results for the TE modes are

$$\left[\frac{\mathrm{d}^2}{\mathrm{d}z^2} + \left(\frac{\omega^2}{c^2} - k_{lm}^2 - \kappa_{lm}^2\right)\right] \delta a_{lm} = \frac{\omega_b^2}{c^2} H_{lm} \left\langle \frac{v_r}{|v_z|} \frac{1}{\kappa_{lm} r} Z_l(\kappa_{lm} r) \sin\alpha_{lm} + \frac{v_\theta}{|v_z|} Z_l'(\kappa_{lm} r) \cos\alpha_{lm} \right\rangle, \quad (8)$$

$$2k_{lm}^{1/2} \frac{\mathrm{d}}{\mathrm{d}z}(k_{lm}^{1/2} \delta a_{lm}) = \frac{\omega_b^2}{c^2} H_{lm} \times \left\langle \frac{v_r}{|v_z|} \frac{1}{\kappa_{lm} r} Z_l(\kappa_{lm} r) \cos\alpha_{lm} - \frac{v_\theta}{|v_z|} Z_l'(\kappa_{lm} r) \sin\alpha_{lm} \right\rangle, \quad (9)$$

where $\delta a_{lm} \equiv e\,\delta A_{lm}/m_e c^2$ is the normalized amplitude of the modes, and

$$H_{lm} \equiv \frac{2\kappa_{lm}^2 (b^2 - a^2)}{(\kappa_{lm}^2 b^2 - l^2) Z_l^2(\kappa_{lm} b) - (\kappa_{lm}^2 a^2 - l^2) Z_l^2(\kappa_{lm} a)}. \quad (10)$$

The beam is assumed to be monoenergetic with an axial energy spread determined by an initial (i.e., $z = 0$) pitch angle spread, and the averaging operator is defined over the initial beam parameters

$$\langle(\cdots)\rangle \equiv \frac{A}{4\pi A_g} \int_0^{2\pi} \mathrm{d}\phi_0 \int_0^{p_0} \mathrm{d}p_{z0}\, \beta_{z0} \exp[-(p_{z0} - p_0)^2/\Delta p_z^2] \times \iint_{A_g} \mathrm{d}x_0\, \mathrm{d}y_0\, \sigma_\perp(x_0, y_0) \times \int_{-\pi}^{\pi} \mathrm{d}\psi_0\, \sigma_\parallel(\psi_0)(\cdots), \quad (11)$$

where A_g is the cross-sectional area of the waveguide, $\beta_{z0} \equiv v_{z0}/c$ for an initial axial velocity v_{z0}, (p_{x0}, p_{y0}, p_{z0}) denote the initial beam momenta, $\phi_0 \equiv \tan^{-1}(p_{y0}/p_{x0})$, p_0 and Δp_z denote the initial total momentum of the beam and the initial axial momentum spread respectively, $\psi_0 (\equiv -\omega t_0$, where t_0 is the time at which the particle crosses the $z = 0$ plane) is the initial ponderomotive phase, $\sigma_\perp$ and $\sigma_\parallel$ are the initial distributions of the beam in cross-section and phase, and

$$A \equiv \left[\pi \int_0^{p_0} \mathrm{d}p_{z0} \exp[-(p_{z0} - p_0)^2/\Delta p_z^2]\right]^{-1} \quad (12)$$

is a normalization constant.

The field equations are integrated simultaneously with

the orbit equations for an ensemble of electrons. We integrate the complete 3D Lorentz force equations for each electron in the aggregate fields of the CHI wiggler and the electromagnetic fields for all the wave modes. In addition, we include the DC self-electric and magnetic fields due to the bulk charge and current densities of the beam. No orbit average is imposed, and we treat the injection of the beam into the wiggler. For this purpose, we model the adiabatic injection region by means of a tapered wiggler amplitude. In addition, we also consider amplitude tapering for the purpose of efficiency enhancement. In order to describe these effects, we assume that the overall coefficient of the periodic component of the field varies as

$$B_w = \begin{cases} 2B_0 \sin^2\left(\dfrac{k_w z}{4N_w}\right) & ;z \le N_w \lambda_w , \\ 2B_0 & ;N_w \lambda_w < z \le z_0 , \\ 2B_0[1 + k_w \varepsilon_w (z - z_0)] & ;z > z_0 , \end{cases} \tag{13}$$

where N_w denotes the number of wiggler periods in the entry taper region, and ε_w is the normalized slope of the taper.

3. Simulation results

The non-linear code was used to simulate the performance of a voltage tunable far-infrared FEL. The nominal device parameters under consideration are shown in Table 1. The electron beam was positioned at the center of the gap, where there is a minimum in radial magnetic field.

The theoretical prediction of output power versus frequency for an ideal beam (energy spread $\Delta\gamma_z = 0$) interacting with the TE_{01} coaxial waveguide mode is plotted in Fig. 2. The simulation shows that by varying the beam voltage from 0.93 to 1.07 MV it is possible to achieve greater than 20% tunable bandwidth (850–1040 GHz) at output power levels above 2 kW. In Fig. 2, the point at 850 GHz corresponds to 0.93 MV. Each following point represents an increase in voltage of 0.1 MV up to the point at 1040 GHz, which corresponds to 1.07 MV.

The dependence of output power on axial energy spread is plotted in Fig. 3. The figure shows a rapid decrease in device performance with increasing energy spread. At an axial energy spread $\Delta\gamma_z/\gamma_z = 0.2\%$ the output power has decreased to approximately 1 kW, less than half of the value at zero spread. Thus, energy spread must be kept a minimum.

Table 1
Nominal design parameters for the FIR CHI wiggler FEL

Beam voltage	1 MV
Beam current	1 A
Inner waveguide radius	0.4 cm
Outer waveguide radius	0.8 cm
Wiggler period	0.5 cm
Axial guide field amplitude	9 kG
Coaxial mode	TE_{01}
Frequency	950 GHz

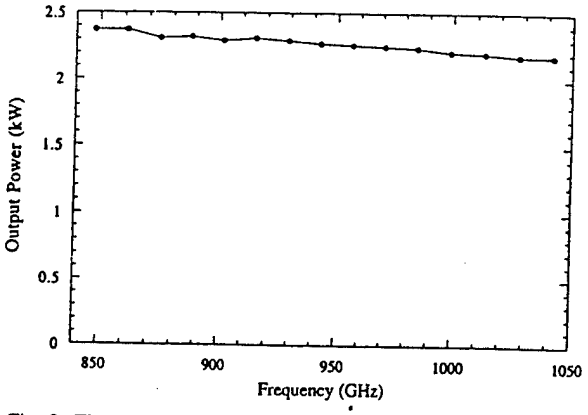

Fig. 2. Theoretical predictions of output power versus frequency for voltage tuning from 930–1070 MV.

4. Summary

Non-linear simulations show that the CHI wiggler can be effectively used in a tunable far-infrared FEL. Theoretical studies indicate that output powers greater than 2 kW can be produced with a 1 MV/1 A annular electron beam interacting with the TE_{01} coaxial waveguide mode in the presence of a CHI wiggler and an axial guide field. In addition, simulations show that greater than 20% voltage tuning is possible. The output power decreases rapidly with increasing axial energy spread so a high quality electron beam is essential for efficient operation. It may prove possible to increase the gain and efficiency by tapering the wiggler field, which is especially simple in the

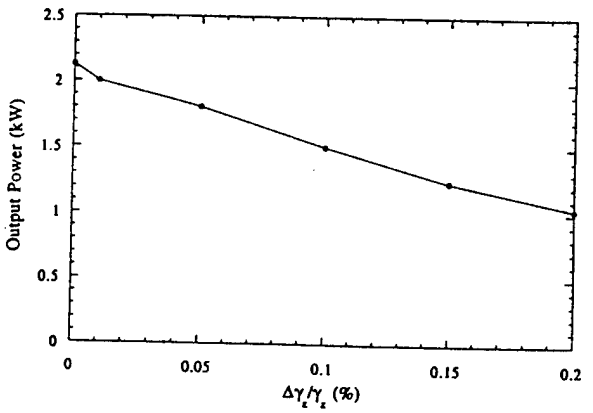

Fig. 3. Theoretical predictions of output power versus axial energy spread at 950 GHz.

CHI configuration. Theoretical studies of this device continue.

Acknowledgements

This work was supported by the Office of Naval Research. The computational work was supported in part by a grant of HPC time from the DoD HPC Center NAVO on a CRAY C90.

References

[1] R.H. Jackson, H.P. Freund, D.E. Pershing and J.M. Taccetti, Nucl. Instr. and Meth. A 341 (1994) 454.
[2] H.P. Freund, R.H. Jackson, D.E. Pershing and J.M. Taccetti, Phys. Plasmas 1 (1994) 1046.
[3] H.P. Freund, M.E. Read, R.H. Jackson, D.E. Pershing and J.M. Taccetti, Phys. Plasmas 2 (1994) 1755.

APPENDIX V

A Free-Electron Laser for Cyclotron Resonant Heating in Magnetic Fusion Reactors

H.P. Freund, M.E. Read, R.H. Jackson, D.E. Pershing,
and J.M. Taccetti
Phys. Plasmas **2**, 1755 (1995)

A free-electron laser for cyclotron resonant heating in magnetic fusion reactors

H. P. Freund[a] and M. E. Read
Physical Sciences, Inc., Alexandria, Virginia 22314

R. H. Jackson, D. E. Pershing,[b] and J. M. Taccetti[c]
Naval Research Laboratory, Washington, D.C. 20375

(Received 21 November 1994; accepted 19 January 1995)

A G-band free-electron laser designed for plasma heating is described using a coaxial hybrid iron (CHI) wiggler formed by insertion into a solenoid of a central rod and an outer ring of alternating ferrite and nonferrite spacers positioned so that the central ferrite (nonferrite) spacers are opposite the outer nonferrite (ferrite) spacers. The CHI wiggler provides for enhanced beam focusing and the ability to handle intense beams and high-power continuous wave radiation. Simulations indicate that a power/efficiency of 3.5 MW/13% are possible using a 690 kV/40 A beam. No beam loss was found in simulation. © *1995 American Institute of Physics.*

I. INTRODUCTION

Sources of plasma heating for thermonuclear fusion reactors employ both ion and electron cyclotron schemes. Electron cyclotron heating requires approximately 20 MW of continuous wave (CW) power at frequencies of 140–280 GHz depending upon whether the fundamental or second harmonic resonance is utilized.[1] No source currently under consideration, or even anticipated, is expected to produce the full power requirement in a single module, and a system composed of several sources is envisioned. In this paper, we describe the design of a G-band (140–150 GHz) free-electron laser (FEL) amplifier based upon a coaxial hybrid iron (CHI) wiggler[2,3] which can meet these requirements.

The CHI wiggler is produced by insertion into a solenoid of a central rod and an outer ring composed of alternating ferromagnetic and nonferromagnetic (or dielectric) spacers. A schematic representation of the structure is shown in Fig. 1. The position of the spacers is such that the ferrite (nonferrite) spacers on the central rod are opposite the nonferrite (ferrite) spacers on the outer ring. The field is cylindrically symmetric and exhibits minima in the center of the gap providing for enhanced beam focusing.

The CHI wiggler has two major advantages for the application of interest. First, even a small amount of beam loss in a high-power CW design can result in catastrophic failure. For example, the average beam power under discussion is ≈28 MW, and a beam loss of 1% implies that 28 kW is dissipated in the drift tube walls. This poses a difficult design problem. Hence, the favorable focusing properties of the CHI wiggler are ideally suited to high-power CW applications. Indeed, no beam loss was observed in simulation. Second, short wiggler periods are desirable to minimize the required beam energy, while high wiggler fields are required for high gains. This is difficult to achieve in conventional wiggler designs. However, high fields at short wiggler periods can be achieved with the CHI wiggler by using narrow spacers and a ferrite with a high saturation level in a strong solenoid. Hence, a CHI wiggler-based FEL is capable of producing high power at the required wavelengths with a relatively low energy beam.

II. THE THEORETICAL FORMULATION

An analytic form for the CHI wiggler field can be found by solution of Laplace's equation $\nabla^2\mathbf{B}(r,z)=0$ for appropriate boundary conditions. The solution is cylindrically symmetric and has the form[2,3]

$$B_z(r,z)=B_{0,\mathrm{ext}}+B_0+B_w\sum_{n=1}^{\infty}\cos(nk_wz)\times\frac{[S_nI_0(nk_wr)-T_nK_0(nk_wr)]}{G(nk_wR_{\mathrm{out}},nk_wR_{\mathrm{in}})},\tag{1}$$

and

$$B_r(r,z)=B_w\sum_{n=1}^{\infty}\sin(nk_wz)\,\frac{[S_nI_1(nk_wr)+T_nK_1(nk_wr)]}{G(nk_wR_{\mathrm{out}},nk_wR_{\mathrm{in}})},\tag{2}$$

where $B_w\equiv 2B_0$, $G(\xi,\zeta)\equiv I_0(\xi)K_0(\zeta)-I_0(\zeta)K_0(\xi)$,

$$S_n\equiv\left(\frac{2}{n\pi}\right)\sin\left(\frac{n\pi}{2}\right)[K_0(nk_wR_{\mathrm{in}})+K_0(nk_wR_{\mathrm{out}})],\tag{3}$$

and

$$T_n\equiv\left(\frac{2}{n\pi}\right)\sin\left(\frac{n\pi}{2}\right)[I_0(nk_wR_{\mathrm{in}})+I_0(nk_wR_{\mathrm{out}})].\tag{4}$$

Here B_0 and $B_{0,\mathrm{ext}}$ both relate to the external solenoidal field. The former value B_0 denotes the solenoidal field strength up to the saturation value of the ferromagnetic spacers. In contrast, $B_{0,\mathrm{ext}}$ denotes the remainder of the field in excess of the saturation level. Thus, $B_{0,\mathrm{ext}}=0$ if the ferromagnetic spacers are not driven to saturation. This solution is in substantial

[a]Permanent address: Science Applications International Corp., McLean, Virginia 22102.
[b]Permanent address: Mission Research Corp., Newington, Virginia 22122.
[c]Permanent address: University of Maryland, College Park, Maryland 20742.

 1070-664X/95/2(5)/1755/5/$6.00

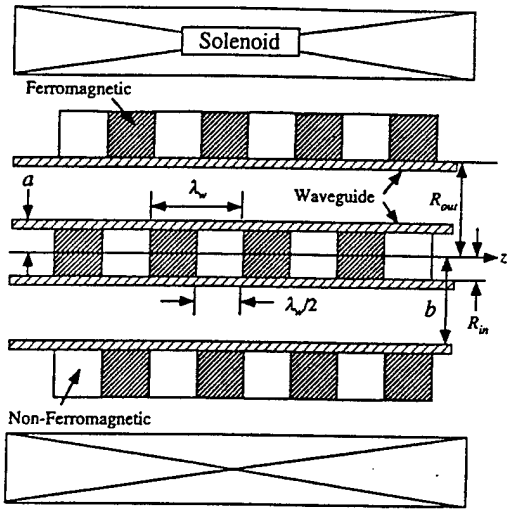

FIG. 1. Schematic illustration of the CHI wiggler configuration.

agreement with the numerical results for the field obtained with the POISSON/SUPERFISH family of magnetics codes.[4]

One advantage of the CHI wiggler design is that the field amplitude exhibits minima at the center of the coaxial gap.[2,3] This provides for good focusing of the electron beam which is important for high average power applications in which even small levels of beam loss are unacceptable for CW or long pulse operation.

We consider propagation within a coaxial waveguide with inner and outer radii a and b, respectively. Space-charge effects are negligible as long as $\omega_b/ck_w < \gamma_z^3 v_w^2/8\gamma_0 c^2$, where ω_b denotes the beam plasma frequency, v_w is the bulk transverse wiggler velocity, γ_0 is the bulk relativistic factor of the beam, and $\gamma_z=(1-v_\parallel^2/c^2)^{-1/2}$ for a bulk streaming velocity $v_\parallel$. Space-charge effects can also be neglected if (1) the wavelength is less than the Debye length and the space-charge waves are subject to strong Landau damping, or (2) the bandwidth of the interaction is greater than the plasma frequency. These conditions for the neglect of space-charge effects are valid even for relatively high-current electron beams.[5]

A detailed discussion of the mathematical formulation and the simulation is given in Ref. 3. Since we are primarily interested in a specific application in this paper, we shall merely give a brief description of the formulation here. The boundary conditions of the fields at the coaxial waveguide walls (inner radius a and outer radius b) are satisfied by a superposition of the transverse electric (TE), transverse magnetic (TM), and transverse electric and magnetic (TEM) modes of the waveguide which constitute a complete and orthogonal set of basis vectors. The interaction strength depends both upon the wave–particle resonance and upon the polarization of the modes. The CHI wiggler induces an oscillation which is predominantly in the azimuthal direction; hence, the modes with the highest gains are those which are largely polarized in that direction. For the present case, the predominant resonance is with an azimuthally polarized TE_{01} mode. The other modes are farther from resonance and have less favorable polarizations. Hence, we limit the discussion here to the case of the TE modes. As such, the vector potential can be expressed in cylindrical coordinates as[3]

$$\delta\mathbf{A}(\mathbf{x},t)=\sum_{\substack{l=0\\m=1}}^{\infty}\delta A_{lm}(z)\left(\frac{l}{\kappa_{lm}r}Z_l(\kappa_{lm}r)\hat{\mathbf{e}}_r\sin\alpha_{lm}+Z_l'(\kappa_{lm}r)\hat{\mathbf{e}}_\theta\cos\alpha_{lm}\right), \tag{5}$$

where the phase for angular frequency ω and wave number k_{lm} is

$$\alpha_{lm}\equiv\int_0^z dz'\,k_{lm}(z')+l\theta-\omega t, \tag{6}$$

where $\omega^2=c^2k_{lm}^2+c^2\kappa_{lm}^2$ for a given cutoff κ_{lm}. The amplitudes and wave numbers are assumed to vary slowly in z over a wavelength. The cutoffs are given by solution of the dispersion equation $J_l'(\kappa_{lm}a)Y_l'(\kappa_{lm}b)=J_l'(\kappa_{lm}b)Y_l'(\kappa_{lm}a)$, where J_l and Y_l denote the regular Bessel and Neumann functions, and $Z_l(\kappa_{lm}r)\equiv J_l(\kappa_{lm}r)+\Delta_{lm}Y_l(\kappa_{lm}r)$, where $\Delta_{lm}\equiv -J_l'(\kappa_{lm}b)/Y_l'(\kappa_{lm}b)$.

The dynamical equations for the modes in coaxial waveguides have been described in detail,[3] and the results for the TE modes are

$$\left[\frac{d^2}{dz^2}+\left(\frac{\omega^2}{c^2}-k_{lm}^2-\kappa_{lm}^2\right)\right]\delta a_{lm} =\frac{\omega_b^2}{c^2}H_{lm}\left(\frac{v_r}{|v_z|}\frac{l}{\kappa_{lm}r}Z_l(\kappa_{lm}r)\sin\alpha_{lm}+\frac{v_\theta}{|v_z|}Z_l'(\kappa_{lm}r)\cos\alpha_{lm}\right), \tag{7}$$

$$2k_{lm}^{1/2}\frac{d}{dz}(k_{lm}^{1/2}\delta a_{lm})=\frac{\omega_b^2}{c^2}H_{lm}\left(\frac{v_r}{|v_z|}\frac{l}{\kappa_{lm}r}Z_l(\kappa_{lm}r)\cos\alpha_{lm}-\frac{v_\theta}{|v_z|}Z_l'(\kappa_{lm}r)\sin\alpha_{lm}\right), \tag{8}$$

where $\delta a_{lm}\equiv e\,\delta A_{lm}/m_ec^2$ is the normalized amplitude of the modes, and

$$H_{lm}\equiv\frac{2\kappa_{lm}^2(b^2-a^2)}{(\kappa_{lm}^2b^2-l^2)Z_l^2(\kappa_{lm}b)-(\kappa_{lm}^2a^2-l^2)Z_l^2(\kappa_{lm}a)}. \tag{9}$$

The beam is assumed to be monoenergetic with an axial energy spread determined by an initial (i.e., at $z=0$) pitch angle spread, and the averaging operator is defined over the initial beam parameters

$$\langle(\cdots)\rangle \equiv \frac{A}{4\pi A_g}\int_0^{2\pi} d\phi_0 \int_0^{p_0} dp_{z0}\,\beta_{z0} \times \exp\left(-\frac{(p_{z0}-p_0)^2}{\Delta p_z^2}\right) \times \int_{A_g}\int dx_0\,dy_0 \sigma_\perp(x_0,y_0)\int_{-\pi}^{\pi} d\psi_0\,\sigma_\parallel(\psi_0)(\cdots), \tag{10}$$

where A_g is the cross-sectional area of the waveguide, $\beta_{z0}\equiv v_{z0}/c$ for an initial axial velocity v_{z0}, $\phi_0\equiv\tan^{-1}(p_{y0}/p_{x0})$, (p_{x0},p_{y0},p_{z0}) denote the initial beam momenta, p_0 and Δp_z denote the initial total momentum of the beam and the initial axial momentum spread, respectively, $\psi_0(\equiv-\omega t_0$, where t_0 is the time at which the particle crosses the $z=0$ plane) is the initial ponderomotive phase, $\sigma_\perp$ and $\sigma_\parallel$ are the initial distributions of the beam in cross section and phase, and

$$A\equiv\left[\pi\int_0^{p_0} dp_{z0}\exp\left(-\frac{(p_{z0}-p_0)^2}{\Delta p_z^2}\right)\right]^{-1}, \tag{11}$$

is a normalization constant.

The field equations must be solved simultaneously with the orbit equations for an ensemble of electrons. We integrate the complete three-dimensional (3-D) Lorentz force equations for each electron in the aggregate fields of the CHI wiggler and electromagnetic fields for all the wave modes. No orbit average is imposed, and we treat the injection of the beam into the wiggler. This describes any increase in the effective beam emittance due to the injection mechanism. For this purpose, we model the adiabatic injection region by means of a tapered wiggler amplitude. In addition, we also consider amplitude tapering for the purpose of efficiency enhancement. In order to describe these effects within the CHI wiggler model, we assume that the overall coefficient of the periodic component of the field varies as

$$B_w=\begin{cases} 2B_0\sin^2\left(\dfrac{k_w z}{4N_w}\right); & z\leq N_w\lambda_w, \\ 2B_0; & N_w\lambda_w<z\leq z_0, \\ 2B_0[1+k_w\epsilon_w(z-z_0)]; & z>z_0, \end{cases} \tag{12}$$

where N_w denotes the number of wiggler periods in the entry taper region, and ϵ_w is the normalized slope of the taper for purposes of efficiency enhancement. Note that the CHI wiggler field can be tapered in a variety of ways including tapering the solenoidal field or varying the radial thickness of the spacers.

III. NUMERICAL RESULTS

The wiggler amplitudes and periods which can be achieved are determined using the POISSON codes.[4] To this end, we specified vanadium permendur spacers and found that a 6 kG solenoid saturates the ferrite for spacers with inner and outer radii of $a=0.7$ and $b=1.5$ cm, and a wiggler period of $\lambda_w=1.5$ cm. We also assume that a and b are the inner and outer radii of the waveguide. Using these dimensions, we operate with a 10 kG solenoid which drives the ferromagnetic spacers in the CHI wiggler to saturation (i.e., $B_0=4.0$ kG and $B_{0,\text{ext}}=6.0$ kG). Note that a magnetoresonant enhancement in the gain and efficiency is also present when the Larmor period associated with the uniform axial field component is close to the wiggler period. We assume that $N_w=5$ to preserve the initial beam quality through injection.

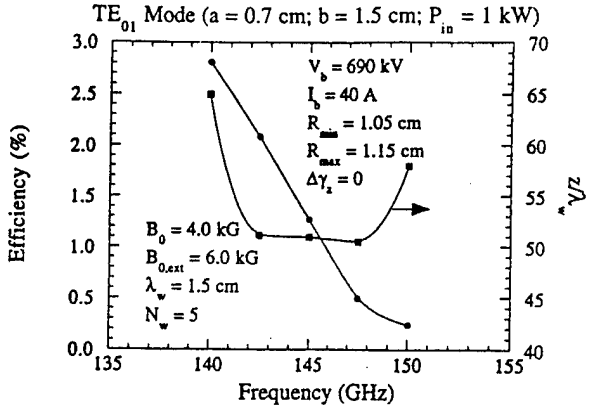

FIG. 2. Efficiency and saturation distance versus frequency at 690 kV.

Since FEL performance is critically dependent upon beam quality, we must have an electron gun which produces an annular beam with a low energy spread. The design tool we used for this is the EGUN code.[6] Since operation in G-band is desired, we chose an electron beam voltage in the neighborhood of 690 kV and a current of 40 A. Assuming that the inner and outer radii of the beam at the exit of the gun were 1.05 cm and 1.15 cm, respectively, it is possible to design a gun which produces an axial energy spread of substantially less than 0.1%. The results from the gun calculation were used as initial conditions in the FEL simulation.

We first address the interaction for a uniform wiggler, and consider the case of an ideal beam in which the axial energy spread $\Delta\gamma_z=0$. We also deal with the TE_{01} mode at an injected power of 1 kW. The efficiency and saturation distance versus frequency are plotted in Fig. 2. It is clear that the efficiency decreases with frequency over the resonant band from 140–150 GHz. Observe that the maximum efficiency occurs at the minimum resonant frequency and does not correspond to the peak gain. This is a common feature of the interaction in FEL's,[7] and stems from the fact that the efficiency varies with the difference between the beam velocity v_b and the phase velocity of the ponderomotive wave formed by the beating of the wiggler and radiation fields $[\Delta v=v_b-\omega/(k+k_w)]$. Since the saturation distance is relatively constant over the range of 142–147 GHz, the peak gain of ≈0.5 dB/cm occurs at ≈142 GHz for an efficiency of ≈2.2%. As such, we assume a frequency of 142.5 GHz in the remainder of the paper. It is possible, however, to retune to higher frequencies using higher voltages or shorter wiggler periods.

Before proceeding to the study of the tapered wiggler interaction, we turn to the effect of the axial beam energy

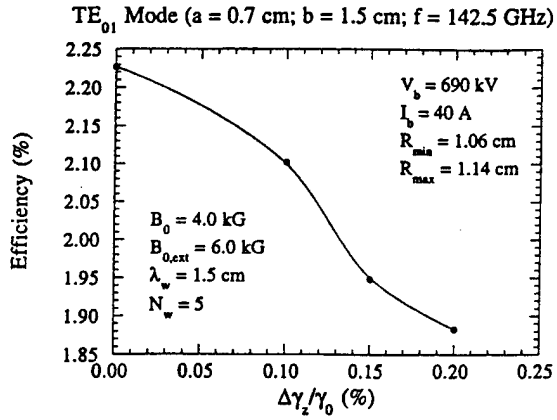

FIG. 3. Variation in the efficiency and saturation distance versus beam thickness.

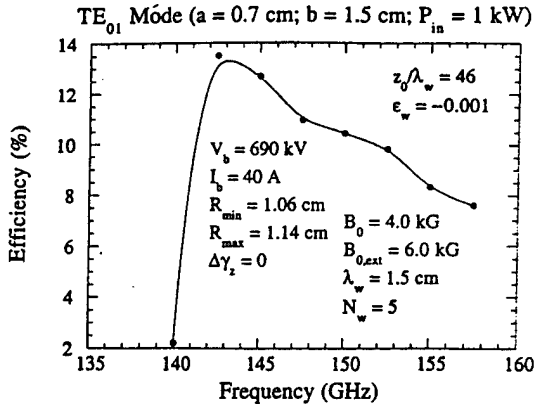

FIG. 5. The bandwidth for the tapered wiggler interaction.

spread. The variation in the efficiency as a function of $\Delta\gamma_z$ is shown in Fig. 3. Observe that the efficiency falls from about 2.24% to 2.10% as the axial energy spread increases to 0.10%. This is a relatively modest decrease in efficiency, and a beam quality within this range has been demonstrated in the gun design code.

Finally, it is important to note that no beam loss was found in the simulation prior to saturation for the uniform wiggler cases studied.

Turning to a tapered wiggler, it should be noted that there is an optimum both in the start-taper point and in the slope of the taper. Optimizing in both of these parameters, we find that for 1 kW input power the optimal start-taper point is $z_0/\lambda_w=46$ and the optimal slope is $\epsilon_w=-0.001$. The evolution of the power with axial distance for this choice is shown in Fig. 4 for the cases of an ideal beam ($\Delta\gamma_z=0$) and for $\Delta\gamma_z/\gamma_0=0.2\%$. Note that the interaction length is $\sim 200\lambda_w$ which is the length required to taper the wiggler amplitude to zero (note that the uniform axial field component does not vanish). It is clear that the efficiency does not change greatly with the decrease in beam quality over this range, and rises to over 13% for an output power of better than 3.5 MW.

The bandwidth of the tapered wiggler interaction is quite large. Consider the case of the optimum parameters for the interaction at 142.5 GHz, including the total length of the system. The bandwidth is determined by the response of this system at different drive frequencies. In Fig. 5 we plot the tapered efficiency versus frequency. It is evident that the efficiency remains high over a frequency range of $\approx$142.5–160 GHz, for a large instantaneous bandwidth. This agrees with an earlier study using a simpler FEL model.[8] Finally, note that despite the extended interaction length for the tapered wiggler cases shown, no beam loss was found in simulation for any of these parameters.

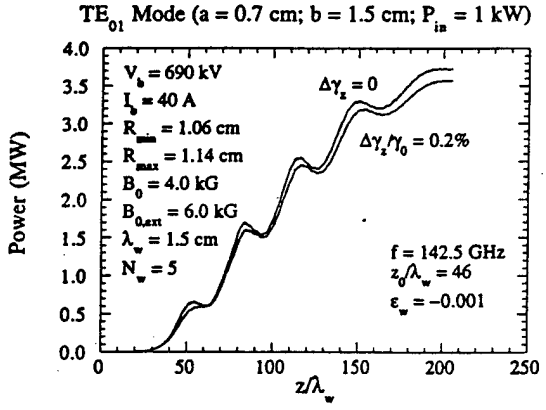

FIG. 4. Evolution of the power with axial position for two choices of the energy spread.

IV. SUMMARY AND DISCUSSION

In conclusion, we feel that a CHI wiggler-based FEL is a promising candidate as a driver for cyclotron resonant heating of magnetic fusion reactors. The efficiencies were found to be fairly high. The tapered wiggler interaction produced efficiencies of 13%–14% which represents a single source capable of producing 3–4 MW tunable over a large instantaneous bandwidth. These conclusions hold for both an ideal beam and for one with the more realistic beam energy spread of $\leq$0.2%. It should be remarked that such beams are quite reasonable with careful gun design. Furthermore, no beam loss was found to occur for either the uniform or tapered wiggler runs. This is required for the design of a CW device.

Alternate source concepts for plasma heating purposes include both FEL's and gyrotrons. An alternate FEL design is under construction which makes use of an electrostatic accelerator producing a 2 MeV/12 A electron beam and a planar wiggler with an amplitude of 1.8 kG and a period of 2 cm.[9] This device is configured as a CW oscillator, and is designed to produce powers of 1 MW at frequencies up to 260 GHz. This yields an extraction efficiency of approximately 4%. The wall plug efficiency is expected to be much higher, however, due to the use of an energy recovery system. Indeed, an energy (or at least charge) recovery system is necessary in order for the electrostatic accelerator to operate

in CW mode. In contrast to this design, the CHI wiggler-based FEL requires a lower voltage electron beam and has a higher extraction efficiency. In addition, the wall plug efficiency of the CHI wiggler design can also be increased by using a depressed collector for energy recovery. Thus, overall efficiencies much higher than 13%–14% are possible. Using an energy recovery system, we expect that overall efficiencies comparable to gyrotron oscillators are possible, but with higher power and broader instantaneous bandwidth than is available with gyrotrons. The instantaneous bandwidth may prove to be an important advantage if the source is to be used for plasma profile modification and control.

The major source of concern for the present CHI wiggler-based design is the length of the interaction. At 200 wiggler periods in length, the support of the central rod becomes a serious issue. However, we feel that it is not insurmountable, and can be addressed in several ways. First, a vertical mount is necessary in which the central rod is supported from the top by the collector. Second, it is not necessary to taper the wiggler to saturation. A shorter tapered wiggler would sacrifice some power but facilitate the support of the central rod. Last, this design is for an amplifier configuration; however, an oscillator can also be constructed which would be more compact without the sacrifice of efficiency. The only drawback to an oscillator would be a narrower bandwidth. Tuning of an oscillator would have to be accomplished by varying the voltage, and whether the bandwidth would be sufficiently narrow to impair the device's usefulness depends upon the Q factor of the cavity. This is an area of future study. Note, however, that we do not expect the bandwidth to be less than that of the current generation of gyrotrons which are used for this purpose. It should be emphasized that this study represents an initial design only, and higher gains and shorter lengths are likely with proper optimization of parameters. Preliminary estimates of the efficiency and interaction length made on the basis of simple scaling laws[7] indicate that it should be possible to shrink the interaction length by $\approx$50% with only a minor reduction in the efficiency using a somewhat shorter wiggler period and a beam with a lower voltage but a higher current. Operation closer to the magnetoresonance is also an attractive means of achieving this goal.

Cooling is not expected to be a major problem even for long pulse/CW operation since this is a low loss mode. Estimates indicate that loading on the central rod is ≈ 10 W/cm^2 at a power of 5 MW, and that the loading on the outer conductor is even less. As a result, cooling would be required only near the end of the interaction region using relatively narrow water passages in the rod.

In summary, the CHI wiggler-based FEL is attractive for a high-power CW radiation source. It is a robust design in which high efficiencies are possible over a wide parameter range, and the required beam quality is well within current gun technology. Finally, overall system efficiency can be substantially increased by incorporation of depressed collectors for energy recovery.

ACKNOWLEDGMENTS

This work was supported by the U.S. Department of Energy and the Office of Naval Research.

[1] V. L. Granatstein and R. Colestock (editors), *Wave Heating in Plasmas* (Gordon & Breach, New York, 1986).
[2] R. H. Jackson, H. P. Freund, D. E. Pershing, and J. M. Taccetti, Nucl. Instrum. Methods A **341**, 454 (1994).
[3] H. P. Freund, R. H. Jackson, D. E. Pershing, and J. M. Taccetti, Phys. Plasmas **1**, 1046 (1994).
[4] A. M. Winslow, J. Comput. Phys. **2**, 149 (1967).
[5] H. P. Freund, Nucl. Instrum. Methods A **331**, 496 (1993).
[6] W. B. Herrmannsfeldt, *Electron Trajectory Program*, Stanford Linear Accelerator Center Report 226. Copies may be ordered by SLAC Report number from the National Technical Information Service, 5285 Fort Royal Road, Springfield Virginia, 22161.
[7] H. P. Freund and T. M. Antonsen, Jr., *Principles of Free-electron Lasers* (Chapman & Hall, London, 1992), Chap. 5.
[8] B. Levush, H. P. Freund, and T. M. Antonsen, Jr., Nucl. Instrum. Methods A **341**, 234 (1994).
[9] W. H. Urbanus, C. A. J. van der Geer, W. A. Bongers, G. van Dijk, B. S. Q. Elzendoorn, J. P. van Ieperen, A. van der Linden, P. Manintveld, A. B. Sterk, A. V. Tulupov, A. G. A. Verhoeven, M. J. van der Wiel, A. A. Varfolomeev, S. N. Ivanchenkov, A. S. Khlebnikov, V. L. Bratman, and G. G. Denisov, Nucl. Instrum. Methods A **358**, 155 (1995).

APPENDIX VI

Design Study of a G-Band FEL Amplifier for Application to Cyclotron Resonant Heating in Magnetic Fusion Reactors

H.P. Freund, M.E. Read, R.H. Jackson, D.E. Pershing,
and J.M. Taccetti
Nucl. Instrum. Meth. **A358**, 163 (1995)

Nuclear Instruments and Methods in Physics Research A 358 (1995) 163–166

ELSEVIER

NUCLEAR INSTRUMENTS & METHODS IN PHYSICS RESEARCH Section A

Design study of a G-band FEL amplifier for application to cyclotron resonant heating in magnetic fusion reactors

H.P. Freund [a,*,1], M.E. Read [a], R.H. Jackson [b], D.E. Pershing [b,2], J.M. Taccetti [b,3]

[a] *Physical Sciences, Inc., Alexandria, VA 22314, USA*
[b] *Naval Research Laboratory, Washington, DC 20375, USA*

Abstract

A G-band (140–150 GHz) free-electron laser is described using a coaxial hybrid iron (CHI) wiggler. The CHI wiggler is produced by insertion into a solenoid of a central rod and an outer ring composed of alternating ferrite and nonferrite spacers. The position of the spacers is such that the ferrite (nonferrite) spacers on the central rod are opposite the nonferrite (ferrite) spacers on the outer ring. The field is cylindrically symmetric and exhibits minima in the center of the gap providing for enhanced beam focusing. We describe a tapered wiggler amplifier for plasma heating applications. Preliminary design studies using a nonlinear simulation indicates that output powers of 3.5 MW are possible using a 690 kV/40 A electron beam for a total efficiency of 13%. It is important to note that no beam loss was observed even for realistic values of beam energy spread.

1. Introduction

Auxiliary sources of plasma heating for currently-planned thermonuclear fusion reactors employ both ion and electron cyclotron schemes. The electron cyclotron heating schemes necessitate approximately 20 MW of CW power at frequencies ranging from 140 to 280 GHz depending upon whether it is desired to use the fundamental or second harmonic resonance [1]. At the present time no source under consideration, or even anticipated, is expected to produce the full power requirement in a single module, and a system composed of several similar sources is envisioned. In this paper, we describe the design and operation of a G-band (140–150 GHz) free-electron laser (FEL) amplifier based upon a coaxial hybrid iron (CHI) wiggler [2–4] which can meet these requirements.

The CHI wiggler is produced by insertion into a solenoid of a central rod and an outer ring composed of alternating ferrite and nonferrite spacers. A schematic representation of the structure is shown in Fig. 1. The position of the spacers is such that the ferrite (nonferrite) spacers on the central rod are opposite the nonferrite (ferrite) spacers on the outer ring. The field is cylindrically symmetric and exhibits minima in the center of the gap providing for enhanced beam focusing. Since high fields at short wiggler periods can be achieved with this design by the relatively simple expedient of using narrow spacers and a ferromagnetic material with a high saturation level in a strong solenoid, a CHI wiggler-based FEL is capable of producing power at the required wavelengths using a relatively low energy electron beam.

The analysis and design of a CHI-wiggler FEL herein is based upon a 3-D slow-time-scale nonlinear simulation. Interested readers are referred to Refs. [3,4] in which the formulation is described in detail. In this formulation a set of second order nonlinear differential equations is derived for the evolution of the amplitudes and phases of an arbitrary ensemble of the TE, TM, and TEM modes of a coaxial waveguide. These equations are simultaneously integrated with the complete 3-D Lorentz force equations for an ensemble of electrons using an analytic model of the CHI wiggler [2,3]. The orbit equations are not averaged over a wiggler period; hence, we model the adiabatic injection of the beam into the wiggler self-consistently, and can specify the initial conditions of the beam prior to injection. This is advantageous since the design codes for electron guns and beam diagnostics generally give information on the beam conditions outside the wiggler.

* Corresponding author. Tel. +1 703 734 5840, fax +1 703 821 1134, e-mail freund@mmace.nrl.navy.mil.
[1] Permanent address: Science Applications International Corp., McLean, VA 22102, USA.
[2] Permanent address: Mission Research Corp., Newington, VA 22122, USA.
[3] Permanent address: University of Maryland, College Park, MD 20742, USA.

SSDI 0168-9002(94)01561-9

The wiggler amplitudes and periods which can be achieved have been determined using the POISSON/SUPERFISH group of codes [5]. To this end, we have specified vanadium permendur spacers and found that a 4 kG solenoid would saturate the ferrite for spacers with inner and outer radii of $R_{in} = 0.7$ and $R_{out} = 1.5$ cm, and a wiggler period of $\lambda_w = 1.5$ cm. For convenience, we shall also assume that R_{in} and R_{out} are also the inner and outer radii of the coaxial waveguide. Using these wiggler dimensions, we choose to operate with a 10 kG solenoid which provides a wiggler amplitude of ~ 2 kG at the center of the gap (corresponding to a maximum of the periodic field amplitude of ~ 4 kG at the pole faces) and a uniform axial field component of ≈ 6 kG to provide for additional focusing. Note that a magneto-resonant enhancement in the gain and efficiency is also present when the Larmor period associated with the uniform axial field component is close to the wiggler period. We also assume an entry taper region of $N_w = 5$ wiggler periods in length. This is found to be sufficiently long to preserve the initial electron beam quality through the injection process.

Since the performance of an FEL is critically dependent upon the electron beam quality, we must design an electron gun which produces an annular beam with a low energy spread. The design tool we used for this is the EGUN code [6]. In designing the electron beam, we first need to specify the energy, current, and inner and outer radii of the beam. Bearing in mind that the wiggler period is 1.5 cm and that operation in G-band is desired, we choose an electron beam voltage in the neighborhood of 690 kV and a current of 40 A. Assuming that the inner and outer radii of the beam at the exit of the gun were 1.05 cm and 1.15 cm respectively, it was found to be possible to design a gun which produced a beam with an axial energy spread of substantially less than 0.1%.

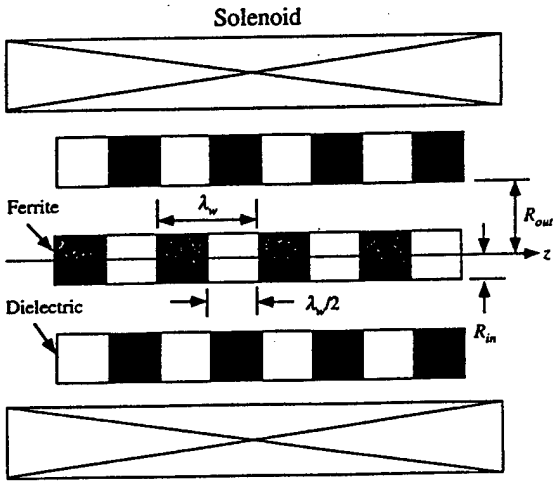

Fig. 1. Schematic illustration of the CHI wiggler configuration.

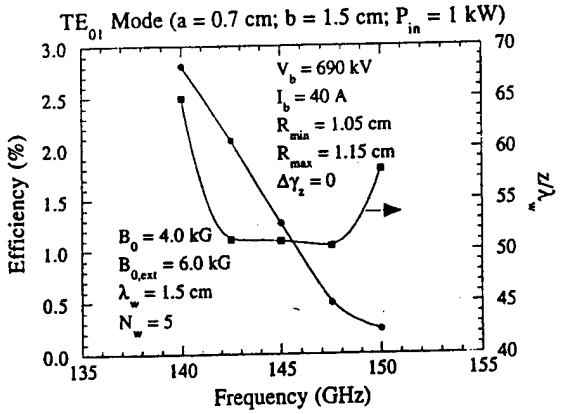

Fig. 2. Efficiency and saturation distance versus frequency at 690 kV.

Finally, throughout the paper we shall deal with the TE_{01} mode and an injected power level of 1 kW.

2. Uniform wiggler case

We first address the interaction for the case of a uniform wiggler, and consider the above-mentioned wiggler, waveguide and beam parameters for the case of an ideal beam in which the axial energy spread $\Delta\gamma_z = 0$. The first issue to be addressed is the frequency tuning for these parameters. To this end, the efficiency and saturation distance is plotted in Fig. 2 versus frequency. It is clear from the figure that the efficiency decreases with frequency over this entire band from 140 to 150 GHz. Since the saturation distance is relatively constant over the range of 142–147 GHz, this implies that the peak gain is found in the vicinity of 142 GHz for an efficiency of $\approx 2.2\%$. As such, we consider the highest gain and efficiency possible and assume a frequency of 142.5 GHz in the remainder of the paper. Note that this type of tuning is expected to occur at all beam voltages and wiggler periods. Thus, it should be possible to retune to 150 GHz just as readily if you are willing to go to higher beam voltages or shorter wiggler periods.

The interaction is sensitive to the beam position. In the first place, we hold the cross-sectional beam area fixed at that used in Fig. 2 and vary the mean beam radius R_0. The results of this study are shown in Fig. 3 in which the variation in efficiency and saturation distance is plotted versus R_0. As seen in the figure, a beam center of 1.10 cm (which is that used previously) seems to be the optimum. Although the efficiency is somewhat higher at $R_0 = 1.12$ cm, this is near the edge of a steep decrease in efficiency with increasing R_0. Therefore, we use the more conservative choice of $R_0 = 1.10$ cm henceforth.

In the second place, the interaction is sensitive to the thickness of the beam. In order to illustrate this, consider

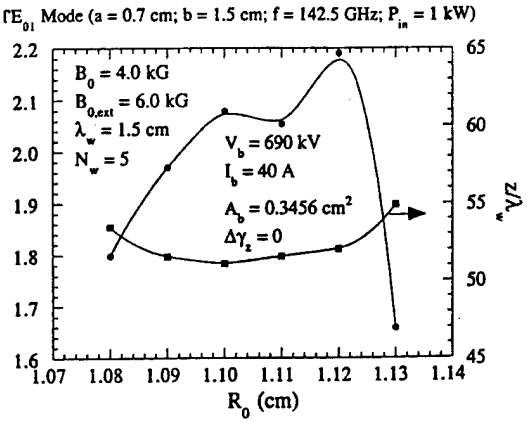

Fig. 3. Efficiency and saturation distance versus R_0.

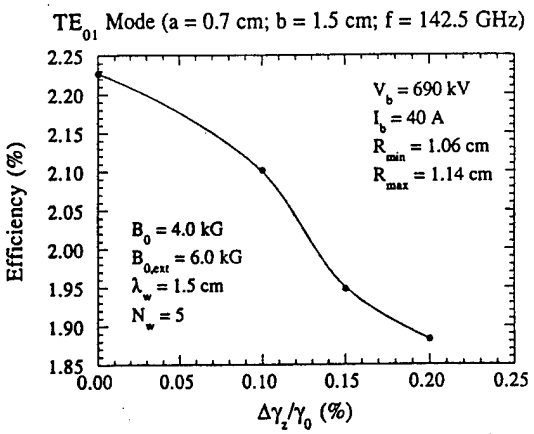

Fig. 5. Variation in the efficiency and saturation distance versus beam thickness.

variation in the efficiency as a function of beam kness ΔR for a mean beam radius fixed at $R_0 = 1.10$ The efficiency and saturation distance are shown in 4 as a function of beam thickness. It is clear from the re that the gain remains relatively constant for $\Delta R \lesssim$ cm and that the efficiency decreases with increasing over the entire range surveyed. Since it is difficult to is the beam down to an extremely narrow thickness, we e a conservative choice of $\Delta R = 0.4$ cm which maxies the gain and still yields a respectively high effiicy. This is the value of the beam thickness which we l use for the remainder of the paper.

Before proceeding to the study of the tapered wiggler raction, we turn to the effect of the axial beam energy ad. The variation in the efficiency as a function of $\Delta\gamma_z$ hown in Fig. 5. Observe that the efficiency falls from ut 2.24% to 2.10% as the axial energy spread increases 1.10%. This is a relatively modest decrease in effiicy, and a beam quality within this range has been onstrated with the gun design code.

Finally, since CW operation is required, the amount of beam loss during the course of the interaction is an important consideration. Since the total beam power is in the neighborhood of 28 MW, even 1% beam loss could pose an insurmountable problem. As a result of the favorable focusing properties of the CHI wiggler, however, no beam loss was found in the simulation prior to saturation for the uniform wiggler cases studied.

3. Tapered wiggler case

Turning to the case of a tapered wiggler, it should be remarked that there is an optimum both in the start-taper point and in the slope of the taper for the efficiency enhancement process. We have optimized both of these parameters and found that for a 1 kW input power that the optimal start-taper point is given by $z_0/\lambda_w = 46$ and the optimal slope of the taper is $\varepsilon_w = -0.001$ (where $\varepsilon_w \equiv$

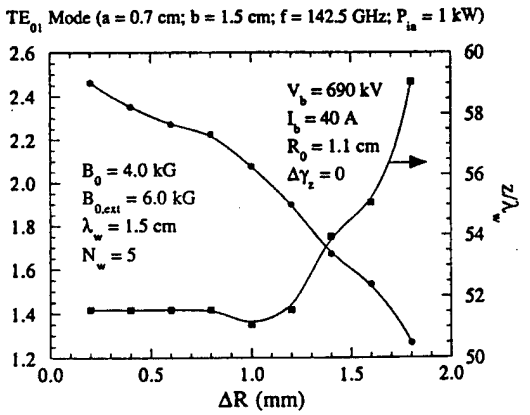

4. Variation in efficiency versus the axial energy spread of eam.

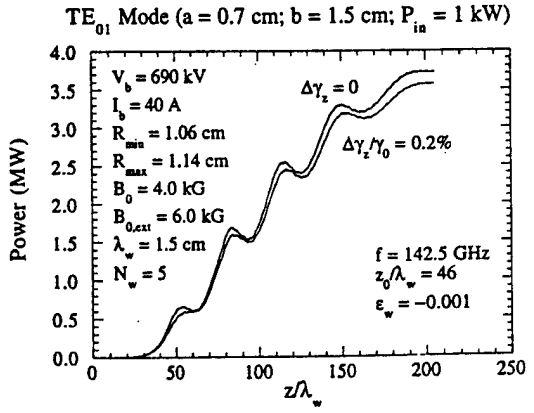

Fig. 6. Evolution of the power with axial position for two choices of the energy spread.

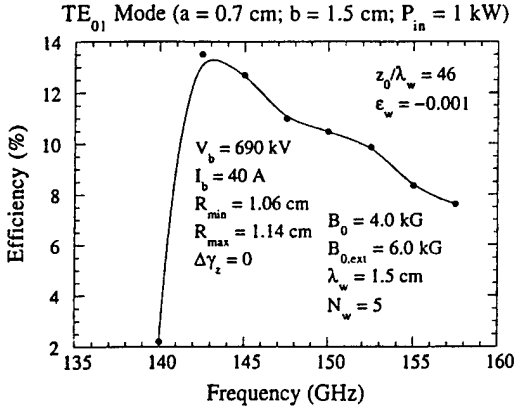

Fig. 7. The bandwidth for the tapered wiggler interaction.

$k_w^{-1} d \ln B_w/dz$). The evolution of the power with axial distance for this choice is shown in Fig. 6 for the cases of an ideal beam with $\Delta\gamma_z = 0$ and for $\Delta\gamma_z/\gamma_0 = 0.2\%$. Note that the interaction is shown over a length of $\approx 200\lambda_w$ which represents the length required to taper the wiggler amplitude to zero for this choice of the taper. It is clear from the figure that the efficiency does not change a great deal with the decrease in beam quality over this range, and that the efficiency rises to a value over 13% for an output power of better than 3.5 MW. This represents a substantial improvement over the uniform wiggler efficiency, and occurs due to the relatively high wiggler field strength.

We now turn to the bandwidth of the tapered wiggler interaction, and find that the bandwidth can be quite large. Consider the case in which we start with the optimum parameters for the interaction at 142.5 GHz including the total length of the system. The bandwidth will then be determined by the response of the identical system to different drive frequencies. The result of this study is shown in Fig. 7 in which the efficiency at the end of the interaction region is plotted as a function of frequency. As is evident from the figure, the efficiency remains high over a frequency range of approximately 142.5 GHz through 160 GHz, which represents a rather large instantaneous bandwidth. This is in accord with an earlier study made using a simpler FEL model [7].

Finally, it should be noted that despite the extended interaction length for the tapered wiggler cases shown, no beam loss was found in simulation for any of these parameters.

4. Summary

The results of this study of a G-band amplifier based upon the CHI wiggler can be summarized rather simply. In the first place, no beam loss was found to occur for either the uniform or tapered wiggler runs. This is a require from the standpoint of designing a CW device. In second place, the efficiencies were found to be fairly l In the uniform wiggler case, efficiencies are in the ne borhood of 2–3% for the chosen parameters, while tapered wiggler interaction produced efficiencies of 14% at 142 GHz. These conclusions hold for both an i beam and for one with the more realistic beam en spread of less than or of the order of 0.2%. It shoul remarked here that beam qualities of this order are c reasonable with careful gun design. We also observe given the sensitivity of the interaction to the beam dir sions, careful gun design is required.

The principal source of concern with the above-n tioned design is the length of the tapered wiggler inte tion. At 200 wiggler periods in length, the support of central rod becomes a serious design issue. However, feel that it is not insurmountable. Most importantly vertical mount would be preferable. Secondly, it is necessary to taper the wiggler to saturation. A shc tapered wiggler would sacrifice some output power facilitate the support of the central rod. Lastly, it shoulc emphasized that this study represents an initial des only. On the basis of this work, we can now undertak optimize the design for higher gain and shorter interact length. This might include several variations in the par eters. Shorter wiggler periods and lower beam volta would help to shorten the overall interaction length. addition, operation closer to the magneto-resonance also enhance the gain. Finally, it should be noted that kW source at these frequencies might require the design a gyrotron oscillator as a source of the drive power.

Acknowledgement

This work was supported by the Department of Ener and the Office of Naval Research.

References

[1] V.L. Granatstein and R. Colestock (eds.), Wave Heating Plasmas (Gordon & Breach, New York, 1986).
[2] R.H. Jackson, H.P. Freund, D.E. Pershing and J.M. Tacce Nucl. Instr. and Meth. A 341 (1994) 454.
[3] H.P. Freund, R.H. Jackson, D.E. Pershing and J.M. Tacce Phys. Plasmas 1 (1994) 1046.
[4] H.P. Freund, R.H. Jackson, D.E. Pershing and J.M. Tacce these Proceedings (16th Int. Free Electron Laser Conf., Sta ford CA, USA, 1994) Nucl. Instr. and Meth. A 358 (199 139.
[5] A.M. Winslow, J. Comp. Phys. 2 (1967) 149.
[6] W.B. Herrmannsfeldt, SLAC Report No. 226 (1979).
[7] B. Levush, H.P. Freund and T.M. Antonsen, Jr., Nucl. Ins and Meth. A 341 (1994) 234.

APPENDIX VII

Theory of a Ubitron in a Corrugated Waveguide

H.P. Freund, K. Nguyen, and D.E. Pershing
Nucl. Instrum. Meth. **A393**, 304 (1997)

Nuclear Instruments and Methods in Physics Research A 393 (1997) 304–307

NUCLEAR INSTRUMENTS & METHODS IN PHYSICS RESEARCH Section A

ELSEVIER

Theory of a ubitron in a corrugated waveguide

H.P. Freund*, K. Nguyen[1], D.E. Pershing[2]

Naval Research Laboratory, Washington, DC 20357-5347, USA

Abstract

A K_a band ubitron is currently under development at NRL using a corrugated waveguide and a helical wiggler. The corrugated waveguide is used for low-voltage operation. A 3-D nonlinear formulation has been derived, and a simulation code TARANTULA has been developed. The model treats HE and EH modes in the vacuum waveguide. No wiggler average is imposed on the electron dynamics. Preliminary calculations indicate that 20% bandwidth operation in K_a band is possible at voltages of about 90 kV with a 7–8 mm period wiggler generating a 500–600 G transverse magnetic field. Detailed results of the theory and simulation will be presented.

1. Introduction

A K_a band ubitron is under development at NRL using grazing intersection for wide instantaneous bandwidth and a high-quality Pierce gun generating a cylindrical, uniform density electron beam for high efficiency. The dispersion characteristics of a periodic waveguide can be exploited for low-voltage ubitron operation. While the phase velocity is 'slower' than the smooth waveguide dispersion characteristic, the amplifier still operates as a fast-wave device.

A 3-D nonlinear formulation of this configuration has been derived, and a simulation code TARANTULA has been developed. No wiggler average is imposed on the electron dynamics, and the simulation includes the self-consistent injection of the beam into the wiggler, as well as the effects of betatron and Larmor motion in the wiggler and emittance growth due to the beam-wave interaction. Preliminary calculations indicate that 20% bandwidth operation in K_a band is possible at voltages of about 90 kV with a 7–8 mm period wiggler generating a 500–600 G transverse magnetic field.

2. General formulation

The external magnetic field used in the analysis can be represented as $\boldsymbol{B}_{ext}(x) = B_0\hat{\boldsymbol{e}}_z + \boldsymbol{B}_w(x)$, where B_0 denotes the magnitude of the axial guide field,

$$\boldsymbol{B}_w(x) = 2B_w(z)\left[I_1'(\lambda)\hat{\boldsymbol{e}}_r\cos\chi - \frac{1}{\lambda}I_1(\lambda)\hat{\boldsymbol{e}}_\theta\sin\chi + I_1(\lambda)\hat{\boldsymbol{e}}_z\sin\chi\right], \quad (1)$$

is the wiggler field, and I_1 and I_1' denote the modified Bessel function of the first kind and its derivative, $\lambda \equiv k_w r$, $\chi \equiv \theta - k_w z$, k_w is the wiggler wave number ($\equiv 2\pi/\lambda_w$), and the wiggler amplitude is assumed to vary adiabatically as

$$B_w(z) = \begin{cases} B_w\sin^2\left(\dfrac{k_w z}{4N_w}\right), & 0 \le z \le N_w\lambda_w, \\ B_w, & N_w\lambda_w < z. \end{cases} \quad (2)$$

This lets us to model the adiabatic injection of the beam over the first N_w wiggler periods.

The corrugated waveguide is shown schematically in Fig. 1, where R_g denotes the inner radius of the waveguide, R_{sl} denotes the maximum radius in the slots, s is the axial length of the slots, and p is the periodicity of the corrugations. The dispersion equation and structure of these modes have been discussed in the literature [1]. The modes contain spatial harmonics corresponding to the period of the structure. The fields in the region outside the slots [i.e., $r \le R_g$] are

$$\delta A(x,t) = \sum_{l,m,n=-\infty}^{\infty} \delta A_{l,m,n}(z)[R_{l,m,n}(r)\hat{\boldsymbol{e}}_r\cos\alpha_{l,m,n} + \Theta_{l,m,n}(r)\hat{\boldsymbol{e}}_\theta\sin\alpha_{l,m,n} + Z_{l,m,n}(r)\hat{\boldsymbol{e}}_z\sin\alpha_{l,m,n}], \quad (3)$$

* Correspondence address: Science Applications International Corporation, 1710 Goodridge Drive, McLean, VA 22102, USA.

[1] Permanent Address: KN Research, Silver Spring, MD 20906.

[2] Permanent Address: Mission Research Corp., Newington, VA 22122.

PII S0168-9002(97)00498-1

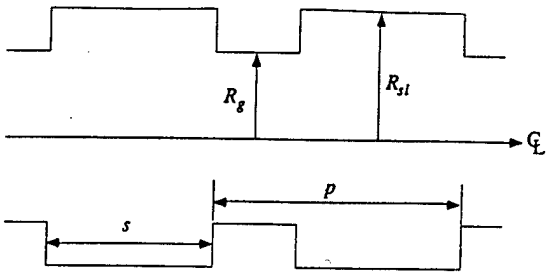

Fig. 1. Schematic representation of the corrugated waveguide.

where

$$\alpha_{l,m,n} = \int_0^z dz' k_{l,m,n}(z') + l\theta - \omega t \tag{4}$$

denotes the phase corresponding to frequency ω and wave number $k_{l,m,n} = k_{l,m,0} + nk_p$, and $k_p[\equiv 2\pi/p]$ defines the wave number of the corrugations. The indices over l and m refer to the azimuthal and radial mode numbers, while the index over n refers to the spatial harmonic. In addition, the polarization functions are given by

$$R_{l,m,n} = J_l'(\kappa_{l,m,n}R_g)J_l'(\kappa_{l,m,n}r) - \frac{l}{\kappa_{l,m,n}R_g}J_l(\kappa_{l,m,n}R_g)\frac{l}{\kappa_{l,m,n}r}J_l(\kappa_{l,m,n}r), \tag{5}$$

$$\Theta_{l,m,n}(r) = \frac{l}{\kappa_{l,m,n}R_g}J_l(\kappa_{l,m,n}R_g)J_l'(\kappa_{l,m,n}r) - \frac{l}{\kappa_{l,m,n}r}J_l(\kappa_{l,m,n}r)J_l'(\kappa_{l,m,n}R_g), \tag{6}$$

and

$$Z_{l,m,n}(r) = \frac{\kappa_{l,m,n}}{k_{l,m,n}}J_l'(\kappa_{l,m,n}R_g)J_l'(\kappa_{l,m,n}r), \tag{7}$$

where $\kappa_{l,m,n}^2 \equiv \omega^2/c^2 - k_{l,m,n}^2$, and J_l and J_l' denote the regular Bessel function and its derivative.

Within the slots [i.e., $R_g < r \le R_{sl}$], the field is assumed to be transverse magnetic and uniform in z where $\delta E_r = \delta E_\theta = \delta B_z = 0$, and

$$\delta E_z = \sum_{l=-\infty}^{\infty} \hat{E}_l S_l\left(\frac{\omega}{c}R_{sl}, \frac{\omega}{c}r\right)\cos(l\theta - \omega t), \tag{9}$$

$$\delta B_r = \sum_{l=-\infty}^{\infty} \frac{lc}{\omega r}\hat{E}_l S_l\left(\frac{\omega}{c}R_{sl}, \frac{\omega}{c}r\right)\cos(l\theta - \omega t), \tag{10}$$

$$\delta B_\theta = -\sum_{l=-\infty}^{\infty} \hat{E}_l S_l'\left(\frac{\omega}{c}R_{sl}, \frac{\omega}{c}r\right)\sin(l\theta - \omega t), \tag{11}$$

where $S_l(x,y) \equiv Y_l(x)J_l(y) - J_l(x)Y_l(y)$, $S_l'(x,y) \equiv Y_l'(x)J_l(y) - J_l'(x)Y_l(y)$, Y_l and Y_l' denote the regular Neumann function and its derivative, and where

$$\delta A_{l,m,n} = -\frac{c}{\omega}\frac{2}{\kappa_{l,m,n}p}\hat{E}_l\frac{S_l((\omega/c)R_{sl}, (\omega/c)R_g)}{J_l(\kappa_{l,m,n}R_g)J_l'(\kappa_{l,m,n}R_g)} \times \sin\left(\frac{k_{l,m,n}s}{2}\right). \tag{12}$$

The dispersion equation can be written in the form

$$\frac{S_l'((\omega/c)R_{sl}, (\omega/c)R_g)}{S_l((\omega/c)R_{sl}, (\omega/c)R_g)} = \frac{s}{p}\sum_{n=-\infty}^{\infty}\frac{\omega/c\kappa_{l,m,n}}{J_l(\kappa_{l,m,n}R_g)J_l'(\kappa_{l,m,n}R_g)}\frac{\sin(k_{l,m,n}s/2)}{(k_{l,m,n}s/2)} \times\left[J_l'^2(\kappa_{l,m,n}R_g) - \frac{c^2k_{l,m,n}^2}{\omega^2}\frac{l^2}{\kappa_{l,m,n}^2R_g^2}J_l^2(\kappa_{l,m,n}R_g)\right]. \tag{13}$$

It is found, in practice, that the sum can be truncated to $-5 \le n \le 5$.

The dispersion equation is solved numerically and two modes are found corresponding to the transverse-electric (TE) and transverse-magnetic (TM) modes in the limit of a smooth-bore waveguide, and are referred to as the EH and HE modes. The dispersion equation for the HE_{11} mode is plotted in Fig. 2 for $R_{sl} = 0.82$ cm, $R_g = 0.41$ cm, $p = 0.2$ cm, and $s = 0.1$ cm. We also show the light-line, the TE_{11} mode dispersion curve for a smooth-bore waveguide, and the results of an HFSS electromagnetic structures simulation code [2] for this structure. It is evident that the HE_{11} and TE_{11} modes have similar dispersion properties for $\omega/ck_w < 2$; however, the HE_{11} mode dispersion curve is somewhat flatter than the TE_{11} mode resulting in lower voltage operation for a given bandwidth. It should also be remarked that both the dispersion relation and the HFSS codes are in good

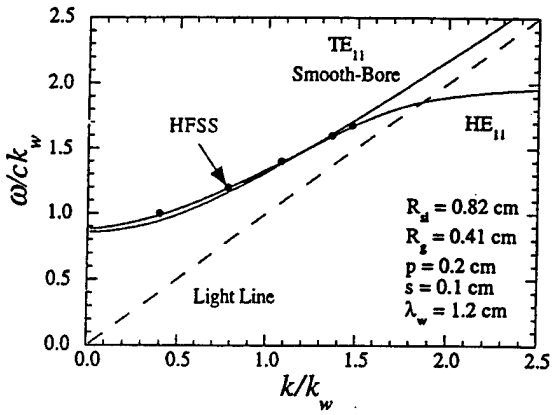

Fig. 2. Dispersion relations for the HE_{11} mode and the TE_{11} mode in a smooth bore waveguide.

agreement with the measured dispersion for a test structure. We focus on the wiggler-mediated interaction in an FEL, and confine the discussion to operation to the supraluminous part of the HE_{11} mode.

The Poynting flux for each mode can be represented as

$$P_{l,m,n}\frac{m_e^2c^4}{8e^2}R_g^2\delta a_{l,m,n}^2\omega k_{l,m,n}(P_{l,m,n}^{(TE)}+P_{l,m,n}^{(TM)}), \tag{14}$$

where $\delta a_{l,m,n}\equiv e\delta A_{l,m,n}/m_ec^2$,

$$P_{l,m,n}^{(TE)}\equiv\frac{l^2}{\kappa_{l,m,n}^2R_g^2}J_l^2(\kappa_{l,m,n}R_g)[J_l^2(\kappa_{l,m,n}R_g)-A_{l,m,n}], \tag{15}$$

is the TE-like component of the Poynting flux, and

$$P_{l,m,n}^{(TM)}\equiv J_l'^2(\kappa_{l,m,n}R_g)[J_l^2(\kappa_{l,m,n}R_g)-A_{l,m,n}] - \frac{2A_{l,m,n}}{\kappa_{l,m,n}R_g}J_l(\kappa_{l,m,n}R_g)J_l'(\kappa_{l,m,n}R_g) \tag{16}$$

is the TM-like component, and $A_{l,m,n}\equiv J_{l-1}(\kappa_{l,m,n}R_g)J_{l+1}(\kappa_{l,m,n}R_g)$.

The dynamical equations which govern the evolution for the amplitude and phase of each mode is found by substitution of the field representation into Maxwell's equations and the subsequent orthogonalization in the azimuthal, radial, and spatial harmonic mode structures, and the average over a wave period. We find that

$$P_{l,m,n}^{(TE)}\left[\frac{d^2}{dz^2}+\left(\frac{\omega^2}{c^2}-k_{l,m,n}^2-\kappa_{l,m,n}^2\right)\right]\delta a_{l,m,n} - P_{l,m,n}^{(R)}\left(\frac{\omega^2}{c^2}-k_{l,m,n}^2-\kappa_{l,m,n}^2\right)\Bigg]\delta a_{l,m,n} + P_{l,m,n}^{(TM)}\left[\frac{d^2}{dz^2}+\left(1+\frac{\kappa_{l,m,n}^2}{k_{l,m,n}^2}\right)\left(\frac{\omega^2}{c^2}-k_{l,m,n}^2-\kappa_{l,m,n}^2\right)\right]\delta a_{l,m,n} = \frac{\omega_b^2}{c^2}\left\langle\frac{v_1}{|v_3|}T_{l,m,n}^{(1)}+\frac{v_2}{|v_3|}T_{l,m,n}^{(2)}+\frac{2\kappa_{l,m,n}}{k_{l,m,n}} \times J_l'(\kappa_{l,m,n}R_g)J_l(\kappa_{l,m,n}r)\sin\alpha_{l,m,n}\right\rangle, \tag{17}$$

$$2k_{l,m,n}^{1/2}P_{l,m,n}^{(TE)}\frac{d}{dz}(k_{l,m,n}^{1/2}\delta a_{l,m,n})-k_{l,m,n}P_{l,m,n}^{(R)}\frac{d}{dz}\delta a_{l,m,n} + 2P_{l,m,n}^{(TM)}\left(k_{l,m,n}+\frac{\kappa_{l,m,n}^2}{k_{l,m,n}}\right)^{1/2}\left[\left(k_{l,m,n}+\frac{\kappa_{l,m,n}^2}{k_{l,m,n}}\right)^{1/2}\delta a_{l,m,n}\right] = \frac{\omega_b^2}{c^2}\left\langle\frac{v_1}{|v_3|}T_{l,m,n}^{(3)}+\frac{v_2}{|v_3|}T_{l,m,n}^{(4)}+\frac{2\kappa_{l,m,n}}{k_{l,m,n}} \times J_l'(\kappa_{l,m,n}R_g)J_l(\kappa_{l,m,n}r)\cos\alpha_{l,m,n}\right\rangle, \tag{18}$$

where $\omega_b^2\equiv 4\pi e^2n_b/m_e$, the velocity components (v_1, v_2, v_3) are defined in the wiggler frame in which $\hat{e}_1=\hat{e}_x\cos k_wz+\hat{e}_y\sin k_wz$, $\hat{e}_2=-\hat{e}_x\sin k_wz+\hat{e}_y\cos k_wz$, $\hat{e}_3=\hat{e}_z$, and

$$P_{l,m,n}^{(R)}=-\frac{\kappa_{l,m,n}^2}{k_{l,m,n}^2}\frac{2A_{l,m,n}}{\kappa_{l,m,n}R_g}J_l(\kappa_{l,m,n}R_g)J_l'(\kappa_{l,m,n}R_g). \tag{19}$$

describes the radial power flow into and out of the slots. In addition,

$$\begin{bmatrix}T_{l,m,n}^{(1)}\\T_{l,m,n}^{(2)}\\T_{l,m,n}^{(3)}\\T_{l,m,n}^{(4)}\end{bmatrix}=J_{l+1}(\kappa_{l,m,n}R_g)J_{l-1}(\kappa_{l,m,n}r)\begin{bmatrix}-\cos(\alpha_{l,m,n}-\chi)\\\sin(\alpha_{l,m,n}-\chi)\\\sin(\alpha_{l,m,n}-\chi)\\\cos(\alpha_{l,m,n}-\chi)\end{bmatrix} + J_{l-1}(\kappa_{l,m,n}R_g)J_{l+1}(\kappa_{l,m,n}r)\begin{bmatrix}-\cos(\alpha_{l,m,n}+\chi)\\-\sin(\alpha_{l,m,n}+\chi)\\\sin(\alpha_{l,m,n}+\chi)\\-\cos(\alpha_{l,m,n}+\chi)\end{bmatrix}. \tag{20}$$

and the averaging operator is defined as

$$\langle(\cdots)\rangle\equiv\frac{1}{A_g}\frac{1}{4\pi^2}\iiint d^3p_0\beta_{z0}F_b(p_0)\int_{A_g}\int dx_0\,dy_0\sigma_\perp(x_0,y_0) \times\int_0^{2\pi}d\psi_0\sigma_\psi(\psi_0)\int_0^{2\pi}d\zeta_0\sigma_z(\zeta_0)(\cdots), \tag{21}$$

where $\beta_{z0}(\equiv v_{z0}/c)$ denotes the initial axial velocity, ψ_0 is the initial ponderomotive phase, and $\zeta_0(\equiv k_pz_0)$ is the initial phase relative to the spatial harmonics of the corrugations. These equations reduce to those for the smooth-bore guide in the limit $R_{sl}\to R_g$ [3].

The initial distributions in the cross section and entry time model a beam with a uniform pulse structure and a flat-top radial profile, and the initial momentum distribution models a monoenergetic beam with a pitch-angle spread of the form

$$F_b(p_0)=\frac{\exp[-(p_{z0}-p_0)^2/\Delta p_z^2]\delta(p_0^2-p_{\perp0}^2-p_{z0}^2)H(p_{z0})}{\pi\int_0^{p_0}dp_{z0}\exp[-(p_{z0}-p_0)^2/\Delta p_z^2]}, \tag{22}$$

where p_0 and Δp_z denote the bulk momentum and the axial momentum spread, and H is the Heaviside function. The axial energy spread associated with the distribution is

$$\frac{\Delta\gamma_z}{\gamma_0}=1-\frac{1}{\sqrt{1+2(\gamma_0^2-1)\dfrac{\Delta p_z}{p_0}}}, \tag{23}$$

where $\gamma_0=1+p_0^2/m_e^2c^2$.

Electron dynamics are integrated subject to the magnetostatic, electromagnetic, and self-electric and self-magnetic fields using the 3D Lorentz force equations. The effect of beam space-charge waves is not included in the analysis. Hence, we integrate in z via

$$v_z \frac{\mathrm{d}}{\mathrm{d}z} p = -e[\delta E(x,t) + E^{(s)}(r,z)] - \frac{e}{c} v \times [B_{ext}(x) + \delta B(x,t) + B^{(s)}(r,z)], \quad (24)$$

where $B_{ext}(x)$ describes the axial magnetic field and the wiggler field, and δE and δB represent the electromagnetic field due to the aggregate of all the spatial harmonics. The self-fields are represented as [4]

$$E^{(s)} = -\frac{m_e}{2e}\omega_b^2[(x - \langle x\rangle)\hat{e}_x + (y - \langle y\rangle)\hat{e}_y],$$
$$B^{(s)} = -\frac{m_e}{2e}\omega_b^2\langle\beta_z\rangle[(y - \langle y\rangle)\hat{e}_x - (x - \langle x\rangle)\hat{e}_y]. \quad (25)$$

3. Numerical analysis

The dynamical equations for the fields and the electrons are solved numerically for an amplifier configuration in which a single wave of frequency ω is injected into the system at $z = 0$ in concert with the electron beam. The initial conditions on the waveguide modes are chosen to model the injection of each mode at the same frequency with some arbitrary power level and with a wave number equal to that of the vacuum value. The effect of the self-electric field on the initial kinetic energy includes the space-charge depression in kinetic energy across the beam.

We consider amplification of an HE_{11} mode in a waveguide with parameters corresponding to the cold waveguide dispersion studies shown in Fig. 2. The results of the simulation for a variety of beam voltages near 200 kV and a beam current of 82 A and a beam radius of 0.205 cm are shown in Fig. 3 where we plot the saturation efficiency versus frequency. It is evident from the figure that efficiencies ranging from 15 to 25% are achievable over a bandwidth extending from about 26–45 GHz for beam voltages which may vary from 195–210 kV. The runs illustrated in Fig. 3 were made for an ideal beam in which the axial energy spread vanishes. We can estimate the limits on the energy spread which can be tolerated by noting that the thermal regime occurs when $\Delta v_z/v_0 \approx \mathrm{Im}\, k/(\mathrm{Re}\, k + k_w)$. For the example shown of a beam voltage of 200 kV and a frequency of 35 GHz which is in the center of the band, we find that $\mathrm{Im}\, k/k_w \approx 0.035$ and $\mathrm{Re}\, k/k_w \approx 1.08$ so that $\Delta v_z/v_0 \approx 1.7\%$. This translates into and axial energy spread which must be less than $\Delta\gamma_z/\gamma_0 \approx 1.6\%$, which is well within the state-of-the-art in electron gun design.

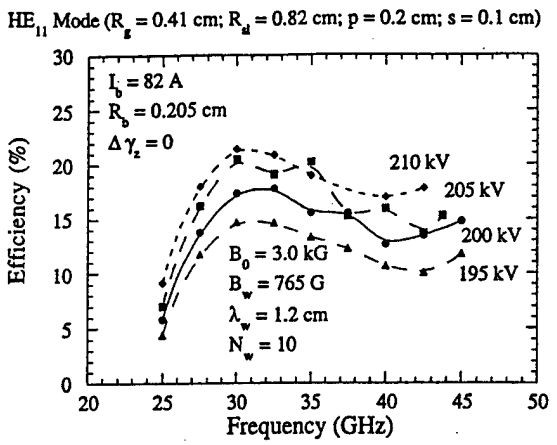

Fig. 3. Plot of the saturation efficiency versus frequency for the HE_{11} mode.

4. Summary and discussion

In summary, we have compared the analytic dispersion relation for a corrugated waveguide with both the HFSS structure code and with the measured dispersion of a test structure and found good agreement. Based upon this analytic mode structure, we have then derived a nonlinear formulation and simulation code for the interaction of an electron beam with a helical wiggler field in a corrugated waveguide. Preliminary results indicate are encouraging in that both good efficiencies and broad bandwidth are possible.

Acknowledgements

This work was supported in part by the US Office of Naval Research. Computational work was supported in part by grants of High Performance Computing (HPC) time from the Department of Defense HPC Shared Resource Centers CEWES and NAVO.

References

[1] P.J.B. Clarricoats, M.I. Sobhy, Proc. IEE 115 (1968) 652.
[2] HFSS refers to the High-Frequency Structure Simulation code available from Hewlett-Packard Corp.
[3] H.P. Freund, T.M. Antonsen Jr., Principles of Free-electron Lasers, 2nd ed., Chapman & Hall, London, 1996.
[4] H.P. Freund, R.H. Jackson, D.E. Pershing, Phys. Fluids B 5 (1993) 2318.

APPENDIX VIII

Simulation of an Annular Beam Free-Electron Laser

M. Blank, H.P. Freund, R.H. Jackson, D.E. Pershing,
and J.M. Taccetti
Nucl. Instrum. Meth. **A375**, 169 (1996)

Nuclear Instruments and Methods in Physics Research A 375 (1996) 169–170

NUCLEAR INSTRUMENTS & METHODS IN PHYSICS RESEARCH Section A

ELSEVIER

Simulation of an annular beam free-electron laser

M. Blank*, H.P. Freund[1], R.H. Jackson, D.E. Pershing[2], J.M. Taccetti[3]

Naval Research Laboratory, Washington, DC 20375, USA

Abstract

A nonlinear analysis of an annular beam FEL with a helical wiggler and axial guide field is presented. An annular beam has the advantage of reduced DC self-fields, facilitating beam transport in short period wigglers. A 55 kV/5 A annular beam interacting with the TE_{11} cylindrical waveguide mode is considered. The inner and outer beam radii are 0.27 and 0.33 cm, respectively. The wiggler amplitude is 250 G and the period is 0.9 cm. Axial guide fields up to 3 kG are studied. The ARACHNE slow-time-scale simulation code shows that efficiencies of 10%, corresponding to gains >40 dB, are possible for grazing incidence with the TE_{11} mode in Ku-band. In addition, the 3 dB instantaneous bandwidth is found to be greater than 20%.

1. Introduction

The free-electron laser (FEL) operation is based on the beating of the wiggler and radiation fields to produce a slowly varying ponderomotive wave in phase with the electron beam. The resonant wavelength depends upon the beam energy and the wiggler parameters as $\lambda \approx (1 + a_w^2)\lambda_w/2\gamma_0^2$, where λ_w is the wiggler period, γ_0 is the bulk relativistic factor of the beam, and $a_w \approx 0.0934 B_w \lambda_w$ for a wiggler amplitude B_w in kG and period in cm. The wavelength, gain, and efficiency all decrease as the energy increases for fixed wiggler parameters. A great deal of effort has been devoted to the design of short period wigglers for high frequency operation with low beam energies. However, this is a self-defeating process since reductions in the wiggler period often result in reductions in the wiggler amplitude with a deleterious impact on the efficiency and gain.

In order to circumvent these restrictions, we consider the effect of using an annular electron beam. This has the advantage that the DC self-fields are smaller than in a solid beam of comparable current, which facilities propagation through the small gaps required of short period wigglers. This configuration is simulated using the ARACHNE code [1,2] which is a slow-time-scale amplifier formulation which describes the interaction of the beam propagating through a helical wiggler and an axial guide field with the modes in a cylindrical waveguide and includes collective effects both in the beam-space-charge waves (i.e., Raman effects) and in the DC self-electric and self-magnetic fields due to the bulk beam charge and current densities.

2. Simulation results

The ARACHNE code was used to simulate the performance of an annular beam FEL amplifier with a helical wiggler and an axial guide field. The device parameters, which correspond to grazing incidence for the fundamental TE_{11} mode, are listed in Table 1.

The theoretical prediction of efficiency versus frequency for an ideal beam (energy spread $\Delta\lambda_z = 0$) interacting with the TE_{11} cylindrical waveguide mode is plotted in Fig. 1. The simulation shows a peak efficiency of 10.6% and a 3 dB bandwidth of 22%. The degradation of peak ef-

Table 1
Nominal design parameters for the Ku-band annular beam FEL

Beam voltage	55 kV
Beam current	5 A
Waveguide radius	0.6 cm
Wiggler period	0.9 cm
Wiggler field amplitude	0.25 kG
Axial guide field amplitude	3 kG
Centre frequency	17.0 GHz
Input power	1 W

* Corresponding author. Tel. +1 202 767 6656, fax +1 202 767 1280, e-mail blank@mmace.nrl.navy.mil.

[1] Permanent address: Science Applications International Corp., McLean, VA 22102.

[2] Permanent address: Mission Research Corp., Newington, VA 22122.

[3] Permanent address: University of Maryland, College Park, MD 20742.

PII S0168-9002(96)00045-9

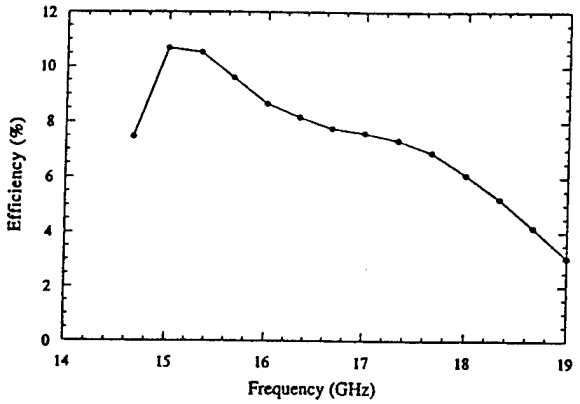

Fig. 1. Theoretical predictions of efficiency versus frequency for a 55 kV/5 A electron beam interacting the a TE_{11} mode in the presence of a helical wiggler with 250 G magnetic field on axis.

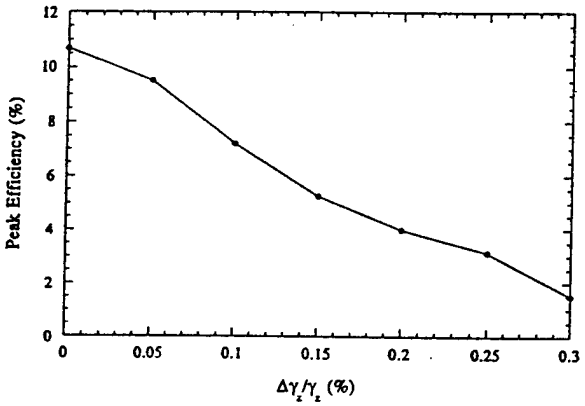

Fig. 2. Theoretical predictions of peak efficiency versus axial velocity spread.

ficiency with increasing axial energy spread is shown in Fig. 2. At an energy spread $\Delta\gamma_z/\gamma_z = 0.2\%$, the peak efficiency is reduced to approximately 4%, which is less than half the peak efficiency for an ideal beam. Thus, it is important to keep energy spread extremely low.

The performance predictions for the annular beam interaction were compared to simulations for a solid beam interaction and the results are shown in Fig. 3. In the simulations, the total current, voltage, and wiggler field were held constant. The annular beam was assumed to have an inner radius of 0.27 cm and an outer radius of

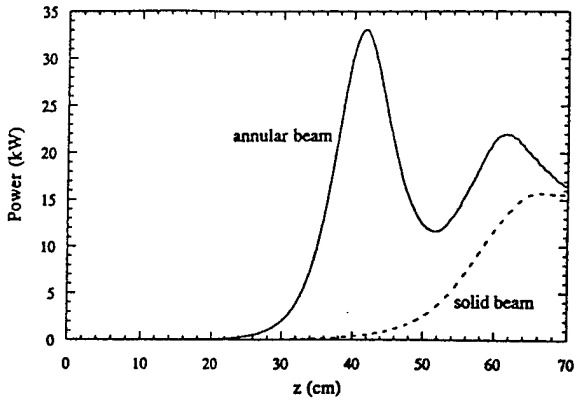

Fig. 3. Comparison of output power versus interaction length for an annular electron beam (inner and outer radii of 0.27 cm and 0.33 cm, respectively), shown with the solid line, and a solid beam (0.3 cm radius), shown with the dashed line.

0.33 cm, while the radius of the radius of the solid beam was 0.3 cm. For both cases self fields were included and the energy spread was assumed to be zero. Fig. 3 shows that the annular beam interaction offers dramatic performance improvements over the solid beam. The saturated power for the annular beam interaction is more than twice that of the solid beam case. In addition, the saturation length is significantly reduced for the hollow beam, indicating that a shorter device is possible.

Acknowledgements

This work was supported by the Office of Naval Research. The computational work was supported in part by a grant of HPC time from the DoD HPC Center NAVO on a CRAY C90.

References

[1] H.P. Freund and T.M. Antonsen, Jr., Principles of Free-electron Lasers (Chapman & Hall, London, 1992) Chap. 5.
[2] H.P. Freund, R.H. Jackson and D.E. Pershing, Phys. Fluids B5 (1993) 2318.

APPENDIX IX

Electron Trajectories in a Self-Consistent Wiggler Field Composed of a Dipole Lattice

H.P. Freund, and L.H. Yu
Nucl. Instrum. Meth. **A375**, 304 (1996)

Nuclear Instruments and Methods in Physics Research A 375 (1996) 304–308

NUCLEAR INSTRUMENTS & METHODS IN PHYSICS RESEARCH Section A

Electron trajectories in a self-consistent wiggler field composed of a dipole lattice

H.P. Freund[a,*], L.H. Yu[b]

[a]Science Applications International Corp., McLean, VA 22102, USA
[b]National Synchrotron Light Source, Brookhaven National Laboratory, Upton, NY 11973, USA

Abstract

We study the electron trajectories using two wiggler models. The first is a dipole wiggler (DW) constructed from the superposition of four arrays of individual magnetic dipoles with alternating orientations. This field has the advantage that since the field representation for each dipole is self-consistent, the aggregate field is also. The second model is the parabolic-pole-face (PPF) wiggler which is not self-consistent when wiggler imperfections are included. These two models are used to study the effects of wiggler imperfections on electron trajectories. In addition, the orbits in the PPF wiggler were qualitatively similar to those in the DW model.

1. Introduction

Wiggler imperfections in free-electron lasers (FEL) have been studied using a random walk model of the electron orbits including their effects on spontaneous emission [1] and the linear gain [2,3]. Nonlinear modeling has typically employed the random walk model in conjunction with a wiggler-averaged formalism [4–7], however, non-wiggler-averaged models of the interaction have also been conducted [8–10]. Non-wiggler-averaged models indicate that the specific model used has important implications for FEL performance.

This paper is the first phase of a comprehensive study of wiggler imperfections in FELs using non-wiggler-averaged techniques with self-consistent wiggler models. Here, we confine the analysis to the orbit dynamics. To this end, we construct a self-consistent wiggler model based upon the superposition of multiple magnetic dipoles arranged in four lattices placed symmetrically about the symmetry axis. Imperfections are introduced into this model by randomly varying the strength of each dipole, and the electron orbits are determined by integrating the 3-D Lorentz force equations.

The orbits in this dipole wiggler (DW) are compared with the orbits for a comparable set of imperfections in a parabolic-pole-face (PPF) wiggler model. In contrast to the DW model, the PPF model does not satisfy the curl- and divergence-free requirements when wiggler imperfections are included.

* Corresponding author. Tel. +1 202 767 0034, fax +1 703 734 1134, e-mail freund@mmace.nrl.navy.mil.

2. The wiggler configurations

The dipole wiggler configuration we employ is a superposition of four lattices each of which is composed of an array of magnetic dipoles with alternating orientations. This is illustrated schematically in Fig. 1. As shown, each lattice is displaced from the symmetry axis by $\pm g_y$ in the y-direction and $\pm g_x$ in the x-direction. This produces a field which is periodic in the z-direction and the separation between the dipoles is one half of the wiggler period (λ_w). Our purpose in using four symmetrically placed lattices is to obtain a field with a local minimum along the symmetry axis to provide focusing in both transverse directions.

The field produced by each dipole is known in closed form, and the aggregate field produced by the superposition of the field of each dipole is both curl- and divergence-free. We can write the aggregate field in the form

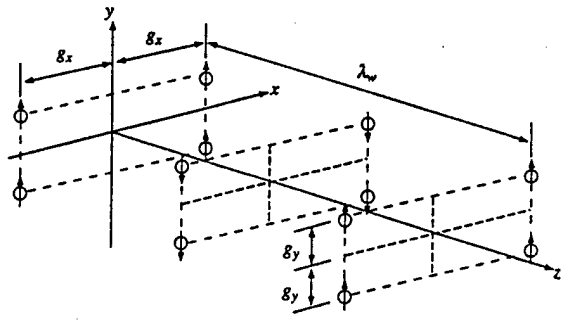

Fig. 1. Schematic representation of the dipole wiggler.

SSDI 0168-9002(95)01354-7

$$B_{w,x} = (x - g_x) \sum_{n=1}^{N_p} B_n[P_n(x - g_x, y - g_y, z) + P_n(x - g_x, y + g_y, z)] + (x + g_x) \times \sum_{n=1}^{N_p} B_n[P_n(x + g_x, y - g_y, z) + P_n(x + g_x, y + g_y, z)], \quad (1)$$

$$B_{w,y} = \sum_{n=1}^{N_p} B_n[(y - g_y)P_n(x - g_x, y - g_y, z) + (y + g_y) \times P_n(x - g_x, y + g_y, z)] + \sum_{n=1}^{N_p} B_n[(y - g_y)P_n(x + g_x, y - g_y, z) + (y + g_y)P_n(x + g_x, y + g_y, z)] - \sum_{n=1}^{N_p} B_n[R_n(x - g_x, y - g_y, z) + R_n(x - g_x, y + g_y, z)] - \sum_{n=1}^{N_p} B_n[R_n(x + g_x, y - g_y, z) + R_n(x + g_x, y + g_y, z)], \quad (2)$$

$$B_{w,z} = \sum_{n=1}^{N_p} B_n[S_n(x - g_x, y - g_y, z) + S_n(x - g_x, y + g_y, z)] + \sum_{n=1}^{N_p} B_n[S_n(x + g_x, y - g_y, z) + S_n(x + g_x, y + g_y, z)], \quad (3)$$

where B_n is the strength of each consecutive period, N_p is the number of wiggler periods,

$$P_n(x, y, z) \equiv \frac{y}{[x^2 + y^2 + (z - n\lambda_w)^2]^{5/2}} - \frac{y}{[x^2 + y^2 + (z - n\lambda_w - \lambda_w/2)^2]^{5/2}}, \quad (4)$$

$$R_n(x, y, z) \equiv \frac{1}{[x^2 + y^2 + (z - n\lambda_w)^2]^{3/2}} - \frac{1}{[x^2 + y^2 + (z - n\lambda_w - \lambda_w/2)^2]^{3/2}}, \quad (5)$$

and

$$S_n(x, y, z) \equiv \frac{y(z - n\lambda_w)}{[x^2 + y^2 + (z - n\lambda_w)^2]^{5/2}} - \frac{y(z - n\lambda_w - \lambda_w/2)}{[x^2 + y^2 + (z - n\lambda_w - \lambda_w/2)^2]^{5/2}}, \quad (6)$$

While this field is periodic it is not sinusoidal. An infinity long array produces a field with a uniform peak-to-peak field strength and period. However, since the field is composed of contributions from all the dipoles, both the amplitude and period shift with displacement from the midpoint of a finite length DW. This is illustrated in Fig. 2 where we plot the normalized [$a_w \approx 0.09337 B_w \lambda_w$ is the wiggler parameter] y-component of the on-axis field versus z for a 50 period DW with $\lambda_w = 1.8$ cm, a peak amplitude of 5.2 kG, $g_x = 1.8$ cm, and $g_y = 1.225$ cm. As shown, the amplitude varies rapidly near the ends of the wiggler where large spikes are found. Note that the period (as indicated by the positions of the field zeroes) also varies with displacement from the midpoint. In a real wiggler, these end effects would be compensated for by tapering the dipole strengths near the ends of the wiggler; however, for our purposes, we adopt the simpler procedure of using a very long wiggler and focus on the trajectories near the center where the field is nearly uniform.

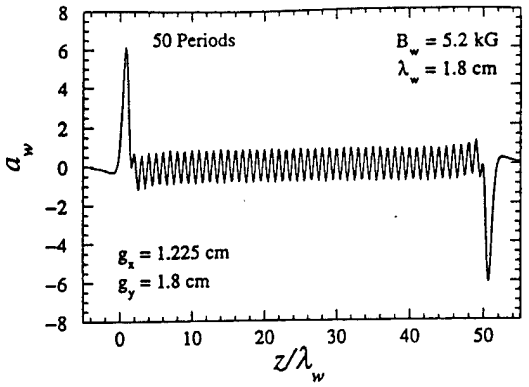

Fig. 2. Axial variation of the normalized on-axis y-component of the dipole wiggler field.

To compare trajectories in the DW with those in a PPF wiggler, g_x and g_y are chosen so that a_w varies as $\cosh(k_w x/\sqrt{2})\cosh(k_w y/\sqrt{2})$ as in the PPF model. This is illustrated in Fig. 3 where we plot the variation of a_w in the wiggle-plane (i.e., the x-direction), where the solid line represents the variation of the DW model and the dots represent the variation found from the PPF model. Note

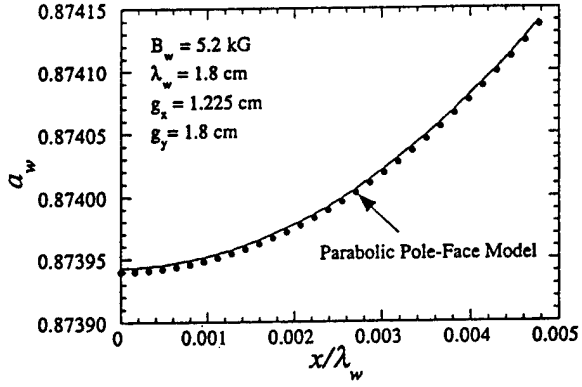

Fig. 3. Variation in the y-component of the field with displacement in the x-direction.

that the variation in the DW in the y-direction is similarly close to the PPF model. It is clear that with this choice of g_x and g_y, the transverse focusing of the DW matches that found for the PPF model.

Finally, imperfections are introduced into the DW model by making random variations in the period-to-period dipole strengths. An actual wiggler would also have imperfections due to random variations in the offsets and spacing between the dipoles; however, we shall postpone the study of these effects for the future.

The field in a PPF wiggler can be represented as

$$B_w(x) = B_w(z)\Bigg\{\cos k_w z\Bigg[\hat{e}_x \sinh\left(\frac{k_w x}{\sqrt{2}}\right)\sinh\left(\frac{k_w y}{\sqrt{2}}\right) + \hat{e}_y \cosh\left(\frac{k_w x}{\sqrt{2}}\right)\cosh\left(\frac{k_w y}{\sqrt{2}}\right)\Bigg] - \sqrt{2}\hat{e}_z \sin k_w z \cosh\left(\frac{k_w x}{\sqrt{2}}\right)\sinh\left(\frac{k_w y}{\sqrt{2}}\right)\Bigg\}, \quad (7)$$

where the amplitude varies in z to model wiggler imperfections. However, this model is curl- and divergence-free only when the amplitude B_w is constant. If B_w varies with z, then only the z-component of the curl vanishes, and this model is not self-consistent.

Imperfections will be introduced into the PPF model under the assumption that $B_w(z) = B_{w0} + \Delta B_w(z)$, where $\Delta B_w(z)$ describes random fluctuations in the amplitude. The random component is determined using a random sequence $\{\Delta B_n\}$, where $\Delta B_n [\equiv \Delta B_w(n\lambda_w/2)$ for integer $n]$ denotes the random fluctuation at half wiggler period intervals. The amplitude is mapped between these points via $\Delta B_w(z) = \Delta B_n + (\Delta B_{n+1} - \Delta B_n)\sin^2(\pi\delta z/\lambda_w)$, where $z = n\lambda_w/2 + \delta z$ for $0 \le \delta z \le \lambda_w/2$ which is continuous.

Observe that random variations in the DW result in both amplitude and period fluctuations. Period fluctuations occur because field zeroes are determined by cancellation in the fields produced by each dipole, and variation in the dipole strengths or offsets cause fluctuations in the positions of the on-axis field nulls. However, the PPF model is sinusoidal and no period fluctuations are included.

3. Numerical analysis

We integrate electron orbits in the DW and PPF models using the 3-D Lorentz force equations. In the DW model, we inject electrons near the midpoint of a long 800 period wiggler using the same parameters shown in Figs. 2 and 3. This gives ≈200 wiggler periods on either side of the midpoint over which the field is relatively uniform.

We first consider the ideal DW where the dipole strengths are identical and assume an electron energy of 30 MeV; hence, if we inject the electron at z_0 corresponding to a field maximum, then the initial conditions are $x_0/\lambda_w = 0.00023296$, $y_0 = 0$, $z_0/\lambda_w = 399.5$, $p_{x0} = p_{y0} = 0$, and $p_{z0}/m_e c = 59.703$. The motion in the y-direction is negligible and can be ignored. The resulting orbit is shown in Fig. 4, and very regular wiggler motion is found.

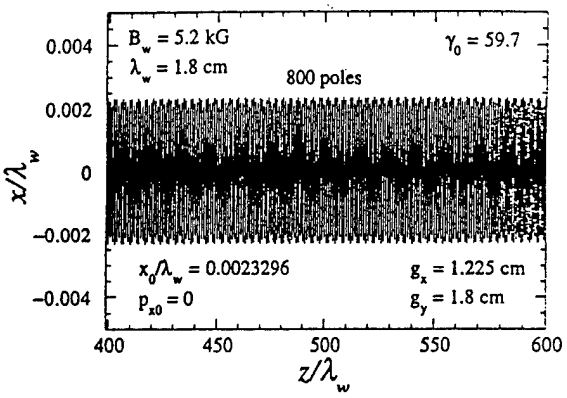

Fig. 4. Electron orbit in an ideal dipole wiggler field.

We nw turn to the effect of imperfections, and randomly vary the dipole strengths for each of the 800 periods in the DW. The specific choice of imperfections is shown in Fig. 5 where we plot the change in a_w versus z. For this specific case, the rms fluctuation level is ≈1%. The variation in the distance between the field nulls is shown in Fig. 6. We find an rms jitter in the separation in the field nulls for this case of ≈0.7%.

Injection of an electron with the same initial conditions used for the case shown in Fig. 4 results in a trajectory which displays both a large-scale betatron oscillation and orbit fluctuations. Focusing on the orbit jitter, we compensate for the betatron oscillation by giving the electron an initial $p_{x0}/m_e c = 0.0275$. The resulting orbit is shown in Fig. 7. The rms amplitude of the jitter is $(\Delta x/\lambda_w)_{rms} \approx 0.024$, and the average displacement of the orbit from the x-axis is $x_{avg}/\lambda_w \approx -1.1 \times 10^{-4}$. Observe that for this case there is no coherent "walk-off" of the beam over an extended interaction length.

Turning to the PPF model, we remark that the initial

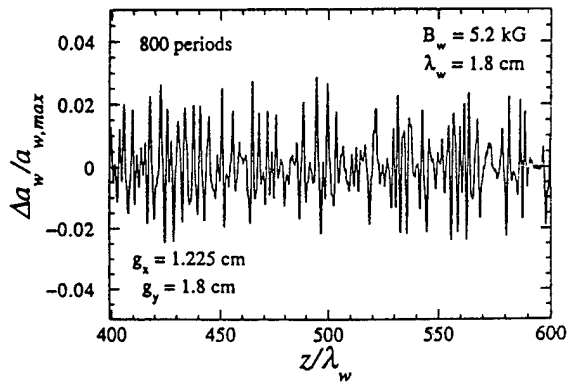

Fig. 5. Peak-to-peak variations in the normalized on-axis y-component of the dipole wiggler field.

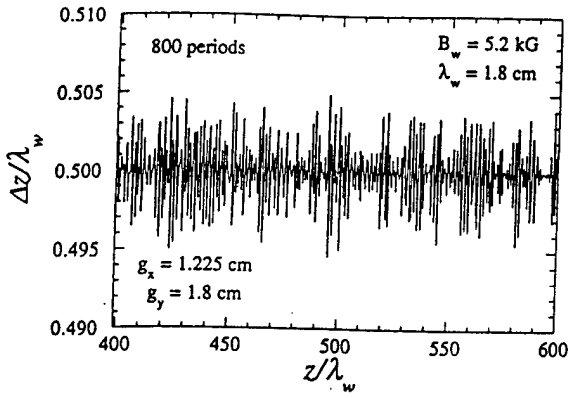

Fig. 6. Variation in the separation between the field nulls for the error distribution corresponding to the amplitude fluctuations in Fig. 5

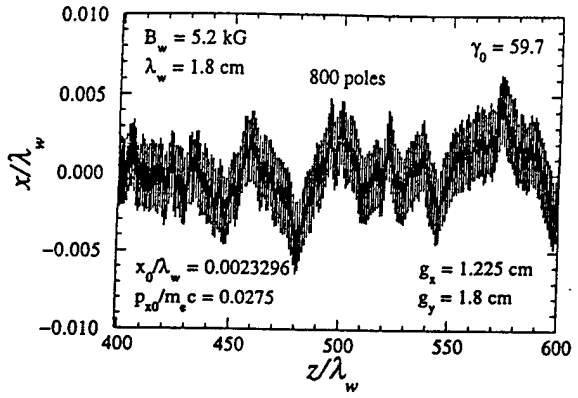

Fig. 7. Electron orbit in the dipole wiggler with the imperfections shown in Figs. 5 and 6.

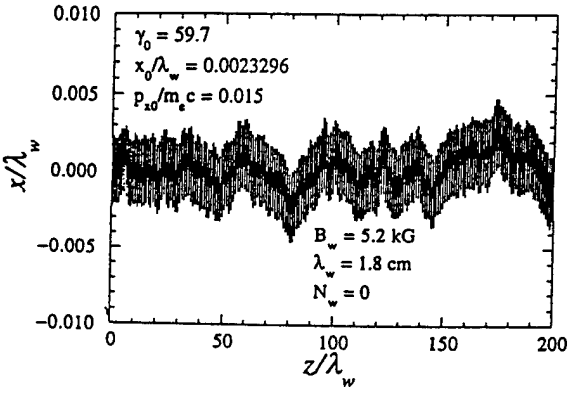

Fig. 8. Electron trajectory in the parabolic-pole-face wiggler with imperfections.

conditions used for the ideal DW also result in very uniform wiggler motion for the PPF wiggler. Imperfections have been introduced into the PPF wiggler model by mapping the peak amplitude at half wiggler period intervals from the DW onto ΔB_n for the PPF model. This does not reproduce all the imperfections from the DW model since there are no period fluctuations in the PPF model. As a result, this misses some peaks and results in a smaller field fluctuation for the PPF wiggler than for the DW. In this case the rms amplitude fluctuation used in the PPF model is approximately 0.77%. While this is some 23% smaller than the rms fluctuation for the DW model, it provides as close a match as is possible to obtain with a sinusoidal wiggler.

With no compensation, betatron oscillations are found as well as the expected orbit jitter (as for the DW). The betatron period is in close agreement with that of the DW, but the amplitude is smaller (due to the smaller rms amplitude fluctuation); hence, we require $p_{x0}/m_e c = 0.015$ to compensate for the betatron oscillations. The resulting orbit shown in Fig. 8 is very similar to that found with the DW model. The rms amplitude of the jitter for the PFF wiggler is $(\Delta x/\lambda_w)_{rms} \approx 0.0017$ which is 29% less than that for the DW.

4. Summary and conclusions

In this paper, we have analyzed electron orbits in two specific wiggler models to study the impact of imperfections. The fundamental conclusions from this study can be divided into two categories relating to the DW and PPF models.

The DW is self-consistent and the introduction of imperfections does not violate the curl- and divergence-free requirements, and no coherent "walk-off" was found for a select choice of imperfections. While we have not yet performed a complete statistical analysis over a large ensemble of randomly generated imperfections, this is significant since the performance of an FEL is not a statistical process and is determined by one specific wiggler rather than an ensemble. If coherent "walk-off" is not to a corollary to the presence of imperfections, then this has important implications for FEL performance and it is important to incorporate this (or similar) wiggler models into full-scale device simulations.

Comparison with the PPF wiggler is important since this is a commonly used in both orbit and full-scale device simulations. To facilitate the comparison, we tailored the DW to provide PPF-like transverse focusing, and tailored the amplitude imperfections in the PPF model to correspond as closely as possible to the DW model. The orbits for the two models were identical for ideal wigglers, and surprisingly close when imperfections were present despite the fact that the PPF model was neither curl- nor divergence-free.

Acknowledgements

This work was supported, in part, by the Office of Naval Research.

References

[1] B.M. Kincaid, J. Opt. Soc. Am. B 2 (1985) 1294.
[2] W.P. Marable, E. Esarey and C.M. Tang, Phys. Rev. A 42 (1990) 3006.
[3] L.H. Yu, S. Krinsky, R.L. Gluckstern and J.B.J. van Zeijts, Phys. Rev. A 45 (1992) 1163.
[4] C.J. Elliott and B. McVey, in: Undulator Magnets for Synchrotron Radiation and Free Electron Lasers, eds. R. Bonifacio, L. Fonda and C. Pellegrini (World Scientific, Singapore, 1987) p. 142.
[5] H.D. Shay and E.T. Scharlemann, Nucl. Instr. and Meth. A 272 (1988) 601.
[6] W.P. Marable, C.M. Tang and E. Esarey, IEEE J. Quantum Electron. QE-27 (1991) 2693.
[7] A. Friedman S. Krinsky and L.H. Yu, IEEE J. Quantum Electron. QE-30 (1994) 1295.
[8] H.P. Freund and R.H. Jackson, Phys. Rev. A 45 (1992) 7488.
[9] H.P. Freund and R.H. Jackson, Nucl. Instr. Meth. A 331 (1993) 461.
[10] H.P. Freund and T.M. Antonsen, Jr., Principles of Free-electron Lasers, 2nd Ed. (Chapman & Hall, London, 1995) chap. 12.

APPENDIX X

Long Wavelength Free-Electron Lasers in 1994

H.P. Freund and V.L. Granatstein
Nucl. Instrum. Meth. **A358**, 551 (1995)

Nuclear Instruments and Methods in Physics Research A 358 (1995) 551–554

NUCLEAR INSTRUMENTS & METHODS IN PHYSICS RESEARCH Section A

ELSEVIER

Long wavelength free electron lasers in 1994

H.P. Freund [a,*], V.L. Granatstein [b]

[a] *Naval Research Laboratory, Washington, DC 20375, USA*
[b] *University of Maryland, College Park, MD 20742, USA*

Abstract

A short summary of the current status and most important future directions for long wavelength free-electron lasers is presented. For the purposes of the discussion, long wavelength refers to wavelengths longer than 0.5 mm. The distinction between long and short wavelengths is not entirely arbitrary since different physical processes may be important. For example, higher current beams are typically employed at long wavelengths and space-charge effects may be important. Indeed, the dominant interaction mechanism is often coherent Raman rather than coherent Compton scattering. In addition, dispersion due to the beam dielectric effects and finite transverse dimensions in the drift tubes and cavities are important effects at longer wavelengths. The ultimate goals of long wavelength FEL research are to achieve much higher average powers with good overall efficiency in a compact design, and the highest average power produced in an FEL to date (36 W) has been recorded in the Ku-band. At the present time, electrostatic accelerators and long pulse modulators appear to be the prime candidates for drivers for these systems; however, advances in induction linac technology which lead to higher repetition rates and improved beam quality could alter this conclusion.

Our purpose in this paper is to provide a summary of long wavelength ($\geqslant 0.5$ mm) free-electron lasers (FELs) which are currently either in operation or under construction that can be used as a guide to the current state of this branch of the field. Note that a companion paper appears in this volume dealing with "short wavelength" FELs [1]. Our basic criterion for inclusion in the table is that the FEL must either be in operation or under construction. Projects which are still in the proposal stage, therefore, fall outside of the scope of this table and have been excluded. In compiling this list, we conducted a search which relies upon (1) contributions to general literature and the proceedings of the annual Free-Electron Laser Conferences, and (2) personal contacts. Personal contacts have proven to be an important source of information concerning FEL programs which are either in the early operational stages or still under construction and have not as yet been described in archival literature. As a consequence, the best reference for many of the entries to the table are personal communcations. In addition, despite our best efforts to compile an exhaustive list, it is possible that several long wavelength FELs have been inadvertently omitted. Our intention is for this compilation to become an annual process associated with the FEL Conference, and we hope that each group will keep us abreast of their experimental results and that any groups we might have missed will contact us with the relevant data on their experiments.

The distinction between long and short wavelength FELs is not entirely arbitrary since different physical processes may be important at longer wavelengths. For example, higher current beams are typically employed in this regime and space-charge effects are more important. In particular, the dominant interaction mechanism is often coherent Raman rather than coherent Compton scattering. In addition, while short wavelength FELs excite optical modes, dispersion due to the beam dielectric effects and finite transverse dimensions in the drift tubes and cavities are important effects at longer wavelengths.

At the present time, we have identified 28 long wavelength FEL experiments which are either in operation or under construction around the world. The table lists the most relevant parameters describing the experiments including: wavelength/frequency, peak power, pulse time, repetition rate, beam voltage and current, wiggler period and field strength, and the type of device and accelerator employed. We have chosen to denote the wiggler parameter by K ($= 0.0934 B_w \lambda_w$, where B_w is the wiggler amplitude in kG and λ_w is the wiggler period in cm); however,

* Corresponding author. Tel. +1 703 734 5840, fax +1 703 821 1134, e-mail freund@mmace.nrl.navy.mil. Permanent address: Science Applications International Corp., McLean, VA 22102, USA.

SSDI 0168-9002(94)01601-1

this parameter is often called a_w in the literature. Since it is impossible to give all the relevant information concerning each device in this format, some compromises have been made. For example, most of these FELs operate over a fairly broad spectral range, and the wavelength and frequency listed have been chosen to correspond to the shortest accessible wavelength. We have also chosen to list the peak powers since the average powers can be obtained from the specified pulse times and repetition rates. The wiggler type shown refers to helical (H), planar (P), circular (C), and coaxial hybrid iron (CH) [2] wigglers. It is important to note that an axial guide field is often used in

Table 1

FEL [Ref.]	λ (mm)/ f (GHz)	P_{peak} (MW)	τ_p (μs)	ν_{rep} (Hz)	V_b/I_b (MV/A)	λ_w (cm)/ K (type)	Type/ acc.
TAU [11]	370/0.8	10^{-5}	100	SS	0.001/0.2	2/0.04 (P)	A/IC
TAU [12]	76/4.9	UC	10	100	0.07/1	4.4/0.12 (P)	SASE/ES
UL [13]	35/8	5×10^{-10}	CW		0.055/0.001	1.9/0.05 (P)	A & O/M
KEK [7]	32/9.4	100	0.015	0.07	1.5/450	16/1.5 (P)	A/IL
ISAS [14]	26/12	0.6	0.4	SS	0.44/150	3.25/0.27 (C)	O/PL
NRL [10]	20/15	4.2	1	6	0.25/100	2.5/0.07 (H)	A/M
MIT [15]	8/33	60	0.025	SS	0.75/300	3.1/0.4 (H)	A/PL
CESTA [16]	8/35	50	0.03	SS	1.8/400	8/2.24 (H)	A/PL
NRL [17]	8/35	UC	1	6	150/10	0.75/0.2 (CH)	A/M
UT [18]	8/35	0.04	100	SS	0.5/200	3/0.53 (H)	SASE/PL
IEE [19]	8/35	140	0.05		3.4/800	11/3.5 (P)	A/IL
JINR [20]	8/35	4	0.2	SS	1.5/200	7.2/1.3 (H)	O/IL
JINR [20]	8/35	30	0.2	SS	1.5/200	7.2/1.3 (H)	A/IL
SIOFM [21]	8/35	UC	0.02	SS	0.4/800	2.2/1 (H)	SASE/PL
ISAS [14]	7/40	1	0.5	SS	0.5/150	3.27/0.27 (C)	O/PL
IAP [20]	6/47	6	0.02	SS	0.5/100	2/0.2 (H)	O/PL
ENEA [22]	2/150	0.001	4	40	2.3/0.27	2.5/1.42 (P)	O/MI
JAERI [23]	5/60	UC	0.12	1	1/1000	4.5/0.76 (P)	O/IL
IAP/INP [24]	4/70	1500	2	SS	1/15000	4/0.3 (H)	O/PL
INP [20]	4/70	30	2	SS	1/1500	4/0.3 (H)	O/PL
UM [25]	3.5/85	0.2	0.02	SS	0.45/17	0.96/0.36 (P)	PL/A
NSWC/MRC [26]	3/95	10	0.25	SS	2.5/100	10/1.9 (H)	O/PL
DLR [27]	3/100	1–2	0.1	SS	0.5/150	2/0.19 (H)	SASE/PL
KAERI [28]	3/100	UC	CW		0.43/2	3.6/0.4 (H)	O/ES
TAU/WI [29]	3/100	UC	1000/CW		2.5/1	4.4/1.8 (P)	O/ES
CU [30]	2/150	5	0.15	SS	0.8/150	1.85/0.25 (H)	A/PL
FOM [9]	1/260	UC	1×10^5	1	2/12	2/0.67 (P)	O/ES
UCLA [31]	0.5/560	UC	2×10^{-6}		15/150	10/2.8 (P)	O/RFL

A – amplifier
C – circular
CESTA – Centre d'Etudes Scientifique e Techniques d'Aquitaine
CH – CHI wiggler
CU – Columbia University, USA
CW – continuous wave
DLR – German Aerospace Research Establishment
ES – electrostatic accelerator
H – helical wiggler
IAP – Institute of Applied Physics, Russia
INP – Institute of Nuclear Physics, Russia
IC – Ignition Coil
IEE – Institute of Electroni Engineering, China
IL – Induction Linac
ISAS – Institute of Space and Astronautical Science, Japan
JAERI – Japan Atomic Energy Research Institute
JINR – Joint Institute for Nuclear Research, Russia
KAERI – Korean Atomic Energy Research Institute
KEK – National Laboratory for High Energy Physics, Japan
NRL – Naval Research Laboratory
NSWC – Naval Surface Weapons Center, USA
M – modulator
MI – microtron
MRC – Mission Research Corp.
O – oscillator
P – planar wiggler
PL – pulse line accelerator
RFL – radio frequency linac
SASE – self amplified spontaneous emission
SIOFM – Shanghai Institute of Optics and Fine Mechanics
SS – single shot
TAU – Tel Aviv University
UC – under construction
UL – University of Liverpool, UK
UM – University of Maryland, USA
UT – University of Twente, The Netherlands
WI – Weizmann Institute, Israel

conjunction with helical wigglers in intense beam FELs, but that the brevity of this format did not permit inclusion of this information in the table.

As the table illustrates, long wavelength FELs employ many types of accelerator (modulators, pulse line accelerators, electrostatic accelerators, microtrons, induction and radio frequency accelerators, and even an automobile ignition coil). As a result, the group exhibits a wide variety of pulse formats and peak and average powers. However, the bulk of the experiments employ pulse line accelerators which operate in a single-shot (SS) mode with high peak powers. Historically, the pioneering work on long wavelength FELs was performed by R.M. Phillips [3] prior to 1964 using modulator technology developed in the microwave tube community (note that Phillips referred to his devices as ubitrons and that the term free-electron laser first came into usage in the early 1970s when it was coined by J.M.J. Madey). Long wavelength FEL research began again at various laboratories in the early 1970s with the intention of extending Phillips' work using intense relativistic electron beams. Much of this work was directed at exploring the basic physics of the Raman regime [4], and high average power was not an essential goal. As a result, single-shot pulse line accelerators are often used since they are capable of producing beams with energies of several MeV and currents of many kiloamperes.

In order to achieve the necessary beam quality from pulse line accelerators, careful design of the diode is essential. The fundamental diode design used in most of the pulse line accelerator-based FELs [5] employ a shaped cathode/anode which is immersed in a converging axial guide field. The anode is designed to "scrape" a large fraction of the beam so that only a central core with a low velocity spread is injected into the wiggler. Typically, the diodes are designed in these configurations to scrape off approximately 90% of the beam but, since pulse line accelerators often produce beam currents in the tens of kiloamperes, this still leaves an appreciable current. As a result, collective FELs built using pulse line accelerators have produced high peak powers, although they suffer from the disadvantages of a low wall-plug efficiency and a low average power.

The principal thrusts of current long wavelength FEL research include the achievements of high average powers, broad bandwidths, and compact systems. In this sense, pulse line accelerator FELs must be considered as proof-of-principle experiments, and the development of practical long wavelength FELs depends upon other accelerator technologies.

Induction linacs have the advantage over pulse line accelerators in that they can be repetitively pulsed. Hence, it is possible, at least in principle, to produce high average powers and high efficiencies. However, there are two practical difficulties with induction linacs for FEL applications. The first is that it is difficult to operate at high repetition rates. The ELF experiment [6] which produced a peak power of approximately 1 GW at 35 GHz operated with a pulse time of 10–20 ns and a repetition rate of 0.5 Hz which represents an average power of only about 7 W. The second is emittance growth which often results in unacceptably high thermal spreads, and the necessity of beam scraping. For example, approximately 80% of the beam was scraped off in the ELF experiment. Thus, while the extraction efficiency was about 34% from the beam that passed through the wiggler, the overall efficiency (using the total beam power prior to scaping) was closer to 7%. In view of this, the recent results from the induction linac-based FEL at KEK [7] which produced a peak power of 100 MW using some beam scraping and ion channel guiding represents a possibly significant advance.

Other approaches which may hold more promise for achieving high average powers and efficiencies involve long pulse modulators and electrostatic accelerators. In the case of electrostatic accelerators, full CW operation is possible if nearly total beam recycling can be achieved. This has been accomplished at infrared wavelengths at the University of California at Santa Barbara [8]. However, the level of beam recovery which can be achieved decreases with increasing extraction efficiency from the FEL, and this may prove to be a limiting factor in the technology. A significant experiment using electrostatic accelerators is currently under construction at FOM in The Netherlands [9]. The ultimate goal of this experiment is to build a CW FEL designed to produce 1 MW at 260 GHz for the heating of plasmas in magnetic fusion reactors. Based upon a beam current of 12 A and a kinetic energy of 2 MeV, this yields an extraction efficiency of the order of 4%. However, the overall system efficiency can be much larger due to the beam recovery system. It will be interesting to see how effective beam recovery can be in a system with this level of extracted power.

One disadvantage associated with electrostatic accelerators is that they are low current devices which often implies low gains as well. For this reason, the FOM configuration is that of an oscillator. A related disadvantage arises since high output power requires high beam power; hence, a high power electrostatic accelerator-based FEL also requires high energies which implies a large physical size. This would be inconsistent with applications requiring compact devices.

For applications which require more compact devices, long pulse modulators may have advantages. A research program at the Naval Research Laboratory has been devoted to the development of this concept with goals of high average power. The present experiment [10] employs a 250 kV/100 A modulator with a pulse time of 1 μs and a repetition rate of 6 Hz to produce approximately 4.2 MW in Ku-band. This represents an average power of about 36 W which is the highest average power produced in an FEL to date. The direction of this program is to achieve still higher powers at higher frequencies using lower voltage electron beams. To this end, a follow-on experiment is in

the design stages now which will employ some form of dispersion control (i.e., a rippled-wall waveguide) to permit lower voltage operation.

In summary, the highest average power produced in an FEL has now been recorded in a Ku-band FEL; however, the ultimate goals of long wavelength FEL research are to achieve much higher average powers with good overall efficiency. In addition, many applications require more compact designs than have yet been achieved. At the present time, electrostatic accelerators and long pulse modulators appear to be the prime candidates for drivers for these systems; however, advances in induction linac technology which lead to higher repetition rates and improved beam quality could change this conclusion.

References

[1] W.B. Colson, these Proceedings (16th Int. Free Electron Laser Conf., Stanford, CA, USA, 1994) Nucl. Instr. and Meth. A 358 (1995) 555.

[2] R.H. Jackson, H.P. Freund, D.E. Pershing and J.M. Taccetti, Nucl. Instr. and Meth. A 341 (1994) 454.

[3] R.M. Phillips, IRE Trans. Electron Devices ED-7 (1960) 231.

[4] H.P. Freund and T.M. Antonsen, Jr., Principles of Free-electron Lasers (Chapman & Hall, London, 1992).

[5] R.H. Jackson, S.H. Gold, R.K. Parker, H.P. Freund, P.C. Efthimion, V.L. Granatstein, M. Herndon, A.K. Kinkead, J.E. Kosakowski and T.J.T. Kwan, IEEE J. Quantum Electron. QE-19 (1983) 346.

[6] T.J. Orzechowski, B.R. Anderson, J.C. Clark, W.M. Fawley, A.C. Paul, D. Prosnitz, E.T. Scharlemann, S.M. Yarema, D.B. Hopkins, A.M. Sessler and J.S. Wurtele, Phys. Rev. Lett. 57 (1986) 2172.

[7] K. Takayama, J. Kishiro, K. Ebihara, T. Ozaki, S. Hiramatsu and H. Katoh, these Proceedings (16th Int. Free Electron Laser Conf. Stanford, CA, USA, 1994) Nucl. Instr. and Meth. A 358 (1995) 122.

[8] G. Ramian, Nucl. Instr. and Meth. A 318 (1992) 225.

[9] W.G. Urbanus, W.A. Bongers, G. van Dijk, C.A.J. van der Geer, J.P. van Ieperen, A. van der Linden, P. Manintveld, A.B. Stuk, A.V. Tulupov, A.G.A. Verhoeven and M.J. van der Wiel, these Proceedings (16th Int. Free Electron Laser Conf., Stanford, CA, USA, 1994) Nucl. Instr. and Meth. A 358 (1995) 155.

[10] D.E. Pershing, R.D. Seeley, R.H. Jackson and H.P. Freund, ibid., p. 104.

[11] R. Drori, E. Jerby and A. Shahadi, ibid., p. 151.

[12] M. Cohen, A. Kugel, D. Chairman, M. Arbel, H. Kleinman, D. Ben-Haim, A. Eichenbaum, M. Drainin, Y. Pinhasi, Y. Yakover and A. Gover, ibid., p. 82.

[13] G. Dearden, E.G. Quirk, A.I. Al-Shamma'a, R.A. Stuart and J. Lucas, Nucl. Instr. and Meth. A 341 (1994) 80.

[14] T. Mizuno, T. Ootuki and H. Saito, these Proceedings (16th Int. Free Electron Laser Conf., Stanford, CA, USA, 1994) Nucl. Instr. and Meth. A 358 (1995) 131.

[15] M.E. Conde and G. Bekefi, Phys. Rev. Lett. 67 (1991) 3082.

[16] J.L. Rullier, A. Devin, J. Gardelle, J. Labrouche and P. Le Taillandier, Phys. Rev. E, submitted for publication.

[17] R.H. Jackson, J.M. Taccetti, M. Blank, H.P. Freund, D.E. Pershing and V.L. Granatstein, these Proceedings (16th Int. Free Electron Laser Conf., Stanford, CA, USA, 1994) Nucl. Instr. and Meth. A 358 (1995) 193.

[18] P. Zambon, W.J. Witteman and P.J.M. van der Slot, these Proceedings (16th Int. Free Electron Laser Conf., Stanford, CA, USA, 1994) Nucl. Instr. and Meth. A 358 (1995) 126.

[19] M. Fanbao, personal communication.

[20] N.S. Ginzburg, personal communication.

[21] M.C. Wang, J.B. Zhu, Z.J. Wang, J.K. Lee and T.H. Chung, these Proceedings (16th Int. Free Electron Laser Conf., Stanford, CA, USA, 1994) Nucl. Instr. and Meth. A 358 (1995) ABS 38.

[22] F. Ciocci, R. Bartolini, A. Doria, G.P. Gallerano, E. Giovenale, M.F. Kimmitt, G. Messina and A. Renieri, Phys. Rev. Lett. 70 (1993) 928.

[23] S. Kawasaki, H. Ishizuka, S. Musyoki, A. Watanabe and M. Shiho, these Proceedings (16th Int. Free Electron Laser Conf., Stanford, CA, USA, 1994) Nucl. Instr. and Meth. A 358 (1995) 114.

[24] A.V. Arzhannikov, V.B. Bobylev, S.L. Sinitsky, A.V. Tarasov, N.S. Ginzburg and N.Yu. Peskov, ibid., p. 112.

[25] S. Cheng and W.W. Destler, ibid., p. 200.

[26] J. Pasour, personal communication.

[27] G. Renz and G. Spindler, these Proceedings (16th Int. Free Electron Laser Conf., Stanford, CA, USA, 1994) Nucl. Instr. and Meth. A 358 (1995) ABS 13.

[28] Lee Byung-Cheol, Kim Sun-Kook, Jeong Young-Ug, Cho Sung-Oh and Lee Jongmin, Experiments on millimeter-wave free electron laser, presented at this Conference (16th Free Electron Laser Conf., Stanford, CA, 1994).

[29] A. Arensburg, M. Cohen, M. Draiznin, A. Goldring, A. Gover, Y. Pinhasi, S. Witman, I.M. Yakover, J. Sokolowski, B. Mandelbaum, A. Rosenberg, J. Shiloh, G. Hazak, L.A. Levin, O. Shahal, M. Shapira and V.L. Granatstein, these Proceedings (16th Free Electron Laser Conf., Stanford, CA, 1994) Nucl. Instr. and Meth. A 358 (1995) ABS 7.

[30] L.-Y. Lin and T.C. Marshall, Phys. Rev. Lett. 70 (1993) 2403.

[31] F. Hartemann, personal communication.

APPENDIX XI

Long Wavelength Free-Electron Lasers in 1995

H.P. Freund and V.L. Granatstein
Nucl. Instrum. Meth. **A375**, 665 (1996)

Nuclear Instruments and Methods in Physics Research A 375 (1996) 665–668

ELSEVIER

NUCLEAR INSTRUMENTS & METHODS IN PHYSICS RESEARCH Section A

Long wavelength free-electron lasers in 1995

H.P. Freund[a,*], V.L. Granatstein[b]

[a]*Naval Research Laboratory, Washington, DC 20375, USA*
[b]*University of Maryland, College Park, MD 20742, USA*

Abstract

A summary of the current status and most important future directions for long wavelength (≥0.5 mm) free-electron lasers is presented. The distinction between long and short wavelengths is a natural one since different physical processes may be important. Space-charge effects may be important for the high currents typically employed at long wavelengths, and the dominant interaction mechanism is often coherent Raman scattering. In addition, dispersion due to the dielectric effects and finite transverse dimensions in the drift tubes and cavities are important at longer wavelengths. The principal goals at long wavelengths are to achieve much higher average powers with good overall efficiency in a compact design, and the highest average power produced in an FEL to date (36 W) has been recorded in the Ku-band.

This is the second paper dealing with the status of long wavelength free-electron lasers (FEL) and our purpose, as in the first paper [1], is to provide a summary of long wavelength (≥0.5 mm) FELs which are currently either in operation or under construction. Also, as before, a companion paper appears in this volume dealing with "short wavelength" FELs [2]. Our search in compiling this list relies upon (1) contributions to general literature and the proceedings of the annual Free-Electron Laser Conferences, and (2) personal contacts. The latter was an important source of information concerning FEL programs which are either in the early operational stages or still under construction and have not as yet been described in archival literature. Despite our best efforts, however, inadvertent omissions are still possible.

The distinction between long and short wavelength FELs is natural because higher current and lower energy beams are typically employed in this regime and space-charge effects are more important. In particular, the dominant interaction mechanism is often coherent Raman scattering. Also, while short wavelength FELs excite optical modes, dispersion due to the beam dielectric effects and finite transverse dimensions in the drift tubes and cavities are important effects at longer wavelengths.

Table 1 lists parameters describing: wavelength/frequency, peak power, pulse time, repetition rate, beam voltage and current, wiggler period and field strength, and the type of device and accelerator employed. We have chosen to denote the wiggler parameter by K [$=0.0934 B_w \lambda_w$, where B_w is the wiggler amplitude in kG and λ_w is the wiggler period in cm]; however, this parameter is often called a_w in the literature. The wiggler type shown refers to helical (H), planar (P), circular (C), and coaxial hybrid iron (CH) [3] wigglers. Note that an axial guide field is often used in conjunction with helical wigglers in intense beam FELs, but that the brevity of this format did not permit inclusion of this information in the table.

Long wavelengths FELs employ many types of accelerator. However, most of the experiments employ pulse line accelerators which operate in a single-shot (SS) mode with high peak powers. Historically, the pioneering work on long wavelength FELs was peformed by Phillips [4] prior to 1964 using modulators. Long wavelength FEL research began again at various laboratories in the early 1970s with the intention of extending Phillips' work using intense relativistic electron beams. Much of this work was directed at exploring the basic physics of the Raman regime [5], and high average power was not an essential goal. Hence, pulse line accelerators are often used since they produce beam currents of many kiloamperes. In order to achieve the necessary beam quality from pulse line accelerators, careful design of the diode is essential [6] and a large fraction (~90%) of the beam is typically "scraped" off so that only a central core with a low velocity spread is injected into the wiggler. As a result, collective FELs built using pulse line accelerators suffer from the disadvantages of a low wall-plug efficiency and single-shot operation.

* Corresponding author. Permanent address: Science Applications International Corp., McLean, VA 22102, USA. Tel. +1 202 767 0034, fax +1 703 734 1134, e-mail freund@mmace.nrl.navy.mil.

SSDI 0168-9002(95)01221-X

Table 1
Summary of long wavelength FELs

FEL [Ref.]	λ [mm]/ f [GHz]	P_{peak} [MW]	τ_p [μs]	ν_{rep} [Hz]	V_b/I_b [MV/A]	λ_w [cm] K (type)	Type/ Acc.
UCSB [9]	≤2.5 mm	≤0.5	6	2	6/2	7.14/1.0 (P)	O/ES
UCSB [23]	1/260	UC	CW		2/2	3/0.73 (P)	O/ES
TAU [29]	300/1	10^{-5}	1000	SS	0.001/0.2	2/0.04 (P)	O/IC
TAU [37]	30/10	10^{-5}	1000	SS	0.01/0.2	2/0.02 (P)	O/M
TAU [27]	68/4.48	0.0023	5	1	0.07/0.8	4.4/0.12 (P)	SASE/ES
UL [18]	35/8.2	1×10^{-6}	CW		0.13/0.0018	3.8/0.16 (P)	O/M
KEK [8]	32/9.4	120	0.04	0.07	1.5/700	16/1.94 (P)	SASA/IL
ISAS [20]	26/12	3.6	0.4	SS	0.43/190	3.27/0.27 (C)	O/PL
ILT/ILE [24]	2.7/109	1	4×10^{-6}	2.856	9/50	6/4 (P)	O/RFL
MIT [15]	8/33	60	0.025	SS	0.75/300	3.1/0.4 (H)	A/PL
CESTA [32]	8/35	50	0.03	SS	1.8/400	8/2.24 (H)	A/PL
NRL [16]	8/35	UC	1	6	150/10	0.75/0.2 (CH)	A/M
UT [25]	8/35	2.3	0.1	SS	0.5/750	3/0.53 (H)	SASE/PL
IEE [35]	8/35	140	0.05		3.4/800	11/3.5 (P)	A/IL
JINR/INP [30]	8/37	23	0.2	SS	0.8/150	6/0.84 (H)	O/IL
SIOFM [33]	3/100	1	0.015	SS	0.4/400	1/0.14	SASE/PL
IAP [17]	6.7/45	7	0.025	SS	0.5/120	2.4/0.07 (P)	O/PL
ENEA [21]	2/150	0.0015	5.5	40	2.3/0.35	2.5/1.42 (P)	O/MI
JAERI [34]	6/45	10	0.1	1	1/600	4.5/1.3 (P)	A/IL
JAERI [34]	0.8/300	UC	0.16	1	3.5/1000	UC (P)	A/IL
NRL [12]	8/35	UC	1	6	0.15/45	0.85/0.08 (H)	A/M
INP/IAP [31]	4/75	50	1	SS	1/1500	4/0.3 (P)	O/PL
UM [13]	3.5/85	0.25	0.02	SS	0.45/17	0.96/0.34 (P)	A/PL
NSWC/MRC [19]	3/95	10	0.25	SS	2.5/100	10/1.9 (H)	O/PL
DLR [22]	3/100	1	1.5×10^{-2}	SS	0.5/100	2/0.28 (H)	SASE/PL
KAERI [26]	1/260	0.001	10–30	SS	0.4/1.7	3.2/0.39 (H)	O/ES
TAU/WI [28]	3/100	UC	100	SS	1.5/0.5	4.4/0.82 (P)	O/ES
CU [14]	2/150	5	0.15	SS	0.8/150	1.85/0.25 (H)	A/PL
FOM [9]	1/260	UC	1×10^5	1	2/12	2/0.67 (P)	O/ES
LLNL/SLAC [36]	38/11.4	DS	0.25	120	0.5/1000	3.4/0.5 (CA)	A/M
DU [38]	0.4/650	UC	10	60	40/0.2	3/1.4 (P)	O/RFL

A – amplifier.
C – circular.
CA – coaxial.
CESTA – Centre d'Etudes Scientifique e Techniques d'Aquitaine.
CH – CHI wiggler.
CU – Columbia University, USA.
DLR – German Aerospace Research Establishment.
DS – design study.
DU – Duke University.
ES – electrostatic accelerator.
H – helical wiggler.
IAP – Institute of Applied Physics, Russia.
INP – Institute of Nuclear Physics, Russia.
IC – ignition coil.
IEE – Institute of Electronic Engineering, China.
IL – induction linac.
ILT/ILE – Institute for Laser Technology/Institute for Laser Engineering, Osaka, Japan.
ISAS – Institute of Space and Astronautical Science, Japan.
JAERI – Japan Atomic Energy Research Institute.
JINR – Joint Institute for Nuclear Research, Russia.
KAERI – Korean Atomic Energy Research Institute.
KEK – National Laboratory for High Energy Physics, Japan.
LLNL/SLAC – Lawrence Livermore National Laboratory/ Stanford Linear Accelerator Center.
NRL – Naval Research Laboratory.
NSWC – Naval Surface Weapons Center, USA.
M – modulator.
MI – microtron.
MRC – Mission Research Corp.
O – oscillator.
P – planar wiggler.
PL – pulse line accelerator.
RFL – radio frequency linac.
SASE – self amplified spontaneous emission.
SIOFM – Shanghai Institute of Optics and Fine Mechanics.
SS – single shot.
TAU – Tel Aviv University.
UC – under construction.
UL – University of Liverpool, UK.
UM – University of Maryland, USA.
UT – University of Twente, the Netherlands.
WI – Weizmann Institute, Israel.

The principal thrusts of current long wavelength FEL research remains the achievements of high average powers, broad bandwidths, and compact systems. Hence, the development of practical long wavelength FELs depends upon other accelerator technologies.

Induction linacs have the advantage that they can be repetitively pulsed and it is possible, at least in principle, to produce high average powers and high efficiencies. However, there are two practical difficulties. The first is the achievement of high repetition rates. The ELF experiment [7] which produced a peak power of ~1 GW at 35 GHz operated with a pulse time of 10–20 ns and a repetition rate of 0.54Hz for an average power of only ≈7 W. The second is emittance growth resulting in unacceptably high thermal spreads, and the necessity of beam scraping (~80% of the beam was scraped off in the ELF experiment). Thus, while the extraction efficiency was about 34% from the beam that passed through the wiggler, the overall efficiency was closer to 7%. In view of this, the recent results from the induction linac-based FEL at KEK [8] which produced a peak power of 120 MW using some beam scraping and ion channel guiding represents a significant advance.

Other promising approaches for achieving high average powers involve long pulse modulators and electrostatic accelerators. In the case of electrostatic accelerators, full CW operation is possible if a high degree of beam energy recovery can be achieved by using depressed collectors. This has been accomplished at the University of California at Santa Barbara [9]. However, the degree of beam energy recovery which can be achieved decreases with increasing extraction efficiency of the FEL, and this may prove to be a limiting factor in the technology. A significant experiment using electrostatic accelerators is currently under construction at FOM in the Netherlands [10]. The goal of this experiment is to build a 1 MW CW FEL operating in the frequency range 130–260 GHz to heat plasmas in magnetic fusion reactors. Based on a 2 MeV/12 A beam, the design value of extraction efficiency is 4%, but with effective beam energy recovery in a depressed collector, the overall system efficiency can be much larger. It will be interesting to see how effective energy recovery can be in a system with this level of extracted power.

For applications requiring more compact devices, long pulse modulators have advantages. A research program at the Naval Research Laboratory has been devoted to the development of this concept with goals of high average power. An experiment [11] reported in the previous status paper employed a 250 kV/100 A modulator with a characteristic 1.4 μs flat top and a repetition rate of 6 hz to produce ≈4.2 MW peak in Ku-band. This represents an average power of ≈36 W which is the highest average power produced in an FEL to date. The direction of this program is to achieve still higher powers at higher frequencies using lower voltage electron beams. To this end, a follow-on experiment is under construction which will employ a ridged waveguide to permit lower voltage operation [12].

In summary, the ultimate goals of long wavelength FEL research are to achieve much higher average powers with good overall efficiency and more compact designs than have yet been achieved. At the present time, high voltage/low current DC accelerators and long pulse modulators remain the prime candidates for drivers for these systems; however, advances in induction linac technology which lead to higher repetition rates and improved beam quality could change this conclusion.

References

[1] H.P. Freund and V.L. Granatstein, Nucl. Instr. and Meth. A 358 (1995) 551.

[2] W.B. Colson, these Proceedings (17th Int. Free Electron Laser Conf., New York, NY, USA, 1995) Nucl. Instr. and Meth. A 375 (1996) 669.

[3] R.H. Jackson, H.P. Freund, D.E. Pershing and J.M. Taccetti, Nucl. Instr. and Meth. A 341 (1994) 454.

[4] R.M. Phillips, IRE Trans. Electron Dev. ED-7 (1960) 231.

[5] H.P. Freund and T.M. Antonsen, Jr., Principles of Free-Electron Lasers (Chapman & Hall, London, 1992).

[6] R.H. Jackson, S.H. Gold, R.K. Parker, H.P. Freund, P.C. Efthimion, V.L. Granatstein, M. Herndon, A.K. Kinkead, J.E. Kosakowski and T.J.T. Kwan, IEEE J. Quantum Electron. QE-19 (1983) 346.

[7] T.J. Orzechowski, B.R. Anderson, J.C. Clark, W.M. Fawley, A.C. Paul, D. Prosnitz, E.T. Scharlemann, S.M. Yarema, D.B. Hopkins, A.M. Sessler and J.S. Wurtele, Phys. Rev. Lett. (1986) 2172.

[8] K. Saito, K. Takeyama, T. Ozaki, J. Kioshiro, K. Ebihara and S. Hiramatsu, Ref. [2], p. 237.

[9] G. Ramian, Nucl. Instr. and Meth. A 318 (1992) 225.

[10] W.H. Urbanus, W.A. Bongers, G. van Dijk, C.A.J. van de Geer, A.G.R.J.E. van Honk, P. Manintveld, A.B. Sterk, M. Valentini, A.G.A. Verhoeven, R.M.M. Weijman, M.J. van de Wiel, A.A. Varfolomeev, S.N. Ivanchenkov, A.S. Khlebnikov, V.L. Bratman, G.G. Denisov and M. Caplan, Ref. [2], p. 401.

[11] D.E. Pershing, R.D. Seeley, R.H. Jackson and H.P. Freund, Nucl. Instr. and Meth. A 355 (1995) 104.

[12] D.E. Pershing, R.H. Jackson, H.P. Freund, M. Blank and J.M. Taccetti, Ref. [2], p. 226.

[13] S. Cheng, V.L. Granatstein, W.W. Destler, B. Levush, J. Rodgers and T.M. Antonsen, Jr., Ref. [2], p. 160.

[14] J.W. Dodd and T.C. Marshall, IEEE Trans. Plasma Sci. 18 (1990) 447.

[15] M.E. Conde and G. Bekefi, Phys. Rev. Lett. 67 (1991) 3082.

[16] J.M. Taccetti, R.H. Jackson, H.P. Freund, D.E. Pershing, M. Blank and V.L. Granatstein, Ref. [2], p. 496.

[17] G.G. Denisov, V.L. Bratman, N.S. Ginzburg, B.D. Kol'chugn, N. Yu. Peskov, S.V. Samsonov and A.B. Volkov, Ref. [2], p. 377.

[18] A. Al'Shamma'a, R.A. Stuart and J. Lucas, Ref. [2], p. 424.

[19] J. Pasour, personal communication.

[20] T. Mizuno, T. Ohtsuki, T. Ohshima and H. Saito, Nucl. Instr. and Meth. A 358 (1995) 131.

APPENDIX XII

Long Wavelength Free-Electron Lasers in 1996

H.P. Freund and V.L. Granatstein
Nucl. Instrum. Meth. **A393**, 9 (1997)

Nuclear Instruments and Methods in Physics Research A 393 (1997) 9–12

NUCLEAR INSTRUMENTS & METHODS IN PHYSICS RESEARCH Section A

ELSEVIER

Long wavelength free electron lasers in 1996

H.P. Freund[a,*], V.L. Granatstein[b]

[a] *Naval Research Laboratory, Washington, DC 20375, USA*
[b] *University of Maryland, College Park, MD 20742, USA*

Abstract

A summary of the current status and most important future directions for long wavelength (≥ 0.5 mm) free-electron lasers is presented. The distinction between long and short wavelengths is a natural one since different physical processes may be important. Space-charge effects may be important for the high currents typically employed at long wavelengths, and the dominant interaction mechanism is often coherent Raman scattering. In addition, dispersion due to the dielectric effects and finite transverse dimensions in the drift tubes and cavities are important at longer wavelengths. The principal goals at long wavelengths are to achieve much higher average powers with good overall efficiency in a compact design, and the highest average power produced in an FEL to date (36 W) has been recorded in the Ku-band

This is the third paper dealing with the status of long wavelength free-electron lasers (FEL) and our purpose, as in the first two papers [1,2], is to provide a summary of long wavelength (≥ 0.5 mm) FELs which are currently either in operation or under construction. Also, as before, a companion paper appears in this volume dealing with "short wavelength" FELs [3]. Our search in compiling this list relies upon (1) contributions to the general literature and the proceedings of the annual Free-Electron Laser Conferences, and (2) personal contacts. The latter was an important source of information concerning FEL programs which are either in the early operational stages or still under construction and have not as yet been described in archival literature. Despite our best efforts, however, inadvertent omissions are still possible.

The distinction between long and short wavelength FELs is natural because higher current and lower energy beams are typically employed in this regime and space-charge effects are more important. In particular, the dominant interaction mechanism is often coherent Raman scattering. Also, while short wavelength FELs excite optical modes, dispersion due to the beam dielectric effects and finite transverse dimensions in the drift tubes and cavities are important effects at longer wavelengths.

The long wavelength FEL Table 1 lists parameters describing: wavelength/frequency, peak power, pulse time, repetition rate, beam voltage and current, wiggler period and field strength, and the type of device and accelerator employed. We have chosen to denote the wiggler parameter by K ($= 0.0934 B_w \lambda_w$, where B_w is the wiggler amplitude in kG and λ_w is the wiggler period in cm); however, this parameter is often called a_w in the literature. Note that in the case of planar wiggler designs this does denote the peak and not the rms amplitude. The wiggler type shown refers to helical (H), planar (P), circular (C), and coaxial hybrid iron (CH) wigglers [4]. Note that an axial guide field is often used in conjunction with helical wigglers in intense beam FELs, but that the brevity of this format did not permit inclusion of this information in the table.

Long wavelength FELs employ many types of accelerator. However, most of the experiments employ pulse line accelerators which operate in a single-shot (SS) mode with high peak powers. Historically, the pioneering work on long wavelength FELs was performed by Phillips [5] prior to 1964 using modulators. Long wavelength FEL research began again at various laboratories in the early 1970s with the intention of extending Phillips' work using intense relativistic electron beams. Much of this work was directed at exploring the basic physics of the Raman regime [6], and high average power was not an essential goal. Hence, pulse line accelerators are often used since they produce beam currents of many kiloamperes. In order to achieve the necessary beam quality from pulse line accelerators, careful design of the diode is essential [7] and a large fraction ($\approx 90\%$) of the beam is typically "scraped" off so that only a central core with a low-velocity spread is injected into the wiggler. As a result,

* Correspondence address: Science Applications International Corporation, 1710 Goodridge Drive, McLean, VA 22102, USA.

PII S0168-9002(97)00419-1

Table 1

FEL [Ref.]	λ(mm)/ f(GHz)	P_{peak} (MW)	τ_p (μs)	υ_{rep} (Hz)	V_b/I_b (MV/A)	λ_w(cm)/ K(type)	Type/ Acc
UCSB [13]	≤ 2.5/120	≤ 0.015	6	2	6/2	7.14/1.0 (P)	O/ES
UCSB [13]	1/300	UC	CW		2/2	3/0.73 (H)	O/ES
TAU [14]	1070/0.28	10^{-6}	2000	SS	0.0007/0.1	4/0.05 (P)	O/PS
TAU [15]	30/10	10^{-5}	1000	SS	0.01/0.2	2/0.02 (P)	O/M
TAU [16]	68/4.48	0.0035	5	1	0.07/0.8	4.4/0.12 (P)	O/ES
UL [17]	32–37/8–9.3	10^{-5}	CW		0.04–0.08/0.01	1.9/0.03 (P)	SASE/PS
UL [18]	30/9.9	10^{-6}	CW		0.05/0.01	1.9/0.03 (P)	A/PS
UL [19]	25–37/8–12.4	2×10^{-5}	CW		0.12/0.18	3/0.28 (P)	O/PS
KEK [9]	32/9.4	150	0.015	0.07	1.5/450	16/1.5 (P)	A/IL
KEK [9]	32/9.4	100	0.015	0.07	1.5/450	16/1.5 (P)	A/IL
ISAS [20]	26/12	3.6	0.4	SS	0.43/190	3.3/0.27 (C)	O/PL
ILT/ILE [21]	2.7/109	0.01	5×10^{-6}	2.856	9/50	6/4 (P)	O/RFL
CESTA [22]	8/35	50	0.03	SS	1.8/400	8/2.24 (H)	A/PL
NRL [23]	8/35	UC	1	6	0.1/10	0.64/0.2 (CH)	A/M
UT [24]	8/35	2.3	0.1	SS	0.5/750	3/0.53 (H)	SASE/PL
IFP/IEE [25]	8/35	140	0.05	SS	3.4/800	11/3.1 (P)	A/IL
JINR/INP [26]	9.7/31	31	0.2	2	0.8/150	6/0.84 (H)	O/IL
SIOFM [27]	3/100	1	0.02	SS	0.3/400	1/0.14 (H)	SASE/PL
IAP [28]	6.7/45	7	0.025	SS	0.5/120	2.4/0.07 (P)	O/PL
ENEA [29]	2/150	0.0015	5.5	40	2.3/0.35	2.5/1.4 (P)	O/MI
ENEA [30]	0.6/500	UC	5.5	20	5.5/0.25	2.5/1.7 (P)	O/MI
JAERI [31]	6/45	10	0.1	SS	1/3000	4.5/1.3 (P)	A/IL
JAERI/KEK [31]	2–15/20–140	UC	0.1	SS	4/1000	UC (P)	A/IL
INP/IAP [32]	4/75	200	1	SS	1/2000	4/0.3 (P)	O/PL
DLR [33]	3/100	1	1.5×10^{-2}	SS	0.5/100	2/0.28 (H)	SASE/PL
KAERI [34]	12/26	0.001	10–30	SS	0.4/2	3.2/0.39 (H)	O/ES
TAU/WI [35]	3/100	UC	100	SS	1.5/0.5	4.4/0.82 (P)	O/ES
CU [36]	2/150	5	0.15	SS	0.8/150	1.9/0.25 (H)	A/PL
FOM [11]	1/260	UC	1×10^{5}	1	2/12	2/0.67 (P)	O/ES
UCD/SLAC [37]	38/11.4	DS	0.25	120	0.5/1000	3.4/0.5 (CA)	A/M
DU [38]	0.4/650	DS	10	60	40/0.2	3/1.4 (P)	O/RFL

A – Amplifier.
C – Circular.
CA – Coaxial.
CESTA – Centre d'Etudes Scientifique e Techniques d'Aquitaine.
CH – CHI Wiggler.
CU – Columbia University, USA.
DLR – German Aerospace Research Establishment.
DS – Design Study
DU – Duke University.
ES – Electrostatic accelerator.
H – Helical wiggler.
IAP – Institute of Applied Physics, Russia.
INP – Institute of Nuclear Physics, Russia.
IFP/IEE – Institute of Fluid Physics/Institute of Electronic Engineering, China.
IL – Induction Linac.
ILT/ILE – Institute for Laser Technology/Institute for Laser Engineering Osaka, Japan.
ISAS – Institute of Space and Astronautical Science, Japan.
JAERI – Japan Atomic Energy Research Institute.
JINR – Joint Institute for Nuclear Research, Russia.
KAERI – Korean Atomic Energy Research Institute.
KEK – National Laboratory for High Energy Physics, Japan.
UCD/SLAC – University of California at Davis/Stanford Linear Accelerator Center.
NRL – Naval Research Laboratory.
NSWC – Naval Surface Weapons Center, USA.
M – Modulator.
MI – Microtron.
MRC – Mission Research Corporation.
O – Oscillator
P – Planar wiggler.
PL – Pulse line accelerator.
PS – Power Supply.
RFL – Radio Frequency Linac.
SASE – Self Amplified Spontaneous Emission.
SIOFM – Shanghai Institute of Optics and Fine Mechanics.
SS – Single Shot.
TAU – Tel Aviv University.
UC – Under Construction.
UL – University of Liverpool, UK.
UM – University of Maryland USA.
UT – University of Twente, the Netherlands.
WI – Weizmann Institute, Israel.

collective FELs built using pulse line accelerators suffer from the disadvantages of a low wall-plug efficiency and single-shot operation.

At present, the principal thrusts of long wavelength FEL research are the achievements of high average powers, broad bandwidths, and compact systems. Hence, the development of practical long wavelength FELs depends upon accelerator technologies other than pulse line accelerators.

Induction linacs have the advantage that they can be repetitively pulsed and it is possible, at least in principle, to produce high average powers and high efficiencies. However, there are two practical difficulties. The first is the achievement of high repetition rates. The ELF experiment [8] which produced a peak power of $\approx$1 GW at 35 GHz operated with a pulse time of 10–20 ns and a repetition rate of 0.5 Hz for an average power of only $\approx$7 W. The second is emittance growth resulting in unacceptably high thermal spreads, and the necessity of beam scraping ($\approx$80% of the beam was scraped off in the ELF experiment). Thus, while the extraction efficiency was about 34% from the beam that passed through the wiggler, the overall efficiency was closer to 7%. In view of this, the recent results from the induction linac-based FEL at KEK [9] which produced a peak power of 120 MW using less beam scraping and ion channel guiding represents an advance.

Other promising approaches for achieving high average powers involve long-pulse modulators and electrostatic accelerators.In the case of electrostatic accelerators, full CW operation is possible if a high degree of beam energy recovery can be achieved by using depressed collectors. This has been accomplished at the University of California at Santa Barbara [10]. However, the degree of beam energy recovery which can be achieved decreases with increasing extraction efficiency of the FEL, and this may prove to be a limiting factor in the technology. A significant experiment using electrostatic accelerators is currently under construction at FOM in the Netherlands [11]. The goal of this experiment is to build a 1 MW CW FEL operating in the frequency range 130–260 GHz to heat plasmas in magnetic fusion reactors. Based on a 2 MeV/12 A beam, the design value of extraction efficiency is 4%, but with effective beam energy recovery in a depressed collector, the overall system efficiency can be much larger. At the present time the experiment is in a stage in which beam propagation studies are in progress; a 3 A beam has been accelerated to 1.55 MeV and transported with negligible loss through the undulator. When FEL operation is achieved it will be interesting to see how effective energy recovery can be in a system with this predicted level of extracted power.

For applications requiring more compact devices, long-pulse modulators have advantages. In this regard, it is interesting to observe that an experiment at the Naval Research Laboratory [12] reported in a status paper has achieved the highest average power in an FEL to date. This experiment employed a 250 kV/100 A modulator with a characteristic 1.4 μs flat-top and a repetition rate of 6 Hz to produce $\approx$4.2 MW peak in Ku-band with a corresponding average power of $\approx$36 W.

In summary, the ultimate goals of long wavelength FEL research are to achieve much higher average powers with good overall efficiency and more compact designs than have yet been achieved. At the present time, high voltage/low current DC accelerators and long-pulse modulators remain the prime candidates for drivers for these systems; however, advances in induction linac technology which lead to higher repetition rates and improved beam quality could change this conclusion.

This work was supported in part by the Naval Research Laboratory and the Office of Naval Research.

References

[1] H.P. Freund, V.L. Granatstein, Nucl. Instr. and Meth. A 358 (1995) 551.
[2] H.P. Freund, V.L. Granatstein, Nucl. Instr. and Meth. A 375 (1996) 665.
[3] W.B. Colson, these Proceedings (18th Free Electron Laser Conf., Rome, Italy, 1996) Nucl. Instr. and Meth. A 393 (1997) 6.
[4] R.H. Jackson, H.P. Freund, D.E. Pershing, J.M. Taccetti, Nucl. Instr. and Meth. A 341 (1994) 454.
[5] R.M. Phillips, IRE Trans. Electron Dev. ED-7 (1960) 231.
[6] H.P. Freund, T.M. Antonsen Jr., Principles of Free-Electron Lasers, 2nd ed., Chapman & Hall, London, 1996.
[7] R.H. Jackson, S.H. Gold, R.K. Parker, H.P. Freund, P.C. Efthimion, V.L. Granatstein, M. Herndon, A.K. Kinkead, J.E. Kosakowski, T.J.T. Kwan, J. Quantum Electron. QE-19 (1983) 346.
[8] T.J. Orzechowski, B.R. Anderson, J.C. Clark, W.M. Fawley, A.C. Paul, D. Prosnitz, E.T. Scharlemann, S.M. Yarema, D.B. Hopkins, A.M. Sessler, J.S. Wurtele, Phys. Rev. Lett. 57 (1986) 2172.
[9] K. Takayama, personal communication.
[10] G. Ramian, Nucl. Instr. and Meth. A 318 (1992) 225.
[11] W.H. Urbanus, et al., Nucl. Instr. and Meth. A 375 (1996) 401.
[12] D.E. Pershing, R.D. Seeley, R.H. Jackson, H.P. Freund, Nucl. Instr. and Meth. A 355 (1995) 104.
[13] G. Ramian, personal communication.
[14] R. Drori, E. Jerby, Ref. [3], p. 284.
[15] M. Einat, E. Jerby, A. Shahadi, Nucl. Instr. and Meth. A 375 (1996) 21.
[16] M. Cohen, A. Eichenbaum, H. Kleinman, M. Arbel, I.M. Yakover, A. Gover, Phys. Rev. Lett. 74 (1995) 3812.
[17] A. Al'Shamma'a, S. Mayhew, R.A. Stuart, A. Shaw, C. Balfour, J. Lucas, in: Free Electron Lasers 1996, G. Dattoli and A. Renieri eds., North-Holland, Amsterdam.
[18] C. Balfour, A. Al'Shamma'a, A. Shaw, S. Mayhew, R.A. Stuart, and J. Lucas, Ref. [3], p. 300.

[19] A. Al'Shamma'a, A. Shaw, R.A. Stuart, J. Lucas, BNFL Contract FEL3, Report 101A, Department of Electrical Engineering and Electronics, University of Liverpool, 1996.
[20] T. Mizuno, T. Ohtsuki, T. Ohshima, H. Saito, Nucl. Instr. and Meth. A 358 (1995) 131.
[21] M. Asakawa, N. Sakamoto, N. Inoue, T. Yamamoto, K. Mima, S. Nakai, J. Chen, M. Fujita, K. Imasaki, C. Yamanaka, T. Agari, T. Asakuma, N. Ohigashi, Y. Tsunawaki, Appl. phys. Lett. 64 (1994) 1601.
[22] J.L. Rullier, A. Devin, J. Gardelle, J. Labrouche, P. Le Taillandier, Nucl. Instr. and Meth. A 358 (1995) 118.
[23] J.M. Taccetti, R.H. Jackson, H.P. Freund, D.E. Pershing, M. Blank, V.L. Granatstein, Ref. [17].
[24] P.J.M. van der Slot, W.J. Witteman, Nucl. Instr. and Meth. A 331 (1993) 140.
[25] J.J. Deng, B.N. Ding, S.Z. Hu, J.S. Shi, W.J. Zhu, Q. Li, Y. He, C.M. Zou, F.B. Men, Y.T. Chen, High Power Laser and Particle Beams (China) 6(4) (1995).
[26] A.K. Kaminsky, A.A. Kaminsky, S.N. Sedykh, A.P. Sergeev, N.S. Ginzburg, N. Yu. Peskov, A.S. Sergeev, Ref. [17].
[27] M.C. Wang, Proc. SPIE vol. 2013, 1993, pp. 48.
[28] N. Yu. Peskov, V.L. Bratman, N.S. Ginzburg, G nisov, B.D. Kol'chugin, S.V. Samsonov, A.B. Nucl. Instr. and Meth. A 375 (1996) 377.
[29] A. Doria, G.P. Gallerano, E. Giovenale, M.F. K G. Messina, Nucl. Instr. and Meth. A 375 (1996) A
[30] A. Doria, et al., Ref. [17].
[31] S. Maebara, personal communication.
[32] A.V. Arzhannikov, M.A. Agafonov, N.S. Ginzburg, Peskov, S.L. Sinitsky, and A.V. Tarasov, Presented FEL Conf., Rome, Italy, 1996.
[33] G. Renz, personal communication.
[34] B.C. Lee, Y.U. Jeong, S.O. Cho, S.K. Kim, J. Lee Instr. and Meth. A 375 (1996) 28.
[35] A. Arensburg, et al., Nucl. Instr. and Meth. A 375 ABS-1.
[36] J.W. Dodd, T.C. Marshall, IEEE Trans. Plasma (1990) 447.
[37] A.J. Balkcum, D.B. McDermott, R.M. Phillips Lin, N.C. Luhmann Jr., IEEE Trans. Plasma Sci. 24 802.
[38] M.L. Ponds, Y. Feng, J.M.J. Madey, P.G. O'Shea, Instr. and Meth. A 375 (1996) 136.

APPENDIX XIII

Nonlinear Analysis of Helix Traveling Wave Tubes

H.P. Freund, E.G. Zaidman, A. Mankofsky, N.R. Vanderplaats, and M.A. Kodis
Phys. Plasmas **2**, 3871 (1995)

Nonlinear analysis of helix traveling wave tubes

H. P. Freund,[a] E. G. Zaidman, A. Mankofsky,[a] N. R. Vanderplaats, and M. A. Kodis
Naval Research Laboratory, Washington, D.C. 20375

(Received 24 March 1995; accepted 6 July 1995)

A time-dependent nonlinear formulation of the interaction in the helix traveling wave tube is presented for a configuration in which an electron beam propagates through a sheath helix surrounded by a conducting wall. In order to describe both the variation in the wave dispersion and in the transverse inhomogeneity of the electromagnetic field with wave number, the field is represented as a superposition of waves in a vacuum sheath helix. An overall explicit sinusoidal variation of the form $\exp(ikz-i\omega t)$ is assumed (where ω denotes the angular frequency corresponding to the wave number k in the vacuum sheath helix), and the polarization and radial variation of each wave is determined by the boundary conditions in a vacuum sheath helix. Thus, while the field is three-dimensional in nature, it is azimuthally symmetric. The propagation of each wave *in vacuo* as well as the interaction of each wave with the electron beam is included by allowing the amplitudes of the waves to vary in z and t. A dynamical equation for the field amplitudes is derived analogously to Poynting's equation, and solved in conjunction with the three-dimensional Lorentz force equations for an ensemble of electrons. Numerical examples are presented corresponding to both single- and multiwave interactions.

I. INTRODUCTION

The development of the traveling wave tube (TWT) extends over several decades since the pioneering work of Pierce and co-workers[1–3] based upon a coupled-wave analysis utilizing the vacuum modes of the helix and the positive and negative energy space-charge waves of the beam. Improved linear theories based upon an eigenvector analysis of Maxwell's equations in a sheath helix have also been developed,[4,5] and discussions of both the coupled-wave and field theories of the TWT are given by Beck[6] and Hutter.[7] More recently, complete field theories of beam-loaded helix TWTs have been developed for both sheath[8] and tape[9] helix models. Nonlinear theories of the TWT also have a long history in the literature, and can be grouped into two broad classes dealing with steady-state and time-dependent models.

Steady-state models have been extensively used for the analysis and design of amplifiers in order to study the growth of a single frequency wave injected simultaneously with the electron beam. These formulations constitute a slow-time-scale "moving-window" approach[10–13] in which the electromagnetic field is represented in terms of the normal modes in the vacuum structure. The amplitude and phase of the wave are assumed to vary slowly on the scale length of the wave period, and nonlinear differential equations for the evolution of the slowly varying amplitude and phase are obtained form Maxwell's equations. Note that the slow variation in the phase in this case refers to the slow variation with respect to the sinusoidal variation of the wave *in vacuo* [i.e., $\approx\exp(ikz-i\omega t)$, where ω is the angular frequency corresponding to wave number k]. Beam space-charge waves can be included in the formalism in a similar manner. Three-dimensional effects arising from the boundary conditions at the helix and outer wall can be included in the formalism which then describes the overlap of the beam with the transverse variation of the wave. As a result, both the appropriate dispersion and transverse polarization and inhomogeneity of the wave can be included in these formulations. A good review of this technique as applied to TWTs has been given by Rowe,[14] and the approach is well suited to the analysis of a broad class of linear beam amplifiers and has also been applied, for example, to the free-electron laser.[15]

Time-dependent models of helix TWTs rely upon particle-in-cell (PIC) simulation techniques. At the present time, a one-dimensional PIC simulation code is available[16] which treats the wave dispersion by means of a transmission line equivalent circuit model. Hence, the one-dimensional PIC simulation of this form is limited in its ability to model the dispersion of the helix and is unable to deal with radial variation in the mode structure. In order to deal with these effects self-consistently, a fully three-dimensional PIC formalism is required. However, such a simulation code has not yet been implemented due to both the numerical complexity and the computational expense required. The most general PIC formulations of the interaction in a helix TWT to date are two-dimensional simulations of a sheath helix model.[17,18] Since the helix is in reality a three-dimensional structure, the restriction to a two-dimensional PIC formulation requires a prescription for dealing with the boundary condition at the helix. In practice, the simplification made is to treat the so-called *sheath* helix in which the helix is modeled in terms of a conducting sheet which is "thin" in the radial direction and in which the conductivity is infinite in the direction of the helix and zero otherwise. While this approach can provide a good approximation for the dispersion and radial mode variation in the sheath helix, however, it is not adaptable to more realistic helix models that include substantial harmonic components.

The approach we adopt in this article differs from these

[a]Permanent address: Science Applications International Corp., McLean, Virginia 22102.

 1070-664X/95/2(10)/3871/9/$6.00

PIC formulations. As in the case of the two-dimensional PIC formulations, we assume azimuthal symmetry and deal with a sheath helix model. However, we treat the fields in terms of a spectral decomposition in which the electromagnetic field is expressed as a superposition of the normal modes of the vacuum sheath helix. In this representation, an overall sinusoidal variation of the form $\exp(ikz-i\omega t)$ is assumed for each wave, where ω denotes the angular frequency determined from the vacuum sheath helix dispersion equation corresponding to wave number k. The polarization and radial variation of each wave is assumed to be given by the normal mode solutions of Maxwell's equations for the vacuum sheath helix boundary conditions which are three-dimensional in nature.[8] The evolution of each wave either *in vacuo* or in the presence of the electron beam is included by allowing the amplitudes to vary in both axial position and time. The detailed evolution of the waves is governed by a dynamical equation which is analogous to Poynting's equation. This equation includes the coupling of the waves to the electron beam and, hence, the intermodulation between the waves themselves. In conjunction with the equations for the fields, the trajectories of an ensemble of electrons are integrated using the three-dimensional Lorentz force equations.

As in the case of the two-dimensional PIC formulations, this spectral approach provides a good model for the dispersion and radial variation of the electromagnetic field, but requires an explicit choice of the waves of interest to be specified as an initial condition. It has two advantages over the two-dimensional PIC models, however, in that (1) the technique can be readily generalized to deal with more realistic tape helix models that include higher harmonic components, and (2) the numerical technique is considerably less computationally demanding. For the numerical examples discussed in this article, typical run times on a Cray Y-MP supercomputer were substantially less than 1 min.

The present article deals with the first development and application of this technique, and certain simplifications have been made. One restriction that is imposed is the neglect of the beam space-charge modes that restricts the analysis to the ballistic regime in which the Pierce gain parameter[2] is small. The exclusion of the space-charge modes is not an essential element of the formulation, and the inclusion of the space-charge modes is presently under study. It should be remarked that a recent work by Lau and Chernin[19] asserts that the synchronous beam–mode interaction already includes the dominant effects due to the beam space-charge wave. Although we do not consider any examples in the present article in which the space-charge wave is important, this assertion will be tested by comparison of the nonlinear simulation with experiments in the near future.

The self-electric and self-magnetic fields have also been neglected. However, the self-fields can be readily included by means of a technique used for inclusion of the self-fields in free-electron lasers.[20] The numerical examples discussed herein relate to the single-pass propagation of pulses through both vacuum and beam-loaded helix structures, and open boundary conditions have been imposed. However, various degrees of reflecting boundary conditions can also be used to treat various cavity and oscillator configurations. Finally, the formulation can also be generalized to treat more realistic helix models; in particular, a tape helix model is presently under study.[9]

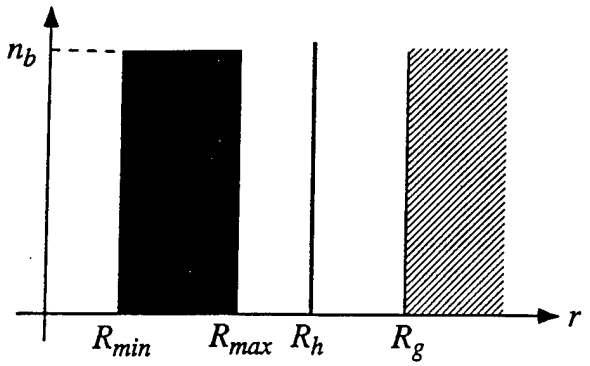

FIG. 1. Schematic representation of the cross section of the system.

The organization of the article is as follows. The general formulation is presented in Sec. II. This includes a discussion of the geometry, the dispersion equation and mode structure in a sheath helix, the field representation and the dynamical equation governing the evolution of the fields, and the Lorentz force equations. Section III deals with the numerical techniques used to solve the dynamical equations as well as the representative solutions for various parameter regimes. A summary and discussion is given in Sec. IV.

II. THE GENERAL FORMULATION

The general formulation is intended to treat the propagation of multiple waves through a sheath helix in the presence of an electron beam. Hence, this is a fully time-dependent problem, and a slow-time-scale formulation such as is commonly used to treat single-frequency operation in TWTs, free-electron lasers, and cyclotron masers cannot be employed for the current problems of interest.

A. The physical configuration

The physical configuration that is treated is that of an energetic electron beam propagating parallel to the axis of symmetry of a helix-loaded cylindrical waveguide. Azimuthal symmetry is assumed throughout. The beam is assumed to be azimuthally symmetric with a "flat-top" radial density profile which can be either annular or solid. A schematic of the cross section of this configuration is shown in Fig. 1 in which R_h and R_g are used to denote the radii of the helix and the outer cylinder respectively, and $R_{\min}$ and $R_{\max}$ denote the inner and outer radii of the electron beam (i.e., a solid profile is described by the simple expedient of setting $R_{\min}=0$). An external solenoidal magnetic field $\mathbf{B}_0$ $[=B_0\hat{\mathbf{e}}_z]$ is also included.

In practical TWTs the helix is composed of a metal strip that is supported at multiple points within the cylinder by posts or rods. A complete self-consistent description of wave dispersion in such a structure is beyond the scope of the present analysis and would require a complete three-dimensional particle-in-cell simulation code. For simplicity, we shall assume that both the helix and the outer cylinder are

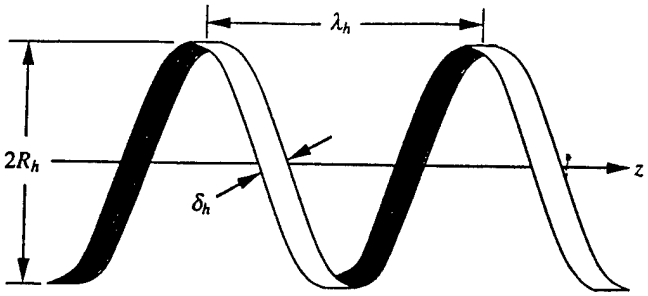

FIG. 2. Schematic illustration of a tape helix structure.

loss-free conductors and represent the electromagnetic field as a superposition of the azimuthally symmetric modes in the vacuum helix. Within the context of this assumption, there are several further simplifications that permit analytic solution for the normal modes of the vacuum helix.

In the commonly applied *tape* helix model it is assumed that only a surface current is induced in the helix and that the effects of the support posts can be neglected. The restriction to surface currents in the helix is equivalent to the assumption that the helix is "thin" in the radial direction. A schematic illustration of a "tape" helix is shown in Fig. 2 where λ_h denotes the helix period and δ_h is the width of the tape. A multiplicity of azimuthally symmetric modes exist in such a system corresponding to the spatial harmonics of the helix period. The importance of the higher order spatial harmonics decreases as the width of the helix increases. Ultimately, if $\delta_h=\lambda_h$ the induced currents in the helix can be modeled as a continuous helical current sheet and the effects of the spatial harmonics disappear. This is referred to a the *sheath* helix approximation. For simplicity, we shall adopt a sheath helix model for the electromagnetic fields, but observe that the technique is readily generalizable to a tape helix model.

B. The modes in a sheath helix

We restrict the analysis to the azimuthally symmetric subluminous waves supported by the helix. The azimuthally symmetric electric and magnetic fields can be represented in the form[8]

$$\begin{aligned}\delta\mathbf{E}(\mathbf{x},t)=&\sum_n \delta\hat{E}_n\{R_n(r)\hat{e}_r\sin(\varphi_n+\delta\varphi_n)\\&-[\beta_{\rm ph}(k_n)\Theta_n(r)\hat{e}_\theta-Z_n^{(e)}(r)\hat{e}_z]\\&\times\cos(\varphi_n+\delta\varphi_n)\},\\ \delta\mathbf{B}(\mathbf{x},t)=&\sum_n \delta\hat{E}_n\{\Theta_n(r)\hat{\mathbf{e}}_r\cos(\varphi_n+\delta\varphi_n)\\&+[\beta_{\rm ph}(k_n)R_n(r)\hat{\mathbf{e}}_\theta-Z_n^{(b)}(r)\hat{\mathbf{e}}_z]\\&\times\sin(\varphi_n+\delta\varphi_n)\},\end{aligned}\tag{1}$$

where the summation is over the appropriate modes to be included, and $\delta\hat{E}_n$ denotes the wave amplitudes. The phase is composed of two parts, one given by the phase of the wave propagating in the cold vacuum helix given by $\varphi_n \equiv k_n z-\omega_n t$ for wave number $k_n\equiv n\Delta k$ and angular frequency ω_n, such that (k_n,ω_n) satisfy the vacuum sheath helix dispersion equation, and a part which is governed by the interaction with the electron beam $\delta\varphi_n$. We assume that both $\delta\hat{E}_n$ and $\delta\varphi_n$ vary in z and t. In addition, $\beta_{\rm ph}(k_n)\equiv v_{\rm ph}(k_n)/c=\omega_n/ck_n$ denotes the normalized phase velocity of each wave, and $\kappa_n^2\equiv k_n^2-\omega_n^2/c^2$. The vacuum sheath helix dispersion equation is[8,21]

$$\frac{\omega_n^2}{c^2}+\frac{\kappa_n^2}{k_h^2R_h^2}\frac{I_0(\kappa_nR_h)I_1(\kappa_nR_g)}{I_0(\kappa_nR_g)I_1(\kappa_nR_h)}\frac{W_0(\kappa_nR_g,\kappa_nR_h)}{W_1(\kappa_nR_g,\kappa_nR_h)}=0,\tag{2}$$

where $k_h[\equiv 2\pi/\lambda_h]$ is the helix wave number, $W_n(x,y)\equiv K_n(y)I_n(x)-I_n(y)K_n(x)$, and I_n and K_n denote the modified Bessel functions of the first and second kinds. The components of the polarization vectors depend upon the frequency, wave number, and dimensions of the helix and outer cylinder, and are given by

$$R_n(r)=\frac{k_n}{\kappa_n}\begin{cases}I_1(\kappa_nr), & r\le R_h,\\ I_0(\kappa_nR_h)\dfrac{Z(\kappa_nR_g,\kappa_nr)}{W_0(\kappa_nR_g,\kappa_nR_h)}, & R_h<r\le R_g;\end{cases}\tag{3}$$

$$\Theta_n(r)=\frac{ck_n/\omega_n}{k_hR_h}\times\begin{cases}\dfrac{I_1(\kappa_nr)I_0(\kappa_nR_h)}{I_1(\kappa_nR_h)}, & r\le R_h,\\ I_0(\kappa_nR_h)\dfrac{W_1(\kappa_nR_g,\kappa_nr)}{W_1(\kappa_nR_g,\kappa_nR_h)}, & R_h<r\le R_g;\end{cases}\tag{4}$$

$$Z_n^{(e)}(r)=\begin{cases}I_0(\kappa_nr), & r\le R_h,\\ I_0(\kappa_nR_h)\dfrac{W_0(\kappa_nR_g,\kappa_nr)}{W_0(\kappa_nR_g,\kappa_nR_h)}, & R_h\le r\le R_g;\end{cases}\tag{5}$$

$$Z_n^{(h)}(r)=\frac{c\kappa_n/\omega_n}{k_hR_h}\times\begin{cases}\dfrac{I_0(\kappa_nR_h)I_0(\kappa_nr)}{I_1(\kappa_nR_h)}, & r\le R_h,\\ -I_0(\kappa_nR_h)\dfrac{Z(\kappa_nr,\kappa_nR_g)}{W_1(\kappa_nR_g,\kappa_nR_h)}, & R_h<r\le R_g,\end{cases}\tag{6}$$

where $Z(x,y)\equiv K_0(x)I_1(y)+I_0(x)K_1(y)$.

Energy transport for each wave within the vacuum helix/cylinder is determined by the Poynting flux, the stored energy density, and the group velocity. The Poynting flux for each wave denotes the time-averaged power flux over the entire cross section of the cylinder and helix, and can be expressed as

$$S_n=P_n\delta\hat{E}_n^2,\tag{7}$$

where

$$P_n \equiv \frac{k_n \omega_n}{8\kappa_n^4} \frac{I_0(\kappa_n R_h) I_0(\kappa_n R_g)}{W_0(\kappa_n R_g, \kappa_n R_h)} \left\{ \frac{I_0(\kappa_n R_h)}{I_0(\kappa_n R_g)} \frac{1}{W_0(\kappa_n R_g, \kappa_n R_h)} - \frac{I_1(\kappa_n R_h)}{I_1(\kappa_n R_g)} \frac{1}{W_1(\kappa_n R_g, \kappa_n R_h)} \right.$$
$$\left. + \kappa_n R_h \frac{[I_1^2(\kappa_n R_h) + I_0^2(\kappa_n R_h) - 2 I_0(\kappa_n R_h) I_2(\kappa_n R_h)]}{I_0(\kappa_n R_h) I_1(\kappa_n R_h)} - \kappa_n R_h \left[\frac{Z(\kappa_n R_g, \kappa_n R_h)}{W_0(\kappa_n R_g, \kappa_n R_h)} - \frac{Z(\kappa_n R_h, \kappa_n R_g)}{W_1(\kappa_n R_g, \kappa_n R_h)} \right] \right\}. \tag{8}$$

In addition, the time-averaged energy density per unit axial length over the entire cross section of the helix and cylinder is given by

$$W_n = U_n \delta \hat{E}_n^2, \tag{9}$$

where

$$U_n \equiv \frac{\omega_n}{k_n c^2} P_n + \frac{1}{4\kappa_n^2} \frac{I_0(\kappa_n R_g) I_0(\kappa_n R_h)}{W_0(\kappa_n R_g, \kappa_n R_h)}. \tag{10}$$

Finally, the group velocity of each individual wave is given by

$$v_{gr}(k_n) \equiv \frac{\partial \omega_n}{\partial k_n} = \frac{P_n}{U_n}. \tag{11}$$

For convenience, we rewrite the electric and magnetic fields in the form

$$\delta \mathbf{E}(\mathbf{x},t) = \sum_n [\delta \hat{E}_n^{(1)} \mathbf{e}_n(\mathbf{x},t) + \delta \hat{E}_n^{(2)} \mathbf{e}_n^*(\mathbf{x},t)],$$
$$\delta \mathbf{B}(\mathbf{x},t) = \sum_n [\delta \hat{E}_n^{(1)} \mathbf{b}_n(\mathbf{x},t) + \delta \hat{E}_n^{(2)} \mathbf{b}_n^*(\mathbf{x},t)], \tag{12}$$

where $\delta \hat{E}_n^{(1)} = \delta \hat{E}_n \cos \delta\varphi_n$ and $\delta \hat{E}_n^{(2)} = \delta \hat{E}_n \sin \delta\varphi_n$, and the polarization vectors are given in cylindrical coordinates by

$$\mathbf{e}_n(\mathbf{x},t) \equiv \{R_n(r)\hat{\mathbf{e}}_r \sin \varphi_n - [\beta_{ph}(k_n)\Theta_n(r)\hat{\mathbf{e}}_\theta - Z_n^{(e)}(r)\hat{\mathbf{e}}_z]\cos \varphi_n\},$$
$$\mathbf{b}_n(\mathbf{x},t) \equiv \{\Theta_n(r)\hat{\mathbf{e}}_r \cos \varphi_n + [\beta_{ph}(k_n)R_n(r)\hat{\mathbf{e}}_\theta - Z_n^{(b)}(r)\hat{\mathbf{e}}_z]\sin \varphi_n\},$$
$$\mathbf{e}_n^*(\mathbf{x},t) \equiv \{R_n(r)\hat{\mathbf{e}}_r \cos \varphi_n + [\beta_{ph}(k_n)\Theta_n(r)\hat{\mathbf{e}}_\theta - Z_n^{(e)}(r)\hat{\mathbf{e}}_z]\sin \varphi_n\}, \tag{13}$$
$$\mathbf{b}_n^*(\mathbf{x},t) \equiv \{-\Theta_n(r)\hat{\mathbf{e}}_r \sin \varphi_n + [\beta_{ph}(k_n)R_n(r)\hat{\mathbf{e}}_\theta - Z_n^{(b)}(r)\hat{\mathbf{e}}_z]\cos \varphi_n\},$$

Observe that the polarization vectors satisfy the source-free Maxwell equations; hence,

$$\nabla \times \mathbf{e}_n = -\frac{1}{c}\frac{\partial}{\partial t}\mathbf{b}_n \quad \text{and} \quad \nabla \times \mathbf{b}_n = \frac{1}{c}\frac{\partial}{\partial t}\mathbf{e}_n, \tag{14}$$

as well as

$$\nabla \times \mathbf{e}_n^* = -\frac{1}{c}\frac{\partial}{\partial t}\mathbf{b}_n^* \quad \text{and} \quad \nabla \times \mathbf{b}_n^* = \frac{1}{c}\frac{\partial}{\partial t}\mathbf{e}_n^*. \tag{15}$$

C. The dynamical equations for the fields

The hyperbolic dispersion equation in a smooth-bore cylindrical waveguide ensures that κ_n remains constant for each wave frequency corresponding to a given radial mode. As a result, the transverse variation for any TE_{ln} or TM_{ln} mode in the waveguide does not vary with frequency. This is not the case in a helix TWT where the solution of the dispersion equation in a sheath helix indicates that κ_n varies with frequency; hence, the radial variation of the electromagnetic field differs for each wave in the superposition. In order to treat this variation in the radial mode structure, we represent the electromagnetic field in terms of the superposition given in Eqs. (12) under the assumption that the mode amplitudes vary more slowly in z and t [i.e., $\delta \hat{E}_n^{(1)} = \delta \hat{E}_n^{(1)}(z,t)$ and $\delta \hat{E}_n^{(2)} = \delta \hat{E}_n^{(2)}(z,t)$]. This spatial and temporal variation in the wave amplitudes will describe the propagation of a pulse through either a vacuum helix or in the presence of an electron beam subject to (1) the dispersion of the waves in a sheath helix, and (2) the variations in the radial inhomogeneities of each wave with frequency.

The dynamical equations for the wave amplitudes are obtained in a manner analogous to the derivation of Poynting's theorem. Bearing in mind that $\mathbf{e}_n(\mathbf{x},t)$ and $\mathbf{b}_n(\mathbf{x},t)$ satisfy Maxwell equations in the absence of a source, Ampère's law is of the form

$$\sum_n \left(\hat{\mathbf{e}}_z \times \mathbf{b}_n \frac{\partial}{\partial z} \delta \hat{E}_n^{(1)} - \mathbf{e}_n \frac{\partial}{\partial t} \delta \hat{E}_n^{(1)} \right)$$
$$+ \sum_n \left(\hat{\mathbf{e}}_z \times \mathbf{b}_n^* \frac{\partial}{\partial z} \delta \hat{E}_n^{(2)} - \mathbf{e}_n^* \frac{\partial}{\partial t} \delta \hat{E}_n^{(2)} \right) = \frac{4\pi}{c} \mathbf{J}(\mathbf{x},t), \tag{16}$$

and Faraday's law is

$$\sum_n \left(\hat{\mathbf{e}}_z \times \mathbf{e}_n \frac{\partial}{\partial z} \delta \hat{E}_n^{(1)} + \mathbf{b}_n \frac{\partial}{\partial t} \delta \hat{E}_n^{(1)} \right)$$
$$+ \sum_n \left(\hat{\mathbf{e}}_z \times \mathbf{e}_n^* \frac{\partial}{\partial z} \delta \hat{E}_n^{(2)} + \mathbf{b}_n^* \frac{\partial}{\partial t} \delta \hat{E}_n^{(2)} \right) = 0, \tag{17}$$

where $\mathbf{J}(\mathbf{x},t)$ denotes the microscopic source current. The dynamical equations for the fields are obtained in a manner analogous to the derivation of Poynting's equation by (1) taking the inner product of $\mathbf{b}_m$ (and $\mathbf{b}_m^*$) with Faraday's law (17) and $\mathbf{e}_m$ (and $\mathbf{e}_m^*$) with Ampère's law (16), (2) subtracting the equations, (3) integrating the result over the entire cross section of the helix and cylinder, and (4) averaging the result over the axial length $2\pi/\Delta k$. The average is performed under the assumption that $\delta \hat{E}_n^{(i)}$ $(i=1,2)$ varies on a slower spatial

scale length; hence, this operation diagonalizes the equations so that the evolution of each $\delta\hat{E}_n^{(i)}$ satisfies equations of the form

$$\frac{\partial}{\partial t}\delta\hat{E}_n^{(1)}+v_{gr}(k_n)\frac{\partial}{\partial z}\delta\hat{E}_n^{(1)}$$
$$=\frac{2\Delta k}{cU_n}\int_0^{2\pi/\Delta k}dz'\int\int_{A_h}dx\,dy\mathbf{J}(x,y,z',t)\cdot\mathbf{e}_n(x,y,z',t),$$
$$\frac{\partial}{\partial t}\delta\hat{E}_n^{(2)}+v_{gr}(k_n)\frac{\partial}{\partial z}\delta\hat{E}_n^{(2)} \tag{18}$$
$$=\frac{2\Delta k}{cU_n}\int_0^{2\pi/\Delta k}dz'\int\int_{A_h}dx\,dy\mathbf{J}(x,y,z',t)\cdot\mathbf{e}_n^*(x,y,z',t),$$

where A_h denotes the cross-sectional area enclosed by the helix. This equation describes the propagation of a pulse, or pulses, through the helix/cylinder at the appropriate group velocities. Intermodulation between the various waves is implicitly included through the particle trajectories.

It is important to observe that these dynamical equations depend upon the field structure explicitly through (1) the group velocity, (2) the energy density, and (3) the polarization of the wave. As such, it also depends implicitly upon the Poynting flux and the dispersion equation. In any case, similar dynamical equations can be readily obtained for more realistic helix models as well as a wide range of both slow- and fast-wave devices such as free-electron lasers, and cyclotron and Čerenkov masers. Indeed, the technique has been applied to the analysis of backward-wave oscillators[22,23] and gyrotrons[24] with good results.

D. Electron dynamics

The electron dynamics are treated using the full three-dimensional Lorentz force equations. It should be noted here that the present formulation is fully three-dimensional and relativistic. The azimuthal symmetry is imposed in the sense (1) that the beam distribution upon entry to the helix is azimuthally symmetric, and (2) that each of the vector components of the electromagnetic fields varies only in (r,z,t). One important restriction in the present analysis is that the fluctuating radio-frequency (RF) space-charge fields are not explicitly included. Hence, the analysis is strictly valid only subject to the neglect of the positive and negative beam space-charge waves (i.e., the ballistic regime in which the Pierce gain parameter is small). Similarly, the effect of the direct current (DC) self-electric and self-magnetic fields are also neglected. The inclusion of the RF space-charge and DC self-fields are presently under study. As such, we integrate the Lorentz force equation for each electron in the simulation subject to both the external axial magnetic field and the electromagnetic fields. Hence,

$$\frac{d}{dt}\mathbf{p}=-e\,\delta\mathbf{E}(\mathbf{x},t)-\frac{e}{c}\mathbf{v}\times[B_0\hat{\mathbf{e}}_z+\delta\mathbf{B}(\mathbf{x},t)]. \tag{19}$$

Observe that the electron dynamics are treated relativistically.

III. NUMERICAL ANALYSIS

Equations (17) and (18) are solved for a system of length L on a grid with spacing Δz using the MacCormack method[25] and electrons are injected at $z=0$ on each time step Δt. The source current is represented as

$$\mathbf{J}(\mathbf{x},t)=-q\sum_{i=1}^{N}v_i(t)\,\delta(x-x_i(t))\,\delta(y-y_i(t))$$
$$\times S(z-z_i(t)), \tag{20}$$

where N is the number of electrons in the system at time t, $(\mathbf{x}_i,\mathbf{v}_i)$ represents the location and velocity of the ith electron at time t, q is the charge per electron, and S is the shape function. The shape function describes the interpolation of the electron charge to the grid locations. We use a triangular shape algorithm

$$S(z-z_i)=\begin{cases}\dfrac{z-z_i+\Delta z}{\Delta z^2}, & z_i-\Delta z\leq z\leq z_i,\\ -\dfrac{z-z_i-\Delta z}{\Delta z^2}, & z_i<z\leq z_i+\Delta z,\end{cases} \tag{21}$$

which provides a linear weighting in which the charge is mapped onto the two nearest neighbor grid points. The charge per electron includes a weight factor dependent upon the beam current. Since we are injecting electrons on each time step, we choose

$$q=\frac{I_b\Delta t}{N_{\Delta t}}, \tag{22}$$

where I_b is the average beam current, and $N_{\Delta t}$ is the number of electrons injected per time step. As a result, the dynamical equations for the field amplitudes are

$$\frac{\partial}{\partial t}\delta\hat{E}_n^{(1)}+v_{gr}(k_n)\frac{\partial}{\partial z}\delta\hat{E}_n^{(1)}$$
$$=-\frac{2q\Delta k}{cU_n}\sum_{i=1}^{N}\int_0^{2\pi/\Delta k}dz'S(z'-z_i)\mathbf{v}_i(t)$$
$$\cdot\mathbf{e}_n(x_i,y_i,z',t),$$
$$\frac{\partial}{\partial t}\delta\hat{E}_n^{(2)}+v_{gr}(k_n)\frac{\partial}{\partial z}\delta\hat{E}_n^{(2)} \tag{23}$$
$$=-\frac{2q\Delta k}{cU_n}\sum_{i=1}^{N}\int_0^{2\pi/\Delta k}dz'S(z'-z_i)\mathbf{v}_i(t)$$
$$\cdot\mathbf{e}_n^*(x_i,y_i,z',t).$$

Open boundary conditions for the field are imposed at both $z=0$ and L.

The orbit equations are integrated by means of a fourth-order Runge–Kutta algorithm. In order to be consistent with the electron shape function that maps electron charge onto the grid, we use a linear interpolation scheme to map the field amplitude from the grid to the particle locations.

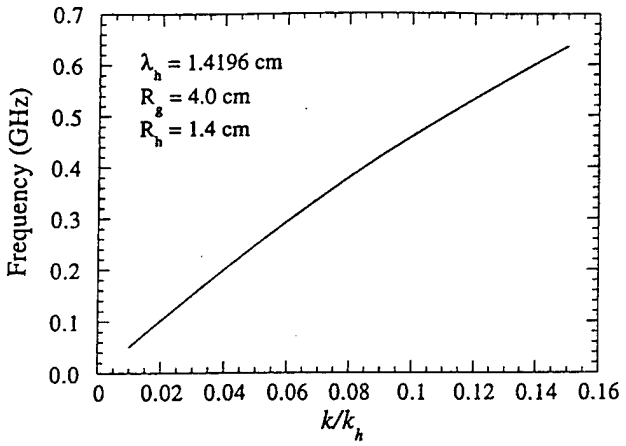

FIG. 3. Plot of the variation of the frequency with wave number for the reference helix and waveguide.

We now turn to the consideration of some numerical examples. We arbitrarily choose waveguide and helix dimensions of $R_g=4.0$ cm, $R_h=1.4$ cm, and $\lambda_h=1.4196$ cm, and we will use these dimensions throughout the remainder of the article. The group and phase velocities of waves in this vacuum helix can be calculated using the dispersion equation (5). Plots showing (1) the variation of the frequency versus wave number, and (2) the variation of the group and phase velocity versus frequency is shown in Figs. 3 and 4.

A. Propagation in the vacuum helix

We first consider the case of the propagation of a pulse through the vacuum helix, and assume that a pulse is injected at $z=0$ with a smooth temporal shape given by

$$\delta\hat{E}_n^{(1)}(z=0,t)=\delta\hat{E}_0^{(1)}\sin^2\left(\frac{\pi}{2}\frac{t}{\tau_p}\right), \tag{24}$$

and $\delta\hat{E}_n^{(2)}(z=0,t)=0$ for $0\leq t\leq\tau_p$, where τ_p describes both the rise and fall time of the pulse and $\delta\hat{E}_0^{(1)}$ is chosen to describe the peak power via Eq. (7). We use this same model for the injection of either single or multiple waves in the remaining sections.

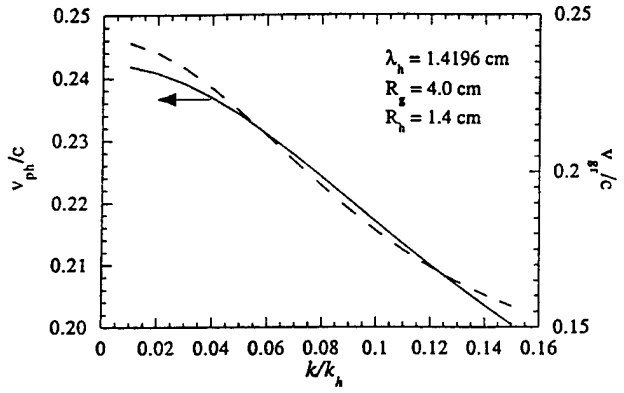

FIG. 4. Plots of the group (dashed line) and phase (solid line) velocities vs frequency for the reference helix and waveguide.

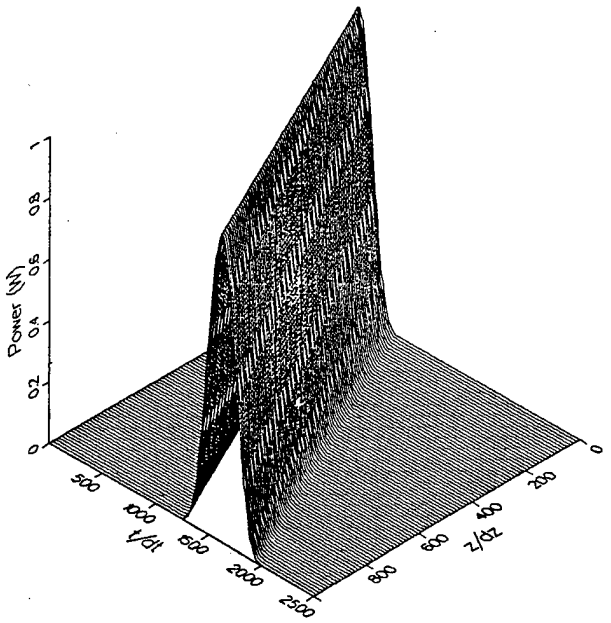

FIG. 5. Perspective plot of the propagation of a pulse through the vacuum helix.

Consider the propagation of a pulse having a peak power of 1 W and a wave number $k/k_h=0.1$. This corresponds to a wavelength of 14.196 cm, a frequency of approximately 459 MHz, and a group velocity of $v_{gr}/c\approx0.18$. We choose a system of length $L=141.96$ cm (i.e., 10 helix periods) and assume that $\tau_p=10$ ns corresponding to approximately five wave periods. A perspective plot of the propagation of the pulse is shown in Fig. 5 in which we plot the wave power on the vertical axis and the axial position and time on the horizontal axes. As shown in the figure, the pulse propagates through (and out of) the system with very little distortion. Energy conservation is satisfied to within several parts in 10^5.

More detail can be obtained by consideration of the instantaneous Poynting flux at $z=L$ as a function of time. This is shown in Fig. 6. Given the length of the system and the group velocity of the wave, we expect to see the peak of the pulse arrive after 36 ns have elapsed, and this is clearly shown in the figure.

B. Single-wave propagation with beam

We now turn to the interaction of a single wave in the helix with an electron beam. For simplicity, we shall assume the injection of an identical electromagnetic pulse as described in Sec. III A with a helix length of $L=141.96$ cm. We also consider the injection of a 16 kV/0.5 A electron beam with an flat-top annular beam profile with inner and outer radii of 0.99 and 1.01 cm, respectively. The rise time of the beam current is assumed to be 1 ns. For simplicity, we shall also assume that the beam has a zero emittance and energy spread.

A linear stability analysis of the interaction of an annular beam in a sheath helix has appeared in Ref. 8, and we shall

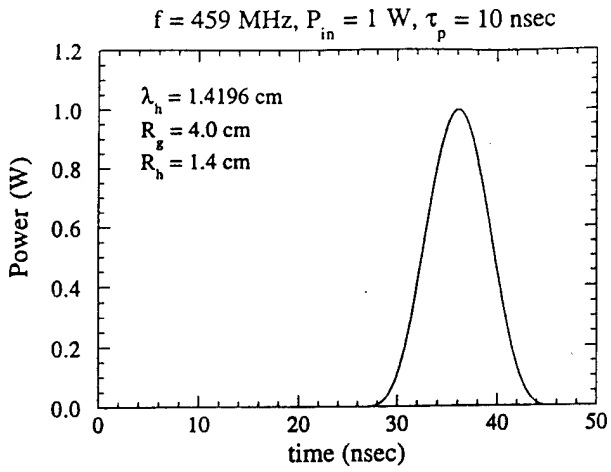

FIG. 6. Plot of the output power at $z=L$ as a function of time for a pulse propagating through a vacuum helix.

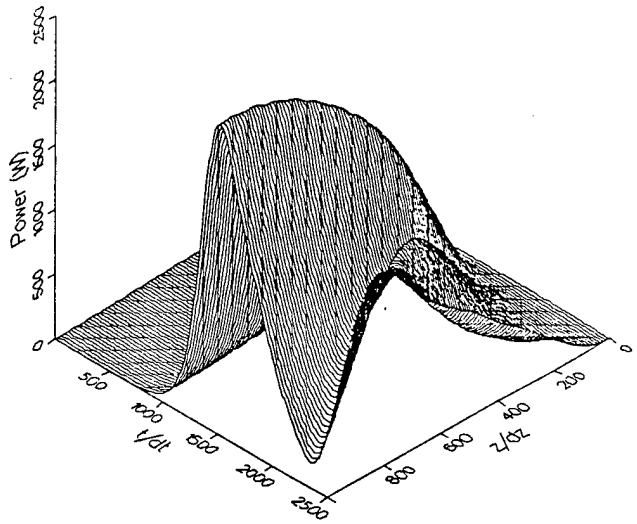

FIG. 7. Perspective plot of the propagation of a pulse through a beam-loaded helix.

make use of the results of that analysis for comparison purposes. The gain predicted by the theory for this choice of beam parameters and wave number is approximately 0.30 dB/cm. The efficiency of the interaction can be estimated by the usual phase trapping argument; specifically, that at saturation the beam electrons will lose an amount of energy corresponding to a deceleration of $2\Delta v$, where $\Delta v = v_b - v_{\rm ph}$ and v_b is the initial bulk axial velocity of the beam. This technique was originally formulated by Slater for traveling wave tubes,[26] but has also been used successfully for free-electron lasers[15] and gives a predicted efficiency of

$$\eta \approx \frac{2\gamma^3}{\gamma - 1}\frac{v_b}{c}\left(\frac{v_b}{c} - \frac{v_{\rm ph}}{c}\right). \tag{25}$$

For the case under discussion in which $v_b/c \approx 0.244$ and $v_{\rm ph}/c \approx 0.217$, this yields a predicted efficiency of $\eta \approx 45\%$. Using this value of the saturation efficiency and the linear gain, we obtain a saturation length of approximately 117 cm for an input power of 1 W.

It should be noted that the device is in the ballistic regime at this current level where the beam space-charge waves can be neglected. The transition current beyond which the space-charge waves must be included is in the range of some tens of amperes.[15]

A perspective plot of the propagation and growth of the wave is shown in Fig. 7. This plot is directly analogous to that shown in Fig. 5 in which the vertical axis represents the wave power while the horizontal axes represent time and axial distance. It is evident from the figure that substantial growth is found and saturation sets in at a power level of more than 2 kW. The differences shown between this plot and Fig. 7 are due to the beam interaction, and it is important to observe that substantial pulse lengthening and distortion has occurred.

This signal distortion is also observed in a plot of the output power as a function of time as shown in Fig. 8. Note that the transmit time of the beam through the helix is approximately 20 ns, and no output power is observed prior to that time. The wave power grows rapidly after that time and reaches a peak at a power level of approximately 2.3 kW after 42 ns. This delay can be explained by noting that (1) the group velocity for this signal is $v_{\rm gr}/c \approx 0.18$ and the transit time for the signal through the helix is about 26 ns, and (2) the predicted growth time to saturation (give the linear gain and efficiency estimate) is approximately 15 ns. Hence, the peak of the signal should not be found prior to 41 ns after the start of the interaction.

A plot of the electron distributions in axial momentum and radial position as functions of axial position are shown in Fig. 9 at a late stage in the interaction. It is clear from the figure that electron trapping and subsequent bunching in axial position begins at $k_h z \approx 300$ with saturation of the signal at $k_h z \approx 500$ (i.e. $z \approx 113$ cm) as evidenced by the relatively unchanging subsequent momentum distribution.

We note that there is substantial agreement between the simplified linear gain theory that predicts a gain of 0.30 dB/cm and the nonlinear simulation which for an input

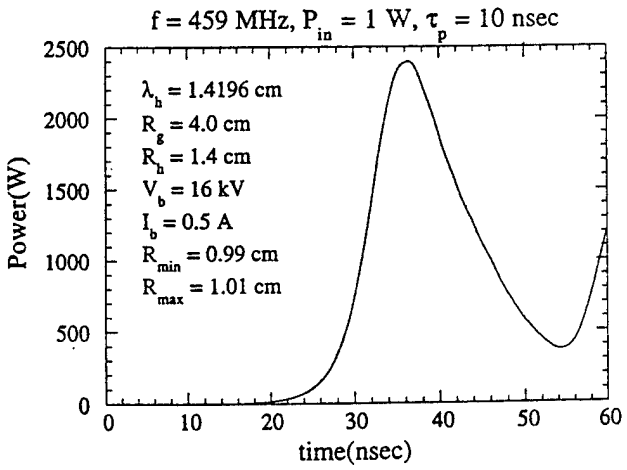

FIG. 8. Plot of the output power at $z=L$ as a function of time for the beam-loaded helix.

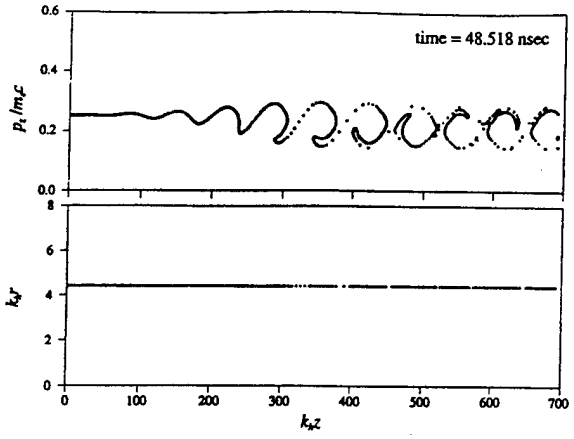

FIG. 9. Phase space plot showing the distribution of axial momenta and radial position of the beam electrons as a function of axial position at a late time of the interaction.

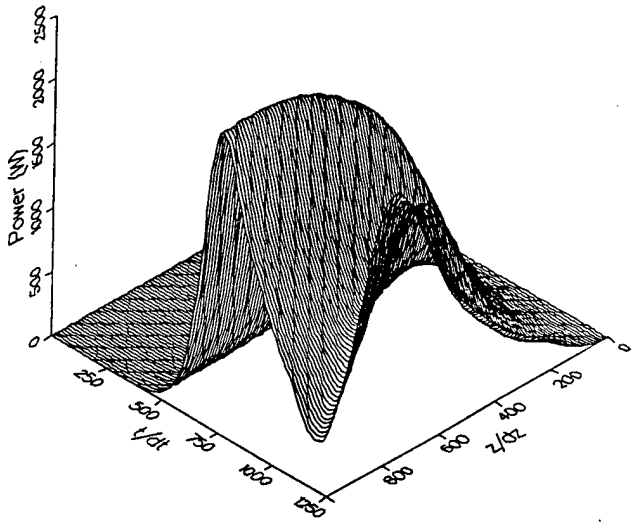

FIG. 10. Perspective plot of the propagation of the pulse corresponding to the faster growth rate through the beam-loaded helix.

power of 1 W and an output power of 2.3 kW over a saturation length of 113 cm yields a gain of ≈0.29 dB/cm; however, the efficiency $\eta \approx 29\%$ found in the nonlinear simulation is somewhat less than predicted by Eq. (25). We attribute this to deficiencies in the simplified phase trapping argument. Finally, energy conservation is good to within several parts in 10^3.

C. Multiwave propagation with beam

We now turn to the multiwave case and consider the injection of two waves in conjunction with an electron beam identical to that considered in Sec. III B. We also choose identical helix and waveguide dimensions as used in the preceding sections. One of the waves is chosen to be identical to that considered in the two preceding sections (i.e., $k/k_h=0.1$), and an additional wave is included for which $k/k_h=0.05$ ($f=362$ MHz). Both waves are assumed to have injected powers of 1 W and $\tau_p=10$ ns. As shown in Fig. 4, this second wave has higher phase and group velocities ($v_{ph}/c \approx 0.234$ and $v_{gr}/c \approx 0.220$), but the linear theory predicts a substantially lower gain of approximately 0.19 dB/cm. Hence, we would not expect the second wave to exhibit substantial growth over the length of the helix under consideration.

Perspective plots of the evolution of the power of each wave with both axial position and time are shown in Figs. 10 and 11. Figure 10 corresponds to the wave for which $k/k_h=0.1$, which is the dominant wave by virtue of its higher growth rate. Observe that this result is very similar to the single-wave result shown in Fig. 7. The two waves are coupled through the electron beam, and this calculation includes the intermodulation between the waves. Hence, we conclude that the intermodulation provides a relatively small perturbation to the evolution of this wave. However, that is not the case for the slower growing wave (for $k/k_h=0.05$) which is shown in Fig. 11. In the absence of the second wave, this wave would grow in a fashion similar to that shown for the single-wave case in the preceding section, although it would not reach saturation over the length of the present helix. The intermodulation between these two waves, however, results in a substantial distortion in the pulse of the slower-growing wave.

A clearer representation of the effects of the two waves on the output power is shown in Fig. 12 where the total output power at $z=L$ is shown as a function of time. This figure is similar Fig. 8 for the single-wave case. The principal differences in the two-wave case are that (1) the total power is reduced somewhat from 2.3 kW for the single-wave case to 2.2 kW for these two waves, and (2) the peak power now occurs at 43 ns, which is somewhat later than found for the single wave.

The phase space in this case is not substantially different from that shown for the single-wave sample. These conclusions regarding the magnitude of the intermodulation, however, should not be assumed to hold in general for arbitrary choices of the wave numbers and higher numbers of injected

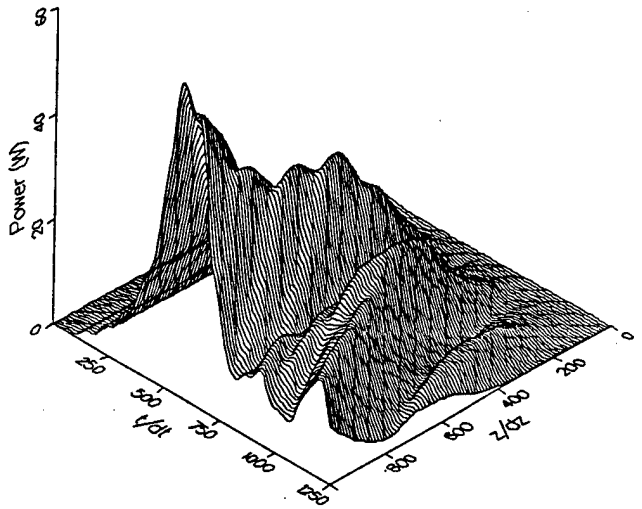

FIG. 11. Perspective plot of the propagation of the pulse corresponding to the slower growth rate through the beam-loaded helix.

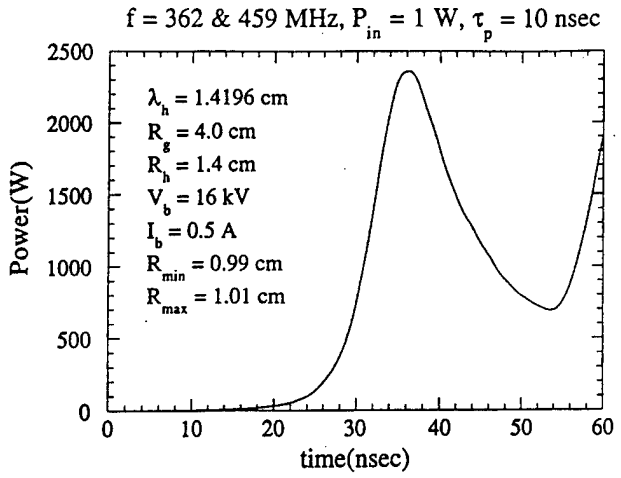

FIG. 12. Plot of the output power at $z=L$ as a function of time for the beam-loaded helix with two waves.

waves. Detailed calculations are necessary to assess the importance of the intermodulation for different choices of the wave(s), beam, and helix parameters.

IV. SUMMARY AND DISCUSSION

In this article, we have described a nonlinear formulation of the interaction of an electron beam and multiple waves in a sheath helix TWT. The formulation is in the time domain and is able to treat the propagation of multiple pulses through the helix structure, and includes the intermodulation between the waves. In addition, the results are in substantial agreement with a linear theory of the gain in a helix TWT.

The fundamental dynamical equations for the fields (17) are quite general in form, and rely largely on a knowledge of the dispersion, polarization, energy density, and Poynting flux for the waves under consideration. Thus, the technique is readily generalized to other configurations and structures. For example, we have considered open boundary conditions here, but it is straightforward to include reflections at either end of the interaction length and deal with cavities and oscillator configurations. The model of the beam we have employed is also very specific in that we studied an annular beam with a continuous temporal structure and zero emittance and energy spread. This can also be readily generalized to consider solid beams with a pulse temporal structure and a nonvanishing momentum and energy spread, as well as the inclusion of self-electric and self-magnetic fields. Other generalizations that can be included are (1) to include a taper in the helix model, and (2) to generalize the helix model to more realistic configurations including, but not limited to, tape helix models. Each of these generalizations is currently in progress.

In view of the computational efficiency and generality of the present formulation to more complex and realistic helix models, the technique has advantages over PIC simulations for treating interactions in helix TWTs.

ACKNOWLEDGMENTS

The authors would like to acknowledge helpful technical discussions withs Dr. A. T. Drobot, Dr. D. Chernin, and Dr. B. Levush.

This work was supported by the Office of Naval Research and the Office of Naval Technology. The computational work was supported in part by a grant of High Performance Computing (HPC) time from the Department of Defense HPC Shared Resource Center of the Corps of Engineers Waterways Experiment Station (CEWES).

[1] J. R. Pierce and L. M. Field, Proc. IRE **35**, 108 (1947).
[2] J. R. Pierce, Proc. IRE **35**, 111 (1947).
[3] J. R. Pierce, *Traveling-Wave Tubes* (Van Nostrand, New York. 1950).
[4] O. E. H. Rydbeck, Ericsson Technics **46**, 3 (1948).
[5] L. J. Chu and J. D. Jackson, Proc. IRE **36**, 853 (1948).
[6] A. H. W. Beck, *Space-Charge Waves* (Pergamon, New York, 1958).
[7] R. G. E. Hutter, *Beam and Wave Electronics in Microwave Tubes* (Van Nostrand, New York, 1960).
[8] H. P. Freund, M. A. Kodis, and N. R. Vanderplaats, IEEE Trans. Plasma Sci. **PS-20**, 543 (1992).
[9] H. P. Freund, N. R. Vanderplaats, and M. A. Kodis, IEEE Trans. Plasma Sci. **PS-21**, 654 (1993).
[10] L. Brillouin, J. Appl. Phys. **20**, 1196 (1949).
[11] A. Nordsieck, Proc. IRE **41**, 630 (1953).
[12] P. K. Tien, L. R. Walker, and V. M. Wolontis, Proc. IRE **43**, 260 (1955).
[13] J. E. Rowe, IRE Trans. Electron Devices **ED-3**, 39 (1956).
[14] J. E. Rowe, *Nonlinear Electron-Wave Interaction Phenomena* (Academic, New York, 1965).
[15] H. P. Freund and T. M. Antonsen, Jr., *Principles of Free-Electron Lasers* (Chapman & Hall, London, 1992), Chap. 5.
[16] I. J. Morey and C. K. Birdsall, IEEE Trans. Plasma Sci. **PS-18**, 482 (1990).
[17] R. J. Faehl, B. S. Newberger, and B. B. Godfrey, Phys. Fluids **23**, 2440 (1980).
[18] B. Goplen, D. Smithe, K. Nguyen, M. A. Kodis, and N. R. Vanderplaats, *International Electron Devices Meeting Technical Digest* (Institute of Electrical and Electronic Engineers, Piscataway, NJ, 1992), pp. 759–762.
[19] Y. Y. Lau and D. Chernin, Phys. Fluids B **4**, 3473 (1992).
[20] H. P. Freund, R. H. Jackson, and D. E. Pershing, Phys. Fluids B **5**, 2318 (1993).
[21] H. S. Uhm and J. Y. Choe, J. Appl. Phys. **53**, 8483 (1982).
[22] B. Levush, T. M. Antonsen, Jr., A. Bromborsky, W. R. Lou, and Y. Carmel, IEEE Trans. Plasma Sci. **PS-20**, 263 (1992).
[23] A. Vlasov, G. Nusinovich, B. Levush, A. Bromborsky, W. Lou, and Y. Carmel, Phys. Fluids B **5**, 1625 (1993).
[24] S. Y. Cai, T. M. Antonsen, Jr., G. Saraph, and B. Levush, Int. J. Electron. **72**, 759 (1992).
[25] K. A. Hoffman, *Computational Fluid Dynamics for Engineers* (Engineering Education System, Austin, TX, 1989), p. 171.
[26] J. C. Slater, *Microwave Electronics* (Van Nostrand, New York, 1950).

APPENDIX XIV

Theory of Helix Traveling Wave Tubes with Dielectric and Vane Loading

H.P. Freund, E.G. Zaidman, and T.M. Antonsen, Jr.
Phys. Plasmas **3**, 3145 (1996)

Theory of helix traveling wave tubes with dielectric and vane loading

H. P. Freund,[a] E. G. Zaidman, and T. M. Antonsen, Jr.[a),b)]
Naval Research Laboratory, Washington, D.C. 20375

(Received 5 March 1996; accepted 6 May 1996)

A time-dependent nonlinear analysis of a helix traveling wave tube (TWT) is presented for a configuration where an electron beam propagates through a sheath helix surrounded by a conducting wall. The effects of dielectric and vane loading are included in the formulation as is efficiency enhancement by tapering the helix pitch. Dielectric loading is described under the assumption that the gap between the helix and the wall is uniformly filled by a dielectric material. The vane-loading model describes the insertion of an arbitrary number of vanes running the length of the helix, and the polarization of the field between the vanes is assumed to be an azimuthally symmetric transverse-electric mode. The field is represented as a superposition of azimuthally symmetric waves in a vacuum sheath helix. An overall explicit sinusoidal variation of the form $\exp(ikz-i\omega t)$ is assumed (where ω denotes the angular frequency corresponding to the wave number k in the vacuum sheath helix), and the polarization and radial variation of each wave is determined by the boundary conditions in a vacuum sheath helix. The propagation of each wave *in vacuo* as well as the interaction of each wave with the electron beam is included by allowing the amplitudes of the waves to vary in z and t. A dynamical equation for the field amplitudes is derived analogously to Poynting's equation, and solved in conjunction with the three-dimensional Lorentz force equations for an ensemble of electrons. Electron beams with a both a continuous and emission-gated pulse format are analyzed, and the model is compared with linear theory of the interaction as well as with the performance of a TWTs operated at the Naval Research Laboratory and at Northrop–Grumman Corporation. [S1070-664X(96)02208-2]

I. INTRODUCTION

The development of the traveling wave tube (TWT) extends over several decades since the pioneering work of Pierce and co-workers[1–3] based upon a coupled-wave analysis utilizing the vacuum modes of the helix and the positive and negative energy space-charge waves of the beam. Improved linear theories based upon an eigenvector analysis of Maxwell's equations in a sheath helix have also been developed,[4,5] and discussions of both the coupled-wave and field theories of the TWT are given by Beck[6] and Hutter.[7] More recently, complete field theories of beam-loaded helix TWTs have been developed for both sheath[8] and tape[9] helix models, and dielectric loading has also been incorporated into the sheath helix analyses.[10]

Nonlinear theories of the TWT also have a long history in the literature, and can be grouped into two broad classes dealing with steady-state and time-dependent models. Steady-state models have been used to study the growth of a single frequency wave injected simultaneously with the electron beam. These formulations constitute a slow-time-scale approach.[11–14] A good review of this technique as applied to TWTs has been given by Rowe,[15] and the approach is well suited to the analysis of a broad class of linear beam amplifiers and has also been applied, for example, to the free-electron laser.[16]

Time-dependent models of helix TWTs rely upon particle-in-cell (PIC) simulation techniques. At the present time, a one-dimensional PIC simulation code is available,[17] which treats dispersion by means of a transmission line equivalent circuit model. Hence, the one-dimensional PIC simulation of this form is limited in its ability to model the dispersion of the helix and is unable to deal with radial variation in the mode structure. The most general PIC formulations of the interaction in a helix TWT to date are two-dimensional simulations of a sheath helix model.[18,19] Since the helix is in reality a three-dimensional structure, a two-dimensional PIC formulation requires a prescription for dealing with the boundary condition at the helix. In practice, the simplification made is to treat the so-called *sheath* helix in which the conductivity is infinite in the direction of the helix, and zero otherwise. While this approach can provide a good approximation for the dispersion and radial mode variation in the sheath helix, it is not adaptable to more realistic helix models, which include substantial harmonic components.

The approach we adopt in this paper differs from these PIC formulations. As in the case of the two-dimensional PIC formulations, we assume azimuthal symmetry and deal with a sheath helix model. However, we treat the fields in terms of a spectral decomposition in which the electromagnetic field is expressed as a superposition of the normal modes of the vacuum sheath helix. In this representation, an overall sinusoidal variation of the form $\exp(ikz-i\omega t)$ is assumed for each wave, where ω denotes the angular frequency determined from the vacuum sheath helix dispersion equation corresponding to wave number k. The polarization and radial variation of each wave is assumed to be given by the normal mode solutions of Maxwell's equations for the vacuum sheath helix boundary conditions, which are three-dimensional in nature. The evolution of each wave either *in vacuo* or in the presence of the electron beam is included by

[a)]Science Applications International Corp., McLean, Virginia 22102.
[b)]University of Maryland, College Park, Maryland 20742.

 1070-664X/96/3(8)/3145/17/$10.00

allowing the amplitudes to vary in both axial position and time. The detailed evolution of the waves is governed by a dynamical equation that is analogous to Poynting's equation. This equation includes the coupling of the waves to the electron beam and, hence, the intermodulation between the waves themselves. In conjunction with the equations for the fields, the trajectories of an ensemble of electrons are integrated using the three-dimensional Lorentz force equations.

As in the case of the two-dimensional PIC formulations, this spectral approach provides a good model for the dispersion and radial variation of the electromagnetic field, but requires an explicit choice of the waves of interest to be specified as an initial condition. It has two advantages over the two-dimensional PIC models, however, in that (1) the technique can be readily generalized to deal with more realistic tape helix models, which include higher harmonic components; and (2) the numerical technique is considerably less computationally demanding. For the numerical examples discussed in this paper, typical run times on a Cray Y-MP supercomputer were substantially less than one minute.

One restriction that is imposed in the present analysis is the neglect of the beam space-charge modes that restricts the analysis to the ballistic regime in which the Pierce gain parameter[2] is small. The exclusion of the space-charge modes is not an essential element of the formulation, and the inclusion of the space-charge modes is presently under study. The self-electric and self-magnetic fields have also been neglected. However, the self-fields can be readily included by means of a technique used for inclusion of the self-fields in free-electron lasers.[20]

The numerical examples discussed herein relate to the single-pass propagation of pulses through both vacuum and beam-loaded helix structures, and open boundary conditions have been imposed. However, various degrees of reflecting boundary conditions can also be used to treat various cavity and oscillator configurations. Finally, the formulation can also be generalized to treat more realistic helix models; in particular, a tape helix model is presently under study.[9]

The organization of the paper is as follows. The general formulation is presented in Sec. II. This includes a discussion of the geometry, the dispersion equation and mode structure in a sheath helix, the field representation and the dynamical equation governing the evolution of the fields, and the Lorentz force equations. In Sec. III we deal with the numerical techniques used to solve the dynamical equations as well as the representative solutions for various parameter regimes. A summary and discussion is given in Sec. IV.

II. THE GENERAL FORMULATION

The general formulation treats the propagation of multiple waves through a dielectric- and vane-loaded sheath helix in the presence of an electron beam. This is a fully time-dependent problem, and the electron beam model can represent either a continuous or prebunched pulse format. The prebunched electron beam is referred to in the literature as an *emission-gated beam*. In addition, we permit the injected radiation to have an arbitrary format; that is, we can inject either a definite radiation pulse or a continuous signal.

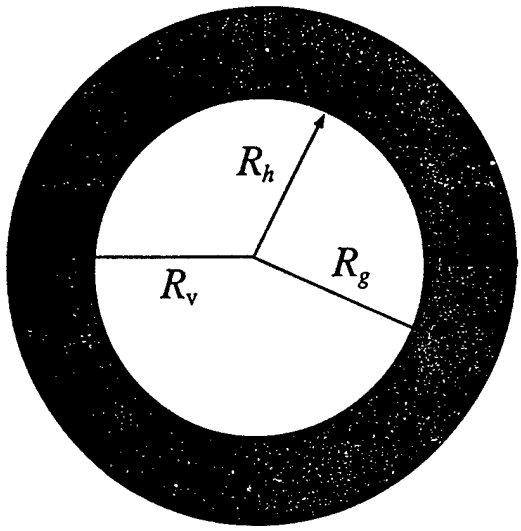

FIG. 1. Schematic representation of the cross section of the helix circuit.

A. The helix circuit configuration

The physical configuration that is treated is that of an energetic electron beam propagating parallel to the axis of symmetry of a dielectric and vane-loaded helix. Azimuthal symmetry is assumed throughout. A schematic of the cross section of the helix circuit is shown in Fig. 1, in which the vanes are positioned radially, and where R_h and R_g are used to denote the radii of the helix and the outer cylinder, R_v denotes the inner radius of the vanes, and ϵ_0 is the dielectric constant.

In practical TWTs the helix is composed of a metal strip or wire that is supported at multiple points within the cylinder by posts or rods. A complete self-consistent description of wave dispersion in such a structure is beyond the scope of the present analysis. For simplicity, we assume that both the helix and the outer cylinder are loss-free conductors and represent the electromagnetic field as a superposition of the azimuthally symmetric modes in the vacuum helix. Within the context of this assumption, there are several further simplications that permit an analytic solution for the normal modes of the vacuum helix.

In the commonly applied *tape* helix model, it is assumed that only a surface current is induced in the helix and that the effects of the support posts can be neglected. The restriction to surface currents in the helix is equivalent to the assumption that the helix is "thin" in the radial direction. A schematic illustration of a "tape" helix is shown in Fig. 2, where R_h is the helix radius, λ_h denotes the helix period and δ_h is the width of the tape. The unit vector describing the pitch of the helix is $\hat{\mathbf{e}}_\phi = \hat{\mathbf{e}}_\theta \cos\phi + \hat{\mathbf{e}}_z \sin\phi$, where $\tan\phi = 1/k_h R_h$ for a helix wave number $k_h (\equiv 2\pi/\lambda_h)$. A multiplicity of azimuthally symmetric modes exist in such a system corresponding to the spatial harmonics of the helix period. The importance of the higher-order spatial harmonics decreases as the width of the helix increases. Ultimately, if $\delta_h = \lambda_h$, the induced currents in the helix can be modeled as a continuous helical current sheet, and the effects of the spatial harmonics disappear. This is referred to as the *sheath* helix approxima-

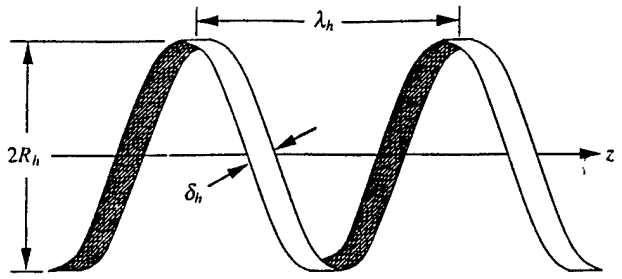

FIG. 2. Schematic illustration of a tape helix structure.

tion. For simplicity, we shall adopt a sheath helix model for the electromagnetic fields, but observe that the general technique we describe is readily generalizable to a tape helix model.

B. The modes in a sheath helix

We restrict the analysis to the azimuthally symmetric subluminous waves supported by the circuit. The azimuthally symmetric electric and magnetic fields can be represented in the form (see the Appendix)

$$\begin{aligned}\delta\mathbf{E}(\mathbf{x},t)&=\sum_n \delta\hat{E}_n\{R_n(r)\hat{\mathbf{e}}_r \sin(\varphi_n+\delta\varphi_n)\\&\quad-[\beta_{\mathrm{ph}}(k_n)\Theta_n(r)\hat{\mathbf{e}}_\theta-Z_n^{(e)}(r)\hat{\mathbf{e}}_z]\cos(\varphi_n\\&\quad+\delta\varphi_n)\},\\ \delta\mathbf{B}(\mathbf{x},t)&=\sum_n \delta\hat{E}_n\{\Theta_n(r)\hat{\mathbf{e}}_r \cos(\varphi_n+\delta\varphi_n)\\&\quad+[\beta_{\mathrm{ph}}(k_n)R_n(r)\hat{\mathbf{e}}_\theta-Z_n^{(b)}(r)\hat{\mathbf{e}}_z]\sin(\varphi_n\\&\quad+\delta\varphi_n)\},\end{aligned} \tag{1}$$

where the summation is over the modes to be included, and $\delta\hat{E}_n$ denotes the wave amplitudes. The phase is composed of two parts: one given by the phase of the wave propagating in the cold vacuum helix given by $\varphi_n\equiv k_n z-\omega_n t$ for wave number $k_n\equiv n\,\Delta k$ and angular frequency ω_n, such that (k_n,ω_n) satisfy the vacuum sheath helix dispersion equation and Δk is the separation in wave number between the waves, and a part governed by the interaction with the electron beam $\delta\varphi_n$. We assume that both $\delta\hat{E}_n$ and $\delta\varphi_n$ vary in z and t. In addition, $\beta_{\mathrm{ph}}(k_n)\equiv v_{\mathrm{ph}}(k_n)/c=\omega_n/ck_n$ denotes the normalized phase velocity of each wave. The vacuum sheath helix dispersion equation is (see the Appendix)

$$\frac{\omega_n^2}{c^2}-\frac{p_n q_n}{k_h^2R_h^2}\frac{J_0(p_nR_h)}{J_1(p_nR_h)}\frac{W_{0,0}(q_nR_v,q_nR_h)}{W_{1,1}(q_nR_v,q_nR_h)}\frac{[p_nJ_0(p_nR_h)W_{1,1}(q_nR_g,q_nR_h)-q_nJ_1(p_nR_h)W_{1,0}(q_nR_g,q_nR_h)]}{[q_nJ_1(p_nR_h)W_{0,0}(q_nR_v,q_nR_h)+\epsilon_0p_nJ_0(p_nR_h)W_{1,0}(q_nR_h,q_nR_v)]}=0, \tag{2}$$

where $k_h(\equiv 2\pi/\lambda_h)$ is the helix wave number, $p_n^2\equiv\omega_n^2/c^2-k_n^2$, $q_n^2\equiv\epsilon_0\omega_n^2/c^2-k_n^2$, $W_{m,n}(x,y)\equiv Y_m(x)J_n(y)-J_m(x)Y_n(y)$, and J_n and Y_n denote the Bessel and Neumann functions. The components of the polarization vectors depend upon the frequency, wave number, and dimensions of the helix and outer cylinder, and are given by

$$R_n(r)=\begin{cases}\dfrac{k_n}{p_n}J_1(p_nr); & \text{I},\\ -\dfrac{k_n}{q_n}J_0(p_nR_h)\dfrac{W_{1,0}(q_nr,q_nR_v)}{W_{0,0}(q_nR_v,q_nR_h)}; & \text{II},\\ 0; & \text{III},\end{cases} \tag{3}$$

$$\Theta_n(r)=\frac{ck_n/\omega_n}{k_hR_h}\begin{cases}\dfrac{J_0(p_nR_h)J_1(p_nr)}{J_1(p_nR_h)}; & \text{I},\\ \dfrac{q_n}{p_n}J_0(p_nR_h)\dfrac{W_{1,1}(q_nR_g,q_nr)}{W_{1,1}(q_nR_g,q_nR_h)}; & \text{II and III},\end{cases} \tag{4}$$

$$Z_n^{(e)}(r)=\begin{cases}J_0(p_nr); & \text{I},\\ J_0(p_nR_h)\dfrac{W_{0,0}(q_nR_v,q_nr)}{W_{0,0}(q_nR_v,q_nR_h)}; & \text{II},\\ 0; & \text{III},\end{cases} \tag{5}$$

$$Z_n^{(b)}(r)=\frac{cp_n/\omega_n}{k_hR_h}\begin{cases}\dfrac{J_0(p_nR_h)J_0(p_nr)}{J_1(p_nR_h)}; & \text{I},\\ \dfrac{q_n}{p_n}J_0(p_nR_h)\dfrac{W_{1,0}(q_nR_g,q_nr)}{W_{1,1}(q_nR_g,q_nR_h)}; & \text{II and III},\end{cases} \tag{6}$$

where region I denotes $0 \leq r < R_h$, region II denotes $R_h \leq r < R_v$, and region III denotes $R_v \leq r \leq R_g$.

It should be noted here that within the vanes in region III the field is azimuthally symmetric, and that $\delta E_r = \delta E_z = \delta B_\theta = 0$. In general, the field within the vanes (and, by extension, the overall field) will contain azimuthal harmonics based upon the number of vanes and the vane spacing. However, we have assumed azimuthal symmetry; this restricts the analysis to the lowest-order azimuthal harmonic, which displays a simple transverse-electric polarization within the vanes.

Energy transport for each wave within the vacuum helix/cylinder is determined by the Poynting flux, the stored energy density, and the group velocity. The Poynting flux for each wave denotes the time-averaged power flux over the entire cross section of the cylinder and helix, and using the fields given in Eqs. (1) can be expressed as

$$S_n = P_n \, \delta\hat{E}_n^2, \tag{7}$$

where

$$\begin{aligned} P_n \equiv \frac{k_n \omega_n R_h^2}{8 p_n^2} \Bigg\{ & \left(\left(1 - \frac{\epsilon_0 p_n^2}{q_n^2} \right) J_0^2(p_n R_h) + \left(J_1^2(p_n R_h) - \frac{\epsilon_0 p_n^2}{q_n^2} J_0^2(p_n R_h) \frac{W_{1,0}^2(q_n R_h, q_n R_v)}{W_{0,0}^2(q_n R_v, q_n R_h)} \right) + \frac{c^2 p_n^2}{\omega_n^2} \frac{1}{k_n^2 R_h^2} \left[\frac{J_0^4(p_n R_h)}{J_1^2(p_n R_h)} \right. \right. \\ & \left. - J_0^2(p_n R_h) \frac{W_{1,0}^2(q_n R_g, q_n R_h)}{W_{1,1}^2(q_n R_g, q_n R_h)} \right] - \frac{2 J_0(p_n R_h)}{p_n R_h} \left(J_1(p_n R_h) + \frac{\epsilon_0 p_n^3}{q_n^3} J_0(p_n R_h) \frac{W_{1,0}(q_n R_h, q_n R_v)}{W_{0,0}(q_n R_v, q_n R_h)} \right) \\ & - \frac{c^2 p_n^2}{\omega_n^2} \frac{2}{k_h^2 R_h^2} \frac{J_0(p_n R_h)}{p_n R_h} \left(\frac{J_0^2(p_n R_h)}{J_1(p_n R_h)} - \frac{p_n}{q_n} J_0(p_n R_h) \frac{W_{1,0}(q_n R_g, q_n R_h)}{W_{1,1}(q_n R_g, q_n R_h)} \right) + \frac{2}{\pi^2} \frac{c^2 p_n^2}{\omega_n^2} \frac{J_0^2(p_n R_h)}{q_n^2 R_h^2} \left(\frac{\epsilon_0 \omega_n^2 / c^2 q_n^2}{W_{0,0}^2(q_n R_v, q_n R_h)} \right. \\ & \left. \left. + \frac{\tan^2 \phi}{W_{1,1}^2(q_n R_g, q_n R_h)} \right) \right). \end{aligned} \tag{8}$$

In addition, the time-averaged energy density per unit axial length over the entire cross section of the helix and cylinder is given by

$$W_n = U_n \, \delta\hat{E}_n^2, \tag{9}$$

where

$$\begin{aligned} U_n \equiv & \frac{\omega_n}{k_n c^2} P_n + \frac{R_h}{4 p_n} J_0(p_n R_h) \left(J_1(p_n R_h) + \frac{\epsilon_0 p_n}{q_n} J_0(p_n R_h) \frac{W_{1,0}(q_n R_h, q_n R_v)}{W_{0,0}(q_n R_v, q_n R_h)} \right) + \frac{R_h^2 (\epsilon_0 - 1)}{8} J_0^2(p_n R_h) \\ & \times \left[\frac{4}{\pi^2 q_n^2 R_h^2} \left(\frac{\epsilon_0 \omega_n^2 / c^2 q_n^2}{W_{0,0}^2(q_n R_v, q_n R_h)} + \frac{\tan^2 \phi}{W_{1,1}^2(q_n R_g, q_n R_h)} \right) - \left(\frac{\epsilon_0 \omega_n^2}{c^2 q_n^2} + \tan^2 \phi \right) - \left(\frac{\epsilon_0 \omega_n^2}{c^2 q_n^2} \frac{W_{1,0}^2(q_n R_h, q_n R_v)}{W_{0,0}^2(q_n R_v, q_n R_h)} \right. \right. \\ & \left. \left. + \tan^2 \phi \frac{W_{1,0}^2(q_n R_g, q_n R_h)}{W_{1,1}^2(q_n R_g, q_n R_h)} \right) - \frac{2}{q_n R_h} \left(\frac{\varepsilon_0 \omega_n^2}{c^2 q_n^2} \frac{W_{1,0}(q_n R_h, q_n R_v)}{W_{0,0}(q_n R_v, q_n R_h)} - \tan^2 \phi \frac{W_{1,0}(q_n R_g, q_n R_h)}{W_{1,1}(q_n R_g, q_n R_h)} \right) \right]. \end{aligned} \tag{10}$$

Finally, the group velocity of each individual wave is given by

$$v_{gr}(k_n) \equiv \frac{\partial \omega_n}{\partial k_n} = \frac{P_n}{U_n}. \tag{11}$$

For convenience, we rewrite the electric and magnetic fields in the form

$$\begin{aligned} \delta\mathbf{E}(\mathbf{x},t) &= \sum_n \left[\delta\hat{E}_n^{(1)} \, \mathbf{e}_n(\mathbf{x},t) + \delta\hat{E}_n^{(2)} \, \mathbf{e}_n^*(\mathbf{x},t) \right], \\ \delta\mathbf{B}(\mathbf{x},t) &= \sum_n \left[\delta\hat{E}_n^{(1)} \, \mathbf{b}_n(\mathbf{x},t) + \delta\hat{E}_n^{(2)} \, \mathbf{b}_n^*(\mathbf{x},t) \right], \end{aligned} \tag{12}$$

where $\delta\hat{E}_n^{(1)} = \delta\hat{E}_n \cos \delta\varphi_n$ and $\delta\hat{E}_n^{(2)} = \delta\hat{E}_n \sin \delta\varphi_n$, and the polarization vectors are given in cylindrical coordinates by

$$\begin{aligned} \mathbf{e}_n(\mathbf{x},t) &\equiv \{ R_n(r)\hat{\mathbf{e}}_r \sin \varphi_n - [\beta_{ph}(k_n)\Theta_n(r)\hat{\mathbf{e}}_\theta - Z_n^{(e)}(r)\hat{\mathbf{e}}_z] \cos \varphi_n \}, \\ \mathbf{b}_n(\mathbf{x},t) &\equiv \{ \Theta_n(r)\hat{\mathbf{e}}_r \cos \varphi_n + [\beta_{ph}(k_n)R_n(r)\hat{\mathbf{e}}_\theta - Z_n^{(b)}(r)\hat{\mathbf{e}}_z] \sin \varphi_n \}, \\ \mathbf{e}_n^*(\mathbf{x},t) &\equiv \{ R_n(r)\hat{\mathbf{e}}_r \cos \varphi_n + [\beta_{ph}(k_n)\Theta_n(r)\hat{\mathbf{e}}_\theta - Z_n^{(e)}(r)\hat{\mathbf{e}}_z] \sin \varphi_n \}, \\ \mathbf{b}_n^*(\mathbf{x},t) &\equiv \{ -\Theta_n(r)\hat{\mathbf{e}}_r \sin \varphi_n + [\beta_{ph}(k_n)R_n(r)\hat{\mathbf{e}}_\theta - Z_n^{(b)}(r)\hat{\mathbf{e}}_z] \cos \varphi_n \}. \end{aligned} \tag{13}$$

Observe that the polarization vectors satisfy the source-free Maxwell equations; hence

$$\nabla\times\mathbf{e}_n=-\frac{1}{c}\frac{\partial}{\partial t}\mathbf{b}_n \quad \text{and} \quad \nabla\times\mathbf{b}_n=\frac{1}{c}\frac{\partial}{\partial t}\mathbf{e}_n, \tag{14}$$

as well as

$$\nabla\times\mathbf{e}_n^*=-\frac{1}{c}\frac{\partial}{\partial t}\mathbf{b}_n^* \quad \text{and} \quad \nabla\times\mathbf{b}_n^*=\frac{1}{c}\frac{\partial}{\partial t}\mathbf{e}_n^*. \tag{15}$$

C. The dynamical equations for the fields

In order to treat the variation in the radial mode structure as well as the axial and temporal evolution of the wave(s), we represent the electromagnetic field in terms of the superposition given in Eqs. (12) under the assumption that the mode amplitudes vary more slowly in z and t [i.e., $\delta\hat{E}_n^{(1)}=\delta\hat{E}_n^{(1)}(z,t)$, and $\delta\hat{E}_n^{(2)}=\delta\hat{E}_n^{(2)}(z,t)$]. This spatial and temporal variation in the wave amplitudes describes the propagation of a pulse through either a vacuum helix or in the presence of an electron beam subject to (1) the dispersion of the waves in a sheath helix, and (2) the variations in the radial inhomogeneities of each wave with frequency.

The dynamical equations for the wave amplitudes are obtained in a manner analogous to the derivation of Poynting's theorem. Bearing in mind that $\mathbf{e}_n(\mathbf{x},t)$ and $\mathbf{b}_n(\mathbf{x},t)$ satisfy Maxwell equations in the absence of a source, Ampère's law is of the form

$$\sum_n\left(\hat{\mathbf{e}}_z\times\mathbf{b}_n\frac{\partial}{\partial z}\delta\hat{E}_n^{(1)}-\mathbf{e}_n\frac{\partial}{\partial t}\delta\hat{E}_n^{(1)}\right)+\sum_n\left(\hat{\mathbf{e}}_z\times\mathbf{b}_n^*\frac{\partial}{\partial z}\delta\hat{E}_n^{(2)}-\mathbf{e}_n^*\frac{\partial}{\partial t}\delta\hat{E}_n^{(2)}\right)=\frac{4\pi}{c}\mathbf{J}(\mathbf{x},t), \tag{16}$$

and Faraday's law is

$$\sum_n\left(\hat{\mathbf{e}}_z\times\mathbf{e}_n\frac{\partial}{\partial z}\delta\hat{E}_n^{(1)}+\mathbf{b}_n\frac{\partial}{\partial t}\delta\hat{E}_n^{(1)}\right)+\sum_n\left(\hat{\mathbf{e}}_z\times\mathbf{e}_n^*\frac{\partial}{\partial z}\delta\hat{E}_n^{(2)}+\mathbf{b}_n^*\frac{\partial}{\partial t}\delta\hat{E}_n^{(2)}\right)=0, \tag{17}$$

where $\mathbf{J}(\mathbf{x},t)$ denotes the microscopic source current. The dynamical equations for the fields are obtained in a manner analogous to the derivation of Poynting's equation by (1) taking the inner product of $\mathbf{b}_m$ (and $\mathbf{b}_m^*$) with Faraday's law (17) and $\mathbf{e}_m$ (and $\mathbf{e}_m^*$) with Ampère's law (16); (2) subtracting the equations; (3) integrating the result over the entire cross section of the helix and cylinder; and (4) averaging the result over the axial length $2\pi/\Delta k$. Observe that for a single wave, this scale length is just the wavelength. The average diagonalizes the equations so that the evolution of each $\delta\hat{E}_n^{(i)}$ satisfies equations of the form

$$\left(\frac{\partial}{\partial t}+v_{\mathrm{gr}}(k_n)\frac{\partial}{\partial z}\right)\delta\hat{E}_n^{(1)}=\frac{2\Delta k}{cU_n}\int_0^{2\pi/\Delta k}dz'\int\int_{A_h}dx\,dy\,\mathbf{J}(x,y,z',t)\cdot\mathbf{e}_n(x,y,z',t),$$
$$\left(\frac{\partial}{\partial t}+v_{\mathrm{gr}}(k_n)\frac{\partial}{\partial z}\right)\delta\hat{E}_n^{(2)}=\frac{2\Delta k}{cU_n}\int_0^{2\pi/\Delta k}dz'\int\int_{A_h}dx\,dy\,\mathbf{J}(x,y,z',t)\cdot\mathbf{e}_n^*(x,y,z',t), \tag{18}$$

where A_h denotes the cross-sectional area enclosed by the helix. This equation describes the propagation of a pulse, or pulses, through the helix/cylinder at the appropriate group velocities. Intermodulation between the various waves is implicitly included through the particle trajectories.

D. The case of a tapered helix

This model can be adapted to treat the case of a helix with a spatially varying period by the relatively simple expedient of allowing the helix wave number to vary in z and recalculating the wave number, group velocity, and the Poynting flux, and energy density of each wave as a function of axial position. In so doing, we neglect any reflected waves that might result from the tapered helix. In practice, this is equivalent to the assumption that the variation in the wavelength that results from the tapered helix period varies slowly in comparison with the wavelengths of interest; hence, $\lambda\gg\Delta z(d\lambda/dz)$.

Using this procedure, we observe that there will be a gradient in the vacuum fields $\mathbf{e}_n$ and $\mathbf{b}_m$ due to the taper. As a result, the vacuum fields satisfy the modified equations

$$\nabla\times\mathbf{e}_n+\frac{1}{c}\frac{\partial}{\partial t}\mathbf{b}_n=h_n, \tag{19}$$

$$\nabla\times\mathbf{b}_n-\frac{1}{c}\frac{\partial}{\partial t}\mathbf{e}_n=g_n, \tag{20}$$

$$\nabla\times\mathbf{e}_n^*+\frac{1}{c}\frac{\partial}{\partial t}\mathbf{b}_n^*=h_n^*, \tag{21}$$

$$\nabla\times\mathbf{b}_n^*-\frac{1}{c}\frac{\partial}{\partial t}\mathbf{e}_n^*=g_n^*, \tag{22}$$

where

$$\mathbf{h}_n(\mathbf{x},t)\equiv\frac{\partial(\beta_{\rm ph}\Theta_n)}{\partial z}\,\hat{\mathbf{e}}_r\cos\varphi_n-\frac{\partial R_n}{\partial z}\,\hat{\mathbf{e}}_\theta\sin\varphi_n, \tag{23}$$

$$\mathbf{g}_n(\mathbf{x},t)\equiv\frac{\partial(\beta_{\rm ph}R_n)}{\partial z}\,\hat{\mathbf{e}}_r\sin\varphi_n-\frac{\partial\Theta_n}{\partial z}\,\hat{\mathbf{e}}_\theta\cos\varphi_n, \tag{24}$$

$$\mathbf{h}_n^*(\mathbf{x},t)\equiv-\frac{\partial(\beta_{\rm ph}\Theta_n)}{\partial z}\,\hat{\mathbf{e}}_r\sin\varphi_n+\frac{\partial R_n}{\partial z}\,\hat{\mathbf{e}}_\theta\cos\varphi_n, \tag{25}$$

$$\mathbf{g}_n^*(\mathbf{x},t)\equiv\frac{\partial(\beta_{\rm ph}R_n)}{\partial z}\,\hat{\mathbf{e}}_r\cos\varphi_n+\frac{\partial\Theta_n}{\partial z}\,\hat{\mathbf{e}}_\theta\sin\varphi_n, \tag{26}$$

and this reflects the effect of the variation in the wave number with axial position on the polarization vectors. Following the same procedure outlined above, we find that the dynamical equations for a tapered helix can be expressed in the relatively simple form

$$\left(\frac{\partial}{\partial t}+v_{\rm gr}(k_n)\,\frac{\partial}{\partial z}\right)(P_n^{1/2}\,\delta\hat{E}_n^{(1)})=\frac{2\,\Delta k\,P_n^{1/2}}{cU_n}\int_0^{2\pi/\Delta k}dz'\int\int_{A_h}dx\,dy\,\mathbf{J}(x,y,z',t)\cdot\mathbf{e}_n(x,y,z',t),$$

$$\left(\frac{\partial}{\partial t}+v_{\rm gr}(k_n)\,\frac{\partial}{\partial z}\right)(P_n^{1/2}\,\delta\hat{E}_n^{(2)})=\frac{2\,\Delta k\,P_n^{1/2}}{cU_n}\int_0^{2\pi/\Delta k}dz'\int\int_{A_h}dx\,dy\,\mathbf{J}(x,y,z',t)\cdot\mathbf{e}_n^*(x,y,z',t). \tag{27}$$

E. Electron dynamics

The electron dynamics are treated using the full three-dimensional relativistic Lorentz force equations. Azimuthal symmetry is imposed in the sense (1) that the beam distribution upon entry to the helix is azimuthally symmetric, and (2) that each of the vector components of the electromagnetic fields varies only in (r,z,t). With this in mind, we integrate the Lorentz force equation for each electron in the simulation subject to both the external axial magnetic field and the electromagnetic fields. Hence

$$\frac{d}{dt}\,\mathbf{p}=-e\,\left[\delta\mathbf{E}(\mathbf{x},t)-\frac{e}{c}\,\mathbf{v}\times[B_0\hat{\mathbf{e}}_z+\delta\mathbf{B}(\mathbf{x},t)]\right]. \tag{28}$$

The initial conditions on the ensemble of electrons reflects the specific pulse structure of interest. Thus, electrons are injected into the interaction region at uniform time intervals for a continuous beam, and at periodic but nonuniform intervals for an emission-gated beam. The specific algorithms used for these purposes are described in the following section.

One important restriction in the present analysis is that the fluctuating rf space-charge fields are not explicitly included. Hence, the analysis is strictly valid only subject to the neglect of the positive and negative beam space-charge waves (i.e., the ballistic regime in which the Pierce gain parameter is small). Similarly, the effect of the dc self-electric and self-magnetic fields are also neglected. The inclusion of the rf space-charge and dc self-fields are presently under study.

III. NUMERICAL ANALYSIS

Equations (18) [or (27) for a tapered helix] are solved for a system of length L on a grid with spacing Δz over a time step Δt using the MacCormack method.[21] The microscopic source current is represented as

$$\mathbf{J}(\mathbf{x},t)=-q\sum_{i=1}^{N}v_i(t)\,\delta[x-x_i(t)]\,\delta[y-y_i(t)]\times S[z-z_i(t)], \tag{29}$$

where N is the number of electrons in the system at time t, $(\mathbf{x}_i,\mathbf{v}_i)$ represents the location and velocity of the ith electron at time t, q is the charge per electron, and S is the shape function. The *shape function* describes the interpolation of the electron charge to the grid locations. We use a triangular shape algorithm,

$$S(z-z_i)=\begin{cases}\dfrac{z-z_i+\Delta z}{\Delta z^2}; & z_i-\Delta z\leq z\leq z_i,\\[2ex] -\dfrac{z-z_i-\Delta z}{\Delta z^2}; & z_i<z\leq z_i+\Delta z,\end{cases} \tag{30}$$

which provides a linear weighting in which the charge is mapped onto the two nearest neighbor grid points. The charge per electron includes a weight factor dependent upon the beam current. Since we are injecting electrons on each time step, we choose

$$q=\frac{I_b\,\Delta t}{N_{\Delta t}}, \tag{31}$$

where I_b is the beam current injected over each specific time step and $N_{\Delta t}$ is the number of electrons injected per time step. Note that the charge per electron injected during each time step is found using the average current for a continuous beam, while this current will vary depending upon the bunch shape for an emission-gated beam. As a result, the dynamical equations for the field amplitudes are

$$\left(\frac{\partial}{\partial t}+v_{\rm gr}(k_n)\,\frac{\partial}{\partial z}\right)(P_n^{1/2}\,\delta\hat{E}_n^{(1)})=-\frac{2q\,\Delta k\,P_n^{1/2}}{cU_n}\sum_{i=1}^{N}\int_0^{2\pi/\Delta k}dz'\,S(z'-z_i)\mathbf{v}_i(t)$$

$$\cdot \mathbf{e}_n(x_i, y_i, z', t).$$

$$\left(\frac{\partial}{\partial t} + v_{gr}(k_n)\frac{\partial}{\partial z}\right)(P_n^{1/2}\,\delta\hat{E}_n^{(2)})$$

$$= -\frac{2q\,\Delta k\,P_n^{1/2}}{cU_n}\sum_{i=1}^{N}\int_0^{2\pi/\Delta k} dz'\,S(z'-z_i)\mathbf{v}_i(t)$$

$$\cdot \mathbf{e}_n^*(x_i, y_i, z', t). \tag{32}$$

Open boundary conditions for the field are imposed at both $z=0$ and L.

The orbit equations are integrated by means of a fourth-order Runge–Kutta algorithm. In order to be consistent with the electron shape function that maps electron charge onto the grid, we use a linear interpolation scheme to map the field amplitude from the grid to the particle locations.

The sequence of operations used in integrating the field and orbit equations are as follows. We first calculate the sources by accumulating electron charge to the grid and averaging over the appropriate scale length and then step the fields using the MacCormack method. Once the updated fields are calculated, we then step the electron trajectories. This procedure is repeated over the time scale of interest.

A. Injection of electromagnetic waves

TWTs are typically operated as amplifiers in which the electron beam has a continuous pulse format and an injected signal is amplified over the length of the helix. In order to model this configuration, we must specify an algorithm for the injection of a signal(s). For this purpose, we can inject a pulse with arbitrary start, rise, flat and fall times in the following way. We assume that a pulse is injected at $z=-\Delta z$ and allowed to propagate into the interaction region. The pulse has a smooth temporal shape given by

$$\delta\hat{E}_n^{(1)}(z=-\Delta z,t) = \delta\hat{E}_0^{(1)}\begin{cases} 0; & t<\tau_{\text{start}}, \\ \sin^2\left(\frac{\pi}{2}\frac{(t-\tau_{\text{start}})}{\Delta\tau_{\text{rise}}}\right); & \tau_{\text{start}}\le t<\tau_{\text{rise}}, \\ 1; & \tau_{\text{rise}}\le t<\tau_{\text{flat}}, \\ \cos^2\left(\frac{\pi}{2}\frac{(t-\tau_{\text{fall}})}{\Delta\tau_{\text{fall}}}\right); & \tau_{\text{flat}}\le t\le\tau_{\text{fall}}, \\ 0; & t>\tau_{\text{fall}}, \end{cases} \tag{33}$$

and $\delta\hat{E}_n^{(2)}(z=-\Delta z,t)=0$ for all t, where $\delta\hat{E}_0^{(1)}$ is chosen to describe the peak power via Eq. (7), τ_{start} denotes the start time of the pulse, $\Delta\tau_{\text{rise}}$ is the rise time of the pulse, $\tau_{\text{rise}}=\tau_{\text{start}}+\Delta\tau_{\text{rise}}$ is the time at which the pulse has risen to its peak value, $\tau_{\text{flat}}-\tau_{\text{rise}}$ is the time interval over which the pulse retains a constant magnitude, $\Delta\tau_{\text{fall}}$ is the time interval over which the pulse falls to zero, and $\tau_{\text{fall}}=\tau_{\text{flat}}+\Delta\tau_{\text{fall}}$ is the time after which the injected pulse vanishes. Note that the injection of power at $z=-\Delta z$ requires the inclusion of a guard cell in the grid outside the interaction region

Observe that this form gives us great flexibility in the pulse format. For example, a square pulse can be injected by the simple expedient of allowing $\Delta\tau_{\text{rise}}=\Delta\tau_{\text{fall}}=0$, and a constant drive power can be imposed by the further requirement that τ_{flat} equal the entire pulse time. In addition, a single well-defined pulse can be injected by requiring that $\Delta\tau_{\text{rise}}=\Delta\tau_{\text{fall}}$ and that $\tau_{\text{flat}}=\tau_{\text{rise}}$. This same model is used for the injection of either single or multiple waves.

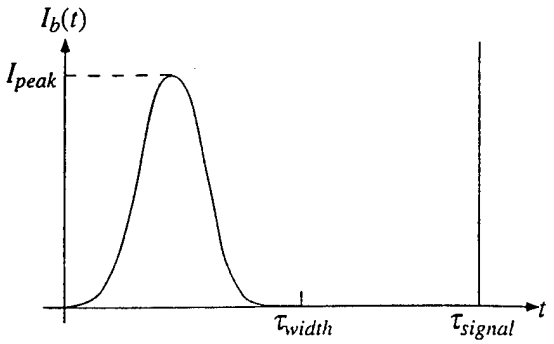

FIG. 3. Schematic illustration of the pulse shape in an emission-gated beam.

B. Injection of the electron beam

The models of electron injection are chosen to correspond to either a continuous electron beam or an emission-gated beam. In the case of the continuous pulse, electrons are injected at the start of each time step. The charge per electron is calculated using Eq. (31) and we allow for an arbitrary current rise time by choosing a current of the form

$$I_b(t)=\begin{cases} I_b\sin^2\left(\frac{\pi}{2}\frac{t}{\tau_r}\right); & t\le\tau_r, \\ I_b; & t>\tau_r, \end{cases} \tag{34}$$

where τ_r denotes the rise time of the beam.

A schematic for a single beam pulse for an emission-gated beam is shown in Fig. 3. In the case of an emission-gated beam, bunching is assumed to occur prior to injection into the helix. This may be accomplished, for example, by a periodic signal applied to a gridded cathode. The detailed pulse shape we use is one in which beam pulses repeat over a period τ_{signal} ($\equiv 1/f$, where f is the signal frequency), and in which the beam is "on" only over a time τ_{width} ($\le\tau_{\text{signal}}$). This is illustrated schematically in Fig. 3. The detailed shape of the current pulse used for the emission over each wave period is

$$I_b(t)=\begin{cases} I_{\text{peak}}\sin^2\left(\frac{\pi}{2}\frac{t}{\tau_{\text{width}}}\right); & 0\le t\le\tau_{\text{width}}, \\ 0; & \tau_{\text{width}}<t\le\tau_{\text{signal}}. \end{cases} \tag{35}$$

The average current for this specific beam pulse shape is given by

$$\frac{I_{\text{avg}}}{I_{\text{peak}}}=\frac{\tau_{\text{width}}}{2\tau_{\text{signal}}}, \tag{36}$$

so that the width of the pulse can be determined by the specification of the frequency of the bunching and the ratio of the average to peak currents. Note that no drive power is required for the electromagnetic waves for the emission-gated beam.

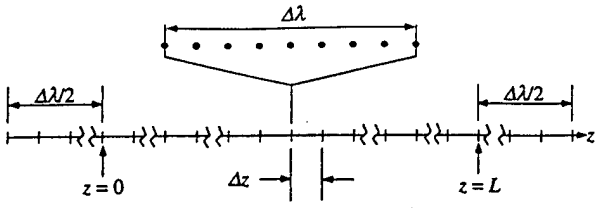

FIG. 4. Schematic illustration of the mapping of charge to the grid and the current average.

As mentioned previously, the sources are determined by first mapping the charge from each electron to the two nearest-neighbor grid points and then averaged over a length $\Delta\lambda$. The specific procedure we employ for this is a "moving-window" average in which the sources at the ith grid cell are determined by averaging over those grid cells within a length $\pm\Delta\lambda/2$ on either side. For example, if $\Delta z=\Delta\lambda/N$ for N even, then the sources at the ith grid cell are determined by averaging the charge over all grid cells within $i\pm N/2$. This necessitates the inclusion of $N/2$ guard cells corresponding to $z<0$ and $z>L$. Thus, electrons are injected at $z=-\Delta\lambda/2$ and allowed to propagate ballistically until they reach $z=0$, at which point the interaction with the radiation is "turned on." Similarly, the electrons also propagate ballistically (i.e., the interaction with the radiation is "turned off") when the electrons exit the interaction region at $z=L$. This is illustrated schematically in Fig. 4. Electrons are ejected form the simulation whenever they pass beyond $z=L+\Delta\lambda/2$ or intersect the radial position of the helix. This procedure is also employed in the case of a tapered helix with the generalization that the averaging length varies with axial position corresponding to the variation in the wavelength(s).

One further point deserves mention before we turn to a discussion of the results of the simulation. Since charge is mapped onto the two nearest neighbor grid cells, the end cells of the average corresponding to the ith grid cell (i.e., the grid cells at $i\pm N/2$) will contain contributions from charges outside the length $\Delta\lambda$. This introduces an additional oscillation with a period of $\Delta\lambda+2\Delta z$ into the sources that must be filtered out.

C. Propagation in a vacuum helix

We first consider propagation of a single pulse through the vacuum helix (i.e., in the absence of the electron beam). The circuit parameters we choose to study correspond to a helix TWT built at Northrop–Grumman Corp.[22] A schematic of the cross section of this tube is shown in Fig. 5. The helix and wall radii were 0.12446 and 0.2794 cm, respectively, and the helix period was 0.080 137 cm. The helix was supported by three dielectric rods with rectangular cross sections running the length of the helix. The dielectric constant of the rods was 6.5 and the rod dimensions were 0.0508 cm $\times$0.147 32 cm. No vanes were used in this structure.

The cold dispersion solutions have been compared with the measured dispersion of this TWT. In order to test the utility of the present model in describing a real circuit, we varied ϵ_0 in the present model to determine the level of agreement that could be achieved over a broad bandwidth.

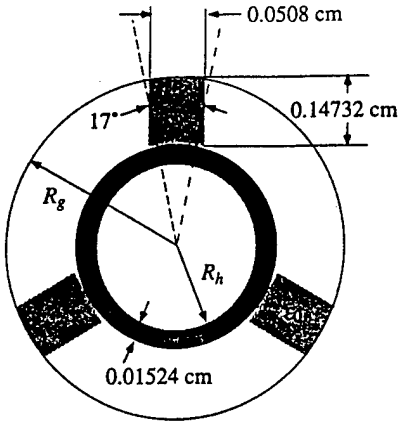

FIG. 5. Schematic illustration of the Northrop–Grumman helix TWT.

The results of this comparison were discussed in detail in a prior publication[10] and are shown in Fig. 6, where we plot the variation in the phase velocity versus frequency as calculated using the cold helix dispersion equation (2) and as measured (dots) over frequencies up to 7.5 GHz for $\epsilon_0=1.75$. It is evident from the figure that the agreement is very good over a broadband of frequencies extending from 3 up to 7 GHz, and we conclude that the effect of the dielectric rods can be modeled using the uniform dielectric loading with an effective dielectric constant of 1.75.

The effective dielectric constant used above can be estimated in a straightforward manner under the assumptions that the effect of the rods do not greatly perturb the field structures and that the field is approximately parallel to the rods. As such, the effective dielectric constant can be determined from an estimate of the energy densities in the stored fields in the vacuum and the dielectric, and the effective dielectric constant is given by a volume-weighted average in which $\epsilon_{\text{eff}}\approx(V_{\text{rod}}\epsilon_{\text{rod}}+V_{\text{vac}})/V_{\text{tot}}$, where V_{rod} and ϵ_{rod} are the volume and dielectric constant of the rod, V_{vac} is the volume of the vacuum in the gap between the helix and the outer wall, and V_{tot} is the total volume in the gap between the helix and the wall. Of course, this formula is expected to yield only an approximation to the effective dielectric constant.

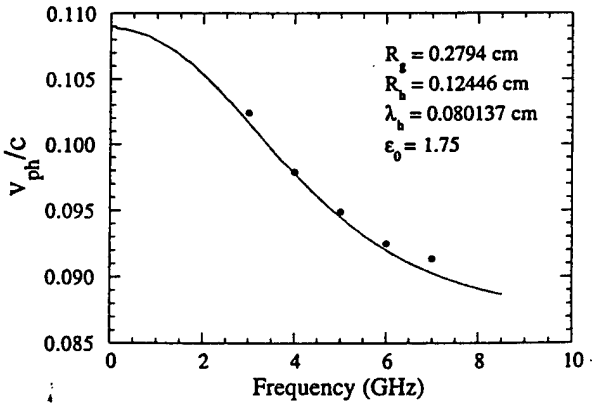

FIG. 6. Comparison of the dispersion in the cold Northrop-Grumman circuit with the solution of the cold helix dispersion equation.

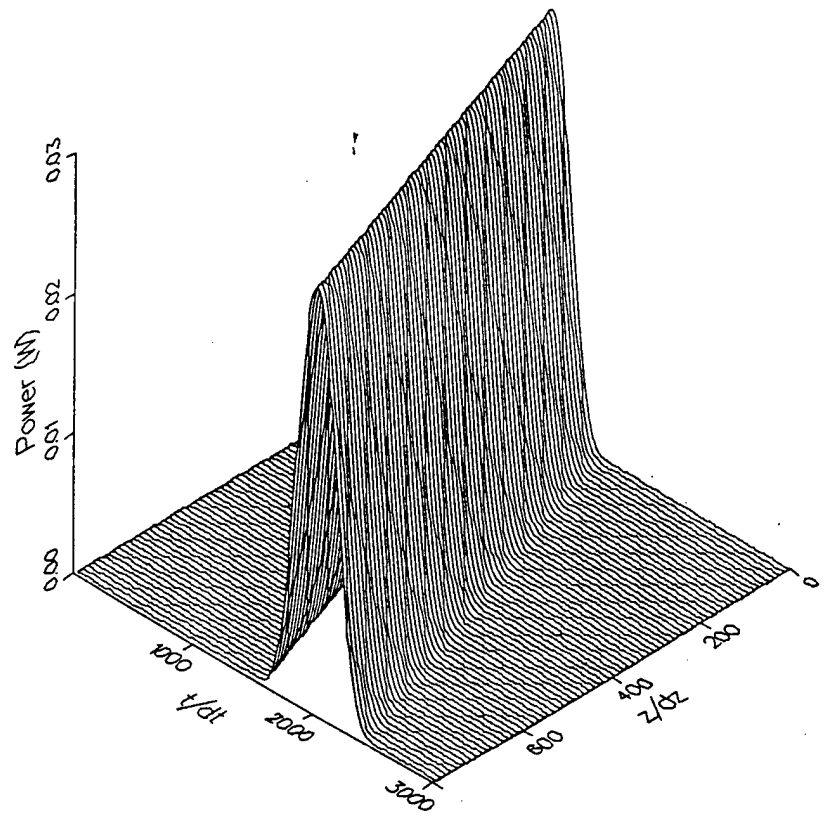

FIG. 7. Perspective plot of the propagation of a pulse through a vacuum helix.

For the parameters of interest, however, we find that $\epsilon_{\text{eff}} \approx 1.66$, which is reasonably close to the value of 1.75 found above.

In propagating a pulse through this helix, we inject a signal with a pulse shape given in Eq. (33) at $t=0$ with a frequency of 5 GHz and a peak power level of 30 mW and a rise and fall time of 1 ns (note that this implies that $\tau_{\text{start}}=0$, $\Delta\tau_{\text{rise}}=\Delta\tau_{\text{fall}}=\tau_{\text{rise}}=\tau_{\text{flat}}=1$ ns, and $\tau_{\text{fall}}=2$ ns). A perspective plot showing the propagation of this pulse through the helix versus both z and t is shown in Fig. 7. It is evident from the figure that the pulse propagates through the helix at the group velocity and with negligible distortion.

D. Continuous beam case—Uniform helix

The continuous beam example we consider corresponds to the TWT built at Northrop–Grumman discussed previously in regard to the propagation of a pulse through the vacuum helix. Gain was measured in this TWT over a frequency range of 3–7 GHz using a 2.84 kV/0.17 A electron beam with a radius of 0.0495 cm. However, direct comparison of the measured gain of this tube with the nonlinear theory is not possible since space-charge effects were important but are not presently included in the nonlinear formulation. A linear theory of the interaction, which did include space-charge effects, however, was in substantial agreement with the observed gain.[10] Hence, we choose to compare the results of the nonlinear simulation for these helix/beam parameters with the aforementioned linear theory subject to the neglect of the space-charge contribution. This will give us a measure of the accuracy of the nonlinear formulation in the absence of space-charge forces.

The linear dispersion equation in the absence of vane loading is of the form[10]

$$\Lambda(\omega,k)\epsilon_{sc}(\omega,k)=-\frac{\omega_b^2\sigma_b}{4\gamma_0^2c^2}\frac{\omega^2}{c^2}p^2\frac{J_0^2(pR_b)}{J_0(pR_h)J_0(pR_g)}W_{0,0}(pR_g,pR_h), \tag{37}$$

where this describes the case of an annular electron beam with a radius R_b, $\sigma_b=2\pi R_b\,\Delta R_b$, $\sigma_b=2\pi R_b\,\Delta R_b$ is the cross-sectional area of the beam, ω_b is the beam plasma frequency, $\gamma_0=(1-v_b^2/c^2)^{-1/2}$,

$$\Lambda(\omega,k)\equiv\frac{\omega^2}{c^2}-\frac{pq}{k_h^2R_h^2}\frac{J_0(pR_h)}{J_1(pR_h)}\frac{W_{0,0}(qR_g,qR_h)}{W_{1,1}(qR_g,qR_h)}\frac{[pJ_0(pR_h)W_{1,1}(qR_g,qR_h)-qJ_1(pR_h)W_{1,0}(qR_g,qR_h)]}{[qJ_1(pR_h)W_{0,0}(qR_g,qR_h)+\epsilon_0pJ_0(pR_h)W_{1,0}(qR_h,qR_g)]}, \tag{38}$$

describes the vacuum helix dispersion function, and

$$\epsilon_{sc}(\omega,k)\equiv\frac{\Delta\omega^2}{c^2}-\frac{\omega_b^2\sigma_b}{4\gamma_0^2c^2}p^2\frac{J_0(pR_b)}{J_0(pR_h)}W_{0,0}(pR_b,pR_h), \tag{39}$$

describes the dielectric function of the beam space-charge waves for $\Delta\omega=\omega-kv_b$ corresponding to a beam velocity v_b. This linear theory corresponds to the case of a strongly magnetized beam.

Equation (37) describes the interaction in terms of the coupling of the vacuum helix mode with the beam space-charge mode. It can be expressed in the conventional form of the Pierce dispersion equation by making a near-resonant approximation in which $\omega\approx kv_b$ after which we obtain

$$(k^2-k_0^2)[\Delta\omega^2-4QC^3k^2v_b^2]=2C^3\omega k_0kv_b, \tag{40}$$

where

$$k_0^2\equiv\frac{\omega^2}{c^2}\left(1-k_h^2R_h^2\frac{p_e}{q_e}\frac{J_1(p_eR_h)}{J_0(p_eR_h)}\frac{W_{1,1}(q_eR_g,q_eR_h)}{W_{0,0}(q_eR_g,q_eR_h)}\frac{[q_eJ_1(p_eR_h)W_{0,0}(q_eR_g,q_eR_h)+\epsilon_0p_eJ_0(p_eR_h)W_{1,0}(q_eR_h,q_eR_g)]}{[p_eJ_0(p_eR_h)W_{1,1}(q_eR_g,q_eR_h)-q_eJ_1(p_eR_h)W_{1,0}(q_eR_g,q_eR_h)]}\right), \tag{41}$$

describes the wave number in the vacuum helix, $p_e=i\omega/\gamma_0v_b$, $q_e=i\omega(1-\epsilon_0v_b^2/c^2)^{1/2}/v_b$, and the Pierce Q and C parameters are given by

$$C^3\equiv-\frac{\omega_b^2\sigma_b}{4\pi\gamma_0^4c^2}\frac{k_h^2R_h^2}{p_eR_h}\frac{J_0^2(p_eR_b)}{J_0^2(p_eR_h)}\frac{p_eJ_1(p_eR_h)W_{1,1}(q_eR_g,q_eR_h)}{p_eJ_0(p_eR_h)W_{1,1}(q_eR_g,q_eR_h)-q_eJ_1(p_eR_h)W_{1,0}(q_eR_g,q_eR_h)}, \tag{42}$$

$$Q\equiv\frac{\pi}{4\beta_0^2}\frac{p_eR_h}{k_h^2R_h^2}\frac{J_0(p_eR_h)}{J_0(p_eR_b)}W_{0,0}(p_eR_b,p_eR_h)\frac{p_eJ_0(p_eR_h)W_{1,1}(q_eR_g,q_eR_h)-q_eJ_1(p_eR_h)W_{1,0}(q_eR_g,q_eR_h)}{p_eJ_1(p_eR_h)W_{1,1}(q_eR_g,q_eR_h)}, \tag{43}$$

and $\beta_0\equiv v_b/c$. Space-charge effects can be neglected when $|\Delta\omega^2|\gg 4|QC^3k^2v_b^2|$ and the term in QC^3 can be neglected. Physically, this corresponds to the regime in which the space-charge potential is too weak to significantly modify the effect of the vacuum helix wave on the electron trajectories. Solution of the dispersion equation indicates that the space-charge forces can be neglected when the Q and C parameters satisfy the inequality[8]

$$|C^3|\ll\frac{(1+8|Q|)^2}{4|Q|}. \tag{44}$$

Calculation indicates that this condition is not satisfied in the Northrop–Grumman TWT, and that space-charge forces are important in the description of that tube.

The effect of space charge on gain of the Northrop–Grumman TWT can also be gauged by comparison of the linear growth rate as calculated by the complete dispersion equation (37) and by a reduced dispersion equation found by neglecting the space-charge terms. This reduced dispersion equation is found in the limit in which $\epsilon_{sc}\to\Delta\omega^2/c^2$, and is equivalent to the neglect of the terms in QC^3 in the reduced Pierce form of the dispersion equation. This dispersion equation is of the form

$$\Lambda(\omega,k)=-\frac{\omega_b^2\sigma_b}{4\gamma_0^2c^2}\frac{\omega^2}{\Delta\omega^2}p^2\frac{J_0^2(pR_b)}{J_0(pR_h)J_0(pR_g)}\times W_{0,0}(pR_g,pR_h). \tag{45}$$

Collective space-charge effects generally act to reduce the gain of a device since they degrade the interaction between the beam and the vacuum mode, and this case is no exception. The maximum gain, both as calculated by the general dispersion equation (37) and measured in the TWT, is approximately 6.1 dB/cm at a frequency of 5.4 GHz. In contrast, the solution of the dispersion equation (45) in the absence of space-charge forces yields a maximum gain of 7.5 dB/cm at a frequency of 4.5 GHz.

In addition to obtaining the linear growth rate from Eq. (45), we can also estimate the nonlinear efficiency by phase trapping arguments. Specifically, that at saturation the beam electrons will lose an amount of energy corresponding to a deceleration of $2\Delta v$, where $\Delta v=v_b-v_{ph}$ and v_{ph} is the phase velocity of the wave. This technique was originally formulated by Slater for traveling wave tubes,[23] but has also been used successfully for free-electron lasers[16] and gives a predicted efficiency of

$$\eta\approx\frac{2\gamma^3}{\gamma-1}\frac{v_b}{c}\left(\frac{v_b}{c}-\frac{v_{ph}}{c}\right). \tag{46}$$

Hence, the solution of Eq. (45) in the presence of the beam will also allow us to estimate the nonlinear efficiency.

A plot of the solution of Eq. (45) for the gain and efficiency corresponding to the Northrop–Grumman parameters is shown in Fig. 8. Since this is an annular beam theory, we have chosen to use the rms beam radius (0.035 cm). As shown in the figure, gain is found over frequencies up to 7 GHz, with the peak gain of approximately 7.5 dB/cm occurring at a frequency of about 4.5 GHz. The efficiency increases with frequency over this band and reaches a maximum of about 40% at 7 GHz.

Although the application of the nonlinear theory in the absence of space-charge effects is unphysical for the

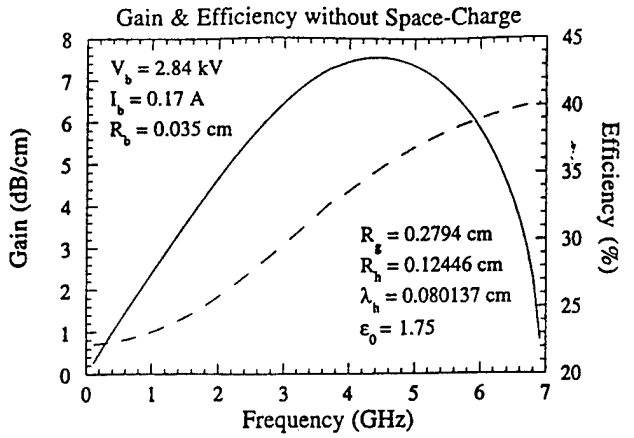

FIG. 8. Plots of the gain (solid line) and efficiency (dashed line) for the parameters of the Northrop–Grumman TWT in the absence of space-charge effects.

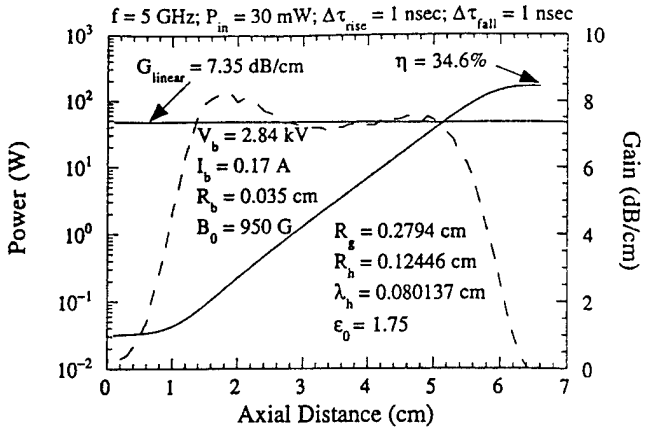

FIG. 9. Plots of the gain (dashed line) and power (solid line) versus axial distance from the nonlinear simulation.

Northrop–Grumman TWT, the comparison with the linear predictions in the absence of space-charge affords another test of the validity of the nonlinear model.

We now turn to the nonlinear simulation of this example. For purposes of comparison, we choose the same circuit parameters for the helix, wall, and dielectric constant as used in the cold circuit dispersion comparison in Fig. 6 and in the linear theory in Fig. 8. The beam is assumed to have a continuous pulse structure with a voltage and current of 2.84 kV/0.17 A, and we inject an annular beam with a radius of 0.035 cm. A magnetic field of 950 G was used. The beam rise time is 1 ns. We inject a single pulse of radiation at 5 GHz, which is identical to that propagated previously through the vacuum helix with a peak power level of 30 mW, except that we start the pulse after 1 ns (i.e., τ_{start}=1 ns corresponding to the end of the beam rise time), and a 1 ns rise and fall time. The results showing the evolution of the gain and power as a function of axial position are shown in Fig. 9.

It is evident from Fig. 9 that saturation occurs over a length of approximately 6.5 cm at a power level of approximately 167 W for an efficiency of 34.6%. This is in good agreement with the efficiency estimate shown in Fig. 7, which yields an efficiency of about 36% at 5 GHz. As shown in the figure, the linear gain is also in substantial agreement

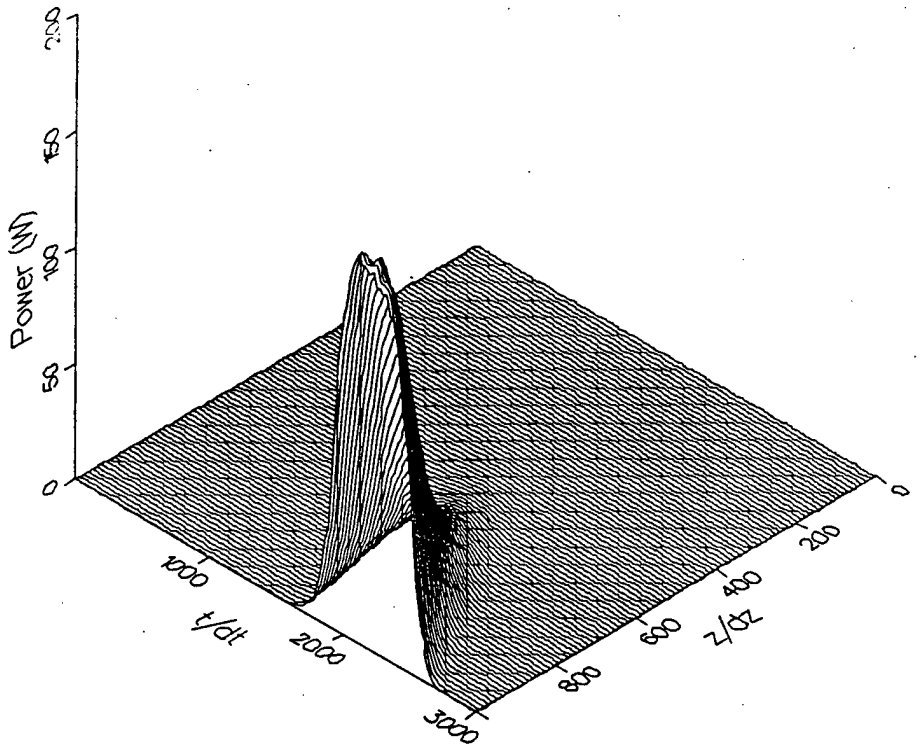

FIG. 10. Perspective plot of the evolution of the injected signal as it propagates through the helix subject to amplification by the beam.

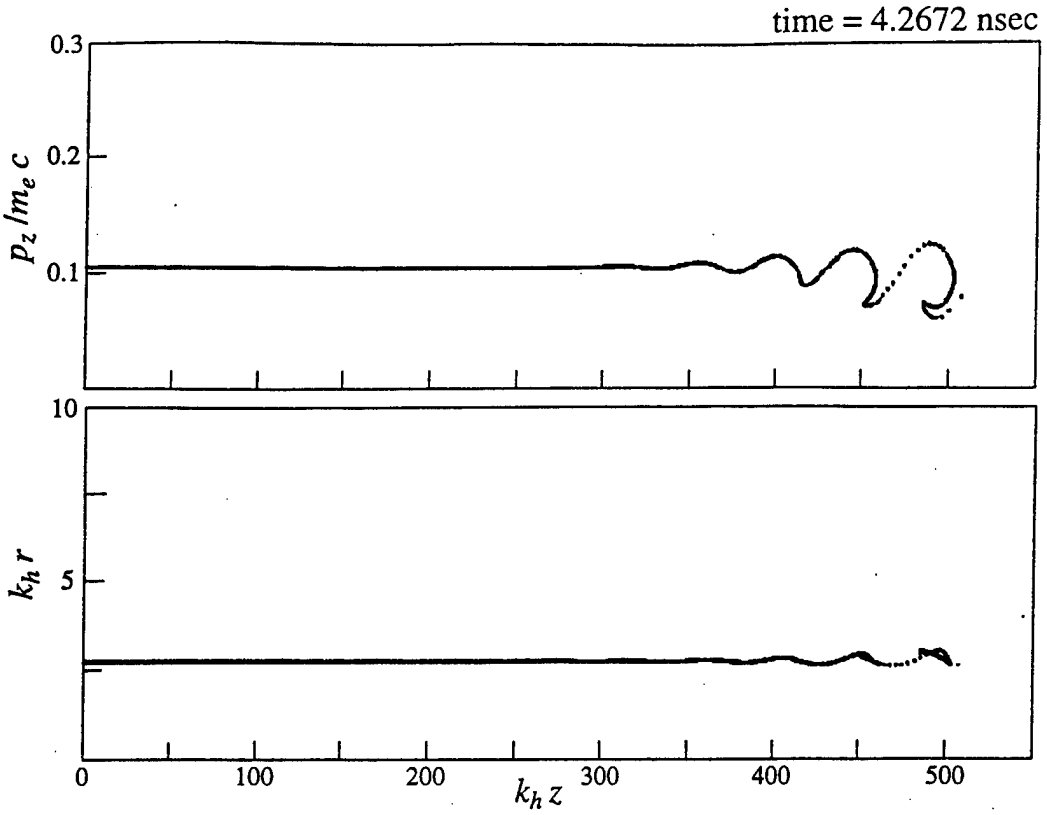

FIG. 11. Plots showing the axial evolution of the phase space and radial structure of electron beam.

with the prediction of the linear theory of a gain of 7.35 dB/cm at 5 GHz. A perspective plot of the evolution of the injected signal as it propagates through the helix subject to amplification by the electron beam is shown in Fig. 10.

Plots of the particle evolution in phase space and in radial position as the beam propagates through the helix are shown in Fig. 11, which is a snapshot of the interaction region once the power has saturated. It is clear from the figure that saturation is by electron trapping in the troughs of the wave and occurs at $k_h z \approx 500$, and that there has been some bunching and overtaking of the beam electrons as they become trapped.

E. Continuous beam case—Tapered helix

In treating a tapered helix, we consider the efficiency enhancements possible for the case considered previously for the uniform helix. The efficiency saturates in a uniform helix after the electrons become trapped in the troughs of the wave, and a state is reached where the number of electrons being decelerated by the wave (and thereby losing energy) is compensated by a similar number of electrons, which are being accelerated by the wave (and gaining energy). At this point the efficiency can be enhanced by decelerating the wave through a downward taper in the helix period. Care must be taken to choose the optimal start-taper point and slope of the taper in order to maximize the rate of efficiency enhancement. The optimum point at which to begin the taper is the point, prior to saturation in the uniform helix, where the electron beam has just become trapped by the wave.

Saturation was found in the uniform helix example considered previously (see Fig. 9) at $z \approx 6.5$ cm, and the nonlinearity in the growth rate begins at $z \approx 5.55$ cm. Hence, we choose this point at which to begin the taper. As a result, we consider an interaction that is identical to that described previously up to $z = 5.5$ cm, after which the helix period will be tapered. The optimum slope of the taper is often not linear, and we choose a two step taper, as shown in Fig. 12, in which $\lambda_h = 0.080\,137$ cm for $0 \leqslant z \leqslant 5.5$ cm after which it decreases linearly in the first step to $\lambda_h = 0.068$ cm at $z = 7.0$ cm, and in the second step down to $\lambda_h = 0.058$ at $z = 10.0$ cm. We now consider the evolution of the signal over this length.

The evolution of the power with axial position is shown in Fig. 13 for the tapered helix. It is evident that the efficiency increases substantially over this length, and reaches a maximum power of approximately 240 W for an efficiency of approximately 50%. The oscillation in the power shown subsequent to the start-taper point with a period of about 1.8 cm corresponds to the bounce period of the electrons trapped in the trough of the wave. The amplitude of the oscillation can be reduced by further optimization on the start-taper point. It should also be noted that even more energy can be extracted from the beam by continuing the taper beyond 10 cm.

The phase space and radial evolution of the electron beam as a function of axial position within the helix are shown in Fig. 14 at 7.0745 ns after the start of the pulse. This corresponds to the time when the peak of the signal exits the interaction region. It is evident from the figure that the beam

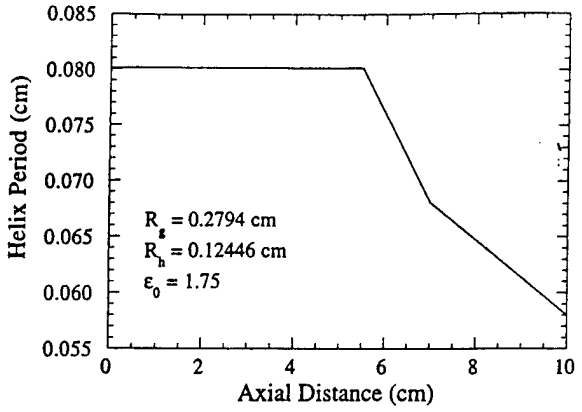

FIG. 12. Variation in the helix period as a function of axial position.

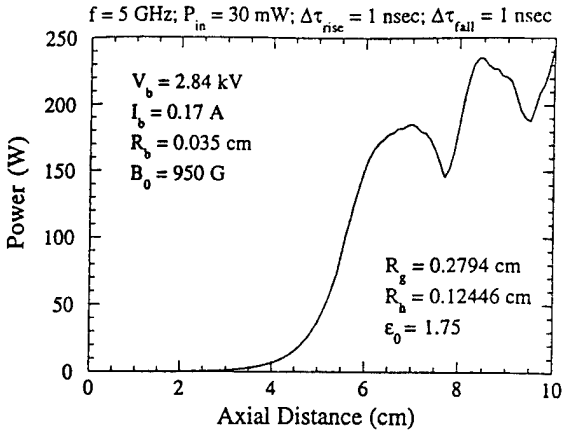

FIG. 13. Plot of the power as a function of axial position for the tapered helix shown in Fig. 12.

is largely trapped after $k_h z \approx 500$ (i.e., $z=6.4$ cm) and then decelerates rapidly corresponding to the taper in the helix period. It should be observed that the beam also experiences large-amplitude radial perturbations corresponding to the enhanced energy loss.

F. Emission-gated case

The emission-gated example we consider corresponds to an experiment conducted at the Naval Research Laboratory.[24] In contrast to the TWT at Northrop–Grumman, the helix in this case was supported by dielectric posts with a spacing of approximately the helix period and supported at the helix and wall by metallic structures. Thus, the dielectric supports occupied a much smaller fraction of the volume of the helix/wall gap than was the case for the Northrop–Grumman TWT, and this circuit requires both dielectric and vane loading to model the cold helix dispersion. The wall radius in this case was 3.63 cm and the helix radius and period were 1.4 and 1.966 cm, respectively. Good agreement between the measured dispersion and the cold helix dispersion equation (2) was found for an effective dielectric constant of 1.25 and a vane radius of 3.23 cm. The length of the helix was 33.5 cm. A comparison of the measured and calculated phase velocity as a function of frequency is shown in Fig. 15.

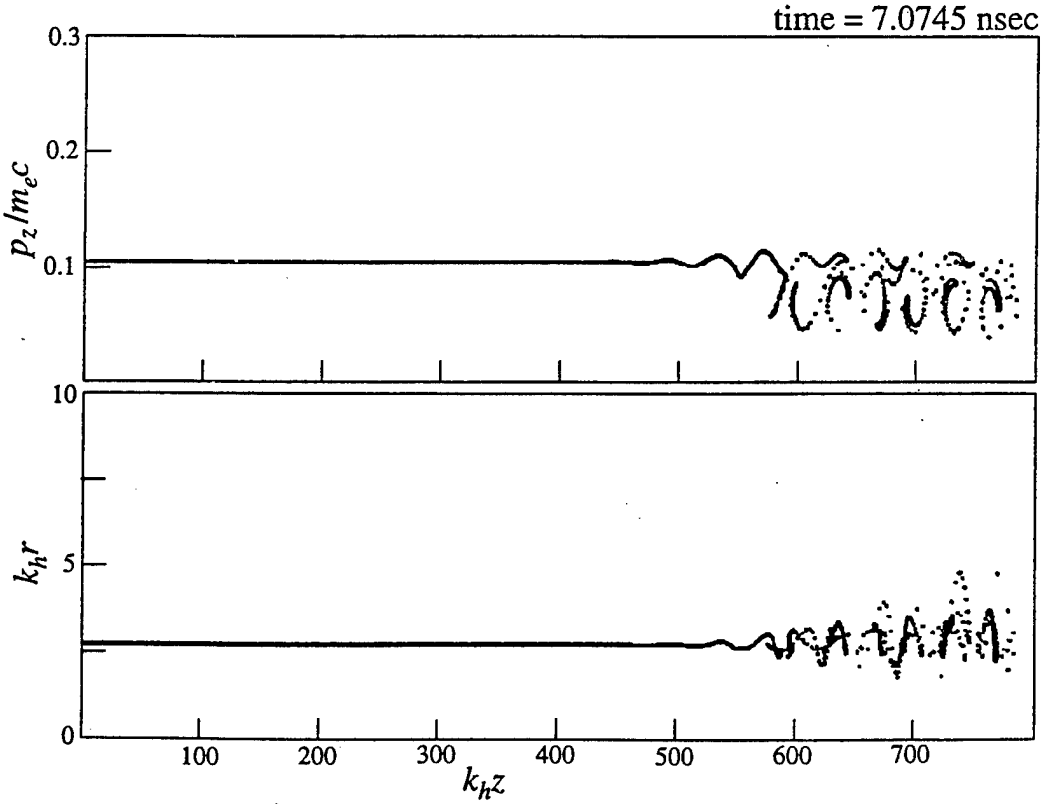

FIG. 14. Plot of the axial evolution of the phase space and radial structure of the beam for the tapered helix interaction.

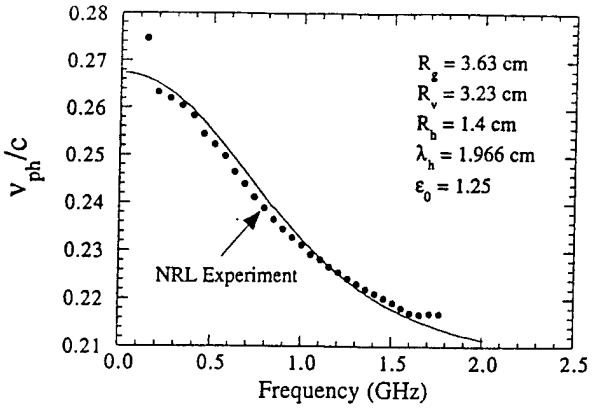

FIG. 15. Comparison of the dispersion as measured in the NRL experiment and as calculated from the dispersion equation (2).

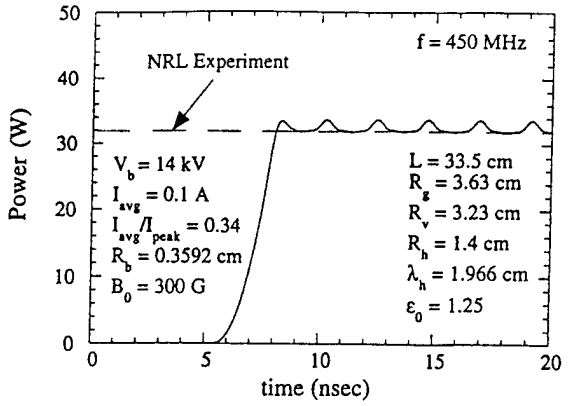

FIG. 16. Evolution of the output power as a function of time for the NRL experiment.

This experiment employed a gridded cathode that was driven at a frequency of approximately 450 MHz. At this frequency, the helix is approximately two wavelengths in length. The specific cases under consideration here used an electron beam with a voltage of 14 kV, a current of 0.1 A, and a radius of 0.508 cm. An external magnetic field of 300 G was imposed. It has been determined from the linear theory that space-charge effects for these beam and circuit parameters do not become important until the current reaches from 1–10 A; hence, we expect that the nonlinear model can treat this experiment. Comparisons between the experiment and simulations bear out this expectation.

In order to minimize the number of electrons in the simulation (and, hence, minimize run times as well), an annular beam model was assumed with a beam radius of 0.3592 cm (i.e., the rms beam radius). The utility of modeling a solid beam by an annular beam with a radius equal to the rms radius of the solid beam has been demonstrated by means of a linear theory of the interaction.[10] No external drive power was assumed in simulation. We used the beam model shown in Eq. (35) to inject electrons into the interaction region, and studied the variation in the output power as a function of the ratio I_{avg}/I_{peak}.

An example of the temporal evolution of the output

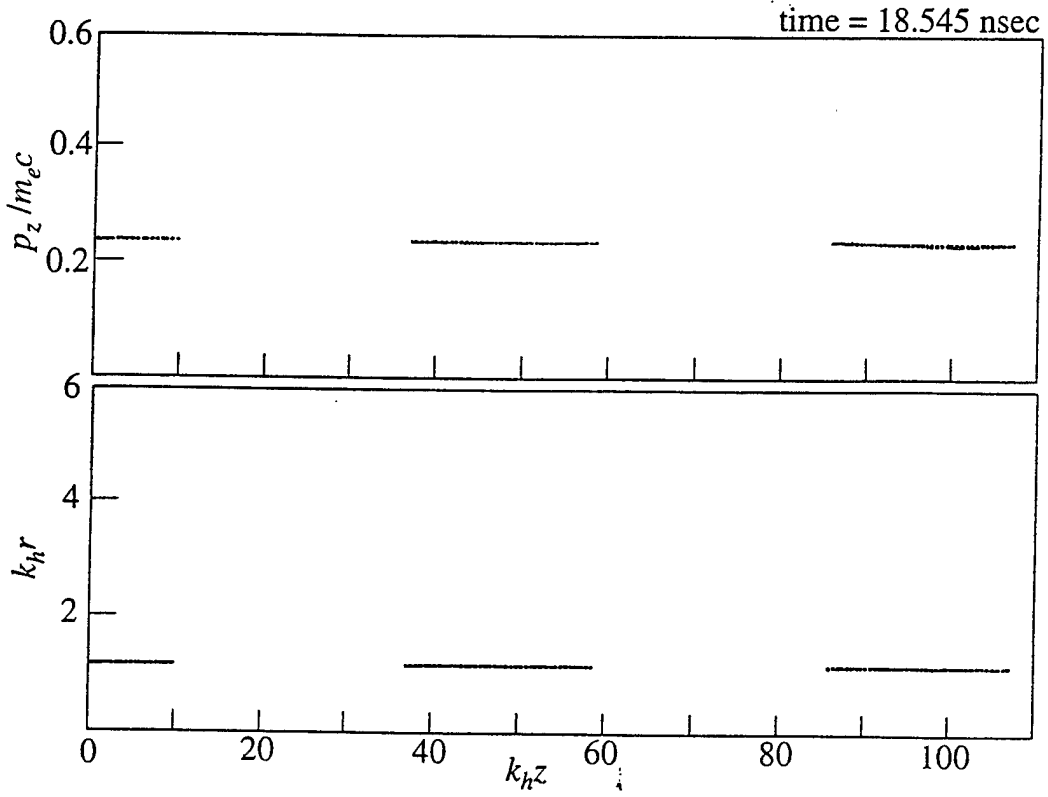

FIG. 17. Plots showing the axial evolution of the phase space and radial structure of the emission-gated electron beam.

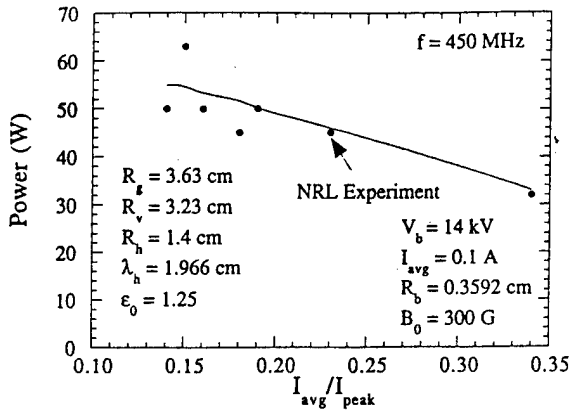

FIG. 18. Comparison of the output power as seen in the experiment and as predicted in simulation as a function of I_{avg}/I_{peak}.

power is shown in Fig. 16 for $I_{avg}/I_{peak}=0.34$. As seen in the figure, there is no output power prior to about 5 ns after the start of the beam pulse, which corresponds to the transit time through the helix. The output power rises rapidly thereafter, however, and rises to its peak value within 2 ns (corresponding to the wave period) and remains relatively constant at a level of approximately 32 W for as long as the beam power is maintained. This corresponds to an efficiency of about 2%, and is in close agreement with the observed output power level of 32 W recorded in the experiment. We also remark that a modulation in the output power at a period of about 2 ns is also observed after the plateau in the output power is achieved. This is a macroscopic effect that stems from to the fact that the electron beam is completely bunched at that period and there are vacuum regions between the bunches.

The evolution of the phase space and the radial positions of the beam are shown in Fig. 17 at time well after the output power has plateaued. It is clear that very little energy is extracted from the beam at an efficiency of only 2%; hence, there has been only a marginal growth in the energy spread of the beam, as shown by the slight depression in the axial momentum of the beam electrons near the end of the interaction region.

The level of agreement between the experiment and the nonlinear simulation at $I_{avg}/I_{peak}=0.34$ is also found as the ratio of average to peak current is varied. This is shown in Fig. 18 in which the average output power (in the plateau) is plotted versus I_{avg}/I_{peak}. As shown in the figure, the agreement between the simulation and the experiment is good over a wide variation in the ratio of average to peak currents.

IV. SUMMARY AND DISCUSSION

In this paper, we have described a nonlinear formulation of the interaction of an electron beam and multiple waves in a dielectric- and vane-loaded sheath helix TWT with and without a tapered period. The formulation is in the time domain and is able to treat the propagation of multiple radiation pulses through the helix structure (including the intermodulation between the waves), as well as both continuous and emission-gated electron beams.

The formulation has been compared with linear theories of the interaction as well as with helix TWT experiments, and good agreement has been obtained. It is found that the essential characteristics of the interaction in the helix TWT can be well described by the nonlinear simulation once the effective dielectric constant and vane radius for the helix have been determined. Good estimates of the effective dielectric constant can be obtained using a relatively straightforward volume-weighted average; however, refinements in the estimates of these parameters can be made by comparison of the predicted cold helix dispersion properties with the measured phase velocities of the cold helix.

The fundamental dynamical equation for the fields (27) is quite general in form, and relies largely on a knowledge of the dispersion, polarization, energy density, and Poynting flux for the waves under consideration. Thus, the technique is readily generalized to other configurations and structures. For example, it is straightforward to include reflections at either end of the interaction length and deal with cavities and oscillator configurations. Future work will be directed toward (1) the inclusion of a taper in the helix model, and (2) the treatment of space-charge effects and self-electric and self-magnetic fields. Each of these generalizations is currently in progress.

In view of the computational efficiency and generality of the present formulation to more complex and realistic helix models, the technique has advantages over PIC simulations for treating interactions in helix TWTs.

ACKNOWLEDGMENTS

The authors would like to acknowledge helpful technical discussions with Dr. B. Levush.

This work was supported by the Office of Naval Research and the Office of Naval Technology. The computational work was supported in part by a grant of High Performance Computing (HPC) time from the Department of Defense HPC Shared Resource Center of the Corps of Engineers Waterways Experiment Station (CEWES).

APPENDIX: MODELS IN A DIELECTRIC- AND VANE-LOADED HELIX

We express the components of the electric and magnetic fields in the generic form

$$\delta f=\delta\hat{f}(r)\exp(ikz-i\omega t), \tag{A1}$$

for which Maxwell's equations for the axial components of the electric and magnetic field are

$$[\nabla_\perp^2+\kappa^2]\begin{pmatrix}\delta\hat{E}_z\\ \delta\hat{B}z\end{pmatrix}=0, \tag{A2}$$

where $\kappa^2\equiv\epsilon(r)\omega^2/c^2-k^2$ and

$$\epsilon(r)=\begin{cases}1; & 0\leq r<R_h,\\ \epsilon_0; & R_h\leq r\leq R_g,\end{cases} \tag{A3}$$

denotes the radial variation of the dielectric coefficient. The transverse components of these fields are given by

$$\delta\hat{E}_r=\frac{ik}{\kappa^2}\frac{\partial}{\partial r}\delta\hat{E}_z, \tag{A4}$$

$$\delta\hat{E}_\theta=-\frac{i\omega/c}{\kappa^2}\frac{\partial}{\partial r}\delta\hat{B}_z, \tag{A5}$$

$$\delta\hat{B}_r=\frac{ik}{\kappa^2}\frac{\partial}{\partial r}\delta\hat{B}_z, \tag{A6}$$

$$\delta\hat{B}_\theta=\frac{i\epsilon(r)\omega/c}{\kappa^2}\frac{\partial}{\partial r}\delta\hat{E}_z. \tag{A7}$$

These equations must be solved subject to the boundary conditions at the helix, vanes, and wall.

In general, the vanes introduce an azimuthal periodicity into the solution that are described by azimuthal harmonics. However, we restrict the analysis to the lowest-order azimuthal harmonic, which describes an azimuthally symmetric solution. Since the electric field components tangent to the surface of the vanes and the magnetic field components normal to the surface of the vanes must vanish, this implies that the azimuthally symmetric solutions in the region of the vanes must be a transverse electric mode with $\delta\hat{E}_z=\delta\hat{E}_r=\delta\hat{B}_\theta=0$. For such a case, the effect of the vanes can be modeled by the inclusion of an additional sheath helix at the vane radius for which the period goes to infinity.[25] As such, we express the solution for the axial electric and magnetic fields in the form

$$\delta\hat{E}_z=\begin{cases} A_eJ_0(pr); & \text{I},\\ B_eJ_0(qr)+C_eY_0(qr); & \text{II},\\ D_eW_{0,0}(qR_g,qr); & \text{III}, \end{cases} \tag{A8}$$

and

$$\delta\hat{B}_z=\begin{cases} A_bJ_0(pr); & \text{I},\\ B_bJ_0(qr)+C_bY_0(qr); & \text{II},\\ D_bW_{1,0}(qR_g,qr); & \text{III}, \end{cases} \tag{A9}$$

where $p^2\equiv\omega^2/c^2-k^2$, $q^2\equiv\epsilon_0\omega^2/c^2-k^2$, and we have already imposed the boundary conditions that the transverse components of the electric field and the normal components of the magnetic field must vanish at the waveguide wall at $r=R_g$. Note that the three regions are as defined in Eqs. (3)–(6). Imposing the boundary conditions that $\delta\hat{E}_z$ and $\delta\hat{E}_\theta$ must be continuous at $r=R_h$ and R_v implies that

$$\delta\hat{E}_z=\begin{cases} A_eJ_0(pr); & \text{I},\\ \dfrac{A_eJ_0(pR_h)W_{0,0}(qR_v,qr)-D_eW_{0,0}(qR_g,qR_v)W_{0,0}(qR_h,qr)}{W_{0,0}(qR_v,qR_h)}; & \text{II},\\ D_eW_{0,0}(qR_g,qr); & \text{III}, \end{cases} \tag{A10}$$

and

$$\delta\hat{B}_z=\begin{cases} A_bJ_0(pr); & \text{I},\\ \dfrac{qA_bJ_1(pR_h)W_{1,0}(qR_v,qr)-pD_bW_{1,1}(qR_g,qR_v)W_{1,0}(qR_h,qr)}{pW_{1,1}(qR_v,qR_h)}; & \text{II},\\ D_bW_{1,0}(qR_g,qr); & \text{III}. \end{cases} \tag{A11}$$

Additional boundary conditions at the helix radii are that the tangential components of the electric field at the helix must be perpendicular to the helix, and that the tangential components of the magnetic field parallel to the helix must be continuous. This means that if the helix period goes to infinity then $\delta\hat{E}_z(R_v+0^\pm)=0$ and $\delta\hat{B}_z(R_v+0^-)=\delta\hat{B}_z(R_v+0^+)$. As a result, the axial components of the fields become

$$\delta\hat{E}_z=A_e\begin{cases} J_0(pr); & \text{I},\\ \dfrac{J_0(pR_h)W_{0,0}(qR_v,qr)}{W_{0,0}(qR_v,qR_h)}; & \text{II},\\ 0; & \text{III}, \end{cases} \tag{A12}$$

and

$$\delta\hat{B}_z=A_h\begin{cases} J_0(pr); & \text{I},\\ \dfrac{qJ_1(pR_h)W_{1,0}(qR_v,qr)}{pW_{1,1}(qR_v,qR_h)}; & \text{II and III}. \end{cases} \tag{A13}$$

Observe that the axial component of the magnetic field is unaffected by the presence of the vanes, while the axial component of the electric field vanishes in the region of the vanes. This yields the transverse-electric polarization in the region of the vanes.

Imposing the same helix boundary conditions at $r=R_h$ implies that

$$\delta\hat{E}_z(R_h+0^\pm)\sin\phi+\delta\hat{E}_\theta(R_h+0^\pm)\cos\phi=0 \tag{A14}$$

and

$$\delta\hat{B}_z(R_h+0^-)\sin\phi+\delta\hat{B}_\theta(R_h+0^-)\cos\phi = \delta\hat{B}_z(R_h+0^+)\sin\phi+\hat{B}_\theta(R_h+0^+)\cos\phi. \tag{A15}$$

These two conditions imply that

$$A_eJ_0(pR_h)\tan\phi=-\frac{i\omega}{cq}A_bJ_1(pR_h) \tag{A16}$$

and

$$A_b \tan\phi\left(J_0(pR_h)-\frac{q}{p}J_1(pR_h)\frac{W_{1,0}(qR_g,qR_h)}{W_{1,1}(qR_g,qR_h)}\right)$$
$$=\frac{i\omega}{cp}A_e\left(J_1(pR_h)+\frac{\epsilon_0 p}{q}J_0(pR_h)\frac{W_{1,0}(qR_h,qR_v)}{W_{0,0}(qR_v,qR_h)}\right). \quad \text{(A17)}$$

The dispersion equation (2) is found by setting the determinant of the coefficients in Eqs. (A16) and (A17) to zero, and the field representation in Eq. (1) is obtained by conversion of these fields to a real representation and allowing the amplitude and phase to vary in z and t.

[1]J. R. Pierce and L. M. Field, Proc. IRE **35**, 108 (1947).
[2]J. R. Pierce, Proc. IRE **35**, 111 (1947).
[3]J. R. Pierce, *Traveling-Wave Tubes* (Van Nostrand, New York, 1950).
[4]O. E. H. Rydbeck, Ericsson Techn. **46**, 3 (1948).
[5]L. J. Chu and J. D. Jackson, Proc. IRE **36**, 853 (1948).
[6]A. H. W. Beck, *Space-Charge Waves* (Pergamon, New York, 1958).
[7]R. G. E. Hutter, *Beam and Wave Electronics in Microwave Tubes* (Van Nostrand, New York, 1960).
[8]H. P. Freund, M. A. Kodis, and N. R. Vanderplaats, IEEE Trans. Plasma Sci. **PS-20**, 543 (1992).
[9]H. P. Freund, N. R. Vanderplaats, and M. A. Kodis, IEEE Trans. Plasma Sci. **PS-21**, 654 (1993).
[10]H. P. Freund, E. G. Zaidman, M. A. Kodis, and N. R. Vanderplaats, IEEE Trans. Plasma Sci. (in press).
[11]L. Brillouin, J. Appl. Phys. **20**, 1196 (1949).
[12]A. Nordsieck, Proc. IRE **41**, 630 (1953).
[13]P. K. Tien, L. R. Walker, and V. M. Wolontis, Proc. IRE **43**, 260 (1955).
[14]J. E. Rowe, IRE Trans. Electron. Devices **ED-3**, 39 (1956).
[15]J. E. Rowe, *Nonlinear Electron-Wave Interaction Phenomena* (Academic, New York, 1965).
[16]H. P. Freund and T. M. Antonsen, Jr., *Principles of Free-Electron Lasers* (Chapman & Hall, London, 1992), Chap. 5.
[17]I. J. Morey and C. K. Birdsall, IEEE Trans. Plasma Sci. **PS-18**, 482 (1990).
[18]R. J. Faehl, B. S. Newberger, and B. B. Godfrey, Phys. Fluids **23**, 2440 (1980).
[19]B. Goplen, D. Smithe, K. Nguyen, M. A. Kodis, and N. R. Vanderplaats, in *International Electron Devices Meeting Technical Digest* (Institute of Electrical and Electronics Engineers, New York, 1992), pp. 759–762.
[20]H. P. Freund, R. H. Jackson, and D. E. Pershing, Phys. Fluids B **5**, 2318 (1993).
[21]G. Groshart, Northrop–Grumman Corp. (personal communication, 1996).
[22]K. A. Hoffman, *Computational Fluid Dynamics for Engineers* (Engineering Education System, Austin, TX, 1989), p. 171.
[23]J. C. Slater, *Microwave Electronics* (Van Nostrand, New York, 1950).
[24]M. A. Kodis, N. R. Vanderplaats, E. G. Zaidman, B. Goplen, D. N. Smithe, and H. P. Freund, in *International Electron Devices Meeting Technical Digest* (Institute of Electrical and Electronics Engineers, New York, 1994), Catalog No. 94CH35706, pp. 795–798.
[25]D. N. Smithe (personal communication, 1996).

APPENDIX XV

Nonlinear Theory of Collective Effects in Helix Traveling Wave Tubes

H.P. Freund and E.G. Zaidman
Phys. Plasmas **4**, 2292 (1997)

Nonlinear theory of collective effects in helix traveling wave tubes

H. P. Freund[a] and E. G. Zaidman
Naval Research Laboratory, Washington, D.C. 20375

(Received 3 December 1996; accepted 5 March 1997)

A time-dependent collective nonlinear analysis of a helix traveling wave tube including fluctuating (ac) space-charge effects is presented for a configuration where an electron beam propagates through a sheath helix surrounded by a conducting wall. The effects of dielectric and vane loading of the helix are included, as is efficiency enhancement by tapering the helix pitch, and external focusing by means of either a uniform solenoidal magnetic field or a periodic field produced by a periodic permanent magnet stack. Dielectric loading is described under the assumption that the gap between the helix and the wall is uniformly filled by a dielectric material. Vane loading describes the insertion of an arbitrary number of vanes running the length of the helix. The electromagnetic field is represented as a superposition of azimuthally symmetric waves in a vacuum sheath helix. The propagation of each wave *in vacuo*, as well as the interaction of each wave with the electron beam, is included by allowing the amplitudes of the waves to vary in z and t. The dynamical equation for the field is solved in conjunction with the three-dimensional Lorentz force equations for an ensemble of electrons. Collective effects from the fluctuating rf beam space-charge waves are also included in the analysis by means of a superposition of solutions of the Helmholtz equation. The simulation is compared with a linear theory of the interaction, and an example is described corresponding to a tube built at Northrop–Grumman Corp. © *1997 American Institute of Physics.* [S1070-664X(97)01706-0]

I. INTRODUCTION

Traveling wave tube (TWT) development extends over several decades and includes both linear[1–8] and nonlinear theories.[9–17] The nonlinear theories can be grouped into two broad classes dealing with steady-state (i.e., slow-time-scale)[9–13] and time-dependent models.[14–17] At the present time, a one-dimensional particle-in-cell (PIC) simulation code is available,[14] which treats dispersion by means of a transmission line equivalent circuit model. Hence, the one-dimensional PIC simulation of this form is limited in its ability to model the dispersion of the helix and is unable to deal with radial variation in the mode structure. The most general PIC formulations of the helix TWT to date are two-dimensional simulations of a sheath helix model.[15,16] While this approach provides a good approximation for the dispersion and radial mode structure for a sheath helix model, it is not adaptable to more realistic helix models, which include substantial harmonic components.

The analysis presented here is based upon a previously described time-dependent spectral approach,[17] which differs from the PIC formulations. As in the case of the two-dimensional PIC formulations, a sheath helix model is assumed; however, in the spectral approach, the fields are expressed as a superposition of the normal modes of the vacuum sheath helix. In this representation, an overall sinusoidal variation is assumed for each wave whose evolution, either *in vacuo* or in the presence of the electron beam, is treated by allowing the amplitude and phase of each wave to vary in both axial position and time. This evolution is governed by a dynamical equation, which is analogous to Poynting's equation. In conjunction with the equations for the fields, the trajectories of an ensemble of electrons are integrated using the three-dimensional Lorentz force equations. One advantage of the spectral approach over the PIC formulations is that it is readily generalizable to treat more realistic tape helix models.

In its original formulation,[17] the spectral approach included such effects as (1) the dielectric and vane loading of the helix for dispersion control, (2) the tapering of the helix period (i.e., the pitch) for efficiency enhancement, (3) the propagation of multiple signals (so-called multitone operation) with the associated intermodulation between waves, (4) the inclusion of variable attenuation or severs in the helix circuit, (5) reflections and backward propagating waves, (6) the injection of either continuous or pulsed drive signal(s), and (7) the injection of either a continuous or pulsed (i.e., emission-gated) electron beam. In the present paper, we extend the prior formulation to include collective effects arising from the beam space-charge waves. In addition, external focusing is treated using either a uniform solenoidal magnetic field or a periodic permanent magnet (PPM) array.

The organization of the paper is as follows: The general formulation is described in Sec. II. This includes a brief description of the dynamical equations governing the evolution of the electromagnetic helix modes, as well as a description of the formalism for treating the beam space-charge waves. The treatment of the external focusing fields is also discussed. The numerical analysis is given in Sec. III. A brief description of the numerical techniques is presented in this section, but the reader is advised that a more complete description is to be found in Ref. 17. Also included in Sec. III is a discussion of several sample TWT parameter sets. A summary is given in Sec. IV.

[a]Also at Science Applications International Corp., McLean, Virginia 22102; electronic mail: freund@mmace.nrl.navy.mil

 1070-664X/97/4(6)/2292/10/$10.00

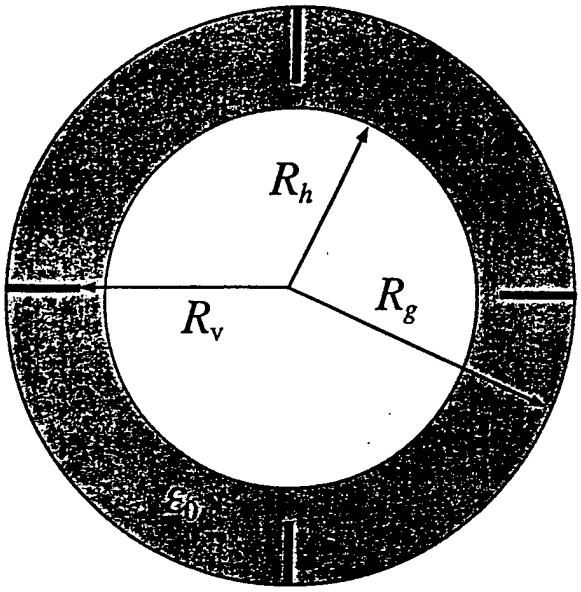

FIG. 1. Schematic illustration of the cross section of the helix circuit.

II. THE GENERAL FORMULATION

The general formulation treats the propagation of multiple waves through a dielectric- and vane-loaded sheath helix in the presence of an electron beam. This is a fully time-dependent problem, and the electron-beam model can represent either a continuous or prebunched pulse format, although we confine the present discussion to the case of a continuous beam. In addition, we permit the injected radiation to have an arbitrary format; that is, we can inject either a definite radiation pulse or a continuous signal. Collective effects due to the fluctuating rf beam space-charge waves are included in the analysis. External focusing by means of either a uniform solenoidal magnetic field or a periodic field produced by a PPM stack is also treated.

A. The electromagnetic modes in a sheath helix

The analysis in the absence of such collective effects as the beam space-charge waves has been discussed previously.[17] The interested reader is referred to the earlier work for the detailed nonlinear analysis of the electromagnetic waves supported by the helix, and we shall only summarize the development here for completeness.

A schematic of the cross section of the helix model is shown in Fig. 1, in which the vanes are positioned radially, and where R_h and R_g are used to denote the radii of the helix and the outer cylinder, R_v denotes the inner radius of the vanes, and ϵ_0 is the dielectric constant. For simplicity, we assume that both the helix and the outer cylinder are loss-free conductors and represent the electromagnetic field as a superposition of the azimuthally symmetric modes in the vacuum sheath helix in which the unit vector describing the pitch of the helix is $\hat{\mathbf{e}}_\phi = \hat{\mathbf{e}}_\theta \cos\phi + \hat{\mathbf{e}}_z \sin\phi$, where $\tan\phi = 1/k_h R_h$ for a helix wave number k_h [$\equiv 2\pi/\lambda_h$, and λ_h is the helix period].

The azimuthally symmetric electric and magnetic fields can be represented in the form[17]

$$\delta\mathbf{E}(\mathbf{x},t) = \sum_n \left[\delta\hat{E}_n^{(1)}\mathbf{e}_n^{(1)}(\mathbf{x},t) + \delta\hat{E}_n^{(2)}\mathbf{e}_n^{(2)}(\mathbf{x},t)\right],$$
$$\delta\mathbf{B}(\mathbf{x},t) = \sum_n \left[\delta\hat{E}_n^{(1)}\mathbf{b}_n^{(1)}(\mathbf{x},t) + \delta\hat{E}_n^{(2)}\mathbf{b}_n^{(2)}(\mathbf{x},t)\right], \tag{1}$$

where the summation is over the waves to be included, and the polarization vectors are

$$\begin{pmatrix}\mathbf{e}_n^{(1)}(\mathbf{x},t)\\ \mathbf{e}_n^{(2)}(\mathbf{x},t)\end{pmatrix} \equiv R_n(r)\hat{\mathbf{e}}_r\begin{pmatrix}\sin\varphi_n\\ \cos\varphi_n\end{pmatrix} + [\beta_{ph}(k_n)\Theta_n(r)\hat{\mathbf{e}}_\theta - Z_n^{(e)}(r)\hat{\mathbf{e}}_z]\begin{pmatrix}-\cos\varphi_n\\ \sin\varphi_n\end{pmatrix},$$
$$\begin{pmatrix}\mathbf{b}_n^{(1)}(\mathbf{x},t)\\ \mathbf{b}_n^{(2)}(\mathbf{x},t)\end{pmatrix} \equiv \Theta_n(r)\hat{\mathbf{e}}_r\begin{pmatrix}\cos\varphi_n\\ -\sin\varphi_n\end{pmatrix} + [\beta_{ph}(k_n)R_n(r)\hat{\mathbf{e}}_\theta - Z_n^{(b)}(r)\hat{\mathbf{e}}_z]\begin{pmatrix}\sin\varphi_n\\ \cos\varphi_n\end{pmatrix}. \tag{2}$$

Here, $\varphi_n \equiv k_n z - \omega_n t$ denotes the phase of the wave propagating in the cold vacuum helix for wave-number $k_n \equiv n\Delta k$ and angular frequency ω_n, such that (k_n, ω_n) satisfy the vacuum sheath helix dispersion equation and Δk is the separation in wave number between the waves. As such, the overall amplitude of the wave is given by $\delta\hat{E}_n^2 = \delta\hat{E}_n^{(1)^2} + \delta\hat{E}_n^{(2)^2}$, and the phase variation governed by the interaction with the electron beam is given by $\delta\varphi_n = \tan^{-1}(\delta\hat{E}_n^{(2)}/\delta\hat{E}_n^{(1)})$, where we assume that both $\delta\hat{E}_n$ and $\delta\varphi_n$ vary in z and t. Observe that in the absence of the electron beam, both $\delta\varphi_n = 0$ and $\delta\hat{E}_n^{(2)} = 0$ and the fields describe the propagation of circuit waves *in vacuo*. In addition, $\beta_{ph}(k_n) \equiv v_{ph}(k_n)/c = \omega_n/ck_n$ denotes the normalized phase velocity of each wave. The vacuum sheath helix dispersion equation is[17]

$$\frac{\omega_n^2}{c^2} - \frac{p_n q_n}{k_h^2 R_h^2}\frac{J_0(p_n R_h)}{J_1(p_n R_h)}\frac{W_{0,0}(q_n R_v, q_n R_h)}{W_{1,1}(q_n R_v, q_n R_h)}\frac{[p_n J_0(p_n R_h)W_{1,1}(q_n R_g, q_n R_h) - q_n J_1(p_n R_h)W_{1,0}(q_n R_g, q_n R_h)]}{[q_n J_1(p_n R_h)W_{0,0}(q_n R_v, q_n R_h) + \epsilon_0 p_n J_0(p_n R_h)W_{1,0}(q_n R_h, q_n R_v)]} = 0, \tag{3}$$

where $p_n^2 \equiv \omega_n^2/c^2 - k_n^2$, $q_n^2 \equiv \epsilon_0 \omega_n^2/c^2 - k_n^2$, $W_{m,n}(x,y) \equiv Y_m(x)J_n(y) - J_m(x)Y_n(y)$, and J_n and Y_n denote the Bessel and Neumann functions, and

$$R_n(r) = \begin{cases} \dfrac{k_n}{p_n} J_1(p_n r); & \text{I}, \\ -\dfrac{k_n}{q_n} J_0(p_n R_h) \dfrac{W_{1,0}(q_n r, q_n R_v)}{W_{0,0}(q_n R_v, q_n R_h)}; & \text{II}, \\ 0; & \text{III}, \end{cases} \tag{4}$$

$$\Theta_n(r) = \frac{ck_n/\omega_n}{k_h R_h} \times \begin{cases} \dfrac{J_0(p_n R_h) J_1(p_n r)}{J_1(p_n R_h)}; & \text{I}, \\ J_0(p_n R_h) \dfrac{W_{1,1}(q_n R_g, q_n r)}{W_{1,1}(q_n R_g, q_n R_h)}; & \text{II and II}, \end{cases} \tag{5}$$

$$Z_n^{(e)}(r) = \begin{cases} J_0(p_n r); & \text{I}, \\ J_0(p_n R_h) \dfrac{W_{0,0}(q_n R_v, q_n r)}{W_{0,0}(q_n R_v, q_n R_h)}; & \text{II}, \\ 0; & \text{III}, \end{cases} \tag{6}$$

$$Z_n^{(b)}(r) = \frac{cp_n/\omega_n}{k_h R_h} \times \begin{cases} \dfrac{J_0(p_n R_h) J_0(p_n r)}{J_1(p_n R_h)}; & \text{I}, \\ \dfrac{q_n}{p_n} J_0(p_n R_h) \dfrac{W_{1,0}(q_n R_g, q_n r)}{W_{1,1}(q_n R_g, q_n R_h)}; & \text{II and III}, \end{cases} \tag{7}$$

where region I denotes $0 \leq r < R_h$, region II denotes $R_h \leq r < R_v$, and region III denotes $R_v \leq r \leq R_g$.

Energy transport for each wave is determined by the Poynting flux, the stored energy density, and the group velocity. The Poynting flux for each wave denotes the time-averaged power flux over the entire cross section of the cylinder and helix, and using the fields given in Eqs. (1) can be expressed as $S_n = P_n \delta \hat{E}_n^2$, where

$$\begin{aligned} P_n \equiv \frac{k_n \omega_n R_h^2}{8p_n^2} \Bigg\{ & \left(1 - \frac{\epsilon_0 p_n^2}{q_n^2}\right) J_0^2(p_n R_h) + \left[J_1^2(p_n R_h) - \frac{\epsilon_0 p_n^2}{q_n^2} J_0^2(p_n R_h) \frac{W_{1,0}^2(q_n R_h, q_n R_v)}{W_{0,0}^2(q_n R_v, q_n R_h)} \right] + \frac{c^2 p_n^2}{\omega_n^2} \frac{1}{k_h^2 R_h^2} \\ & \times \left[\frac{J_0^4(p_n R_h)}{J_1^2(p_n R_h)} - J_0^2(p_n R_h) \frac{W_{1,0}^2(q_n R_g, q_n R_h)}{W_{1,1}^2(q_n R_g, q_n R_h)} \right] - \frac{2J_0(p_n R_h)}{p_n R_h} \left[J_1(p_n R_h) + \frac{\epsilon_0 p_n^3}{q_n^3} J_0(p_n R_h) \frac{W_{1,0}(q_n R_h, q_n R_v)}{W_{0,0}(q_n R_v, q_n R_h)} \right] \\ & - \frac{c^2 p_n^2}{\omega_n^2} \frac{2}{k_h^2 R_h^2} \frac{J_0(p_n R_h)}{p_n R_h} \left[\frac{J_0^2(p_n R_h)}{J_1(p_n R_h)} - \frac{p_n}{q_n} J_0(p_n R_h) \frac{W_{1,0}(q_n R_g, q_n R_h)}{W_{1,1}(q_n R_g, q_n R_h)} \right] \\ & + \frac{2}{\pi^2} \frac{c^2 p_n^2}{\omega_n^2} \frac{J_0^2(p_n R_h)}{q_n^2 R_h^2} \left[\frac{\epsilon_0 \omega_n^2 c^2 q_n^2}{W_{0,0}^2(q_n R_v, q_n R_h)} + \frac{\tan^2 \phi}{W_{1,1}^2(q_n R_g, q_n R_h)} \right] \Bigg\}. \end{aligned} \tag{8}$$

In addition, the time-averaged energy density per unit axial length over the entire cross section of the helix and cylinder is given by $W_n = U_n \delta \hat{E}_n^2$, where

$$\begin{aligned} U_n \equiv \frac{\omega_n}{k_n c^2} P_n + \frac{R_h}{4p_n} J_0(p_n R_h) & \left[J_1(p_n R_h) + \frac{\epsilon_0 p_n}{q_n} J_0(p_n R_h) \frac{W_{1,0}(q_n R_h, q_n R_v)}{W_{0,0}(q_n R_v, q_n R_h)} \right] + \frac{R_h^2(\epsilon_0 - 1)}{8} J_0^2(p_n R_h) \\ & \times \Bigg\{ \frac{4}{\pi^2 q_n^2 R_h^2} \left[\frac{\epsilon_0 \omega_n^2 c^2 q_n^2}{W_{0,0}^2(q_n R_v, q_n R_h)} + \frac{\tan^2 \phi}{W_{1,1}^2(q_n R_g, q_n R_h)} \right] - \left(\frac{\epsilon_0 \omega_n^2}{c^2 q_n^2} + \tan^2 \phi \right) - \left[\frac{\epsilon_0 \omega_n^2}{c^2 q_n^2} \frac{W_{1,0}^2(q_n R_h, q_n R_v)}{W_{0,0}^2(q_n R_v, q_n R_h)} \right. \\ & \left. + \tan^2 \phi \frac{W_{1,0}^2(q_n R_g, q_n R_h)}{W_{1,1}^2(q_n R_g, q_n R_h)} \right] - \frac{2}{q_n R_h} \left[\frac{\epsilon_0 \omega_h^2}{c^2 q_n^2} \frac{W_{1,0}(q_n R_h, q_n R_v)}{W_{0,0}(q_n R_v, q_n R_h)} - \tan^2 \phi \frac{W_{1,0}(q_n R_g, q_n R_h)}{W_{1,1}(q_n R_g, q_n R_h)} \right] \Bigg\}. \end{aligned} \tag{9}$$

Finally, the group velocity of each individual wave is $v_{gr}(k_n) \equiv \partial\omega_n/\partial k_n = P_n/U_n$.

The dynamical equations for the wave amplitudes are of the form[17]

$$\left(\frac{\partial}{\partial t} - \Gamma_n + v_{gr}(k_n)\frac{\partial}{\partial z}\right)\begin{pmatrix} P_n^{1/2}\delta\hat{E}_n^{(1)} \\ P_n^{1/2}\delta\hat{E}_n^{(2)}\end{pmatrix} = -\frac{\Delta k P_n^{1/2}}{4\pi U_n}\int_{z-\pi/\Delta k}^{z+\pi/\Delta k} dz' \int\int_{A_h} dx\, dy \mathbf{J}(\mathbf{x}_\perp, z', t) \cdot \begin{pmatrix} \mathbf{e}_n^{(1)}(\mathbf{x}_\perp, z', t) \\ \mathbf{e}_n^{(2)}(\mathbf{x}_\perp, z', t)\end{pmatrix}, \tag{10}$$

where $\mathbf{J}(\mathbf{x},t)$ denotes the microscopic source current, A_h denotes the cross-sectional area enclosed by the helix, and Γ_n describes the losses for the circuit wave. Observe that for a single wave, this scale length $2\pi/\Delta k$ in the average over z is just the wavelength. This equation describes the propagation of a pulse, or pulses, through the helix/cylinder at the appropriate group velocities. The effect of a tapered helix and intermodulation between the various waves is implicitly included through the particle trajectories.

B. Beam space-charge modes

In treating the collective beam space-charge modes, we assume that the electrostatic field is azimuthally symmetric, and write

$$\mathbf{E}^{(sc)}(r,z,t) = \sum_n \hat{E}_n^{(sc)}(z,t)\mathbf{e}_n^{(sc)}(r,z,t), \tag{11}$$

where $\hat{E}_n^{(sc)}$ is the amplitude,

$$\mathbf{e}_n^{(sc)}(r,z,t) = R_n^{(sc)}(r)\hat{\mathbf{e}}_r \cos(\varphi_n + \delta\varphi_n^{(sc)}) + Z_n^{(sc)}(r) \times \hat{\mathbf{e}}_z \sin(\varphi_n + \delta\varphi_n^{(sc)}), \tag{12}$$

the sum denotes the ensemble of space-charge modes, each one corresponding to the nth electromagnetic mode in the helix, φ_n is the vacuum phase of the helix mode, and $\delta\varphi_n^{(sc)}$, describes the effect of the interaction on the phase of the space-charge mode. As in the case of the electromagnetic modes supported by the helix, we find it convenient to write

$$\mathbf{E}^{(sc)}(r,z,t) = \sum_n [\hat{E}_{n,1}^{(sc)}(z,t)\mathbf{e}_{n,1}^{(sc)}(r,z,t) + \hat{E}_{n,2}^{(sc)}(z,t) \times \mathbf{e}_{n,2}^{(sc)}(r,z,t)], \tag{13}$$

where

$$\begin{pmatrix} \mathbf{e}_{n,1}^{(sc)}(r,z,t) \\ \mathbf{e}_{n,2}^{(sc)}(r,z,t)\end{pmatrix} = R_n^{(sc)}(r)\hat{\mathbf{e}}_r\begin{pmatrix} \cos\varphi_n \\ -\sin\varphi_n\end{pmatrix} + Z_n^{(sc)}(r) \times \hat{\mathbf{e}}_z\begin{pmatrix} \sin\varphi_n \\ \cos\varphi_n\end{pmatrix}, \tag{14}$$

and $\hat{E}_{n,1}^{(sc)} = \hat{E}_n^{(sc)} \cos\delta\varphi_n^{(sc)}$, and $\hat{E}_{n,2}^{(sc)} = \hat{E}_n^{(sc)} \sin\delta\varphi_n^{(sc)}$.

If we now take the time derivative of Poisson's equation and use the continuity equation to replace the time derivative of the charge density by the divergence of the current, then

$$\frac{\partial}{\partial t}\nabla\cdot\mathbf{E}^{(sc)} = 4\pi\frac{\partial}{\partial t}\rho = -4\pi\nabla\cdot\mathbf{J}. \tag{15}$$

Hence, we find that

$$\frac{\partial}{\partial t}\mathbf{E}^{(sc)} = -4\pi\mathbf{J}, \tag{16}$$

to within a contribution of vanishing divergence. Under the assumption that $\partial\hat{E}_n^{(sc)}/\partial t \ll \omega_n\hat{E}_n^{(sc)}$, Poisson's equation can be written as

$$\sum_n \omega_n[\hat{E}_{n,1}^{(sc)}(z,t)\dot{\mathbf{e}}_{n,1}^{(sc)}(r,z,t) + \hat{E}_{n,2}^{(sc)}(z,t)\dot{\mathbf{e}}_{n,2}^{(sc)}(r,z,t)] = -4\pi\mathbf{J}, \tag{17}$$

where

$$\begin{pmatrix} \dot{\mathbf{e}}_{n,1}^{(sc)}(r,z,t) \\ \dot{\mathbf{e}}_{n,2}^{(sc)}(r,z,t)\end{pmatrix} = R_n^{(sc)}(r)\hat{\mathbf{e}}_r\begin{pmatrix} \sin\varphi_n \\ \cos\varphi_n\end{pmatrix} + Z_n^{(sc)}(r) \times \hat{\mathbf{e}}_z\begin{pmatrix} -\cos\varphi_n \\ \sin\varphi_n\end{pmatrix}. \tag{18}$$

We must now specify a procedure for determining the profile functions $R_n^{(sc)}$ and $Z_n^{(sc)}$.

The sheath helix model approximates the helix as a conducting cylinder in which induced currents are constrained to flow helically with the pitch angle ϕ. Within the context of this approximation, it is appropriate to assume that the space-charge potential vanishes on the helix (i.e., at $r = R_h$). The polarization functions, therefore, can be expanded in terms of the solutions of the Helmholtz equation subject to this boundary condition; hence,

$$R_n^{(sc)}(r) = \sum_{m=1}^{\infty} \kappa_m J_1(\kappa_m r), \tag{19}$$

and

$$Z_n^{(sc)}(r) = \sum_{m=1}^{\infty} k_n J_0(\kappa_m r), \tag{20}$$

where $k_m \equiv x_{0m}/R_h$, and x_{0m} is the mth zero of J_0 [i.e., $J_0(x_{0m}) = 0$]. As such, the polarization vectors can be written as ($i = 1,2$)

$$\dot{\mathbf{e}}_{n,i}^{(sc)}(r,z,t) = \sum_{m=1}^{\infty} \dot{\mathbf{e}}_{n,m,i}^{(sc)}(r,z,t), \tag{21}$$

where

$$\begin{pmatrix} \dot{\mathbf{e}}_{n,m,1}^{(sc)}(r,z,t) \\ \dot{\mathbf{e}}_{n,m,2}^{(sc)}(r,z,t)\end{pmatrix} = \kappa_m J_1(\kappa_m r)\hat{\mathbf{e}}_r\begin{pmatrix} \sin\varphi_n \\ \cos\varphi_n\end{pmatrix} + k_n J_0(\kappa_m r)\hat{\mathbf{e}}_z\begin{pmatrix} -\cos\varphi_n \\ \sin\varphi_n\end{pmatrix}. \tag{22}$$

The polarization functions satisfy the Bessel function orthogonality conditions and, after integrating over the cross section and also orthogonalizing over the axial modes, we find that for $i = 1,2$

$$\hat{E}_{n,i}^{(sc)} = -\frac{8\Delta k}{\omega_n R_h^2} \sum_{m=1}^{\infty} \int_{z-\pi/\Delta k}^{z+\pi/\Delta k} dz' \int\int_{A_h} dx\, dy$$

$$\times \frac{\mathbf{J}(\mathbf{x}_\perp, z', t) \cdot \dot{\mathbf{e}}_{n,m,i}^{(sc)}(\mathbf{x}_\perp, z', t)}{[k_n^2 + \kappa_m^2] J_1^2(x_{0m})}. \tag{23}$$

In practice, the application of this procedure requires truncation of the summation over the number of radial modes. This is determined in an empirical manner for each specific configuration by the successive addition of more modes until convergence is achieved.

The specific tests used for convergence relate to both the bulk gain in the linear regime and to the saturation efficiency. Hence, additional radial modes are added to the simulation until the bulk growth rate in the exponential gain regime and the saturation efficiency converge to within some desired accuracy. It should be noted that the number of radial modes required to reach convergence may vary widely depending upon the specific parameters of interest and beam configuration. For example, a large number of radial modes would be required to treat an annular beam profile than a solid beam profile.

C. External focusing

Additional focusing fields in the form of externally applied magnetostatic fields are often necessary components of TWT designs. Two types of focusing fields are typically employed: uniform solenoidal fields, and a rippled field generated by a PPM stack. We employ both fields in the present formulation. The solenoidal field is simply

$$\mathbf{B}_{ext} = B_0 \hat{\mathbf{e}}_z, \tag{24}$$

where B_0 describes the amplitude. The PPM field can be represented as

$$\mathbf{B}_{ext} = B_w [I_1(k_w r)\hat{\mathbf{e}}_r \sin k_w z + I_0(k_w r)\hat{\mathbf{e}}_z \cos k_w z], \tag{25}$$

where B_w describes the on-axis amplitude of the PPM field, k_w [$\equiv 2\pi/\lambda_w$, where λ_w is the period] is the wave number, and I_n denotes the modified Bessel function of the first kind.

D. Electron dynamics

The electron dynamics are treated using the full three-dimensional relativistic Lorentz force equations. Azimuthal symmetry is imposed only in the sense (1) that the beam distribution upon entry to the helix is azimuthally symmetric, and (2) that each of the vector components of the fields varies only in (r,z,t). With this in mind, we integrate the Lorentz force equation for each electron in the simulation subject to external focusing magnetic fields, the electromagnetic fields, and the space-charge field. Hence,

$$\frac{d}{dt}\mathbf{p} = -e[\delta\mathbf{E}(\mathbf{x},t) + \mathbf{E}^{(sc)}(\mathbf{x},t)]$$

$$-\frac{e}{c}\mathbf{v}\times[\mathbf{B}_{ext}(\mathbf{x}) + \delta\mathbf{B}(\mathbf{x},t)]. \tag{26}$$

III. NUMERICAL ANALYSIS

For convenience, we refer to the simulation code as GATOR. The sequence of operations used in integrating the field and orbit equations are as follows: We first calculate the source current for both the electromagnetic field(s) and the space-charge field by accumulating electron charge to the grid and averaging over the appropriate scale length. We then step the electromagnetic fields. Once the updated fields are calculated, we step the electron trajectories subject to the electromagnetic, magnetostatic, and space-charge fields. This procedure is repeated over the time scale of interest.

The dynamical equations for the vacuum helix waves (10) are solved for a system of length L on a grid with spacing Δz over a time step Δt using the MacCormack method.[18] The source current is

$$\mathbf{J}(\mathbf{x},t) = -\sum_{i=1}^{N} q_i \mathbf{v}_i(t)\,\delta[x - x_i(t)]\,\delta[y - y_i(t)]$$

$$\times S[z - z_i(t)], \tag{27}$$

where N is the number of electrons in the system at time t, $(\mathbf{x}_i, v_i)$ represents the location and velocity of the ith macroelectron at time t, q_i is the charge per macroelectron, and S is the shape function. The *shape function* describes the interpolation of the electron charge to the grid locations. We use a triangular shape algorithm

$$S(z - z_i) = \begin{cases} \dfrac{z - z_i + \Delta z}{\Delta z^2}; & z_i - \Delta z \leq z \leq z_i, \\ -\dfrac{z - z_i - \Delta z}{\Delta z^2}; & z_i < z \leq z_i + \Delta z, \end{cases} \tag{28}$$

which provides a linear weighting weighing in which the charge is mapped onto the two nearest-neighbor grid points. The charge per electron includes a weight factor dependent upon the beam current. We inject N rings of electrons on each time step and model a beam with a flat-top radial profile. Hence, we choose $q_i = (2i-1) I_b \Delta t / N_i^2$ for the ith ring, where I_b is the beam current. Analogous models can be developed for either a parabolic beam profile or an annular beam model.

The source current calculated in this fashion is also used to determine the space-charge field(s) using Eq. (23). Note that in contrast to the equations for the vacuum helix waves in which a partial differential equation (10) is integrated to describe the propagation of the waves through the helix subject to gain in the presence of the beam and attenuation, the space-charge fields are evaluated at each grid point at each time step from the source current and mapped to the location of each electron. Hence, these fields are not explicitly propagated but, rather, are "carried along" by the electron beam.

The orbit equations are integrated by means of a fourth-order Runge–Kutta algorithm. In order to be consistent with the electron shape function, which maps electron charge onto the grid, we use a linear interpolation scheme to map the field from the grid to the particle locations. Electrons are injected at the start of each time step. The charge per electron is calculated as described above and we allow for an arbitrary current rise time by choosing a current of the form

$$I_b(t)=\begin{cases} I_b \sin^2\left(\dfrac{\pi}{2}\dfrac{t}{\tau_r}\right); & t\leq\tau_r, \\ I_b; & t>\tau_r, \end{cases} \tag{29}$$

where τ_r denotes the rise time of the beam. The initial momentum space distribution describes a beam that is initially propagating purely parallel to the axis of symmetry in which $p_{z0}/m_e c=\sqrt{\gamma_b^2-1}$ and $p_{\perp 0}=0$.

TWTs are typically operated as amplifiers in which an injected signal(s) grows over the length of the helix. In order to model this, we must specify an injection algorithm. For this purpose, we inject a pulse with arbitrary start, rise, flat, and fall times in the following way. We assume that a pulse is injected at $z=-\Delta z$ and allowed to propagate into the interaction region. The pulse has a smooth temporal shape given by

$$\delta\hat{E}_n^{(1)}(z=-\Delta z,t)$$

$$=\delta\hat{E}_0^{(1)}\begin{cases} 0; t<\tau_{\text{start}}, \\ \sin^2\left[\dfrac{\pi}{2}\dfrac{(t-\tau_{\text{start}})}{\Delta\tau_{\text{rise}}}\right]; & \tau_{\text{start}}\leq t<\tau_{\text{rise}}, \\ 1; & \tau_{\text{rise}}\leq t<\tau_{\text{flat}}, \\ \cos^2\left[\dfrac{\pi}{2}\dfrac{(t-\tau_{\text{fall}})}{\Delta\tau_{\text{fall}}}\right]; & \tau_{\text{flat}}\leq t\leq\tau_{\text{fall}}, \\ 0; & t>\tau_{\text{fall}}, \end{cases} \tag{30}$$

and $\delta\hat{E}_n^{(2)}(z=-\Delta z,t)=0$ for all t, where $\delta\hat{E}_0^{(1)}$ is chosen to describe the peak power, τ_{start} denotes the start time of the pulse, $\Delta\tau_{\text{rise}}$ is the rise time of the pulse, $\tau_{\text{rise}}=\tau_{\text{start}}+\Delta\tau_{\text{rise}}$ is the time at which the pulse has risen to its peak value, $\tau_{\text{flat}}-\tau_{\text{rise}}$ is the time interval over which the pulse retains a constant magnitude, $\Delta\tau_{\text{fall}}$ is the time interval over which the pulse falls to zero, and $\tau_{\text{fall}}=\tau_{\text{flat}}+\Delta\tau_{\text{fall}}$ is the time after which the injected pulse vanishes. Note that the injection of power at $z=-\Delta z$ requires the inclusion of a guard cell in the grid outside of the interaction region. In this work, we assume a smooth rise time for the injected pulse followed by a constant drive power.

We now consider the interaction for circuit parameters corresponding to a helix TWT built at Northrop–Grumman Corp.[19] A schematic of the cross section of this tube is shown in Fig. 2. The helix and wall radii were 0.124 46 and 0.2794 cm, respectively, and the helix period was 0.080 137 cm. The helix was supported by three dielectric rods with rectangular cross sections running the length of the helix. The dielectric constant of the rods was 6.5 and the rod dimensions were 0.0508 cm×0.14732 cm. No vanes were used in this structure. Gain was measured in this TWT over a frequency range of 3–7 GHz using a 2.84 kV/0.17 A electron beam with a radius of 0.05 cm.

The cold dispersion solutions have been compared with the measured dispersion of this TWT, and it was found that the effective dielectric constant can be approximated by a relatively simple volume-weighted average over the cross section of the circuit. The results of this comparison were discussed in detail in prior publications[8,17] and are shown in Fig. 3, where we plot the variation in the phase velocity versus frequency as calculated using the cold helix dispersion equation and as measured (dots) over frequencies up to 7.5 GHz for an effective dielectric constant $\epsilon_0=1.75$. It is evident from Fig. 3 that the agreement is very good over a broadband of frequencies extending from 3 up to 7 GHz, and we conclude that the effect of the dielectric rods on the dispersion can be modeled using the uniform dielectric loading with an effective dielectric constant of 1.75.

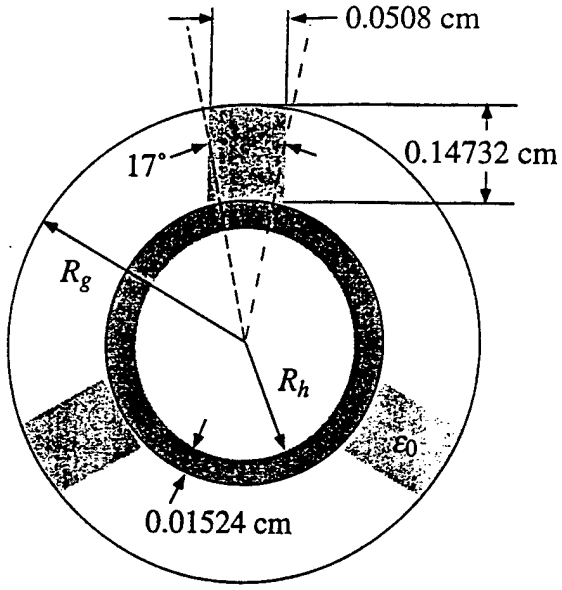

FIG. 2. Schematic illustration of the Northrop–Grumman helix TWT.

It should be remarked that many helix models, such as the one-dimensional PIC formalism described in Ref. 14, employ the impedance as an additional parameter, which describes the coupling of the beam to the circuit. However, there is no explicit use of the interaction impedance in this formulation. Rather, the coupling of the helix waves to the beam is implicitly described by the dispersion, polarization, and the calculated Poynting flux and energy density. Hence, whether the effect of the dielectric-loading model extends beyond the description of the vacuum dispersion to the growth of the wave(s) in the presence of the electron beam must be verified by comparison with both linear theories of

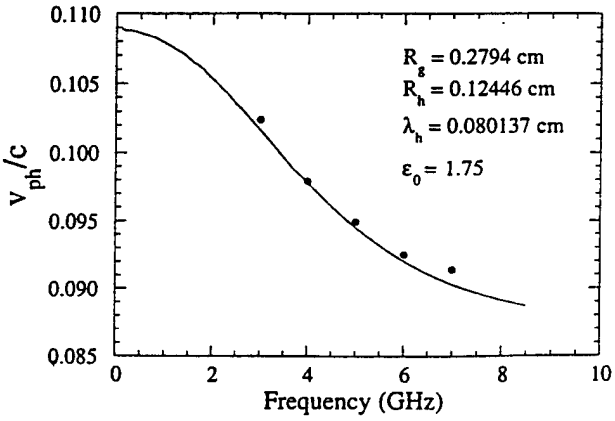

FIG. 3. Comparison of the dispersion in the cold Northrop–Grumman circuit with the solution of the cold helix dispersion equation.

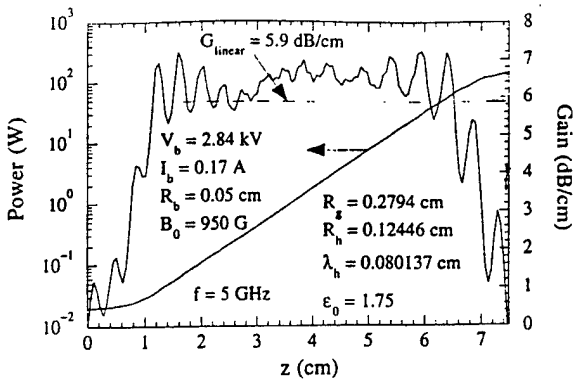

FIG. 4. Plots of the gain and power versus axial distance from the nonlinear simulation at a frequency of 5 GHz. Also shown is the gain as predicted by the linear theory (dashed line).

the interaction and experiment. We also remark that the linear theory used for this comparison[8] employs the same dielectric-loading model as GATOR, but solves the full eigenvector problem for the beam and dielectric-loaded helix. The difference, therefore, is that the linear theory does not use the vacuum helix mode expansion.

In simulation of the interaction, we assume an injected power of 20 mW with a rise time of 1 ns and a constant power thereafter, and a beam with a rise time of 1 ns as well and the voltage, current, and beam radius given above. The beam is modeled with ten annular rings injected per time step, which are initially uniformly spaced. We also assume an axial magnetic field of 950 G, which is close to the Brillouin field for this beam.

A plot of the simulation's predictions for the power and gain at 5 GHz as functions of axial distance is shown in Fig. 4. As is evident in Fig. 4, the power grows exponentially over the axial range of approximately 2–7 cm, and the bulk gain per unit length over this distance is approximately 6.2 dB/cm. The power saturates at a level of approximately 149 W over a distance of 7.5 cm for an efficiency of about 30.7%. This result is in substantial agreement with the linear theory. As indicated by the dashed line in Fig. 4, this value of the bulk gain is close to the value of 5.9 dB/cm found from the linear theory for a solid electron-beam model and an axial field of 950 G.[8] For comparison purposes, it should also be noted that the measured gain in the tube, after corrections for losses and attenuation, was observed to be approximately 6.0 dB/cm.[19]

A total of 15 radial modes were used in the example shown in Fig. 4 for completeness; however, convergence was achieved with fewer radial modes. The convergence properties of the space-charge field model for this example is illustrated in Table I, where we show the evolution of the bulk growth rate in the exponential gain regime and the saturated power with the number of radial modes at a frequency of 5 GHz. The term "bulk growth rate" here refers to the overall growth rate from the start of the exponential gain region to the onset of the nonlinear regime prior to saturation. As seen in Table I, the saturated power is relatively constant for any choice of the number of radial modes, and

TABLE I. Variation in the bulk growth rate and saturated power with the number of radial modes.

Number of radial modes	Bulk growth rate (dB/cm)	Saturated power (W)
1	6.33	149.0
2	6.25	149.4
3	6.23	149.3
4	6.23	149.1
5	6.23	149.0
6	6.23	148.9
7	6.23	149.0
8	6.23	148.9
9	6.23	148.7

the bulk growth rate converges to a value close to 6.23 dB/cm, using only three radial modes.

The fluctuations in the gain seen in GATOR can arise due to a variety of causes. In the first place, there are initial transients associated with the injection of the beam and the radiation into the helix, which contribute to the large oscillations in the growth rate near the entrance to the helix. In the second place, the detailed behavior of the electron beam over the course of the interaction also plays a role. One assumption underlying the linear theory is that of an electron beam with a uniform radial profile, as well as a fixed phase space distribution. However, in GATOR, as well as in an actual tube, the radial extent of the beam may vary over the course of the interaction and the phase space distribution will also evolve as the beam loses energy and oscillates and becomes trapped in the troughs of the growing wave. These effects can result in the gain fluctuations. Plots of the variation in the axial momentum and the radial position of the beam versus axial position are shown in Fig. 5, corresponding to the case shown in Fig. 4. The large oscillations in the radial extent of the beam, as well as the oscillation in the axial phase space, seen in Fig. 5 account for some of the

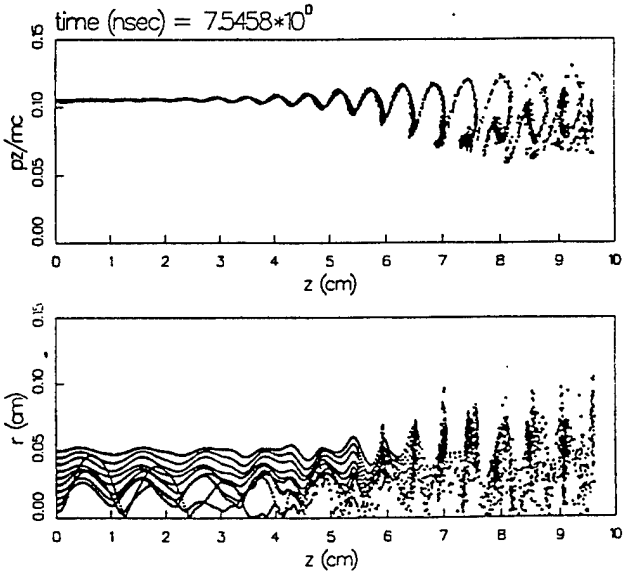

FIG. 5. Plots showing the axial evolution of the phase space and the radial structure of the electron beam.

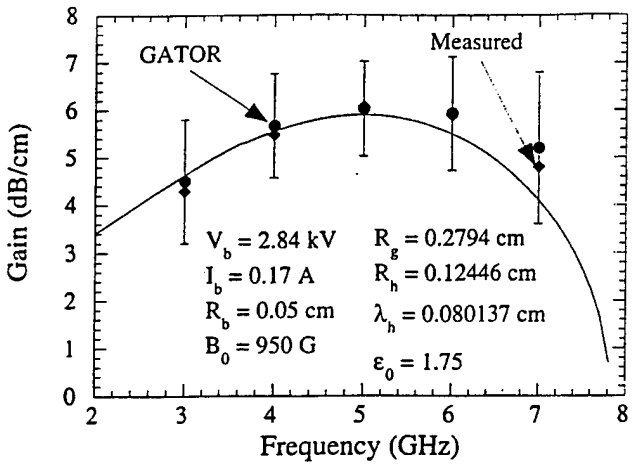

FIG. 6. Plots of the gain versus frequency corresponding to the linear theory (solid line), GATOR (circles), and the measured gain at Northrop–Grumman (diamonds). The "error bars" indicate the level of fluctuations in the gain observed in GATOR.

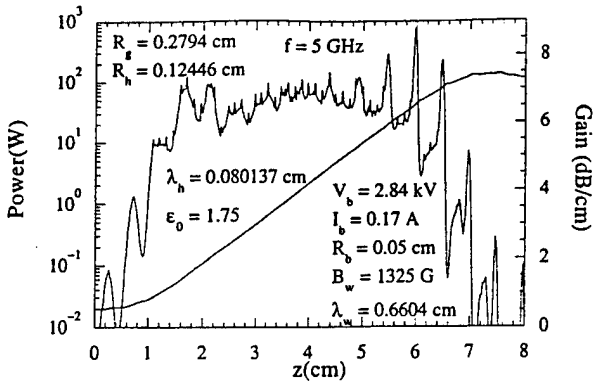

FIG. 7. Plot of the power versus axial distance for the PPM focusing model.

aforementioned fluctuations in the gain. In addition, the form of the source currents used in determining the evolution of the helix and space-charge waves involves the overlap of the current with the wave polarization. This implicitly includes beat phenomena between the wave period and all the myriad oscillations in the beam current and envelope. The beating phenomena become still more complex once the electrons become trapped in the troughs of the helix wave and experience the additional large oscillatory motion associated with trapped orbits, and this can contribute to the large oscillations in the growth rate near the exit from the helix.

The importance of the space charge to the configuration under study is evident from comparison with earlier results for these parameters obtained without space charge in the model.[17] In particular, the results obtained without space charge yield a gain at 5 GHz of approximately 7.4 dB/cm and an efficiency of about 34.6%. As such, the inclusion of space-charge effects results in a degradation of the interaction for these parameters. One reason for this degradation in performance, when space-charge effects are included, is the effect of the space-charge fields on the bunching of the beam. This is evident by a comparison of the phase space shown in Fig. 5 with the equivalent phase space obtained without the inclusion of space-charge effects, which is shown in Fig. 11 of Ref. 17. Comparison of these two figures indicates that the trapped electron dynamics is much more regular without the presence of the space-charge forces.

We also compare the variation in the gain with frequency as found in the linear theory, GATOR, and as measured at Northrop–Grumman.[19] The results of this comparison are shown in Fig. 6, where the solid line denotes the linear theory, the diamonds are the measured gains at Northrop–Grumman, and the circles are from GATOR. Note that the "error bars" denote the limits on the fluctuations observed in the gain in GATOR. Observe that GATOR is in close agreement with the measured gain across the frequency band. In addition, GATOR is close to the linear theory for frequencies below 6 GHz, and the predictions of linear theory fall within the fluctuation range seen in GATOR over the entire frequency band.

These comparisons between GATOR and the linear theory for solenoid focusing represent a good validation of the nonlinear formulation. However, the actual tube built at Northrop–Grumman employed PPM rather than solenoid focusing. The on-axis strength for the PPM was chosen to correspond to a Brillouin beam in a solenoid, which accounts for the agreement seen between both the linear theory and GATOR with the measured gain. However, it is also important to compare GATOR with PPM focusing and the Northrop–Grumman measurements. To this end, we employ a PPM field model with an on-axis field strength of 1325 G with a period of 0.6604 cm. The evolution of the power and growth rate with axial distance at 5 GHz for this PPM field is shown in Fig. 7. The bulk gain for this example is 6.5 dB/cm and saturation is found at a level of 131 W over a distance of 6.9 cm. These results are within 5% of those found with solenoid focusing, and exhibit a similar series of oscillations in the instantaneous values of the growth rate. Finally, the evolution of the axial phase space and the radial structure of the

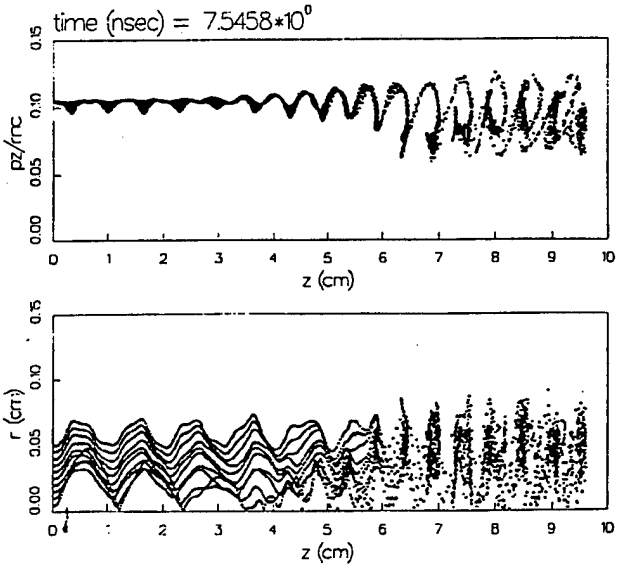

FIG. 8. Plots showing the axial evolution of the phase space and the radial structure of the electron beam for the PPM focusing model.

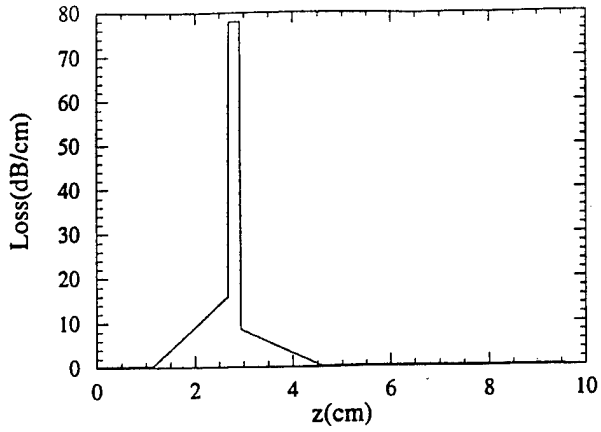

FIG. 9. Attenuation profile in the Northrop–Grumman TWT.

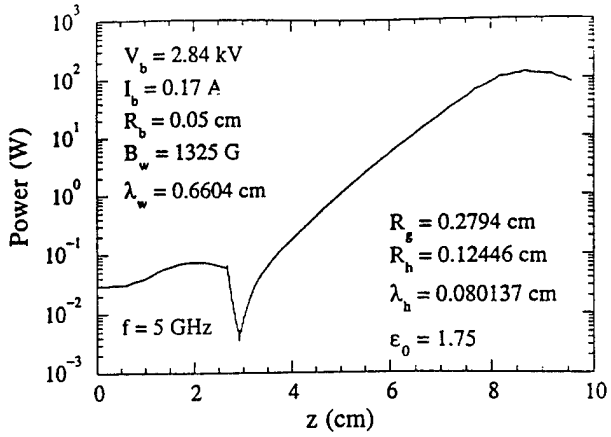

FIG. 10. Evolution of the power in the Northrop–Grumman TWT.

electron beam for the PPM field are shown in Fig. 8. Comparison of Figs. 8 and 5 for the solenoidal field shows substantial similarities. The principal difference lies in the increased fluctuation in the radial structure of the beam, which is expected, due to the nature of the periodic structure of the PPM field.

The aforementioned comparisons between GATOR and the experiment at Northrop–Grumman represent a simplified model that neglects loss and attenuation in the tube, and was studied because it is convenient in the comparison of the linear gain. In order to compare GATOR with the nonlinear behavior of the experiment, we must include losses and attenuation. The actual TWT under consideration was structured to have separate input and output sections separated by a sever, and there are regions of enhanced attenuation both preceding and following the sever in order to minimize reflections.[19] The loss/attenuation profile is illustrated in Fig. 9. The input section is 2.667 cm in length, and there is an overall loss rate of 0.31 dB/cm in the input section. Starting at 1.143 cm from the entrance to the helix, the attenuation rate is gradually increased from that value up to 15.8 dB/cm at the start of the sever, which occurs at 2.667 cm after the entrance to the helix. The sever is modeled by a region of high attenuation (78 dB/cm) over a length 0.254 cm. The attenuation in the output section ramps down from a value of 8.56 dB/cm to the background loss rate of 0.267 dB/cm over a length of 1.651 cm and remains at that value over the remainder of the helix, which is a total length of 9.576 cm.

We first consider the injection of a 30 mW drive signal into the helix using PPM focusing (for the parameters shown in Fig. 7) and the loss profile shown in Fig. 9. The evolution of the power as a function of axial distance through the helix is shown in Fig. 10. The power grows only marginally in the input section and is severely damped in the region of the sever. However, the exponential growth rate found in the output section corresponds to that found in the simpler circuit used in Fig. 7, which at 6.5 dB/cm is about 8% higher than observed in the TWT. In addition, the power saturates at approximately 126 W. This is somewhat higher than the 100 W of saturated power observed in the TWT at Northrop–Grumman.[19] One possible explanation for the discrepancy in the saturated power is that higher frequency harmonics in the space-charge field become important in the nonlinear regime, and this effect is not included in the model at the present time.

IV. SUMMARY AND DISCUSSION

In this paper, we have described a nonlinear formulation of the interaction of an electron beam in a helix TWT. The present study describes a simplified configuration in which a single frequency wave propagates through a helix with a uniform period and dielectric loading. However, the formulation is able to treat a more general problem that includes both dielectric and vane loading with a tapered period. Further, the formulation is in the time domain and is able to treat the propagation of multiple radiation pulses (propagating both in the forward and backward directions) through the helix structure (including the intermodulation between the waves), as well as both continuous and emission-gated electron beams.

The formulation has been compared with a linear theory of the interaction,[8] as well as with helix TWT experiments, and good agreement has been obtained. The gain found in the linear regime is typically in agreement with both the linear theory and the experimental measurements to within about 8%. The discrepancy between the saturated power seen in the simulation and in the experiment is somewhat larger (26%, for the example shown). It is speculated that the discrepancy may be due to frequency harmonics in the space-charge field, which become important in the nonlinear regime. This is presently under investigation. In general, however, it is found that the essential characteristics of the interaction in the helix TWT can be well described by the nonlinear simulation once the effective dielectric constant and vane radius for the vacuum helix have been determined. Good estimates of the effective dielectric constant can be obtained using a relatively straightforward volume-weighted average; however, refinements in the estimates of these parameters can be made by comparison of the predicted cold helix dispersion properties with the measured phase velocities of the cold helix.

The fundamental dynamical equations for the fields are quite general in form, and rely largely on a knowledge of the dispersion, polarization, energy density, and Poynting flux for the waves under consideration. Thus, the technique is readily generalized to other configurations and structures. For example, it is straightforward to include reflections at either end of the interaction length and deal with cavities and oscillator configurations.

ACKNOWLEDGMENTS

The authors would like to acknowledge helpful technical discussions with G. Groshart, Dr. D. Whaley, and Dr. T. M. Antonsen, Jr. This work was supported by the Office of Naval Research and the Office of Naval Technology. The computational work was supported in part by grants of High Performance Computing (HPC) time from the Department of Defense HPC Shared Resource Centers CEWES and NAVO.

[1]J. R. Pierce and L. M. Field, Proc. IRE **35**, 108 (1947).
[2]J. R. Pierce, Proc. IRE **35**, 111 (1947).
[3]J. R. Pierce, *Traveling-Wave Tubes* (Van Nostrand, New York, 1950).
[4]O. E. H. Rydbeck, Ericsson Tech. **46**, 3 (1948).
[5]L. J. Chu and J. D. Jackson, Proc. IRE **36**, 853 (1948).
[6]H. P. Freund, M. A. Kodis, and N. R. Vanderplaats, IEEE Trans. Plasma Sci. **20**, 543 (1992).
[7]H. P. Freund, N. R. Vanderplaats, and M. A. Kodis, IEEE Trans. Plasma Sci. **21**, 654 (1993).
[8]H. P. Freund, E. G. Zaidman, M. A. Kodis, and N. R. Vanderplaats, IEEE Trans. Plasma Sci. **24**, 895 (1996).
[9]L. Brillouin, J. Appl. Phys. **20**, 1196 (1949).
[10]A. Nordsieck, Proc. IRE **41**, 630 (1953).
[11]P. K. Tien, L. R. Walker, and V. M. Wolontis, Proc. IRE **43**, 260 (1955).
[12]J. E. Rowe, IRE Trans. Electron Devices **ED-3**, 39 (1956).
[13]J. E. Rowe, *Nonlinear Electron-Wave Interaction Phenomena* (Academic, New York, 1965).
[14]I. J. Morey and C. K. Birdsall, IEEE Trans. Plasma Sci. **18**, 482 (1990).
[15]R. J. Faehl, B. S. Newberger, and B. B. Godfrey, Phys. Fluids **23**, 2440 (1980).
[16]B. Goplen, D. Smithe, K. Nguyen, M. A. Kodis, and N. R. Vanderplaats, *International Electron Devices Meeting Technical Digest* (Institute of Electrical and Electronics Engineers, Piscataway, NJ, 1992), pp. 759–762.
[17]H. P. Freund, E. G. Zaidman, and T. M. Antonsen, Jr., Phys. Plasmas **3**, 3145 (1996).
[18]K. A. Hoffman, *Computational Fluid Dynamics for Engineers* (Engineering Education System, Austin, TX, 1989), p. 171.
[19]G. Groshart, Northrop–Grumman Corp. (private communication, 1996).

APPENDIX XVI

Linearized Field Theory of a Dielectric-Loaded Helix Traveling Wave Tube Amplifier

H.P. Freund, E.G. Zaidman, M.A. Kodis, and N.R. Vanderplaats

IEEE Trans. Plasma Sci. **24**, 895 (1996)

Linearized Field Theory of a Dielectric-Loaded Helix Traveling Wave Tube Amplifier

H. P. Freund, Ernest G. Zaidman, *Member, IEEE,* Mary Anne Kodis, and N. R. Vanderplaats

Abstract— A linearized relativistic field theory of a helix traveling wave tube (TWT) is presented for a configuration where either a thin annular beam or a solid beam propagates through a sheath helix enclosed within a loss-free wall in which the gap between the helix and the outer wall is filled with a dielectric. A linear analysis of the interaction is solved subject to the boundary conditions imposed by the beam, helix, and wall. In the case of the annular beam, the electrons are assumed to be strongly magnetized. In contrast, the effect of variations in the axial magnetic field are included in the electron dynamics for the solid beam analysis. Determinantal dispersion equations are obtained for the azimuthally symmetric modes which implicitly includes beam space-charge effects without recourse to a heuristic model of the space-charge field. Numerical solutions of the dispersion equations are discussed and compared with experiments.

I. Introduction

THE BASIC theory of the helix traveling wave tube (TWT) was first developed by Pierce and co-workers [1]–[3] some four decades ago based upon a coupled-wave analysis utilizing the vacuum modes of the helix and the positive and negative energy space-charge waves of the beam. Improved theories based upon a more complete electromagnetic analysis of Maxwell's equations in the helix have also been developed by Rydbeck [4] and Chu and Jackson [5]. Detailed analyses of both the coupled-wave and field theories of the TWT are given by Beck [6] and Hutter [7]. More recently, field theories have appeared which included more realistic effects such as the presence of the outer conducting shell [8] and the tape helix [9] have also appeared.

In this paper, we develop a linearized relativistic field theory of the helix TWT by solution of the relativistic fluid equations and Maxwell's equations in a configuration which consists of the propagation of either a thin annular electron beam or a solid electron beam down the axis of a dielectric-loaded sheath helix enclosed by a loss-free conducting wall. The essential idealizations we make are that the gap between the helix and the outer wall is uniformly filled with a dielectric material. Within the context of this model, we divide the cross section of the TWT into three regions: 1) within the beam, 2) between the beam and the helix, and 3) between the helix and the wall. In the treatment of the annular beam, the electrons are assumed to be strongly magnetized in order to simplify the description of the electron dynamics. However, this assumption is not imposed in the treatment of the solid beam, in which case we treat the effect of variations in the axial magnetic field on the electron dynamics. The dispersion equation which determines both the propagation and gain of the modes in the helix is determined by application of the boundary conditions at the position of the beam, helix, and wall to the solutions of Maxwell's equations within these three regions. Note that the assumption of a thin annular beam imposes a jump condition on the parallel electric field at the beam radius. The effects of beam space-charge are implicitly included in the analysis.

Manuscript received October 25, 1995; revised January 2, 1996. This work was supported by the Office of Naval Research.

H. P. Freund is with the Science Applications International Corporation, McLean, VA 22102 USA and the Vacuum Electronics Branch, Naval Research Laboratory, Washington, D.C. 20375 USA (e-mail: freund@mmwave.nrl.navy.mil).

E. G. Zaidman, M. A. Kodis, and N. R. Vanderplaats are with the Vacuum Electronics Branch, Naval Research Laboratory, Washington, D.C. 20375 USA.

Publisher Item Identifier S 0093-3813(96)04644-9.

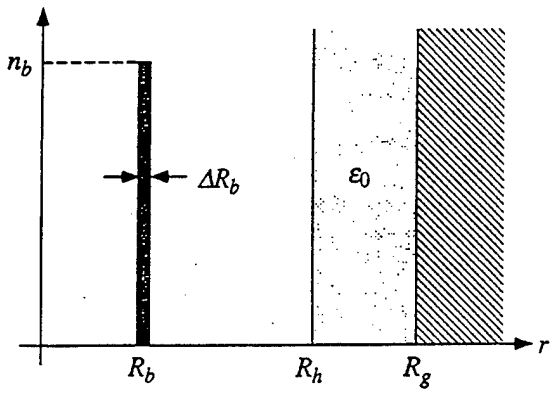

Fig. 1. Schematic representaion of the physical configuration for the thin annular beam.

II. The Case of an Annular Beam

The equilibrium configuration is shown schematically in Fig. 1. We consider the propagation of a thin annular beam through a sheath helix-loaded cylindrical drift tube. Hence, the equilibrium current density of the electron beam is described via an azimuthally symmetric charge density

$$n_0(r) = n_b \Delta R_b \delta(r - R_b) \tag{1}$$

where n_b denotes the beam density, and R_b and ΔR_b denote the mean radius and thickness of the annulus, respectively. The subscript "0" is used throughout to denote equilibrium quantities. The beam is assumed to propagate uniformly along the symmetry [i.e., z] axis of the system, and we take the equilibrium velocity to be $v_0 = v_0 \hat{e}_z$. The beam is assumed to be strongly magnetized.

The circuit configuration describes a sheath helix located within a cylindrical waveguide of radius R_g. The dielectric loading is included under the assumption that the gap between the helix and the outer wall is uniformly filled with a material having a dielectric constant ε_0. The sheath helix model assumes that the conducting wires of the helix are thin enough that the helix can be modeled by a thin conducting cylindrical sheet of radius $R_h[< R_g]$, and with a pitch angle ϕ. Hence, the unit vector describing the pitch of the helix is $\hat{e}_\phi = \hat{e}_\theta \cos\phi + \hat{e}_z \sin\phi$ where for a helix period of λ_h and wavenumber $k_h[\equiv 2\pi/\lambda_h]$

$$\tan\phi = \frac{1}{k_h R_h}. \tag{2}$$

A. Maxwell's Equations

The perturbed current density and beam velocity are obtained by perturbation analysis in which we expand $n = n_0 + \delta n$ and $\boldsymbol{v} = \boldsymbol{v}_0 + \delta\boldsymbol{v}$. From the analysis in [8], the perturbed source current can be expressed as

$$\delta\hat{J} \cong \frac{i}{4\pi}\frac{\omega_b^2}{\delta\omega}\Delta R_b \delta(r - R_b) \cdot \left[\frac{\omega}{\gamma_0^2\Delta\omega}\hat{e}_z\hat{e}_z \cdot \delta\hat{E} + \delta\hat{E}_\perp + \beta_0\hat{e}_z \times \delta\hat{B}\right] \tag{3}$$

where $\omega_b^2 \equiv 4\pi e^2 n_b/\gamma_0 m_e$ denotes the square of the plasma frequency, e and m_e denote the electron charge and rest mass, $\beta_0 \equiv v_0/c, \gamma_0 \equiv (1-\beta_0^2)^{-1/2}, \Delta\omega \equiv \omega - kv_0$ for angular frequency ω and wavenumber k, $\delta\boldsymbol{E}$ and $\delta\boldsymbol{B}$ denote the fluctuating electric and magnetic fields, and the perturbed quantities are obtained by a Fourier analysis in which the perturbed quantities are assumed to vary as $\delta f(\boldsymbol{x},t) = \delta\hat{f}(r)\exp(ikz - i\omega t)$. A similar form is found for the perturbed charge density

$$\delta\hat{\rho} \cong \frac{i}{4\pi}\frac{\omega_b^2}{\gamma_0^2\Delta\omega^2}k\Delta R_b\delta(r - R_b)\hat{e}_z \cdot \delta\hat{E}. \tag{4}$$

Solution for the dispersion equation involves the substitution of these sources into Maxwell's equations subject to the appropriate boundary and jump conditions.

Maxwell's equations for the axial components of the fluctuating electric and magnetic fields are found using the sources and can be written in the form

$$[\nabla_\perp^2 + \kappa^2]\delta\hat{E}_z \cong \frac{\omega_b^2}{\gamma_0^2\Delta\omega^2}\kappa^2\Delta R_b\delta(r - R_b)\delta\hat{E}_z \tag{5}$$

and

$$[\nabla_\perp^2 + \kappa^2]\delta\hat{B}_z \cong 0 \tag{6}$$

where $\kappa^2 \equiv \varepsilon(r)\omega^2/c^2 - k^2$ and

$$\varepsilon(r) = \begin{cases} 1; & 0 \le r < R_h \\ \varepsilon_0; & R_h \le r \le R_g \end{cases} \tag{7}$$

denotes the radial variation of the dielectric coefficient. The transverse components of these fields are given by

$$\delta\hat{E}_r = \frac{ik}{\kappa^2}\frac{\partial}{\partial r}\delta\hat{E}_z \tag{8}$$

$$\delta\hat{E}_\theta = -\frac{i\omega/c}{\kappa^2}\frac{\partial}{\partial r}\delta\hat{B}_z \tag{9}$$

$$\delta\hat{B}_r = \frac{ik}{\kappa^2}\frac{\partial}{\partial r}\delta\hat{B}_z \tag{10}$$

$$\delta\hat{B}_\theta = \frac{i\varepsilon(r)\omega/c}{\kappa^2}\frac{\partial}{\partial r}\delta\hat{E}_z. \tag{11}$$

These equations must be solved for the specific charge and current densities under consideration. Observe that we have neglected the effect of the beam current on the transverse components of the field since the beam is assumed to be a thin annulus and contributes only at $r = R_b$.

These equations are consistent with the physical mechanism in a TWT in that the primary wave-particle coupling is between the axial motion of the beam and the axial component of the electric field. Hence, it is not surprising that the equation for the axial component of the magnetic field is simply the homogeneous wave equation. Note also that the source term for the axial electric field in (4) corresponds to a delta-function in radius; hence, the solution for the axial electric field can be expressed in terms of a jump condition in the radial derivative of the electric field.

In order to obtain the jump condition, we integrate (5) across the beam as follows:

$$\frac{1}{R_b}\lim_{\delta\to 0}\int_{R_b-\delta}^{R_b+\delta} dr r[\nabla_\perp^2 + \kappa^2]\delta\hat{E}_z = \frac{\omega_b^2}{\gamma_0^2\Delta\omega^2}\kappa^2\Delta R_b\delta\hat{E}_z(R_b) \tag{12}$$

which expresses the discontinuity in the derivative of the axial electric field.

B. The Dispersion Equation

The solutions of Maxwell's equations can be expressed in the three regions as follows:

$$\delta\hat{E}_z = \begin{cases} A_e J_0(pr); & \text{I} \\ B_e J_0(pr) + C_e Y_0(pr); & \text{II} \\ D_e J_0(qr) + E_e Y_0(qr); & \text{III} \end{cases} \tag{13}$$

and

$$\delta\hat{B}_z = \begin{cases} A_b J_0(pr); & \text{I} \\ B_b J_0(pr) + C_b Y_0(pr); & \text{II} \\ D_b J_0(qr) + E_b Y_0(qr); & \text{III} \end{cases} \tag{14}$$

where $p^2 \equiv \omega^2/c^2 - k^2, q^2 \equiv \varepsilon_0\omega^2/c^2 - k^2, J_n$ and Y_n denote the regular Bessel and Neumann functions, and the three regions indicated are: region I is $0 \le r \le R_b$, region II denotes $R_b < r \le R_h$, and region III denotes $R_h < r \le R_g$. Application of the jump and boundary conditions permits the elimination of the unknown coefficients and the derivation of the determinantal equation which governs the dispersion of the wave.

A statement of the boundary conditions is fairly straightforward. For convenience, we define

$$W_{m,n}(x,y) \equiv Y_m(x)J_n(y) - J_m(x)Y_n(y). \tag{15}$$

The boundary conditions at the waveguide wall require that the tangential component of the electric field and the normal component of the magnetic field must vanish, hence, $\delta\hat{E}_z(r = R_g) = \delta\hat{E}_\theta(r = R_g) = 0$ and $\delta\hat{B}_r(r =$

$R_g) = 0$. As a result, $E_e = -D_e J_0(qR_g)/Y_0(qR_g)$ and $E_b = -D_b J_1(qR_g)/Y_1(qR_g)$. We also require that $\delta\hat{E}_\theta$ must be continuous at $r = R_b$ and R_h, and that $\delta\hat{B}_z$ must be continuous at $r = R_b$. These conditions imply that $A_b J_0(pR_b) = B_b J_0(pR_b) + C_b Y_0(pR_b)$, $A_b J_1(pR_b) = B_b J_1(pR_b) + C_b Y_1(pR_b)$, and $B_b J_1(pR_h) + C_b Y_1(pR_h) = (p/q) D_b W_{1,1}(qR_g, qR_h)$, hence, $B_b = A_b, C_b = 0$, and $D_b = (q/p) A_b J_1(pR_h)/W_{1,1}(qR_g, qR_h)$. We must also require that $\delta\hat{E}_z$ must be continuous at $r = R_b$ and R_h, hence, $W_{0,0}(pR_b, pR_h)B_e = J_0(pR_b)[D_e Y_0(pR_b) - A_e J_0(pR_h)]$ and $W_{0,0}(pR_b, pR_h)C_e = -J_0(pR_b)[D_e J_0(pR_b) - A_e Y_0(pR_h)]$. As a result, the electric and magnetic fields can be written as (16) shown at the bottom of the page and

$$\delta\hat{B}_z = A_b \begin{cases} J_0(pr); & 0 \le r \le R_h \\ \dfrac{q}{p} J_1(pR_h) \dfrac{W_{1,0}(qR_g, qr)}{W_{1,1}(qR_g, qR_h)}; & R_h < r \le R_g. \end{cases} \tag{17}$$

Observe that the expression for $\delta\hat{B}_z$ is unaffected by the beam. The D_e coefficient may be eliminated by application of the jump condition, which yields

$$D_e = \frac{c^2 \varepsilon_{sc}(\omega, k)}{\Delta\omega^2} A_e \frac{J_0(pR_h)}{J_0(pR_b)} \tag{18}$$

where

$$\varepsilon_{sc}(\omega, k) \equiv \frac{\Delta\omega^2}{c^2} - \frac{\omega_b^2 \sigma_b}{4\gamma_0^2 c^2} p^2 \frac{J_0(pR_b)}{J_0(pR_h)} W_{0,0}(pR_b, pR_h) \tag{19}$$

is the dispersion function for the beam space-charge waves, $\sigma_b = 2\pi R_b \Delta R_b$ is the cross-sectional area of the beam. As a consequence, the axial electric field can be expressed as (20) shown at the bottom of the page.

The problem has now been reduced to two unknown coefficients, A_e and A_b, in (17) and (20). The dispersion equation is obtained after imposition of two remaining boundary conditions. The first condition is that the tangential component of the electric field must be perpendicular to the direction of the helix, which requires that in the limit in which $\delta \to 0$

$$\delta\hat{E}_z(R_h \pm \delta)\sin\phi + \delta\hat{E}_\theta(R_h \pm \delta)\cos\phi = 0. \tag{21}$$

This implies that

$$\frac{c^2 \varepsilon_{sc}(\omega, k)}{\Delta\omega^2} A_e J_0(pR_h)\tan\phi = -\frac{i\omega}{cq} A_b J_1(pR_h). \tag{22}$$

The second boundary condition is that the tangential components of the magnetic field parallel to the helix must be continuous, which can be expressed in the limit in which $\delta \to 0$ as

$$\begin{aligned} &\delta\hat{B}_z(R_h - \delta)\sin\phi + \delta\hat{B}_\theta(R_h - \delta)\cos\phi \\ &\quad = \delta\hat{B}_z(R_h + \delta)\sin\phi + \delta\hat{B}_\theta(R_h + \delta)\cos\phi \end{aligned} \tag{23}$$

which implies

$$\begin{aligned} A_b \tan\phi &\left[J_0(pR_h) - \frac{q}{p} J_0(pR_h) \frac{W_{1,0}(qR_g, qR_h)}{W_{1,1}(qR_g, qR_h)} \right] \\ &= \frac{i\omega}{cp} A_e \left\{ \frac{c^2 \varepsilon_{sc}(\omega, k)}{\Delta\omega^2} \left[J_1(pR_h) \right.\right. \\ &\quad \left. - \frac{\varepsilon_0 p}{q} J_0(pR_h) \frac{W_{1,0}(qR_h, qR_g)}{W_{1,1}(qR_g, qR_h)} \right] \cdot \\ &\quad \left. + \frac{2}{\pi} \frac{1}{pR_h} \frac{J_0(pR_b)}{W_{0,0}(pR_b, pR_h)} \left[\frac{c^2 \varepsilon_{sc}(\omega, k)}{\Delta\omega^2} - 1 \right] \right\}. \end{aligned} \tag{24}$$

The dispersion equation is found by setting the determinant of the coefficients in (22) and (24) equal to zero, and we find (25) and (26) [shown at the top of the next page] where (26) is the dispersion function for the vacuum helix.

The limit in which the dielectric loading vanishes is one in which $\varepsilon_0 \to 1$ and $q \to p$. Noting that

$$\begin{aligned} \lim_{\varepsilon_0 \to 1} &\left[J_1(pR_h) W_{0,0}(qR_g, qR_h) \right. \\ &\left. + \frac{\varepsilon_0 p}{q} J_0(pR_h) W_{1,0}(qR_h, qR_g) \right] = -\frac{2}{\pi} \frac{J_0(pR_g)}{pR_h} \end{aligned} \tag{27}$$

$$\begin{aligned} \lim_{\varepsilon_0 \to 1} &\left[J_0(pR_h) W_{1,1}(qR_g, qR_h) \right. \\ &\left. - \frac{q}{p} J_1(pR_h) W_{1,0}(qR_g, qR_h) \right] = \frac{2}{\pi} \frac{J_1(pR_g)}{pR_h} \end{aligned} \tag{28}$$

$$\delta\hat{E}_z = \begin{cases} A_e J_0(pr); & \text{I} \\ \dfrac{J_0(pR_b)}{W_{0,0}(qR_b, qR_h)} [D_e W_{0,0}(pR_b, pr) - A_e W_{0,0}(pR_h, pr)]; & \text{II} \\ D_e J_0(pR_b) \dfrac{W_{0,0}(qR_g, qr)}{W_{0,0}(qR_g, qR_h)} & \text{III} \end{cases} \tag{16}$$

$$\delta\hat{E}_z = A_e \begin{cases} J_0(pr); & \text{I} \\ \dfrac{J_0(pR_b)}{W_{0,0}(qR_b, qR_h)} \left[\dfrac{c^2 \varepsilon_{sc}(\omega, k)}{\Delta\omega^2} \dfrac{J_0(pR_h)}{J_0(pR_b)} W_{0,0}(pR_b, pr) - W_{0,0}(pR_h, pr) \right]; & \text{II} \\ \dfrac{c^2 \varepsilon_{sc}(\omega, k)}{\Delta\omega^2} \dfrac{J_0(pR_h)}{W_{0,0}(qR_g, qR_h)} W_{0,0}(qR_g, qr); & \text{III} \end{cases} \tag{20}$$

$$\Lambda(\omega,k)\epsilon_{sc}(\omega,k) = \frac{2}{\pi}\frac{p}{R_h}\frac{\omega_b^2\sigma_b}{4\gamma_0^3c^2}\frac{\omega^2}{c^2}\frac{J_0^2(pR_b)}{J_0(pR_h)} \times \frac{W_{0,0}(pR_g,pR_h)}{\left[J_1(pR_h)W_{0,0}(qR_g,qR_h)+\frac{\epsilon_0 p}{q}J_0(pR_h)W_{1,0}(qR_h,qR_g)\right]} \tag{25}$$

$$\Lambda(\omega,k) \equiv \frac{\omega^2}{c^2} - p^2\tan^2\phi\frac{J_0(pR_h)}{J_1(pR_h)}\frac{W_{0,0}(qR_g,qR_h)}{W_{1,1}(qR_g,qR_h)} \times \frac{\left[J_0(pR_h)W_{1,1}(qR_g,qR_h)-\frac{q}{p}J_1(pR_h)W_{1,0}(qR_g,qR_h)\right]}{\left[J_1(pR_h)W_{0,0}(qR_g,qR_h)+\frac{\epsilon_0 p}{q}J_0(pR_h)W_{1,0}(qR_h,qR_g)\right]} \tag{26}$$

and

$$\lim_{\epsilon_0\to 1}\Lambda(\omega,k) = \frac{\omega^2}{c^2} + p^2\tan^2\phi \cdot \frac{J_0(pR_h)J_1(pR_g)}{J_0(pR_g)J_1(pR_h)}\frac{W_{0,0}(qR_g,qR_h)}{W_{1,1}(qR_g,qR_h)} \tag{29}$$

we find that the dispersion equation reduces to

$$\Lambda(\omega,k)\epsilon_{sc}(\omega,k) = -\frac{\omega_b^2\sigma_b}{4\gamma_0^2c^2}\frac{\omega^2}{c^2}p^2\frac{J_0^2(pR_b)}{J_0(pR_h)J_0(pR_g)} \cdot W_{0,0}(pR_g,pR_h) \tag{30}$$

which is in agreement with that found in [7].

C. Numerical Analysis

The dispersion equation (25) is solved for a specific choice of helix, waveguide, and beam parameters. For the purposes of this discussion, we choose a helix period and radius of 0.082 042 and 0.124 46 cm, respectively, and an outer wall radius of 0.2794 cm. Variations in the value of the dielectric constant will then illustrate the effect of dielectric loading. Note that the motivation for this specific choice of parameters is to give maximum gain in the neighborhood of 5 GHz for a 3 kV electron beam.

We first consider the cold (i.e., in the absence of the beam) dispersion of the system and plot the frequency versus wavenumber for $\epsilon_0 = 1$, 1.75, and 3.5 in Fig. 2. Note that the choice of $\epsilon_0 = 1$ corresponds to the absence of any dielectric material. It is clear from the figure that the effect of the dielectric is to 1) progressively reduce the frequency at a given wavenumber as the dielectric constant increases, and 2) to flatten the dispersion curve. This can also be illustrated by consideration of the phase velocity. The phase velocity is plotted versus frequency in Fig. 3 for the family of dispersion curves shown in Fig. 2. As a result, the bandwidth of the interaction can be expected to increase under the action of the dielectric.

The cold dispersion solutions have been compared with the measured dispersion of a test circuit constructed at Northrop–Grumman Corporation [10]. This circuit has the same helix and wall dimensions used in Figs. 2 and 3, but instead of a uniform dielectric material filling the gap between the helix and the wall, three dielectric rods spanning the gap between the helix and the outer wall and running the length of the helix (with a dielectric constant of 6.5 and a thickness of 0.051 cm) were used to support the helix. In order to test

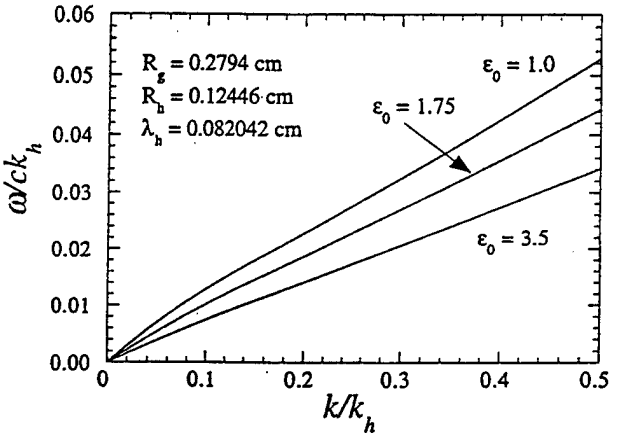

Fig. 2. Plot of frequency versus wavenumber for several choices of the dielectric constant.

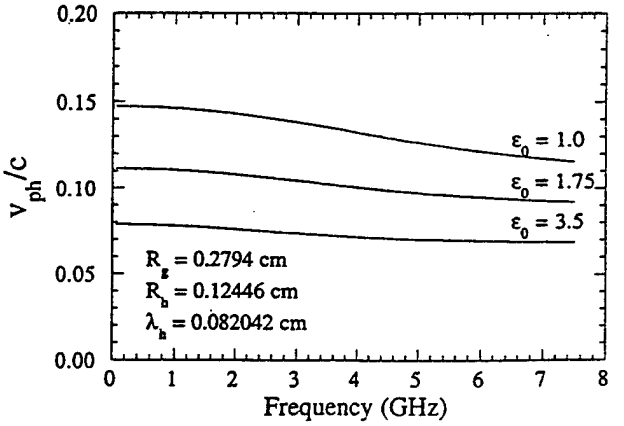

Fig. 3. Variation of the phase velocity with frequency for several choices of the dielectric constant.

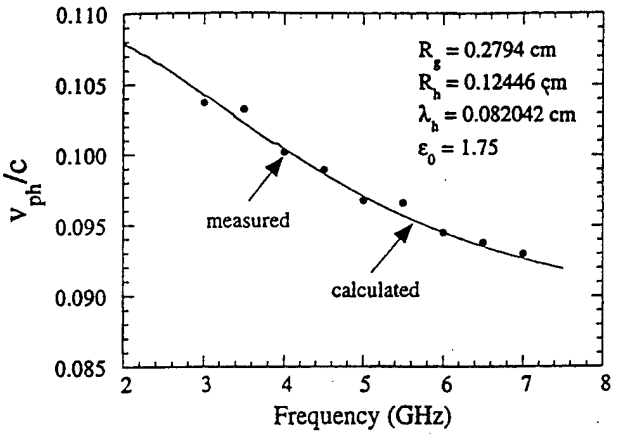

Fig. 4. Comparison of the theory with cold test measurements (dots) from a helix TWT.

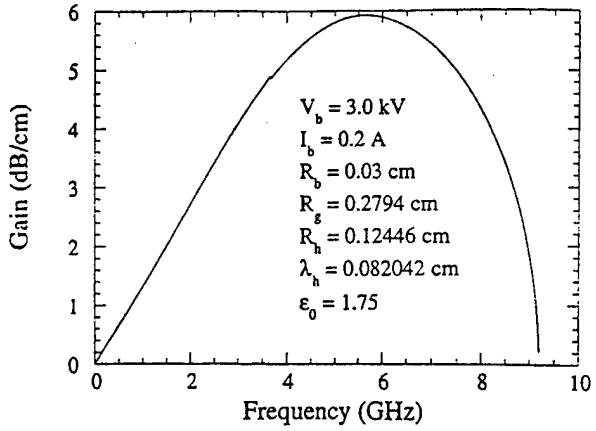

Fig. 5. Plot of the gain versus frequency for a dielectric-loaded helix.

the utility of the present model in describing a real circuit, we varied ε_0 in the present model to determine the level of agreement which could be achieved over a broad bandwidth. The results of this comparison are shown in Fig. 4 in which we plot the variation in the phase velocity versus frequency as calculated using (25) and as measured (dots) over frequencies up to 7.5 GHz for $\varepsilon_0 = 1.75$. It is evident from the figure that the agreement is very good over a broad band of frequencies extending from 3 GHz up to 7 GHz, and we conclude that the effect of the dielectric rods can be modeled using the uniform dielectric loading with an effective dielectric constant of 1.75.

The effective dielectric constant can be estimated in a straightforward way under the assumptions that the effect of the rods do not greatly perturb the field structures and that the field is approximately parallel to the rods. As such, the effective dielectric constant can be determined from an estimate of the energy densities in the stored fields in the vacuum and the dielectric, and the effective dielectric constant is given by a volume weighted average in which $\varepsilon_{\text{eff}} \approx (V_{\text{rod}}\varepsilon_{\text{rod}} + V_{\text{vac}})/V_{\text{tot}}$ where V_{rod} and ε_{rod} are the volume and dielectric constant of the rod, V_{vac} is the volume of the vacuum in the gap between the helix and the outer wall, and V_{tot} is the total volume in the gap between the helix and the wall. Of course, this formula is expected to yield only an approximation to the effective dielectric constant. For the parameters of interest, however, we find that $\varepsilon_{\text{eff}} \approx 1.66$ which is reasonably close to the value of 1.75 found above.

The gain is plotted as a function of frequency in Fig. 5 for $\varepsilon_0 = 1.75$, a beam voltage of 3 kV, a current of 0.2 A, and a beam radius of 0.3 cm. As shown in the figure, the gain band extends to frequencies up to approximately 9 GHz with a peak gain of $\approx$6 dB/cm at a frequency of approximately 5.6 GHz.

The variation in the phase velocity as a function of frequency is shown in Fig. 6 for both the hot (beam-loaded) and cold cases. It is clear from the figure that the effect of the beam is to flatten the dispersion still further relative to the cold helix. In addition, the phase velocity is reduced relative to the cold helix for the low frequency portion of the gain band, but increased in the high frequency range. Note, however, that this behavior is also found in the absence of the dielectric.

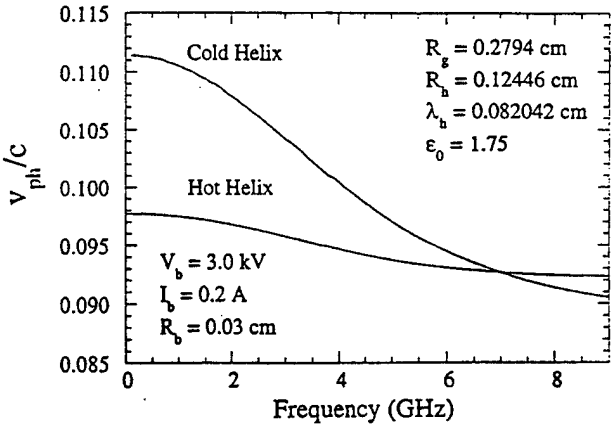

Fig. 6. Comparison of the dispersion in the cold (vacuum) and hot (beam-loaded) helixes.

The transition frequency at which this shift occurs is $\approx$7 GHz for the present case. This implies that the interaction with the beam results in an increase (decrease) in the wavenumber at frequencies below (above) 7 GHz.

The gain in a beam-loaded helix can also be compared with a helix constructed at Northrop–Grumman Corporation. This test circuit is identical to that previously described for the cold test except that the helix period was decreased slightly to 0.080 137 cm. The effective dielectric constant of $\varepsilon_0 = 1.75$ is unaltered by this small change in the helix period, and the agreement between the theory and the measured dispersion for this case is as good as that shown in Fig. 4 for a helix period of 0.082 042. This experiment employed a solid beam with a voltage of 2.84 kV, a current of 0.17 A, and a radius of 0.0495 cm. A magnetic field of about 950 G was used (which corresponds to the Brillouin field), and a maximum gain of approximately 6 dB/cm was found at a frequency of 5 GHz. In order to model this device with the annular beam formulation described in this section, we solve the dispersion equation using the rms beam radius of 0.035 cm. The results are shown in Fig. 7 in which we plot the both the calculated and observed gain as functions of frequency. It is evident from the figure that the agreement between the theory and the experiment is good.

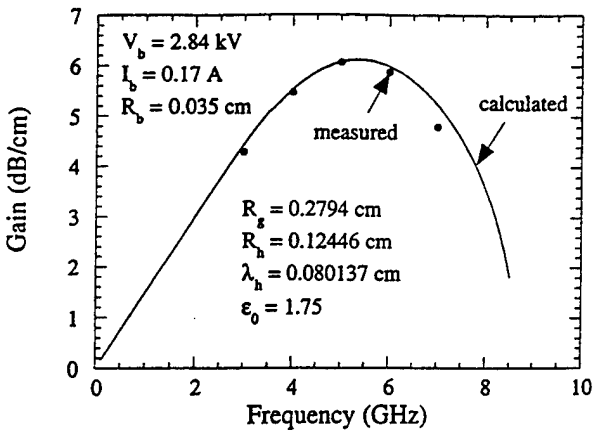

Fig. 7. Comparison of the measured and calculated gains versus frequency for the annular beam model.

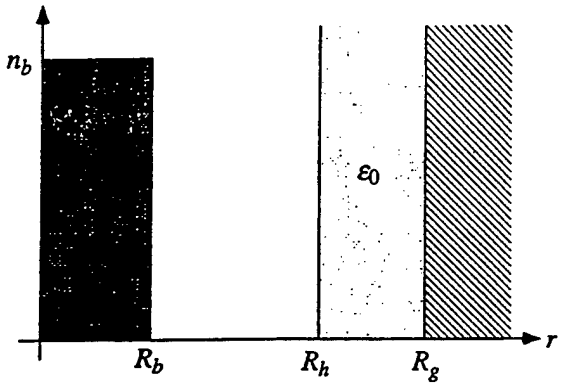

Fig. 8. Schematic representation of the physical configuration for the solid beam.

III. The Case of a Solid Beam

The equilibrium model we employ is that of the propagation of a solid cylindrical beam through a tape helix-loaded cylindrical drift tube in the presence of a uniform axial magnetic field $B_0[\equiv B0\hat{e}_z]$. The equilibrium current density of the electron beam is described via an azimuthally symmetric charge density

$$n_0(r) = n_b H(R_b - r) \tag{31}$$

with a flat-top density profile where n_b denotes the ambient beam density, R_b denotes the beam radius, and H is the Heaviside function. This configuration is illustrated schematically in Fig. 8. As in the annular beam case, the beam is assumed to propagate uniformly along the symmetry axis, and we take the equilibrium velocity to be $v_0 = v_0\hat{e}_z$. The circuit configuration is identical to that employed for the annular beam in Section II and, as in Section II, we define three regions. Region I refers to the volume enclosed by the beam for which $(0 \le r \le R_b)$. Region II is the volume between the beam and the helix for $(R_b < r \le R_h)$, and Region III refers to the gap between the helix and the outer wall $(R_h < r \le R_g)$.

The use of the flat-top density profile is a simplification of the configuration in an actual helix TWT in which the density profile decreases smoothly. The advantage of this model is in the solution of the eigenvalue problem in which solutions of Maxwell's equations within the beam are obtained subject to the inclusion of the dielectric tensor and matched via the boundary conditions to the vacuum solutions exterior to the beam. This procedure is reasonable as long as the scale length for the decrease of the density is much shorter than the transverse variation in the fields.

This equilibrium beam model is a special case of the rigid rotor equilibrium [11], [12] which describes a cylindrical pencil beam with a flat-top density profile which rotates at an angular frequency

$$\dot{\theta} = \frac{\Omega_0}{2} \pm \frac{1}{2}\sqrt{\Omega_0^2 - 2\omega_b^2} \tag{32}$$

where $\Omega_0[\equiv eB_0/\gamma_0 m_e c]$ is the Larmor frequency. The variation in the axial velocity with radius is

$$\beta_z^2(r) - \beta_z^2(0) = \frac{\omega_b^2 r^2}{2c^2} f_{\pm}\left(\frac{\Omega_0}{\sqrt{2}\omega_b}\right) \tag{33}$$

where $f_{\pm}(x) \equiv 1 - x^2 \mp x(x^2 - 1)^{1/2}$. Brillouin flow corresponds to $x = 1$ for which $f_{\pm}(x) = 0$, and there is no variation in the axial velocity across the beam. We now address the question of how the radial variation in the axial velocity varies as the magnetic field increases. If we consider the solution corresponding to the plus sign and note that as $x \to \infty$ then $f_+ \to 1/2$. Therefore, $f_+(x)$ varies between 0 and 1/2 over the entire range of magnetic fields. This means that the maximum possible difference in the axial velocity across the beam is given by

$$\beta_z^2(R_b) - \beta_z^2(0) = \frac{\omega_b^2 R_b^2}{4c^2}. \tag{34}$$

As a result, the maximum difference between the axial velocities at the center and edge of the beam is given by

$$\frac{\beta_z(R_b) - \beta_z(0)}{\beta_z(0)} \approx 2.94 \times 10^{-5} \frac{I_b(\mathrm{A})}{\beta_z^3(0)}. \tag{35}$$

The approximation that the variation in the axial velocity across the beam is negligible is valid as long as this velocity change is small. For parameters used in the paper of $I_b \approx 0.2$ A and $V_b \approx 3$ keV (7) gives $\Delta\beta_z/\beta_z \approx 0.5\%$; hence, the neglect of any radial variation in the axial velocity is justified.

The next question is the validity of the neglect of the rotation of the beam. Note that $f_+(x)$ corresponds to the minus sign in the angular rotation frequency. For Brillouin flow, therefore $\dot{\theta} = \omega_b/\sqrt{2}$, which decreases as the magnetic field increase, while for large magnetic fields $\dot{\theta} = \omega_b^2/2\Omega_0$. Hence, the angular rotation frequency goes to zero as the magnetic field goes to infinity, and we can neglect the beam rotation in the large magnetic field limit. In general, however, the beam rotation can be neglected as long as the axial distance required for one rotation of the beam for Brillouin flow is much less than the helix period. This condition can be expressed as $\omega_b/\sqrt{2} \ll k_h v_z \approx \omega$.

A. Maxwell's Equations

Maxwell's equations in Regions II and III are identical to that given in (5) and (6) in Section II. However, in order to obtain Maxwell's equations in Region I, the dielectric properties of the magnetized electron beam must be used. It has been shown that Maxwell's equations for a uniformly magnetized beam can be expressed as fourth-order differential equations for the axial electric and magnetic fields [9]

$$(\nabla_\perp^2 + \kappa_+^2)(\nabla_\perp^2 + \kappa_-^2)\begin{pmatrix}\delta\hat{E}_z\\ \delta\hat{B}_z\end{pmatrix} = 0 \tag{36}$$

where

$$\kappa_\pm^2 = \kappa^2\left\{1 - \frac{\omega_b^2\Lambda_{sc}}{\gamma_0^2(\Delta\omega^2 - \omega_{uh}^2)} + \frac{\omega_b^2}{2\Delta\omega^2(\Delta\omega^2 - \omega_{uh}^2)} \cdot \left[\frac{\Omega_0^2}{\gamma_0^2} - 2\Lambda_{sc}\frac{(ck - \omega\beta_0)^2\Delta\omega^2}{c^2\kappa^2}\right] \pm \frac{\omega_b^2\Omega_0}{2\Delta\omega^2(\Delta\omega^2 - \Omega_0^2)}\frac{\Delta\omega^2 - \Omega_0^2}{|\Delta\omega^2 - \Omega_0^2|} \cdot \sqrt{\frac{\Omega_0^2}{\gamma_0^4} + 4\Lambda_{sc}\frac{(ck - \omega\beta_0)^2\Delta\omega^4}{c^4\kappa^4}}\right\} \tag{37}$$

where $\omega_{uh}^2 \equiv \Omega_0^2 + \omega_b^2/\gamma_0^2$ denotes the square of the upper hybrid frequency, and $\Lambda_{sc} \equiv 1 - \omega_b^2/\gamma_0^2\Delta\omega^2$. As a consequence, there are two possible modes corresponding to $\kappa_\pm$ rather than the single mode which is found in the absence of the ambient magnetic field. These modes correspond to the Appleton–Hartree magnetoionic wave modes in an infinite uniformly magnetized plasma [13], [14]. It should be observed here that the presence of the magnetic field couples the longitudinal and transverse modes, and these modes represent a mixed polarization between the electromagnetic modes and the beam space-charge waves. For convenience, we refer to the $\kappa_\pm$ mode as the O-mode and the X-mode. In free space these modes are uncoupled and propagate independently; however, in the presence of the helix and outer wall the two modes are coupled and the aggregate axial electric and magnetic fields satisfy the equation [9]

$$\left[\left(1 - \frac{\omega_b^2}{c^2p^2}\frac{\Delta\omega^2}{\Delta\omega^2 - \Omega_0^2}\right)\nabla_\perp^2 + \Lambda_+\Lambda_-p^2\right]\delta\hat{B}_z = i\frac{\omega_b^2}{c^2p^2}\frac{\Omega_0(ck - \omega\beta_0)}{\Delta\omega^2 - \Omega_0^2}\nabla_\perp^2\delta\hat{E}_z \tag{38}$$

where

$$\Lambda_\pm(\omega, k) \equiv 1 - \frac{\omega_b^2}{c^2p^2}\frac{\Delta\omega}{\Delta\omega \mp \Omega_0}. \tag{39}$$

We solve these equations subject to the superposition of modes given by (38) as well as the boundary conditions at the edge of the beam, the helix, and the wall. It is also important to recognize that the dielectric effect of the beam also modifies the relationships between the transverse and axial fields. In Region I, therefore, we have that

$$\delta\hat{E}_r = \frac{ik}{p^2}\left(\frac{\partial}{\partial r}\delta\hat{E}_z + \frac{\omega}{ck}R(\omega,k)\frac{\partial}{\partial r} \cdot \left[\frac{(ck - \omega\beta_0)}{\Delta\omega}\delta\hat{E}_z + i\delta\hat{B}_z\right]\right) \tag{40}$$

$$\delta\hat{E}_\theta = -\frac{i\omega}{cp^2}\left(\frac{\partial}{\partial r}\delta\hat{B}_z - iR(\omega,k)\frac{\partial}{\partial r} \cdot \left[\frac{(ck - \omega\beta_0)}{\Delta\omega}\delta\hat{E}_z + i\delta\hat{B}_z\right]\right) \tag{41}$$

$$\delta\hat{B}_r = \frac{ik}{p^2}\left(\frac{\partial}{\partial r}\delta\hat{B}_z - iR(\omega,k)\frac{\partial}{\partial r} \cdot \left[\frac{(ck - \omega\beta_0)}{\Delta\omega}\delta\hat{E}_z + i\delta\hat{B}_z\right]\right) \tag{42}$$

$$\delta\hat{B}_\theta = \frac{i\omega}{cp^2}\left(\frac{\partial}{\partial r}\delta\hat{E}_z + i\frac{ck}{\omega}R(\omega,k)\frac{\partial}{\partial r} \cdot \left[\frac{(ck - \omega\beta_0)}{\Delta\omega}\delta\hat{E}_z + i\delta\hat{B}_z\right]\right) \tag{43}$$

where

$$R(\omega,k) \equiv \frac{\alpha(\omega,k)\Lambda_0(\omega,k)}{\Lambda_+(\omega,k)\Lambda_-(\omega,k)} \tag{44}$$

and

$$\alpha(\omega,k) \equiv \frac{\omega_b^2}{c^2p^2}\frac{\Delta\omega^2}{\Delta\omega^2 - \Omega_0^2} \tag{45}$$

$$\Lambda_0(\omega,k) \equiv 1 - \frac{\omega_b^2}{c^2p^2}. \tag{46}$$

Observe that (40)–(43) reduce to (8)–(11) in the limit in which the beam vanishes.

B. The Dispersion Equation

The solutions for the axial field components after application of the boundary condition at $r = R_g$ can be written in the form

$$\delta\hat{E}_z = \begin{cases} A_e^{(+)}J_0(\kappa_+r) + A_e^{(-)}J_0(\kappa_-r); & \text{I} \\ B_eJ_0(pr) + C_eY_0(pr); & \text{II} \\ D_eW_{0,0}(qR_g, qr); & \text{III} \end{cases} \tag{47}$$

and

$$\delta\hat{B}_z = \begin{cases} A_b^{(+)}J_0(\kappa_+r) + A_b^{(-)}J_0(\kappa_-r); & \text{I} \\ B_bJ_0(pr) + C_bY_0(pr); & \text{II} \\ D_bW_{1,0}(qR_g, qr); & \text{III.} \end{cases} \tag{48}$$

Note that in Region I the field is given by a superposition of the two Appleton–Hartree modes. Application of (38) yields $A_b^{(\pm)} = i\Gamma_\pm A_e^{(\pm)}$ where

$$\Gamma_\pm \equiv \kappa_\pm^2\frac{\omega_b^2}{c^2p^2}\frac{\Omega_0(ck - \omega\beta_0)}{\kappa_\pm^2(\Delta\omega^2\Lambda_0 - \Omega_0^2) - p^2\Lambda_+\Lambda_-(\Delta\omega^2 - \Omega_0^2)}. \tag{49}$$

The boundary conditions at $r = R_b$ are that the tangential components of the electric field, the axial components of the magnetic field, and the normal components of the electric displacement must be continuous. As a consequence, the axial

$$\delta\hat{E}_z = \begin{cases} A_e^{(+)} J_0(\kappa_+ r) + A_e^{(-)} J_0(\kappa_- r); & \text{I} \\ [a_+ A_e^{(+)} + a_- A_e^{(-)}] J_0(pr) + [b_+ A_e^{(+)} + b_- A_e^{(-)}] Y_0(pr); & \text{II} \\ D_e W_{0,0}(qR_g, qr); & \text{III} \end{cases} \tag{50}$$

$$\delta\hat{B}_z = \begin{cases} i\Gamma_+ A_e^{(+)} J_0(\kappa_+ r) + i\Gamma_- A_e^{(-)} J_0(\kappa_- r); & \text{I} \\ i[c_+ A_e^{(+)} + c_- A_e^{(-)}] J_0(pr) + i[d_+ A_e^{(+)} + d_- A_e^{(-)}] Y_0(pr); & \text{II} \\ D_b W_{1,0}(qR_g, qr); & \text{III} \end{cases} \tag{51}$$

$$D_e = \frac{A_e^{(+)}[a_+ J_0(pR_h) + b_+ Y_0(pR_h)] + A_e^{(-)}[a_- J_0(pR_h) + b_- Y_0(pR_h)]}{W_{0,0}(qR_g, qR_h)} \tag{60}$$

$$D_b = i\frac{q}{p}\frac{A_e^{(+)}[c_+ J_1(pR_h) + d_+ Y_1(pR_h)] + A_e^{(-)}[c_- J_1(pR_h) + d_- Y_1(pR_h)]}{W_{1,1}(qR_g, qR_h)} \tag{61}$$

field components can be reduced to (50) and (51) shown at the top of the page where

$$a_\pm \equiv -\frac{\pi}{2} pR_b \left[J_0(\kappa_\pm R_b) Y_1(pR_b) - \frac{\kappa_\pm}{p} N_\pm J_1(\kappa_\pm R_b) Y_0(pR_b) \right] \tag{52}$$

$$b_\pm \equiv \frac{\pi}{2} pR_b \left[J_0(\kappa_\pm R_b) J_1(pR_b) - \frac{\kappa_\pm}{p} N_\pm J_1(\kappa_\pm R_b) J_0(pR_b) \right] \tag{53}$$

$$c_\pm \equiv -\frac{\pi}{2} pR_b \left[\Gamma_\pm J_0(\kappa_\pm R_b) Y_1(pR_b) - \frac{\kappa_\pm}{p} M_\pm J_1(\kappa_\pm R_b) Y_0(pR_b) \right] \tag{54}$$

$$d_\pm \equiv \frac{\pi}{2} pR_b \left[\Gamma_\pm J_0(\kappa_\pm R_b) J_1(pR_b) - \frac{\kappa_\pm}{p} M_\pm J_1(\kappa_\pm R_b) J_0(pR_b) \right] \tag{55}$$

and

$$M_\pm \equiv \Gamma_\pm (1 + R) - \frac{(ck - \omega\beta_0)}{\Delta\omega} R \tag{56}$$

$$N_\pm \equiv \varepsilon_1 \left[1 - \frac{\omega}{ck}(M_\pm - \Gamma_\pm) \right] + \varepsilon_2 \frac{\omega}{ck} M_\pm \tag{57}$$

$$\varepsilon_1 \equiv 1 - \frac{\omega_b^2}{\omega^2} \frac{\Delta\omega^2}{\Delta\omega^2 \mp \Omega_0^2} \tag{58}$$

$$\varepsilon_2 \equiv \frac{\omega_b^2}{\omega^2} \frac{\Delta\omega\Omega_0}{\Delta\omega^2 \mp \Omega_0^2}. \tag{59}$$

We can eliminate the D_e and D_b coefficients by noting that the axial and azimuthal components of the electric field must be continuous at $r = R_h$, hence, see (60) and (61) at the top of the page.

The solution for the axial fields has now been reduced to two unknown coefficients, $A_e^{(\pm)}$. The dispersion equation can be found by application of the boundary conditions given in (21) and (23); specifically, that the tangential component of the electric field must be perpendicular to the helix, and that the tangential components of the magnetic field parallel to the helix must be continuous. This procedure yields two equations in $A_e^{(\pm)}$, and the dispersion equation results from setting the determinant of the coefficients of $A_e^{(\pm)}$ in these equations to zero. As a result, we find that the general dispersion equation can be written as

$$\frac{\omega^2}{c^2}\cot^2\phi \left[D_{1,1} + \frac{\varepsilon_0 p}{q}\frac{W_{1,0}(qR_h, qR_g)}{W_{0,0}(qR_g, qR_h)} D_{0,1} \right] - p^2 \left[D_{0,0} - \frac{q}{p}\frac{W_{1,0}(qR_g, qR_h)}{W_{1,1}(qR_g, qR_h)} D_{0,1} \right] - \frac{\omega p}{c}\frac{R_b}{R_h}\Delta \cot\phi = 0 \tag{62}$$

where

$$D_{m,n} \equiv [a_+ J_m(pR_h) + b_+ Y_m(pR_h)] \cdot [c_- J_n(pR_h) + d_- Y_n(pR_h)] - [a_- J_m(pR_h) + b_- Y_m(pR_h)] \cdot [c_+ J_n(pR_h) + d_+ Y_n(pR_h)] \tag{63}$$

and

$$\Delta \equiv \frac{\kappa_+}{p} J_0(\kappa_- R_b) J_1(\kappa_+ R_b)(N_+ - \Gamma_- M_+) - \frac{\kappa_-}{p} J_0(\kappa_+ R_b) J_1(\kappa_- R_b)(N_- - \Gamma_+ M_-). \tag{64}$$

It is straightforward to show that the general dispersion equation reduces to the vacuum helix dispersion equation $\Lambda(\omega, k) = 0$ found in Section II.

C. Numerical Analysis

We solve the dispersion equation (62) for the solid beam for the same helix configuration described in Fig. 7 for comparison with the helix TWT built at Northrop–Grumman Corporation. In particular, the helix parameters are $R_g = 0.2794$ cm, $R_h = 0.124\,46$ cm, $\lambda_h = 0.080\,137$ cm, and an effective dielectric constant of $\varepsilon_0 = 1.75$. The solid beam is characterized by a voltage 2.84 kV and a current of 0.17 A

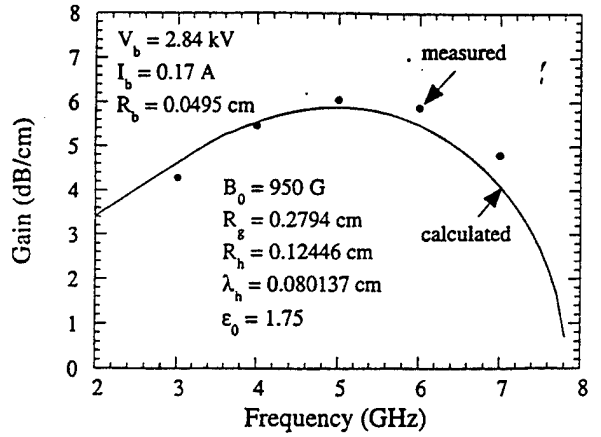

Fig. 9. Comparison of the measured and calculated gains versus frequency for the solid beam model.

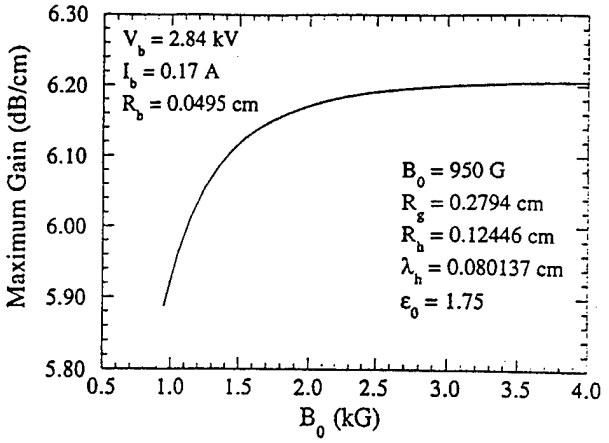

Fig. 11. Variation in the maximum gain with the axial magnetic field.

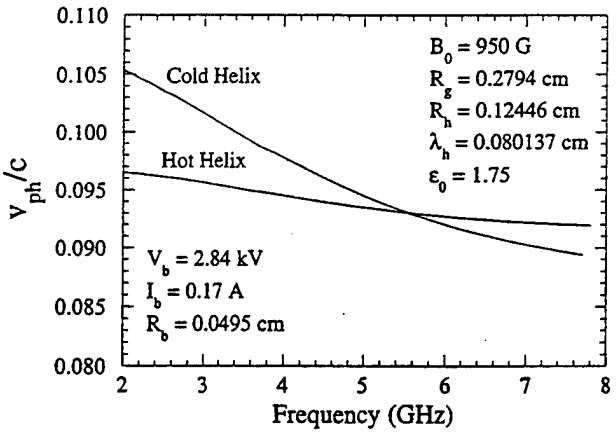

Fig. 10. Variation in the phase velocity with frequency for the cold helix as well as the hot helix.

and a radius of 0.0495 cm, and the Brillouin field for this example is ≈950 G.

The gain is plotted as a function of frequency for this example in Fig. 9. The solid line represents the solution of the dispersion equation (62) and the dots represent the measured values of the gain. Observe that agreement between the solid beam theory and the measured values of the gain is good. The effect of the beam upon the helix dispersion is illustrated in Fig. 10 in which we plot the phase velocity versus frequency for both the cold helix and the beam-loaded helix. It is evident that, as found in the annular beam model, the effect of the beam is to flatten out the dispersion over a broad frequency band.

The peak gain shown in Fig. 7 in the preceding section is approximately 6.1 dB/cm at a frequency of 5.3 GHz. In contrast, the peak gain shown in Fig. 9 is 5.9 dB/cm at 5.0 GHz. The discrepancy between these two results is only partly due to the differing beam models. The principal source of the discrepancy stems from the fact that the annular beam formulation in the preceding section is based upon the assumption of a strongly magnetized beam, while the solid beam analysis deals with a magnetic field which is unconstrained except insofar as it must be greater than the Brillouin field. In order to study the effect of variations in the magnetic field, we plot the maximum gain as a function of axial magnetic field in Fig. 11. As shown in the figure, the maximum gain increases with increasing magnetic field and asymptotes at a value of approximately 6.2 dB/cm for magnetic fields above 3.5 kG at which point the strongly magnetized approximation is good. Since the maximum gain at this point is found at a frequency of 5.2 GHz, we conclude that the annular and solid beam analyzes are in essential agreement in the strongly magnetized regime.

IV. Summary and Discussion

In this paper, we have presented a linearized relativistic field theory of a dielectric-loaded helix TWT which implicitly includes the effects of beam space-charge both in terms of the coupling to beam space-charge waves as well as upon the dielectric loading of the helix modes. The treatment has been formulated for the cases of both 1) a thin annular beam and 2) a solid electron beam. In the former case, the electron dynamics are included under the assumption of an strongly magnetized beam. The latter case is able to treat arbitrary magnetic fields above the Brillouin field. Nevertheless, the two analytic formulations are found to be in essential agreement in the strongly magnetized regime. Agreement between the theory and experiment is also found to be reasonably good.

Acknowledgment

The authors would like to acknowledge helpful discussions with Drs. B. Levush and T. M. Antonsen, Jr.

References

[1] J. R. Pierce and L. M. Field, "Traveling-wave tubes," *Proc. IRE*, vol. 35, pp. 108–111, 1947.
[2] J. R. Pierce, "Theory of the beam-type traveling-wave tube," *Proc. IRE*, vol. 35, pp. 111–123, 1947.
[3] ——, *Traveling-Wave Tubes*. New York: Van Nostrand, 1950.
[4] O. E. H. Rydbeck, "Theory of the traveling wave tube," *Ericsson Technics*, vol. 46, pp. 3–18, 1948.
[5] L. J. Chu and J. D. Jackson, "Field theory of traveling wave tubes," *Proc. IRE*, vol. 36, pp. 853–863, 1948.
[6] A. H. W. Beck, *Space-Charge Waves*. New York: Pergamon, 1958.
[7] R. G. E. Hutter, *Beam and Wave Electronics in Microwave Tubes*. New York: Van Nostrand, 1960.

[8] H. P. Freund, M. A. Kodis, and N. R. Vanderplaats, "Self-consistent field theory of a helix traveling wave tube amplifier," *IEEE Trans. Plasma Sci.*, vol. 20, pp. 543–553, 1992.
[9] H. P. Freund, N. R. Vanderplaats, and M. A. Kodis, "Field theory of a traveling wave tube amplifier with a tape helix," *IEEE Trans. Plasma Sci.*, vol. 21, pp. 654–668 1993.
[10] G. Groshart, Northrop–Grumman Corp., personal communication.
[11] J. D. Lawson, *The Physics of Charged-Particle Beams*. Oxford, England: Clarendon, 1977, pp. 139–142.
[12] R. C. Davidson, *Theory of Nonneutral Plasmas*. Reading, MA: Benjamin, 1974, ch. 2.
[13] T. H. Stix, *The Theory of Plasma Waves*. New York: McGraw-Hill, 1962.
[14] P. C. Clemmow and J. P. Dougherty, *Electrodynamics of Particles and Plasmas*. Reading, MA: Addison-Wesley, 1969.

H. P. Freund, photograph and biography not available at the time of publication.

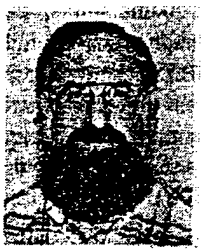

Ernest G. Zaidman (M'94) received the B.S. and M.A. degrees from the University of Florida in 1975 and 1978, respectively, and received the Ph.D. degree from the University of Texas at Austin in 1986.

He provides the Vacuum Electronics Branch at the Naval Research Laboratory, Washington, D.C. with expertise in the creation and development of millimeter wave and microwave source concepts utilizing computational and theoretical techniques. His recent technical efforts, in collaboration with his colleagues, include programs for the nonlinear simulation and analysis of space charge effects in fast wave devices, nonlinear TWT beam-wave interactions including gated beams, and characterization of vacuum microelectronic emission and devices.

Dr. Zaidman is a member of the American Physical Society.

Mary Anne Kodis received the B.S. degree in electrical engineering from the University of California, Davis, in 1978. She received the M.S. degree in 1980 and the Ph.D. degree in 1987 for work on the parametric interaction of microwave fields with plasma density gradients.

She joined the Naval Research Laboratory, Washintgton, D.C., in 1987, where she has been working on emission-gated microwave amplifiers.

N. R. Vanderplaats, photograph and biography not available at the time of publication.

APPENDIX XVII

A Re-examination of Scaling Laws in the Traveling Wave Interaction

H.P. Freund
Nucl. Instrum. Meth. A358, 497 (1995)

ELSEVIER

Nuclear Instruments and Methods in Physics Research A 358 (1995) 497–500

NUCLEAR INSTRUMENTS & METHODS IN PHYSICS RESEARCH Section A

A re-examination of scaling laws in the traveling wave interaction

H.P. Freund *,[1]

Naval Research Laboratory, Washington, DC 20375, USA

Abstract

A re-examination of traveling wave interactions (in the helix traveling wave tube and the free-electron laser) is performed to investigate the validity of the well-known scaling laws in which the gain varies as the cube (fourth) root of the current when space-charge effects are negligible (dominant). The results indicate that these scaling laws are simplistic generalizations which break down for broad bandwidth interactions, and that the actual variation of the gain with the current can be more complex.

1. Introduction

Linear traveling wave devices such as the helix traveling wave tube (TWT) [1–3] and the free-electron laser (FEL) [4,5] have a long history. The TWT interaction is between the axial electric field of a subluminous mode and the axial electron velocity, which results in axial bunching. The FEL interaction is mediated by the ponderomotive force due to the beating of the wiggler and a supraluminous mode also resulting in axial bunching. Similar interactions also occur in devices [6,7] with dielectric linings, gratings, or rippled walls. The equations governing the gain in all such devices bear many similarities.

The particular issue addressed is the scaling of the gain with current in TWTs and FELs. For low currents the maximum gain scales as the cube root of the current. This is called the ballistic (Compton) regime in the TWT (FEL) literature. When the current is large enough that the space-charge potential is important then the maximum gain scales as the fourth root of the current. This is referred to as the space-charge dominated (Raman) regime in TWTs (FELs). The principal purpose of this paper is to show that these simple scaling laws can break down.

The source of these scaling laws lies in the linearized gain. As formulated by Pierce [1] for TWTs, the dispersion equation for frequency ω and wavenumber k is

$$\left[k^2 - k_0^2(\omega)\right]\left[(\omega - kv_\parallel)^2 - 4QC^3k^2v_\parallel^2\right] = 2C^3\frac{\omega}{v_\parallel}k_0(\omega)k^2v_\parallel^2, \tag{1}$$

where $k_0(\omega)$ is the wavenumber in the absence of the beam, $v_\parallel$ is the axial beam velocity, and the Q and C^3 parameters describe the effect of the beam on the space-charge wave and on the interaction gain, where C^3 is proportional to the current.

The scaling laws are obtained upon neglect of the backward waves (i.e., $k \approx k_0$) for which Eq. (1) reduces to

$$(k-k_0)(k-\kappa_+)(k-\kappa_-) = \frac{C^3}{1-4QC^3}\frac{\omega}{v_\parallel}k_0^2, \tag{2}$$

where

$$\kappa_\pm \equiv \frac{\omega/v_\parallel}{1 \pm 2\sqrt{QC^3}} \tag{3}$$

describes the positive and negative energy space-charge waves. In the low current regime, the space-charge waves are negligible and

$$\mathrm{Im}\frac{k_{max}}{k_0} \cong \frac{\sqrt{3}}{2}C. \tag{4}$$

Hence, the gain scales as the cube root of the current. In the space-charge dominated regime, the interaction is with the negative-energy space-charge wave (i.e., $k \approx \kappa_-$) and the maximum gain is given by

$$\mathrm{Im}\frac{k_{max}}{k_0} \cong \frac{1}{2}\sqrt[4]{\frac{C^3}{Q}}, \tag{5}$$

which scales as the fourth root of the current.

2. Linear theory of the TWT

These scaling laws follow from a complete TWT field theory [8] using a sheath helix model with radius R_h, and period λ_h which is surrounded by a conducting wall of

* Corresponding author. Tel. +1 703 734 5840, fax +1 703 821 1134, e-mail freund@mmace.nrl.navy.mil.

[1] Permanent address: Science Applications International Corp., McLean, VA 22102, USA.

SSDI 0168-9002(94)01504-X

radius R_g. The equilibrium model is a thin annulus of radius R_b and thickness ΔR_b; hence, the equilibrium density is $n_0(r) = n_b \Delta R_b \delta(r - R_b)$. The dispersion equation for the azimuthally symmetric subluminous modes is

$$\Lambda_0(k, \omega)\left[(\omega - k v_\parallel)^2 + 4QC^3\beta_\parallel^2\gamma_\parallel^2 c^2\kappa^2\right] = 2\gamma_\parallel^2 C^3 \frac{\omega^2\kappa^2}{k_h^2 R_h^2} \frac{J_0(\kappa R_h)J_1(\kappa R_g)}{J_0(\kappa R_g)J_1(\kappa R_h)} \frac{W_0(\kappa R_h, \kappa R_g)}{W_1(\kappa R_h, \kappa R_g)}, \quad (6)$$

where $\beta_\parallel \equiv v_\parallel/c$, $\gamma_\parallel^2 \equiv (1-\beta_\parallel^2)^{-1}$, $k_h \equiv 2\pi/\lambda_h$ is the helix wavenumber, $\kappa^2 \equiv \omega^2/c^2 - k^2$, $W_n(\zeta, \xi) \equiv Y_n(\zeta)J_n(\xi) - J_n(\zeta)Y_n(\xi)$, J_n and Y_n denote the regular Bessel and Neumann functions of order n,

$$\Lambda_0(k, \omega) = \frac{\omega^2}{c^2} + \frac{\kappa^2}{k_h^2 R_h^2} \frac{J_0(\kappa R_h)J_1(\kappa R_g)}{J_0(\kappa R_g)J_1(\kappa R_h)} \frac{W_0(\kappa R_h, \kappa R_g)}{W_1(\kappa R_h, \kappa R_g)} \quad (7)$$

is the dispersion function of the vacuum helix, and

$$C^3 \equiv k_h^2 R_h^2 \frac{\omega_b^2 \sigma_b^2}{8\gamma_\parallel^5 c^2} \frac{J_0^2(\kappa R_b)J_1(\kappa R_h)}{J_0^2(\kappa R_h)J_1(\kappa R_g)} W_1(\kappa R_h, \kappa R_g),$$

$$Q \equiv \frac{1}{2\beta_\parallel^2 k_h^2 R_h^2} \frac{J_0(\kappa R_h)J_1(\kappa R_g)}{J_0(\kappa R_b)J_1(\kappa R_h)} \frac{W_0(\kappa R_h, \kappa R_b)}{W_1(\kappa R_h, \kappa R_g)}, \quad (8)$$

where $\omega_b^2 \equiv 4\pi e^2 n_b/m_e$ denotes the square of the beam plasma frequency, and $\sigma_b \equiv 2\pi R_b \Delta R_b$ is the cross-sectional area of the beam.

In order to reduce Eq. (6) to the Pierce theory, a near-resonant approximation (i.e., $\omega \approx k v_\parallel$ and $\kappa \to \kappa_e \equiv i\omega/\beta_\parallel\gamma_\parallel$) is made and

$$k_0^2(\omega) \equiv \frac{\omega^2}{c^2}\left[1 + k_h^2 R_h^2 \frac{J_0(\kappa_e R_g)J_1(\kappa_e R_h)}{J_0(\kappa_e R_h)J_1(\kappa_e R_g)} \times \frac{W_1(\kappa_e R_h, \kappa_e R_g)}{W_0(\kappa_e R_h, \kappa_e R_g)}\right] \quad (9)$$

describes the vacuum dispersion relation. In this limit

$$\Lambda_0(k, \omega) = -\frac{(k^2 - k_0^2)}{k_h^2 R_h^2} \frac{J_0(\kappa_e R_h)J_1(\kappa_e R_g)}{J_0(\kappa_e R_g)J_1(\kappa_e R_h)} \times \frac{W_0(\kappa_e R_h, \kappa_e R_g)}{W_1(\kappa_e R_h, \kappa_e R_g)}, \quad (10)$$

and the Pierce theory is recovered.

A comparison is made of the maximum growth rates from the field theory (6) and the three approximate forms of the dispersion equation: the quartic Pierce theory (1), and the solutions in the ballistic (4) and space-charge dominated (5) regimes. Fig. 1 shows the maximum gain

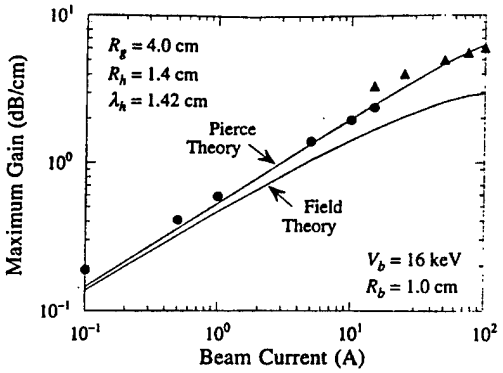

Fig. 1. Scaling of the maximum gain with the current in a helix TWT.

versus current for $R_g = 4.0$ cm, $R_h = 1.4$ cm, $\lambda_h = 1.42$ cm, and a beam with $V_b = 16$ keV and $R_b = 1.0$ cm. The circles and triangles in the figure represent the maximum gain from Eqs. (4) and (5) respectively, and the transition between the ballistic and space-charge dominated regimes occurs for $I_b \approx 20$ A.

The ballistic and space-charge dominated approximations are in reasonable agreement with the Pierce theory over a wide range of currents. In addition, the field and Pierce theories are in reasonable agreement in the ballistic regime. The major discrepancies between the field theory and both the Pierce theory and the ballistic and space-charge dominated approximations are in (1) the scaling of the gain in the ballistic regime, and (2) the magnitude of the gain in the space-charge dominated regime.

In the first case, the gain from the field theory scales closely as $I_b^{1/2}$ over the entire ballistic regime from 0.1 to 20 A, and not as $I_b^{1/3}$. Indeed, the gain increases faster than $I_b^{1/3}$ even for the quartic Pierce theory in this regime. The reasons for this are twofold. Firstly, since the Pierce theory indicates that the gain scales faster than $I_b^{1/3}$, the neglect of the backward wave in the Eq. (3) evidently has broken down. Secondly, the Q and C^3 parameters are not constants, but vary widely with current since the gain increases with current and the frequency of maximum gain is displaced farther from the exact resonance. This is related to the broad bandwidth of the interaction. Hence, the near-resonant approximation breaks down.

In the second case, the gain in the space-charge dominated regime scales as $I_b^{1/4}$ for all three analyses for currents between 20 and 100 A, although the field theory predicts lower gains. However, the gain decreases rapidly with increasing current above 100 A due to dispersive shifts in the gain band. In essence, the dielectric effect of the beam shifts the helix mode out of resonance. Hence, while the field theory does predict the $I_b^{1/4}$ scaling as found in Eq. (5), the predicted gain is much less than that found with the Pierce theory (which breaks down completely for currents in excess of 100 A).

Note that attempt has been made to self-consistently include the effects of DC self-electric and magnetic fields. However, confined flow has been implicitly assumed. In addition, since the equilibrium model is a thin annulus the velocity shear is negligible. Finally, the space-charge limiting current can also be increased under the assumptions that the axial magnetic field is arbitrarily large and that the 16 keV beam energy describes the kinetic energy of the beam after equilibrium has been achieved (i.e., it is not the injection energy).

3. Linear theory of the FEL

A waveguide model is assumed for the FEL [9,10]. In contrast with the TWT, the FEL operates with a smooth-bore waveguide (of radius R_g) and supraluminous TE_{ln} or TM_{ln} modes. The basic analysis employed is 3-D and deals with a thin annular beam propagating through a cylindrical waveguide with a helical wiggler [9,10]. The steady-state orbits describe a velocity $v = v_w(\hat{e}_x \cos k_w z + \hat{e}_y \sin k_w z) + v_\parallel \hat{e}_z$, where $k_w \equiv 2\pi/\lambda_w$ (λ_w denotes the wiggler period). The transverse velocity v_w is proportional to the product of the wiggler period and amplitude and is related to the axial velocity via $v_w^2 + v_\parallel^2 = (1 - \gamma_0^{-2})c^2$, where γ_0 is the relativistic factor. Further, the radius of the orbit is $k_w R_b = |v_w/v_\parallel|$. For simplicity, the analysis is limited to the TE_{1n} modes.

The FEL couples TE_{ln}/TM_{ln} modes with an azimuthal variation $\approx \exp(il\theta)$ to space-charge modes with an azimuthal variation $\approx \exp[i(l-1)\theta]$. At the fundamental resonance, the TE_{1n} dispersion equation is [9,10]

$$\left[\left[\omega - (k + k_w)v_\parallel\right]^2 - \frac{\omega_b^2\sigma_b}{4\gamma_0^3c^2}\frac{c^2\kappa_1^2}{1+\lambda_b^2}D_0(\kappa_1 R_b, \kappa_1 R_g)\right] \times \Lambda_0(k, \omega) = \frac{\lambda_b^2}{1+\lambda_b^2}\frac{\omega_b^2\sigma_b}{16\gamma_0^3c^2}\omega^2 D_1(\kappa R_b, \kappa R_g), \tag{11}$$

where $\lambda_b \equiv k_w R_b$, $\kappa_1^2 \equiv \omega^2/c^2 - (k + k_w)^2$, $D_0(\xi, \zeta) \equiv J_0(\xi)W_0(\xi, \zeta)/J_0(\zeta)$, $D_1(\xi, \zeta) \equiv -J_0(\xi)J_2(\xi)Y_1'(\zeta)$, and $\Lambda_0(k, \omega) \equiv J_1'(\kappa R_g)$ denotes the dispersion function for the vacuum TE_{1n} modes. This notation differs from that used in Refs. [9,10] to more closely match the TWT analysis. Eq. (11) reduces to the Pierce form subject to a near-resonant approximation and replacing $\kappa \to \kappa_{co}$ ($\equiv$ cutoff wavenumber of the mode) in the Bessel functions. However, Eq. (11) will be used in the numerical analysis since this is a more complete form.

The current scaling of the maximum gain is shown in Fig. 2 for $V_b = 1.3$ MeV, $R_g = 0.72$ cm, $\lambda_w = 3.0$ cm, and $B_w = 625$ G, for which $k_w R_b \approx 0.052$ and $\beta_\parallel \approx 0.957$. The dots represent solutions of Eq. (11) for the maximum gain and the solid and dashed lines vary as $I_b^{1/3}$ and $I_b^{1/4}$ for comparison. This FEL has a much narrower bandwidth than the TWT and the frequency of maximum gain varies

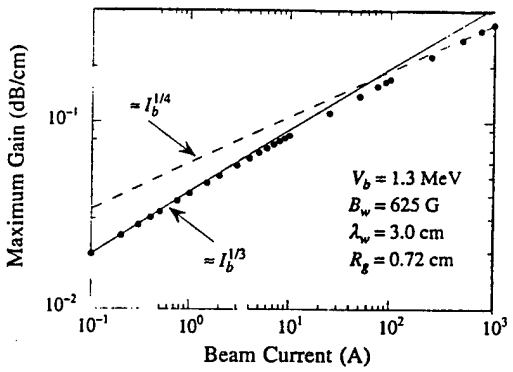

Fig. 2. Scaling of the maximum gain with the current for an FEL.

over 12.7–13.3 GHz over this range of currents. It is evident that, in contrast to the TWT example, the maximum gain follows the expected scaling laws, and for currents below (above) approximately 15 A the gain scales as the cube (fourth) root of the current. The reason for this is that frequency and the Q and C^3 parameters vary less than for the TWT, and the near-resonant approximation is good. Observe that the analysis represented by Eq. (11) has been verified by comparison with experiment [11–13]. In particular, the $I_b^{1/4}$ scaling predicted in the Raman regime has been confirmed [12].

This analysis is an idealized treatment of the gain in TWTs and FELs based upon a thin annular beam model and propagation confined by a waveguide. However, small-signal analyses have been conducted for FELs in the Compton [14] and Raman regimes [15] in which alternate scaling laws were obtained. These analyses in both regimes omitted the waveguide so that the radiation is free to diffract away from the electron beam if the gain is not high enough for optical guiding to confine the radiation field within the electron beam. In cases where diffraction is large, the area of the radiation field is much greater that that of the electron beam, and the gain was found to scale as $I_b\,(\ln I_b)^{1/2}$ in the Compton regime and as $I_b^{1/2}$ in the Raman regime.

4. Nonlinear analysis of the FEL

Nonlinear analyses using more general models of the beam in waveguide-based FELs also exhibit scaling laws which differ from $I_b^{1/3}$ and $I_b^{1/4}$. The particular analysis and simulation code of interest here is referred to as WIGGLIN for convenience, and treats the injection of a solid beam into a rectangular waveguide with a planar wiggler [16,17].

WIGGLIN is a 3-D slow-time-scale description of an FEL. The electromagnetic field is represented as a superposition of the TE and TM modes of a rectangular waveguide, and second order nonlinear differential equations are obtained for the evolution of the amplitude and phase

of each mode. Electron dynamics are treated using the complete 3-D Lorentz force equations. No wiggler average is imposed.

The specific parameters considered correspond to a 35 GHz experiment [18] in which a 3.5 MeV/850 A beam with a 1 cm radius propagated through a rectangular waveguide [9.8 cm × 2.9 cm] with a planar wiggler with $B_w = 3.72$ kG and $\lambda_w = 9.8$ cm. Three wave modes could interact: the TE_{01}, TE_{21}, and TM_{21} modes. The injected power was ≈ 50 kW, the bulk of which was in the TE_{01} mode. The experiment yielded a saturated power of ≈ 180 MW over a length of ≈ 1.3 m. WIGGLIN is in good agreement with the experiment for an initial beam energy spread of $\Delta\gamma_z/\gamma_0 \approx 1.5\%$ [16,17]. We focus here on the predicted scaling of the efficiency with beam current for currents ranging from 100 to 1000 A.

In the present discussion, the efficiency is used rather than the gain. This is because the gain in an experiment, or in the WIGGLIN simulation, is not purely exponential. The instantaneous gain varies widely due to betatron oscillations, multi-mode couplings, velocity shear, and higher order beating between the wiggler and radiation fields to name a few. This makes it more convenient to deal with the efficiency. Since in the case of saturation by phase trapping, the efficiency is also expected to scale as $I_b^{1/3}$ and $I_b^{1/4}$ in the Compton and Raman regimes (see Ref. [10], p. 10), this poses no essential difficulty.

Space-charge effects have been shown to be negligible in the ELF experiment [19]; hence, the efficiency might be expected to scale as $I_b^{1/3}$ in the Compton regime. The efficiency predicted by WIGGLIN is plotted versus beam current in Fig. 3 for both $\Delta\gamma_z/\gamma_0 = 0$ (circles) and 1.5% (triangles). The solid line increases as the cube root of the current for reference. Evidently, the scaling diverges substantially from $I_b^{1/3}$ over the range of currents studied, and that no simple power law can approximate the predicted scaling.

The principal reason for this divergence from the $I_b^{1/3}$ scaling is that, in contrast to the FEL discussed in Section 3, the interaction in this case is extremely broad band. Strong gain is predicted to occur over frequencies ranging from 30 to 43 GHz [16,17]. Hence, the FEL does no always obeys the simple Compton and Raman scalin laws.

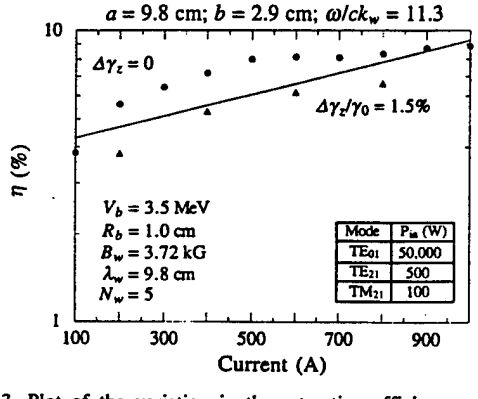

Fig. 3. Plot of the variation in the saturation efficiency versus beam current for parameters consistent with the ELF experiment.

5. Summary and conclusions

The conclusion is that the well-known scaling laws fo the Compton and Raman regimes are overly simplistic The TWT example shown exhibited an $I_b^{1/2}$ scaling law ir the ballistic regime, and an $I_b^{1/4}$ scaling in the space-charg dominated regime. The cause of this is that a broa bandwidth interaction exists in which the near-resonan approximation breaks down. The FEL example in Sectio 3 followed the Compton and Raman regime scaling law due to a narrower bandwidth than in the TWT example However, the nonlinear simulation in Section 4 resulted ir a scaling law which could not be modeled by a simpl power law because of a broader bandwidth than in th example in Section 3. Hence, these scaling laws must b used with some caution for both TWTs and FELs as wel as the entire class of linear traveling wave devices.

Acknowledgments

This work was supported by the Office of Naval Research.

References

[1] J.R. Pierce, Traveling-Wave Tubes (Van Nostrand, New York, 1950).
[2] A.H.W. Beck, Space-Charge Waves (Pergamon, New York, 1958).
[3] R.G.E. Hutter, Beam and Wave Electronics in Microwave Tubes (Van Nostrand, New York, 1960).
[4] H. Motz, J. Appl. Phys. 22 (1951) 527.
[5] R.M. Phillips, IRE Trans. Electron Dev. ED-7 (1960) 231.
[6] J.E. Walsh, Advances Electronics & Electron Devices, ed. C. Marton (Academic, New York, 1982), Vol. 58, p. 271.
[7] B. Johnson and J.E. Walsh, Phys. Rev. A 33 (1986) 3199.
[8] H.P. Freund et al., IEEE Trans. Plasma Sci. PS-20 (1992) 543.
[9] H.P. Freund and A.K. Ganguly, Phys. Rev. A 28 (1983) 3438.
[10] H.P. Freund and T.M. Antonsen, Jr., Principles of Free-Electron Lasers (Chapman & Hall, London, 1992) Chap. 4.
[11] J. Fajans, G. Bekefi, Y.Z. Yin and B. Lax, Phys. Fluids 28 (1985) 1995.
[12] J. Fajans and G. Bekefi, IEEE J. Quantum Electron. QE-23 (1987) 1617.
[13] J. Masud et al., Phys. Rev. Lett. 58 (1987) 763.
[14] G.T. Moore, Nucl. Instr. and Meth. A 239 (1985) 19.
[15] A. Fruchtman, IEEE Trans. Plasma Sci. PS-18 (1990) 424.
[16] H.P. Freund, Phys. Rev. A 37 (1988) 3371.
[17] Ref [10], Chap. 5.
[18] T.J. Orzechowski et al., Phys. Rev. Lett. 57 (1986) 2172.
[19] H.P. Freund, Nucl. Instr. and Meth. A 331 (1993) 496.

APPENDIX XVIII

Traveling Wave Tube Devices with Non-linear Dielectric Elements

T.M. Antonsen, Jr. and B. Levush
IEEE Transactions on Plasma Science
submitted to the special issue on high power electronics

Traveling Wave Tube Devices with Non Linear Dielectric Elements

T. M. Antonsen Jr†. and B. Levush

Vacuum Electronic Branch
Naval Research Laboratory
Washington DC 20375-5320

The performance of traveling wave tube amplifiers incorporating nonlinear dielectric elements is studied via computer simulation. Two different situations are investigated: a) the use of nonlinear dielectric elements to reduce intermodulation distortion, and b) the use of voltage controlled dielectrics to provide rapid modification of the dispersion characteristics of the slow wave structure. In the first case, the use of dielectrics with negative second order susceptibilities is studied as a means of reducing phase and intermodulation distortion. Use of these dielectrics along with dynamic velocity taper to reduce amplitude modulation distortion results in marked reduction of predicted intermodulation distortion. In the second case, the goal is to design an amplifying structure whose gain as a function of frequency can be varied electrically. Preliminary design studies show that relatively large changes in the center frequency of the amplification band can be achieved with relatively modest changes in the dielectric constant of helix support structure.

†Also Science Application International Corporation and University of Maryland

I. Introduction

In many applications of traveling wave tubes (TWTs) in the defense arena, including EW, radar, and communication applications, TWT amplifiers are required to provide simultaneous amplification of multiple frequencies. In these applications intermodulation and amplitude and phase cross modulation will take place as a result of the nonlinearities in the amplification process. In cases when the number of carriers is large, this phenomenon becomes even more complex. In existing tubes, these parasitic effects are avoided by a combination of techniques such as feed-forward compensation [] or operation in the linear regime with depressed energy collection of the electron beam. Associated with these techniques are the cost of increasing the complexity of the tube or weight of the power supply. Some EW applications require intermodulation products at levels of no greater than -30 to -40dBC and phase stability less than 3°/dB. Communication applications can require intermodulation levels as low as -70dBC. These levels can be achieved in narrow band applications by a technique known as predistortion linearization[] in which the signal is deliberately distorted, prior to injection in the TWT, in such a away that the combination of the TWT and predistortion nonlinearities cancel. Alternately, some applications require amplifications of signals over a range in frequency which may exceed the range of optimal performance of the TWT. In this case it would be beneficial to be able to control electrically the band pass characteristics of the amplifier, so that it could adapt rapidly to the changing properties of the signal.

The present paper investigates theoretically the possibility of achieving reduced distortion and dynamic tuning of TWT amplifiers using non linear dielectric elements. In the case of reducing distortion, the basic idea is that a nonlinear dielectric element in the signal path can introduce phase distortion which will cancel the phase distortion inherent in the amplification process. Such an element would be used in conjunction with a TWT which was designed to minimize amplitude distortion. This idea is similar to that of the predistortion linearizer[]. It has possible advantages over the predistortion linearizer in that the phase distortion can be introduced at the output of the amplifier. This results in a cancellation of distortion which is more complete over a greater range of operating powers and frequencies. It suffers from the disadvantage that the nonlinear elements are inserted in the highest power portion of the signal path, and thus, these elements must have low losses. In the second case, that of realizing an electrically controllable amplifier, we consider inserting nonlinear, voltage controlled, dielectric elements in the support structures of the TWT helix. These elements then allow for varying of the phase velocity

and impedance of the slow wave structure and consequently tuning the amplification band of the TWT. In addition to varying the amplification band such elements would allow one to electrical compensate for voltage fluctuations in the injected electron beam[].

The organization of this paper is as follows. In Sec. II we present the theoretical model, describing multifrequency operation of a TWT, on which our subsequent calculations are based. Included in this section is a description of the way in which nonlinear dielectric elements in the circuit are modeled. Section III presents an example of the reduction of intermodulation distortion for a amplifier with a specific set of parameters. Section IV illustrates the way in which nonlinear dielectric elements can be used to control the frequency response of an amplifier. Finally, in Sec. V we discuss some of the issues surrounding the implementation of non linear dielectrics in these devices.

II Physical Model

A. The Electromagnetic Fields of the Structure and their Frequencies

The physical model employed in the current studies is essentially the same as that used in the development of the one dimensional, multifrequency simulation code CHRISTINE[]. We begin the description of the physical model with the representation of the assumed fields of the cold structure. Ultimately, in the type of model presented here, only two frequency dependent quantities; the phase velocity and the coupling impedance, are needed to specify the parameters of the cold structure fields. However, the presentation will start at a more basic level to underscore the nature of the approximations being made.

The fields of the structure are represented in the form of the product of a slowly varying, complex amplitude, δA_n, periodic eigenfunctions $e_n(x)$ and $b_n(x)$, and an exponential phase factor,

$$E_{rf}(x,t) = \sum_n i \frac{\omega_n}{c} \delta A_n(z)\, e_n(x)\, exp\, [i(\int_0^z k_{zn}(z')\, dz' - \omega_n t)] + c.c.\,, \qquad (1a)$$

and

$$B_{rf}(x,t) = \sum_n i \frac{\omega_n}{c} \delta A_n(z)\, b_n(x)\, exp\, [i(\int_0^z k_{zn}(z')\, dz' - \omega_n t)] + c.c.\,. \qquad (1b)$$

Here it is assumed that $\mathbf{e}_n(\mathbf{x})$ and $\mathbf{b}_n(\mathbf{x})$ are the solutions of Maxwell's equations for the empty structure corresponding to angular frequency ω_n and real axial wave number k_{zn}. In this regard $e_n(x)$ and $b_n(x)$ will be periodic in axial distance with a period equal to that of the structure. To allow for the slow axial variation of parameters of the structure the wave number k_{zn} corresponding to frequency ω_n as well as the eigensolutions $e_n(x)$ and $b_n(x)$ will vary with axial distance. It is assumed that such variations are slow and that it is permissible to think of the functions $e_n(x)$ and $b_n(x)$ as being locally periodic. As Maxwell's Equations for the cold structure are linear we can take the eigensolutions $e_n(x)$ and $b_n(x)$ to be dimensionless. In this case the slowly varying amplitude δA_n has the dimensions of a vector potential.

The sum over the subscript n in Eqs. (1a) and (1b) represents a sum over frequencies ω_n. Note, that all the time dependence of the fields is contained in the exponential factors; that is, the amplitudes δA_n depend only on axial distance. This representation of the field corresponds to the case in which the device is excited by a signal consisting of a discrete set of frequencies belonging to the set ω_n. It is assumed that all frequencies are integer multiples of some minimum frequency $\Delta\omega$. In this case, the nonlinear beating of any two signals in the device will produce a signal at a frequency which is a member of the set ω_n. This beating could be in the form of self beating in which case harmonic frequencies are generated, or it could be in the form of beating of two signals of different frequency generating intermodulation distortion. The restriction that members of the set ω_n are integer multiples of some minimum frequency $\Delta\omega$ can be put another way. The input signal and all other quantities of interest are assumed to be periodic in time with period $T = 2\pi/\Delta\omega$.

The time averaged electromagnetic power flux along the structure implied by Eqs. (1a) and (1b) can be evaluated using Poynting's theorem,

$$P = \frac{c}{2\pi} \sum_n \left| \frac{\omega_n}{c} \delta A_n(z) \right|^2 A_{eff,n} , \tag{2}$$

where $A_{eff,n}$ is the effective crossectional area defined by the relation,

$$A_{eff,n} = \frac{1}{2} \int d^2x_\perp \, \hat{z} \cdot (e_n^* \times b_n + e_n \times b_n^*) , \tag{3}$$

and $\hat{z}$ is a unit vector in the axial direction. For a structure with slowly varying parameters the contribution to the power flux from each frequency (i.e. each term in the sum in Eq. (2)) will be independent of axial distance in the absence of a beam or attenuation. Basically, this assumes that the parameters are tapered gently enough so that the amount of power reflected from a forward propagating wave is negligibly small. With tapering, the quantity $A_{eff,n}$ will vary with axial distance as the parameters of the structure vary. Consequently, according to (2), in a structure with slowly varying parameters the amplitude δA_n will vary with axial distance even if the power flux is constant. To account for this we introduce a normalized field amplitude,

$$a_n(z) = \frac{\omega_n}{c} \frac{q\, \delta A_n(z)}{mc^2} A_{eff,n}^{1/2}, \tag{4}$$

where q and m are the charge and mass of an electron respectively. The above choice of normalization gives the following expression for the power flux,

$$P = P_{flux,2} \sum_n |a_n(z)|^2 \tag{5}$$

where

$$P_{flux,2} = \frac{c}{2\pi} \left(\frac{mc^2}{q}\right)^2 = 1.3862 \times 10^9 \; watts, \tag{6}$$

is a constant. A consequence of this choice of normalization is that under the stated assumptions, namely negligibly small reflection of forward propagating power, a_n varies due to attenuation and coupling to the beam, but not due to the slowly changing parameters of the structure.

The evolution of the complex amplitude is obtained by the following standard steps. Expressions (1a) and (1b) are inserted in Maxwell's equations along with the beam current. Ampere's law is dotted with $e_n^*(x)$ and Faraday's law is dotted with $b_n^*(x)$. The two products are combined in the same way as one forms Poynting's theorem, and the resulting expression is averaged over the spatial period of the structure and the temporal period T of the fields. Weak attenuation is introduced by the boundary condition that the tangential electric field of the radiation does not quite vanish on the structure walls. The resulting equation for the amplitude of the n^{th} spectral component is thus,

$$\left(\frac{d}{dz} + \alpha_n(z)\right) a_n = \frac{2\pi i}{I_A A_{eff,n}^{1/2}} \left\langle \int d^2x_\perp \, j \cdot e_n^*(x) \, exp\,[-i(\int_0^z k_{zn}(z')\,dz' - \omega_n t)] \right\rangle , \quad (7)$$

where $\alpha_n(z)$ is the attenuation in Nepers/cm, $I_A = mc^3/q$, j is the beam current density, and the angular brackets denote averages over the temporal period of the radiation and the spatial period of the structure. The right hand side of Eq. (7) will be further refined after a discussion of the equations of motion.

B. Equations of Motion

The beam electrons are treated as annular discs of charge of outer radius r_{bo} and inner radius r_{bi} which are constrained to move in the axial direction only. One expects this approximation to be appropriate when the electrons are confined by either a strong axial magnetic field or a system of periodic focusing magnets. The motion of the electrons will be one dimensional if the frequency of the amplified signal is much smaller than the frequency of particle oscillations in the relevant confining field: the gyrofrequency or the betatron frequency. The disc approximation will be appropriate if the axial electric field of the signal does not vary appreciably over the radial extent of the electron beam.

The rate of change of electron energy is expressed in terms of the rate of change of the relativistic factor $\gamma = 1/\sqrt{1 - v^2/c^2}$,

$$\frac{d\gamma}{dz} = \frac{q}{mc^2} \left\langle \hat{z} \cdot (\boldsymbol{E}_{rf} + \boldsymbol{E}_{sc} + \boldsymbol{E}_{dc}) \right\rangle_{beam} . \quad (8)$$

Here, $\mathbf{E}_{rf}$ is the electric field of the structure field given by Eq. (1a), $\mathbf{E}_{sc}$ is the space charge field which is discussed in part **C** of this section, and $\mathbf{E}_{dc}$ is a steady state axial electric field, if present, which changes the energy of beam electrons as they travel through the structure. Equation (8) describes the Lagrangian rate of change of energy of a particle as it travels down the interaction region. The independent coordinate is the axial location of an electron. One must also determine the arrival time t(z) of an electron at a particular axial location. This is done by solving

$$\frac{dt}{dz} = \frac{1}{v_z(\gamma)} , \quad (9)$$

where, the axial velocity of an electron is given in terms of the relativistic factor γ, and the pitch factor Θ,

$$v_z(\gamma) = c\left(1 - \frac{1 + (\gamma_0^2 - 1)\,\Theta^2}{\gamma^2}\right)^{1/2} . \qquad (10)$$

The pitch factor Θ is the ratio of the transverse component to the total momentum on injection and γ_0 is the electron's relativistic factor on injection. It is assumed that Θ <<1. That is, it is small enough so that the motion is one dimensional, but large enough that there can be a significant spread in axial velocities. The initial conditions for the equations of motion are the following: particles are injected with a specified relativistic factor γ_0, pitch factor Θ, and entrance time *t(0)*. In the present simulations the pitch factor is taken to be zero implying a cold beam.

In the simulations, the quantity *t(z)* is not solved directly using Eq. (9). Instead, the phase relative to the nth signal is determined. This phase is defined as

$$\psi_n = \omega_n(z / v_{z0} - t) \qquad (11)$$

where v_{z0} is the initial axial velocity of a particle with pitch factor zero. The evolution of this phase is then given by

$$\frac{d\psi_n}{dz} = \omega_n(1 / v_{z0} - 1 / v_z) . \qquad (12)$$

Introduction of the phase ψ_n in the expression for the radiation field (1a) gives

$$\left.\frac{d\gamma}{dz}\right]_{rf} = Re\left\{2i \sum_n a_n(z)\, e_2(n,z)\, e^{i\psi_n}\right\} \qquad (13)$$

for the contribution to the rate of change of γ due to the structure fields. In the above the quantity $e_2(n,z)$ is defined as

$$e_2(n,z) = \frac{\langle \hat{z} \cdot e_n \rangle_{beam}}{A_{eff,n}^{1/2}} \exp\left[i \int_0^z (k_{zn}(z') - \omega_n / v_{z0})\, dz'\right] , \qquad (14)$$

where the angular bracket denotes average over the radial extent of the beam and over one axial period of the structure fields.

The above quantity also appears effectively in Eq.(7) for the complex field amplitude. To see this we first represent the current density in the form of a sum over moving charge discs,

$$j_z(r,z,t) = \sum_j \frac{v_{z,j}(t)\,\delta(z - z_j(t))}{\pi(r_{bo}^2 - r_{bi}^2)} \begin{Bmatrix} 0, & r < r_{bi} \\ 1, & r_{bi} < r < r_{bo} \\ 0, & r > r_{bo} \end{Bmatrix}$$

where the sum is over all the electrons. Equation (7) calls for an average over one spatial period of the structure and one temporal period of the fields. Due to the time periodicity of all quantities this average may be evaluated by integration over the shaded region depicted in fig. 1. The shaded region, a parallelogram, is preferable to a rectangle, with upper and lower boundaries at fixed t, for evaluation of the average because it contains the orbits of a group electrons all of which pass through both lateral boundaries. The average in Eq. (7) may be evaluated by first integrating over time,

$$\sum_j \int_z^{z+\lambda_H} \frac{dz\, e_n^*(x)\cdot\hat{z}}{\lambda_H} \int_t^{t+T} \frac{dt}{T} v_{z,j}(t)\,\delta(z - z_j(t))\; exp\,[-i(\int_0^z k_{zn}(z')\,dz' - \omega_n t)]$$

$$= \sum_{j'} \frac{1}{T} \int_z^{z+\lambda_H} \frac{dz\, e_n^*(x)\cdot\hat{z}}{\lambda_H}\, exp\,[-i(\int_0^z k_{zn}(z')\,dz' - \omega_n t_{j'})]$$

where the sum over particles j' represents a sum over the group of particles entering the interaction region during one period, T of time as depicted in fig. 1., and $t_{j'}(z)$ is the time of flight for particle j' to the point z. The number of particles that will contribute to the sum is the number that entered during a time T, viz. TI/q where I is the beam current. Now the integral over z can be carried out. Because the exponent is evaluated along a particle

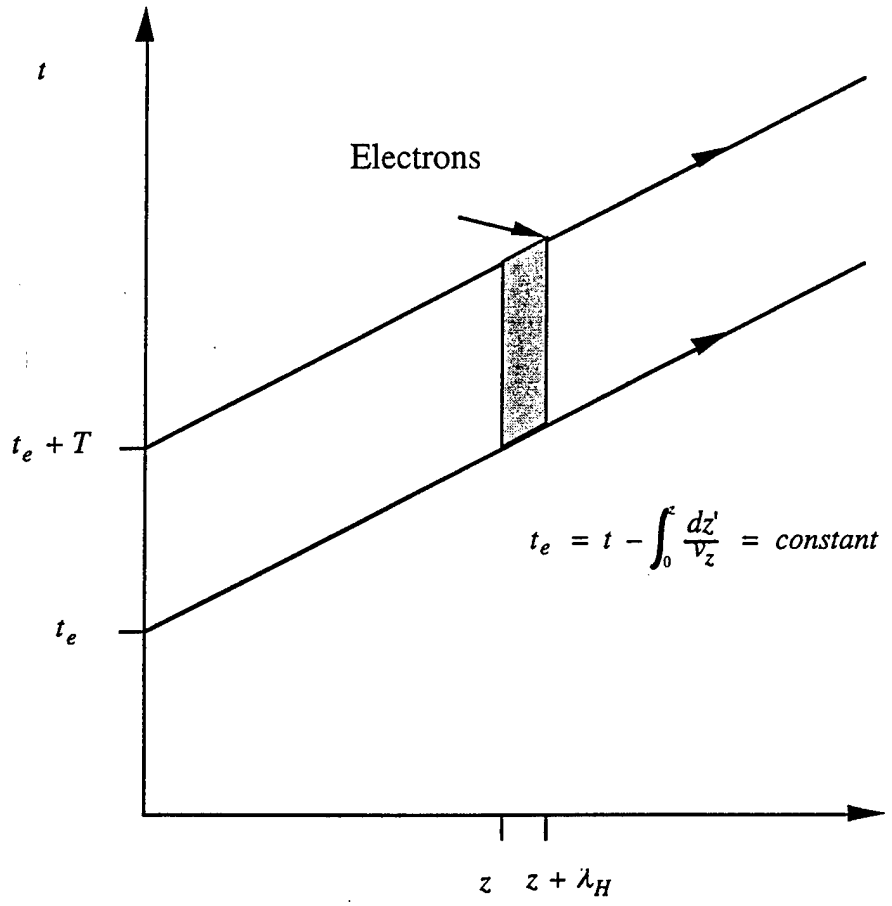

Fig. 1 Characteristics in the t versus z plane for electron trajectories. The shaded region corresponds to one spatial period of the structure and one temporal period of the fields.

trajectory it can be regarded as slowly varying over a distance given by the structure period λ_H. Thus, the average over z reduces to an average of the axial component of the structure field. Including the radial dependence of the current density implied by the disc model we see that Eq. (7) calls for precisely the same average of the structure fields as does the equation of motion. The result is that the average in (7) produces

$$\left(\frac{d}{dz} + \alpha_n(z)\right) a_n = \frac{2\pi i\, I}{I_A}\, e_2^*(n,z)\, \langle e^{-i\psi_n} \rangle\,, \tag{15}$$

where I is the total beam current and the angular bracket now signifies average over particles entering the interaction region during the time interval T. Since the beam current enters in the form of a ratio I/I_A, the beam current and I_A can be evaluated in any system of units. From Eqs. (13) and (15) it is clear that the relevant information concerning the

structure fields is contained in the complex coupling function $e_2(n,z)$. The amplitude of this quantity is related to the axial impedance. In particular,

$$|e_2(n,z)|^2 = \frac{|\langle \hat{z} \cdot e_n \rangle_{beam}|^2}{A_{eff,n}} = \frac{K k_{zn}^2}{377\ \Omega}, \qquad (16)$$

where K is the coupling impedance in ohms. The phase of the coupling function (14) is determined by the phase velocity of the structure fields.

C. The Space Charge Field

In this section we describe the procedure for modeling the space charge electric field which appears in Eq. (8). The effect of this field is to resist the formation of electron bunches and, as a consequence, to give rise to collective oscillations of the beam at a modified plasma frequency. The natural frequency of these oscillations depends of the beam density, its radial profile, and the configuration of the metallic structure surrounding the beam. We assume that the basic form of the field can be written,

$$\langle \hat{z} \cdot E_{sc} \rangle_{beam} = -\sum_n \frac{4I}{\omega_n (r_{b0}^2 - r_{bi}^2)} \left\{ i \langle e^{-i\psi_n} \rangle R_n' + c.c. \right\}, \qquad (17)$$

where R_n' is an unknown coefficient which will be determined subsequently. Were this the only field acting on the particles, the linearized bunching factor would oscillate in time with an angular frequency ω_p, where

$$\omega_p^2 = \frac{4qIR'}{m\gamma_0^3 v_{z0}(r_{bo}^2 - r_{bi}^2)}.$$

This result is obtained by taking the small signal limit of Eqs (8), (10), and (12) and assuming for simplicity that the beam is cold ($\Theta = 0$ in Eq. (10)). Thus, the factor R' describes the reduction in the collective oscillation frequency accounting for the distribution of fields outside the beam.

The space charge field is calculated including the effects of the structure using the sheath helix model. The presentation here will be different from other approaches in that

no attempt will be made to separate fields into electromagnetic and electrostatic components. This approach allows one to identify in an unambiguous way the correct coefficient, R', for the space charge field to be included in the equation of motion. The space charge field that we seek will have a time dependence similar to that of the structure fields, namely it will be periodic in time with period T and thus include frequencies belonging to the set ω_n. In general the number of frequencies that are needed to correctly model the space charge term is higher than that needed to model the structure fields. This is because in the nonlinear regime the bunched current density of the beam has a high harmonic content. Frequency ω_n is generally accompanied by spatial wave number ω_n/v_z. These spectral components of the current will tend to excite modes of the structure over that range of frequencies where the dispersion relation of the structure is linear. However, as the excitation of the space charge field does not rely on resonance with the structure fields the harmonic content of the current density will produce appreciable space charge fields over a greater range of frequencies.

The approach taken here is to assume that the beam current density is known, and to calculate the total ('structure' plus 'space charge') axial electric field at the beam that appears in response to the given current density. From the total field, one can then extract the appropriate factor R'. We take the form of the current density to correspond to an ensemble of moving annular discs oscillating in time with a frequency ω_n and an as yet unspecified wave number k_z. In order to connect the present calculation with the model of the current used in Eq. (7) we write

$$j_z(r,z,t) = \frac{I}{\pi (r_{bo}^2 - r_{bi}^2)} exp\left[i(k_z z - \omega_n t)\right] \langle e^{-i\psi} \rangle \begin{Bmatrix} 0, & r < r_{bi} \\ 1, & r_{bi} < r < r_{bo} \\ 0, & r > r_{bo} \end{Bmatrix} + c.c., \qquad (18)$$

where r_{bo} and r_{bi} are the outer and inner radii of the beam discs, and the angular bracket represents the ensemble average over particles. Inserting the above expression along with its corresponding charge density perturbation determined by continuity into Maxwell's equations results in the following radial differential equation for the complex amplitude of the axial electric field with frequency ω_n and wavenumber k_z,

$$\left[\frac{\partial}{r\partial r} r \frac{\partial}{\partial r} - \kappa^2\right] \tilde{E}_z(r) = \kappa^2 \frac{4I}{\omega_n (r_{bo}^2 - r_{bi}^2)} \langle e^{-i\psi} \rangle \begin{Bmatrix} 0, & r < r_{bi} \\ 1, & r_{bi} < r < r_{bo} \\ 0, & r > r_{bo} \end{Bmatrix} \qquad (19)$$

where

$$\kappa^2 = k_z^2 - \frac{\omega^2}{c^2} .$$

We solve (19) for $r < r_H$, the radius of the sheath helix. In addition, we solve the similar (but homogeneous) equation for the axial magnetic field of the TE component of the radiation for $r < r_H$. Outside the helix, $r > r_H$, we solve similar homogeneous equations for the TE and TM components of the field, but assume that a dielectric with relative permitivity ε is present. The following boundary conditions are imposed: $E_\theta(r)$ vanishes at $r = r_w > r_H$, $E_z(r)$ vanishes at $r = r_v > r_H$ (where $r_w > r_v$), simulating the effect of vanes, and the components of electric field parallel to the helix direction and surface current perpendicular to the helix direction vanish at the helix. Finally, we average the axial electric field over the annular discs. The resulting expression for this averaged field is,

$$\langle E_z \rangle_{beam} = -\frac{2i\,\omega_n}{c^2\,D(k_z,\omega_n)}\, I\,\langle e^{-i\psi}\rangle\,[H]^2 - \frac{4i\,I}{\omega_n(r_{b0}^2 - r_{bi}^2)}\,\langle e^{-i\psi}\rangle\,R\ . \qquad (20)$$

The quantity $D(k_z,\omega_n)$ in the denominator of the first term in Eq. (20) is the vacuum dispersion function for the sheath helix,

$$D(k_z,\omega_n) = \frac{\omega_n^2 r_h^2}{c^2}\left[\frac{I_0'(\kappa r_h)}{\kappa r_h\, I_0(\kappa r_h)} - \frac{\varepsilon\, C_v'(\kappa_\varepsilon r_h)}{\kappa_\varepsilon r_h\, C_v(\kappa_\varepsilon r_h)}\right]$$

$$- \frac{1}{k_H^2 r_h^2}\left[\frac{\kappa r_h\, I_0(\kappa r_h)}{I_0'(\kappa r_h)} - \frac{\kappa_\varepsilon r_h\, D_w(\kappa_\varepsilon r_h)}{D_w'(\kappa_\varepsilon r_h)}\right] , \qquad (21)$$

where k_H is the helix wave number, D_w and C_v are linear combinations of Bessel functions,

$$D_w(\kappa_\varepsilon r_h) = I_0(\kappa_\varepsilon r_h)K_0'(\kappa_\varepsilon r_w) - K_0(\kappa_\varepsilon r_h)I_0'(\kappa_\varepsilon r_w) , \qquad (22a)$$

and

$$C_v(\kappa_\varepsilon r_h) = I_0(\kappa_\varepsilon r_h)K_0(\kappa_\varepsilon r_v) - K_0(\kappa_\varepsilon r_h)I_0(\kappa_\varepsilon r_v) , \qquad (22b)$$

and

$$\kappa_\varepsilon^2 = k_z^2 - \frac{\omega^2 \varepsilon}{c^2} .$$

In Eq. (20) the quantities H and R are defined as follows,

$$H = \frac{2\left[\kappa r_{bo} I_1(\kappa r_{bo}) - \kappa r_{bi} I_1(\kappa r_{bi})\right]}{\kappa^2 (r_{bo}^2 - r_{bi}^2)} \tag{23a}$$

and,

$$R = 1 + \frac{2}{r_{bo}^2 - r_{bi}^2} \left\{ r I_1(\kappa r) \right]_{r_{bi}}^{r_{b0}} \left[r_{bo} K_0'(\kappa r_{bo}) - \frac{K_0(\kappa r_h)}{I_0(\kappa r_h)} r I_1(\kappa r) \right]_{r_{bi}}^{r_{b0}}$$

$$- r_{bi} I_1(\kappa r_{bi}) r K_0'(\kappa r) \Big]_{r_{bi}}^{r_{b0}} \Big\} . \tag{23b}$$

The first term in Eq. (20) is essentially the contribution of the structure field to the axial electric field at the beam, and the second term, involving R, is essentially the space charge field. The quantity R is the space charge reduction factor, and it is an interesting exercise in Bessel function identities to show that R vanishes as $r_{bi} \rightarrow r_{bo}$.

To determine the space charge field to be inserted in Eq. (8), we write it in the form of Eq. (17) where the coefficient R_n' is to be determined. Assuming all fields vary as $exp(ik_z z)$ the total field implied by (17) and (7) is

$$\left\langle \hat{z}\cdot E_{rf} + \hat{z}\cdot E_{sc} \right\rangle_{beam} = \sum_n \frac{2\pi i}{c(k_z - k_{zn})} I \left\langle e^{-i\psi} \right\rangle \frac{|z\cdot e_n|^2}{A_{eff,n}}$$

$$- \frac{4i\,I}{\omega_n (r_{b0}^2 - r_{bi}^2)} \left\langle e^{-i\psi} \right\rangle R_n' + c.c. . \tag{24}$$

As can be seen, Eqs. (20) and (24) have similar behavior with respect to their dependence on k_z. They both diverge as $k_z \rightarrow k_{zn}$ where k_{zn} is the solution of the vacuum dispersion relation at frequency ω_n. We pick the space charge factor R_n' to give agreement between (20) and (24) when both are expanded about $k_z = k_{zn}$. To lowest order, the coefficient of the singular term determines the impedance in the sheath helix model,

$$\frac{K k_{zn}^2}{377\,\Omega} = \frac{|z\cdot e_n|^2}{A_{eff,n}} = -\left.\frac{\pi\,\omega_n [H]^2}{c\,\partial D(k_z,\omega_n)/\partial k_z}\right|_{k_{zn}} . \tag{25}$$

In next order, matching the coefficient of the constant term gives,

$$R' = R - \frac{\omega_n^2 (r_{b0}^2 - r_{bi}^2)\, D_s^{''}}{4\,c^2 \left(D_s^{'}\right)^2}, \tag{26}$$

where,

$$D_s^{'} = \left.\frac{\partial (D/H^2)}{\partial k_z}\right|_{k_{zn}}, \qquad \text{and} \qquad D_s^{''} = \left.\frac{\partial D_s^{'}}{\partial k_z}\right|_{k_{zn}} . \tag{27}$$

The difference between R and R' can be interpreted as the effect of the sheath helix on the space charge reduction factor. In particular, if the helix is replaced by a conducting tube, no structure field can resonate with the beam, and the space charge reduction factor is simply R. With the helix present some of the space charge field is able to penetrate outside the helix, and the reduction factor is modified.

The final equation of motion is thus,

$$\frac{d\gamma}{dz} = Re\left\{2i\sum_n a_n(z)\, e_2(n,z)\, e^{i\psi_n} - \frac{8I\,i}{I_A(r_{bo}^2 - r_{bi}^2)}\sum_{n'} \frac{c\,R_{n'}^{'}}{\omega_{n'}}\, e^{i\psi_{n'}}\langle e^{-i\psi_{n'}}\rangle\right\}$$

$$+ \frac{q}{mc^2}\,\langle \hat{z}\cdot E_{dc}\rangle_{beam}, \tag{28}$$

where the separate sums over n and n' are over frequencies belonging to the set ω_n. In our model, the number of frequencies kept to evaluate the space charge term is independent of the number kept to evaluate the structure fields. In particular, a range of frequencies is specified in the input list for the radiation field as is the number of space charge harmonics. In computing the space charge factor R_n' for each frequency harmonic the simulation code first checks to see if the frequency is in the range corresponding to the structure fields. If it is, the reduction factor is calculated according to (30). If the space charge harmonic frequency is out of the range specified for the structure fields, the reduction factor is taken to be just R and calculated for a spatial wave number $k_z = \omega_n/v_{z0}$.

C. Nonlinear Dielectrics

To treat the effect of nonlinear dielectric elements we assume that the nonlinearity is weak in the sense that the signal field is still described by Eqs (1a) and (1b), but the nonlinearity modifies the wave equation (7). Effectively, we separate the current density, j, into a contribution from the electron beam, calculated as described above, and a contribution from the nonlinearity of dielectrics in the vicinity of the structure. The linear contribution of these dielectrics is included implicitly in the determination of the transverse eigenfunctions e_n and b_n. The nonlinear dielectric contribution to the current density is given by $j = \partial P / \partial t$, where $P(t)$ is the nonlinear polarization. The polarization can be expressed in terms of the instantaneous electric field $4\pi P(t) = \delta\varepsilon^{(3)} | E(t) |^2 E(t)$ where $\delta\varepsilon^{(3)}$ is a constant characterizing the nonlinear response of the dielectric, and we have assumed the dielectric responds instantaneously to the electric field. Inserting the above into Eq. (7) and introducing the normalized amplitudes $a_n(z)$ defined in Eq.(4) results in the following evolution equation for the nth mode,

$$\frac{d}{dz} a_n = \frac{\omega_n}{2c} \int d^2x_\perp \left\langle \delta\varepsilon(t) \frac{e^{-i\phi_n} e_n^*(x)}{A_{eff,n}^{1/2}} \cdot \sum_m \left[\frac{i e^{i\phi_m} e_m(x)\, a_m}{A_{eff,m}^{1/2}} + c.c. \right] \right\rangle \qquad (29)$$

where

$$\delta\varepsilon(t) = \delta\varepsilon^{(3)} \left(\frac{mc^2}{q} \right)^2 \left| \sum_m \left[\frac{i e^{i\phi_m} e_m(x)\, a_m}{A_{eff,m}^{1/2}} + c.c. \right] \right|^2$$

is the time dependent non linear contribution to the dielectric constant, and $\varphi_n = \int_0^z k_{zn}(z')\, dz' - \omega_n t$ is the phase of the nth signal component. It is understood that the right hand side of Eq.(29) is to be added to Eq.(7)

The angular brackets in Eq. (29) indicate that the time dependent quantity is to be averaged over the repetition time $T = 2\pi/\Delta\omega$. In general this induces a nonlinear coupling between all signal components. If only a single frequency is present, Eq. (29) gives rise to a nonlinear wavenumber shift δk_z,

$$\delta k_{zn} = \frac{3\omega_n}{2c} \left(\frac{mc^2}{q} \right)^2 |a_n|^2 \int d^2x_\perp \, \delta\varepsilon^{(3)} \frac{|e_n(x)|^4}{A_{eff,n}^2} . \qquad (30)$$

The sign of the wave number shift depends on the sign of the coefficient $\delta\varepsilon^{(3)}$. We shall find that a negative wave number shift, giving a negative phase shift when integrated over the length of the region where the nonlinear dielectric is located, is required to compensate the positive nonlinear phase shift of the electron beam. Note, that $\delta\varepsilon^{(3)}$ depends both on transverse and axial coordinates. Thus, the wave number shift given by Eq.(30) could be an arbitrary function of z, reflecting the placement of the dielectric elements along the interaction region. In fact, these elements need not be in the interaction region, but could be anywhere in the signal path.

To estimate the degree to which various modes are affected by the nonlinear dielectric, we temporarily assume that the perturbed dielectric constant $\delta\varepsilon(t)$ is independent of time and can be factored into the product of a magnitude, $\delta\varepsilon_0$, and a spatially dependent form factor, $\delta\varepsilon(x_\perp)/\delta\varepsilon_0$. In this case it induces a linear phase shift for each mode given by ,

$$\delta k_{zn,L} = \frac{\omega_n}{2c}\,\tau_n^2 \delta\varepsilon_0 \,. \tag{31}$$

where the dimensionless parameter τ_n characterizes the overlap between the perturbed dielectric and the mode electric field,

$$\tau_n^2 = \int d^2x_\perp \frac{\delta\varepsilon(x_\perp)}{\delta\varepsilon_0} \frac{|e_n(x_\perp)|^2}{A_{eff,n}} \,. \tag{32}$$

This parameter is estimated in the present model by assuming the nonlinear dielectric fills the entire region between the wall and the helix, just as the support structure for the helix is modeled in the sheath helix approximation as a uniform dielectric annulus. Thus, τ_n can be determined by differentiation of the solution of the sheath helix dispersion relation with respect to the dielectric constant in the outer region,

$$\tau_n^2 = \frac{2c}{\omega_n} \frac{\partial k_{zn}}{\partial\varepsilon} \,. \tag{33}$$

Finally, our expression for the nonlinear phase shift in the presence of many signals is written,

$$\frac{d}{dz} a_n = \frac{\omega_n}{2c} \left\langle \delta\varepsilon_0(t)\ \tau_n e^{-i\phi_n} \cdot \sum_m \left[i\tau_m e^{\,i\phi_m} a_m + c.c. \right] \right\rangle , \tag{34}$$

where

$$\delta\varepsilon(t) = \delta\varepsilon_0^{(3)} A_\varepsilon(z) \left(\frac{mc^2}{q} \right)^2 \left| \sum_m \left[i\tau_m e^{\,i\phi_m}\ a_m + c.c. \right] \right|^2 , \tag{35}$$

$\delta\varepsilon_0{}^{(3)}$ is the magnitude of the nonlinear dielectric coefficient, and $A_\varepsilon(z)$ is the effective cross sectional area of the nonlinear dielectric element. In the case of single frequency operation, Eqs. (34) and (35) predict a nonlinear wave number shift,

$$\delta k_{zn} = \frac{3\omega_n}{2c} \left(\frac{mc^2}{q} \right)^2 |a_n|^2 \delta\varepsilon_0^{(3)} A_\varepsilon\, \tau_n^4 , \tag{36}$$

which can be compared with Eq. (30) thus giving the definition of the effective area.

While it seems that many simplifying assumptions and unknown form factors have been introduced to describe the effect of the nonlinear dielectric, this effect depends only on the integrated nonlinear phase shift induced by the signal. Thus, while a specific realization is dependent on details such as the coupling parameters τ_n, the effective area $A_\varepsilon(z)$ and the magnitude of the nonlinear coefficient $\delta\varepsilon_0{}^{(3)}$, once these are selected to give a specific phase shift the operation of the device should be well described by Eqs. (34) and (35).

III Reduction of Intermodulation Distortion

We begin our discussion of intermodulation distortion by considering the nonlinear transfer function for single frequency operation of a traveling wave tube amplifier. Suppose a signal at a single frequency ω_n with complex amplitude $a_n(0)$ is injected into the amplifier. As the phases of injected electrons are uniformly distributed, the phase of the amplified signal at any point along the interaction region is related to the phase of the injected signal by an additive constant which depends only on the magnitude of the injected signal. Further, the magnitude of the signal at any point along the interaction region only depends on the magnitude of the injected signal. Thus, the nonlinear gain of the TWT can be characterized by a complex transfer function,

$$g_n(|a_n(0)|) = a_n(L) / a_n(0)$$

where L is the length of the interaction region.

As mentioned, the transfer function is complex. It's magnitude and phase both depend on the amplitude of the injected signal. This is illustrated in fig. 2, where we plot the magnitude and phase of the transfer function at 5 GHz for a structure with parameters given in table 1. These parameters are similar to, but not identical to, those of the Northrop Grumman research tube #8. In the plot the magnitude of the transfer function is given in dB, and the magnitude of the input signal is given in units of power. As input power is increased, two effects are apparent. First, the gain decreases as the amplifier is driven to saturation. This is known as gain compression. Second, the phase of the transfer function increases with signal power. This is known as AM (amplitude modulation) to PM (phase modulation) distortion. Changing parameters of the amplifier, for example the beam voltage, or introducing dynamic velocity tapering can reduce the amount of gain compression considerably. However, these measures have substantially less influence of the phase distortion. The fundamental reason for the phase distortion is the dependence of the beam speed on the signal amplitude. In a TWT the signal is partially carried by the electromagnetic slow wave and partially carried by the streaming electron beam. The phase delay associated with the beam is $\int_0^L dz\, \omega_n / v_z$. Note that this phase is positive as a consequence of our choice of representation of the complex fields in Eqs. (1a) and (1b). Thus, at high signal levels, when the beam loses substantial energy and slows down, the phase delay associated with the beam goes up.

Table 1

Low Dispersion Structure Parameters

Helix period, λ_H	0.07.779 cm
Helix radius, r_H	0.12446 cm
Wall radius, r_w	0.2794 cm
Vane radius, r_v	0.19 cm
Effective dielectric constant, ε	1.25
Beam voltage, V_B	2.84 kV
Beam current, I	0.17 A
Beam radius, r_{bo} (r_{bi} = 0.)	0.05 cm

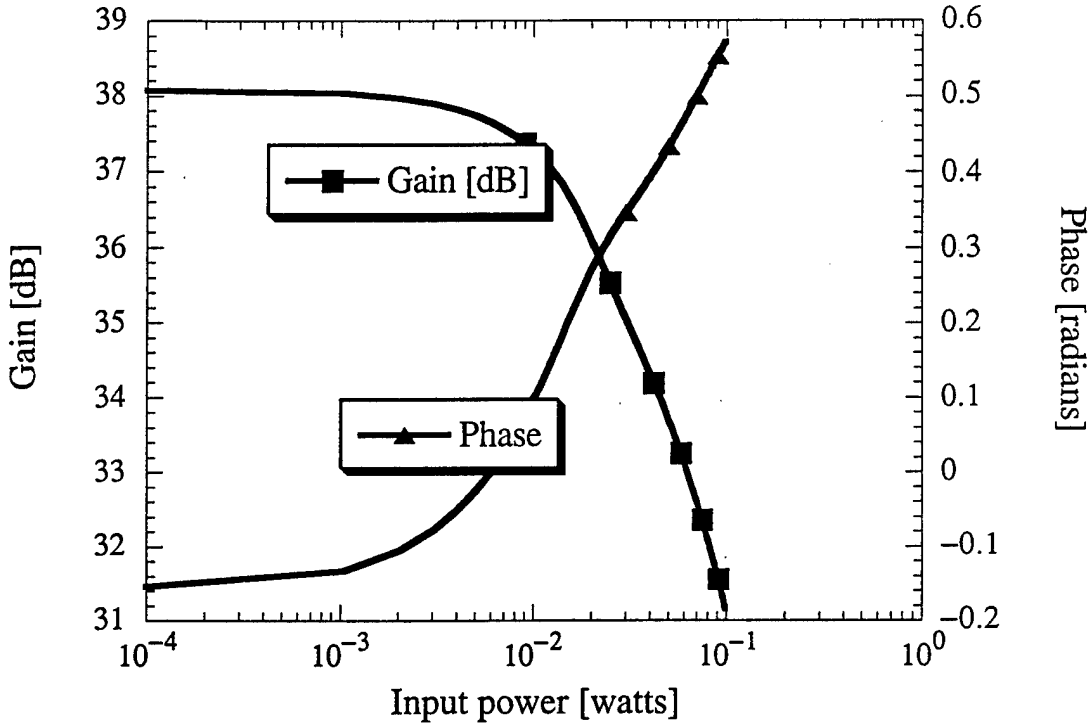

Fig. 2 Gain and phase of the nonlinear transfer function versus input power for a TWT with the parameters shown in Table 1.

The effect of the nonlinearity of the transfer function when multiple signal frequencies are present is illustrated in the output power spectrum of fig. 3. In this case we have injected two signals of equal power (4 mW), one at 5 GHz, and one at 5.5 GHz. The output spectrum consists of all frequencies separated by 0.5GHz intervals. From the figure is seen that for frequencies near the driven signals the largest power is in the third order intermodulation products at 4.5 GHz and 6 GHz respectively. There is also signal power at frequencies corresponding to the second harmonics and sum of the driven signals.

The goal of our study is to reduce the amplitude of the intermodulation products. This will be done by finding ways to improve the linearity of the transfer function. The ideal transfer function would be one in which the complex gain is independent of the injected signal amplitude. Use of predistortion linearizers attempts to reach this goal by passing the signal first through a nonlinear circuit which compensates for gain compression and phase distortion. We instead will use a combination of dynamic velocity taper and

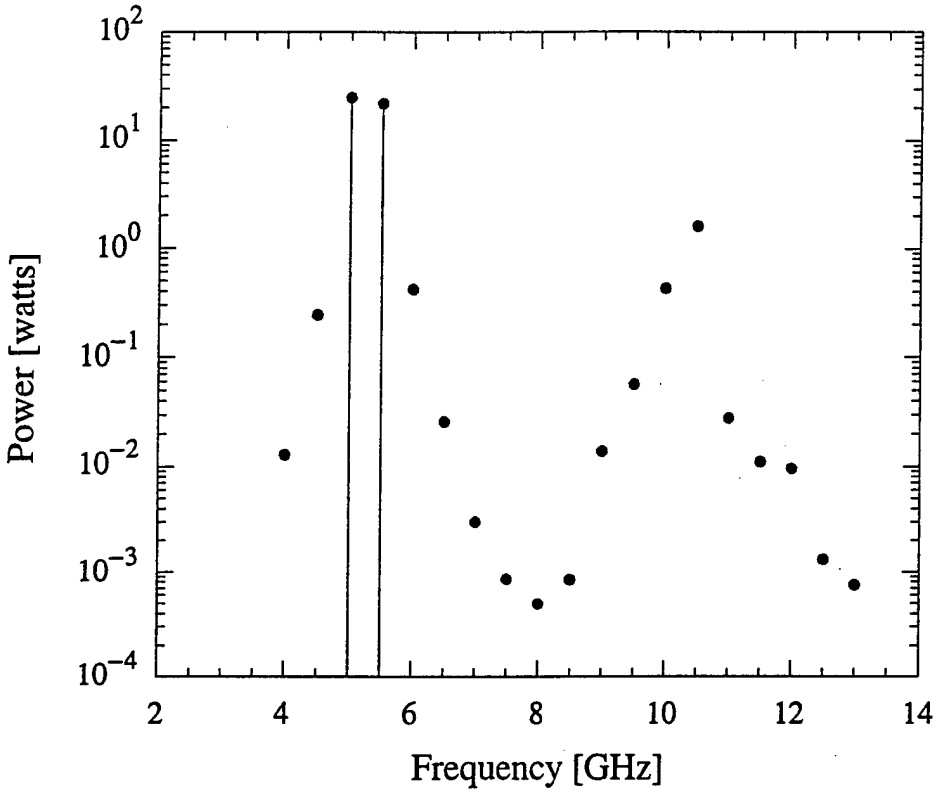

fig. 3 Output power versus frequency for the TWT of table 1. The two vertical lines correspond to the frequencies of the injected signals.

nonlinear phase modification to linearize the tube. To be specific, we take the circuit parameters listed in Table 1 as a starting point. We then add a region of nonlinear dielectric with wave number shift given by Eq.(34) to the last .2 cm of the interaction region. In fact this nonlinear phase shifter could equally well be attached outside the tube. To implement dynamic velocity taper we allow the helix wavelength to be a piecewise linear function of axial distance defined at eight points along the interaction region: z_i= 0., 6., 7., 8., 9., 9.4, 9.41, and 9.6 cm. The nonlinear transfer function then depends parametrically on the eight values of helix period, λ_{Hi} for i = 1to 8, and the strength of the dielectric nonlinearity, $\delta\varepsilon_0^{(3)}$

$$g_n = g_n(|a_n(0)|;\lambda_{Hi},\delta\varepsilon_0^{(3)}) .$$

The degree of linearity is quantified by the square error which we define to be

$$error(\lambda_{Hi}, \delta\varepsilon_0^{(3)}) = \int_o^{P_{max}} \frac{d\,P_{out}}{P_{max}} \left| \frac{g_n(|a_n(0)|) - g_n(0)}{g_n(0)} \right|^2 . \qquad (37)$$

Thus, a perfectly linear amplifier, over the range of output powers, $P_{out} < P_{max}$, would produce zero error. The error defined in Eq.(37) is then minimized numerically with respect to the parameters, λ_{Hi} and $\delta\varepsilon_0{}^{(3)}$. For the circuit under consideration, there is considerable excitation of the second harmonic. Thus, the nonlinear transfer function is calculated including the excitation of the second harmonic signal.

The results of the minimization of the gain error for the case of 60 watts maximum output power are displayed in figs 4 through 8. First, in fig. 4 we display the optimum profile of axial phase velocity. This profile is very similar to one which results in optimum efficiency. By way of comparison, the error value for the untapered, uncompensated circuit is 2.42×10^{-2} whereas the tapered, phase compensated circuit is 3.66×10^{-5}.

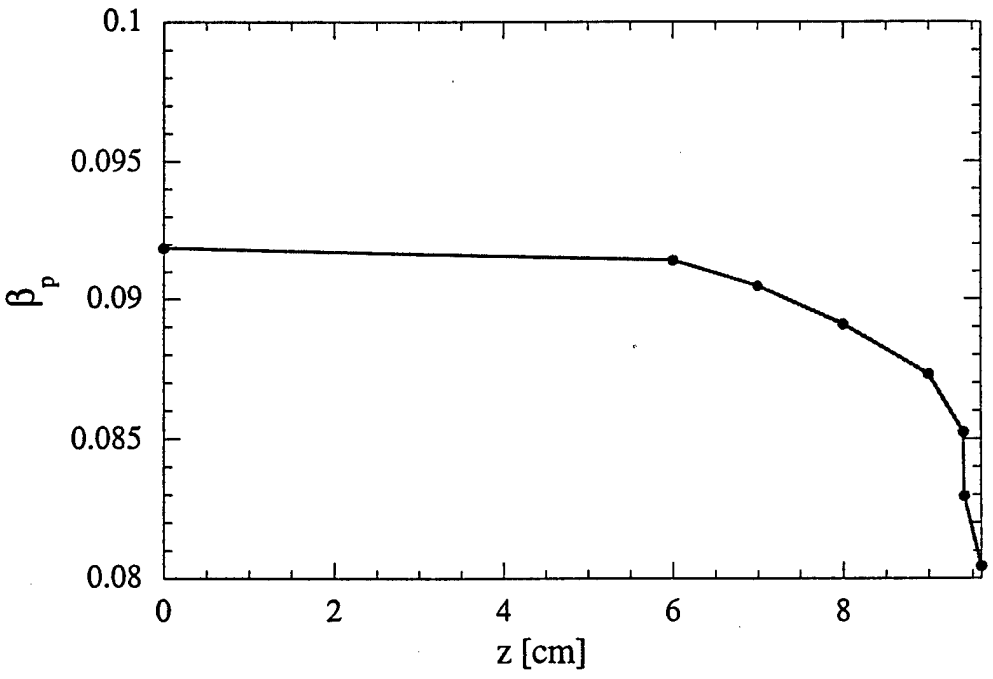

Fig. 4 Profile of normalized phase velocity versus axial distance for optimized circuit.

Figure 5 shows a comparison of the gain compression for the compensated and optimized transfer function and the original transfer function displayed in fig. 2, except here the transfer function is plotted versus output power. Clearly, the improvement in the linearity

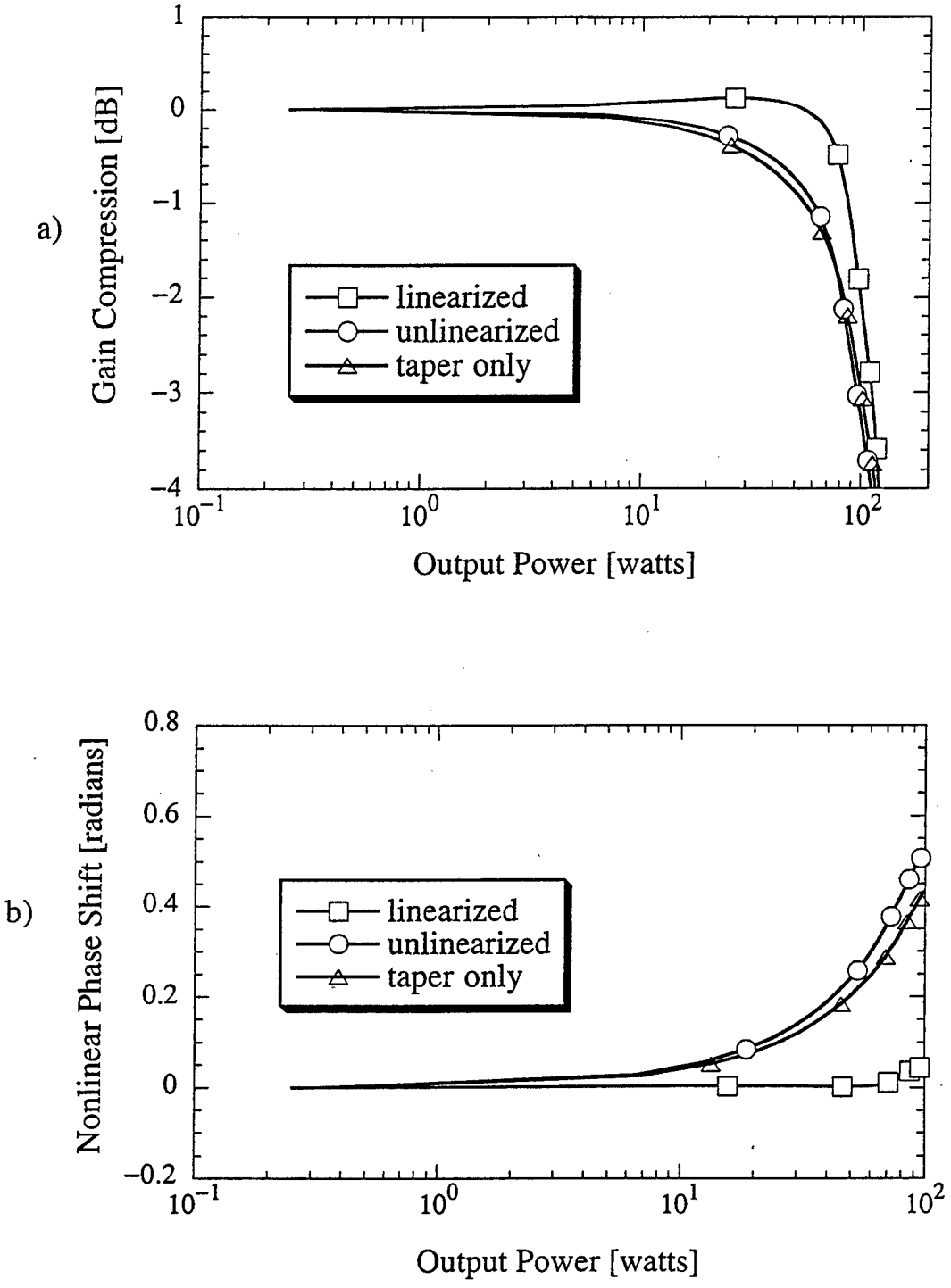

Fig. 5 Comparison of a) gain compression and b) phase distortion for linearized, unlinearized and taper optimized circuits

is particularly evident in the dependence of the phase of the transfer function on output power. For further comparison, fig 5 also displays the transfer function obtained when the

nonlinear phase compensation is not employed but the circuit parameters are chosen to minimize the error defined in Eq. (37). This case shows only a very modest improvement over the unlinearized case, and is not clearly as effective as the combination of phase compensation and circuit tapering. Figure 6 shows the output spectra for the linearized and unlinearized amplifiers when two signals are injected. In this case the signal levels have been adjusted so that the output power is 30 watts in each case. For these parameters there is over an order of magnitude reduction in power in the intermodulation products in the optimized and phase compensated case. The role of the nonlinear dielectric's in reducing the intermodulation product amplitudes is illustrated in fig. 7. Here we have plotted the power in the two driven signals, 5.0 and 5.5 GHz, as well as the power in the third order intermodulation products at 4.5 and 6.0 GHz. Only the last .6 cm of the interaction region as shown; the shaded region corresponds to where the nonlinear dielectrics are present. It can be seen that the intermodulation power is reduced dramatically in this region. We note that this is not attenuation, rather the power from the intermodulation products is converted into power at the driven frequencies.

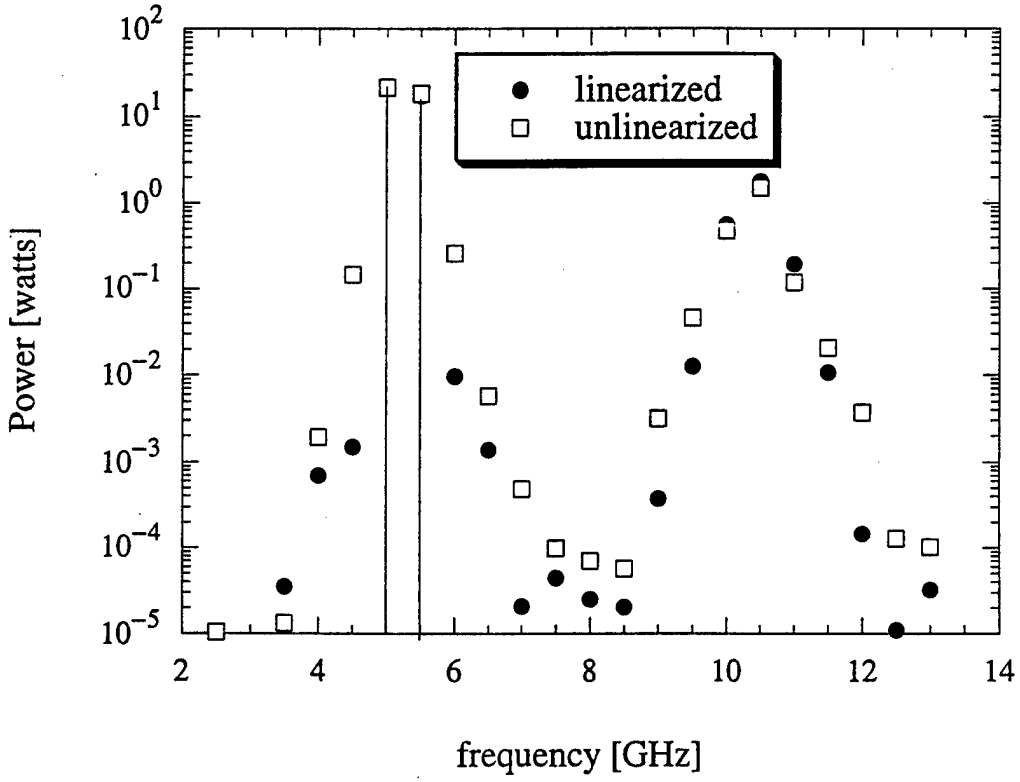

Fig. 6 Comparison of output spectra for linearized and unlinearized circuits.

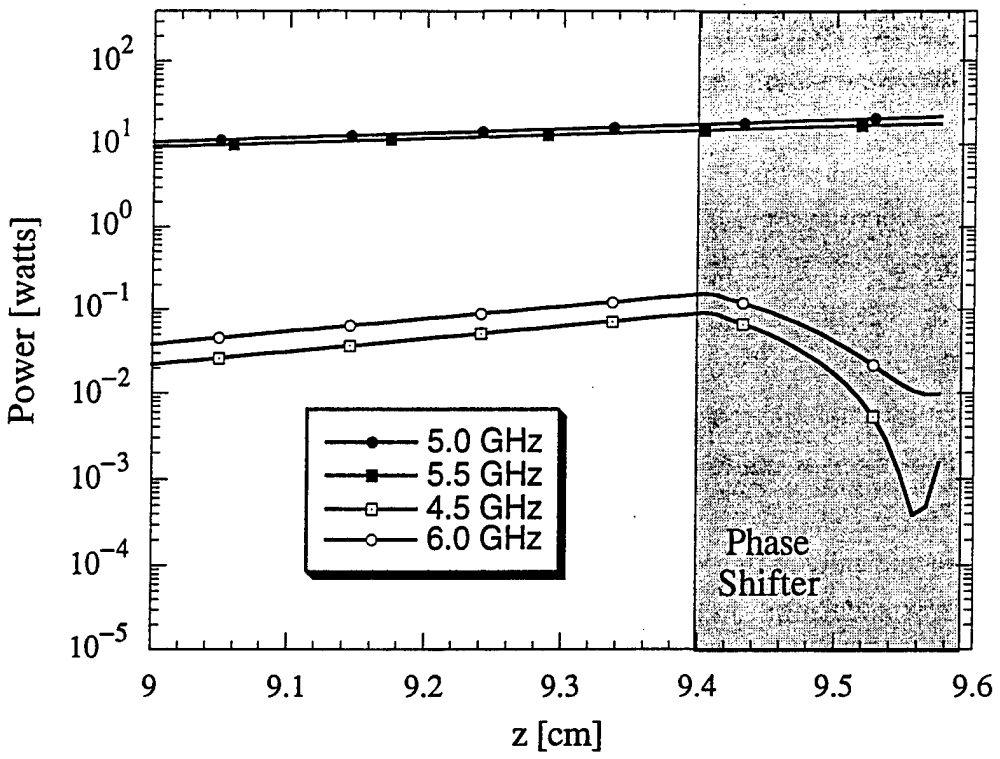

Fig. 7 Power versus axial distance for the linearized circuit. The injected signals are at 5.0 and 5.5 GHz. The shaded region corresponds to the location of the nonlinear dielectric element.

The effectiveness of the linearization over a range of output powers is illustrated in fig. 8 where we have plotted the signal to intermodulation power ratio as a function of output power. This ratio is one to two orders of magnitude higher for the linearized case for powers below 40 watts. At higher powers, approaching the saturated output power of the device the ratio decreases. The unlinearized case shows the expected $(P_{out})^{-2}$ dependence. The linearized case shows this dependence at low output powers, with a slight improvement in the range of powers for which the optimization was performed. The location of this enhancement can be varied by changing the value of P_{max} in the optimization. For the present case, if one requires a signal to intermodulation distortion ratio of 10^4, then the linearized case allows for operation with over six times the output power.

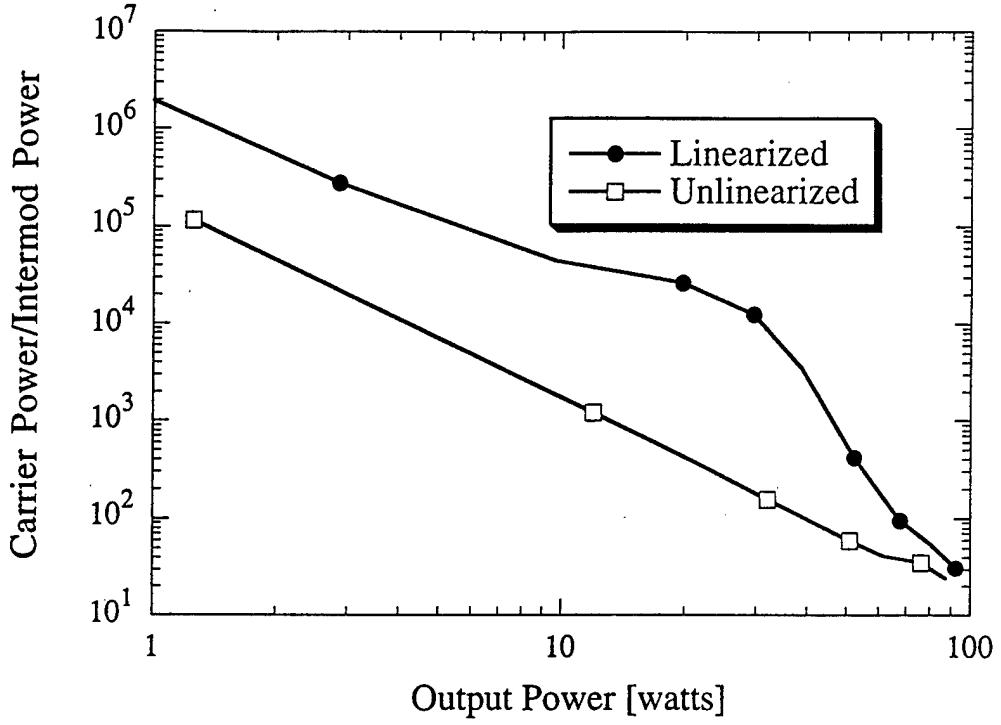

Fig. 8 The ration of power in the driven signals to power in the third order intermodulation products as a function of output power for the linearized and unlinearized circuits.

In the preceding we have compared the unlinearized circuit with one in which nonlinear dielectric elements are added at the output end of the interaction region. We now compare the case in which the nonlinear dielectric element is placed at the input with the case in which it is placed at the output. In the case of input linearization we again perform the optimization over the helix period and the nonlinear dielectric constant.

In this way the performance predicted with input linearization should be comparable to what is achieved with predistortion linearizers. We perform the optimization for P_{max}=60w, and frequency 5 GHz. We then compare the nonlinear transfer functions for a range of drive frequencies. This comparison is illustrated in figs. 9 and 10 where the transfer functions for the cases of output linearization and input linearization are shown receptively. In fig. 9 which shows the gain versus output power there is not much difference between the two cases. However, fig. 10, which shows the phase versus output power is more revealing. As is seen, the linearization which is optimized for 5 GHz is

more effective over a range of frequencies for the output linearization case as compared with the input

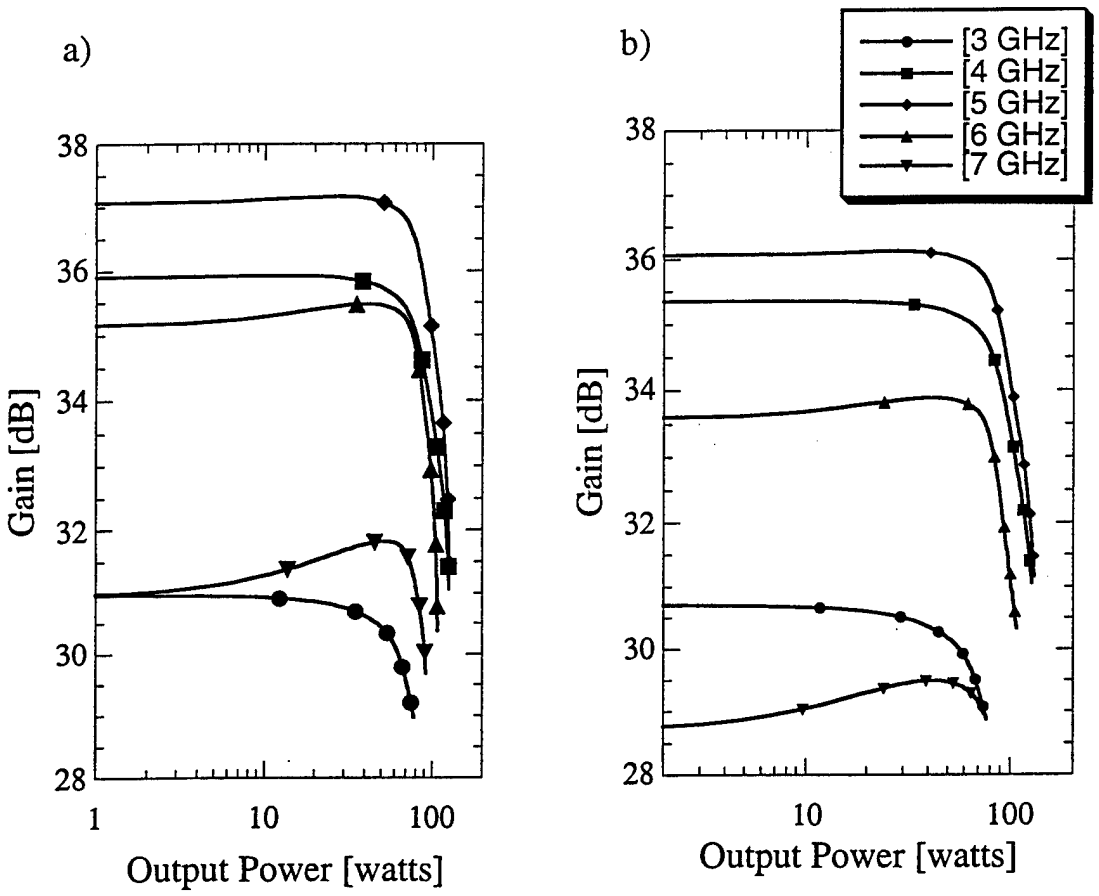

fig. 9 Gain versus output power for a range of drive frequencies, a) for output linearization and b) for input linearization

linearization case. Note that the scales on these two figures differ, and that the variation of phase with output power is much smaller in the output linearization case. This is further illustrated in fig. 11 where we compare the carrier to intermodulation distortion power as a function of frequency for two methods. To generate this plot two signals of equal power are injected, one at the indicated frequency, and one at a frequency .5 GHz higher. The power in the injected signals is adjusted so that the output power is 30 watts. We then plot the ratio of the power in the two driven

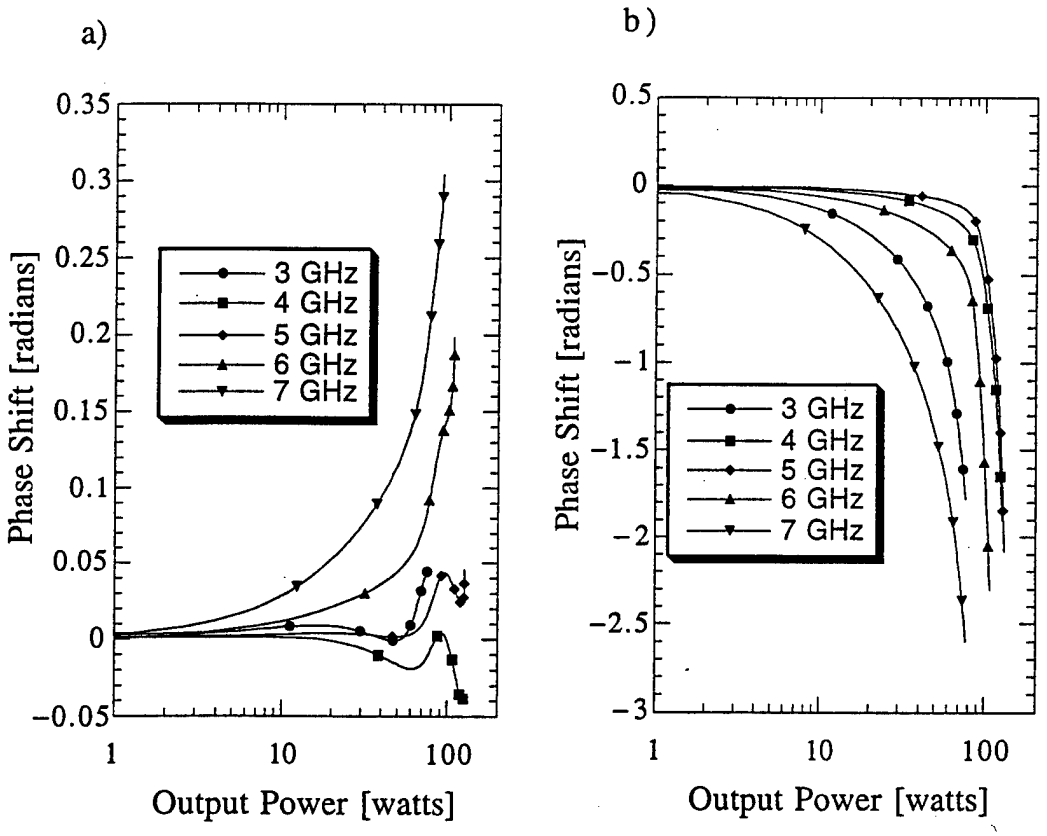

fig. 10. Phase shift versus output power for a range of drive frequencies, a) for output linearization and b) for input linearization

frequencies with that in the two third order intermodulation products. We note that even at 5 GHz where both circuits were optimized, the output linearized circuit has superior linearity as compared with the input linearized circuit. This difference grows as frequency is varies away from 5 GHz. The main cause for this difference is that the distortion in the TWT is generated at the output where the signal is large. Thus, the level of the output power is a more reliable indicator of the distortion than the input power. We conclude that output linearization is an effective way to reduce intermodulation distortion in a TWT amplifier, and the reduced distortion can be realizes over a range of operating frequencies. Figure 11 shows for example that the carrier to intermodulation power ratio remains well over 10^3 for frequencies 4 and 6.5 GHz.

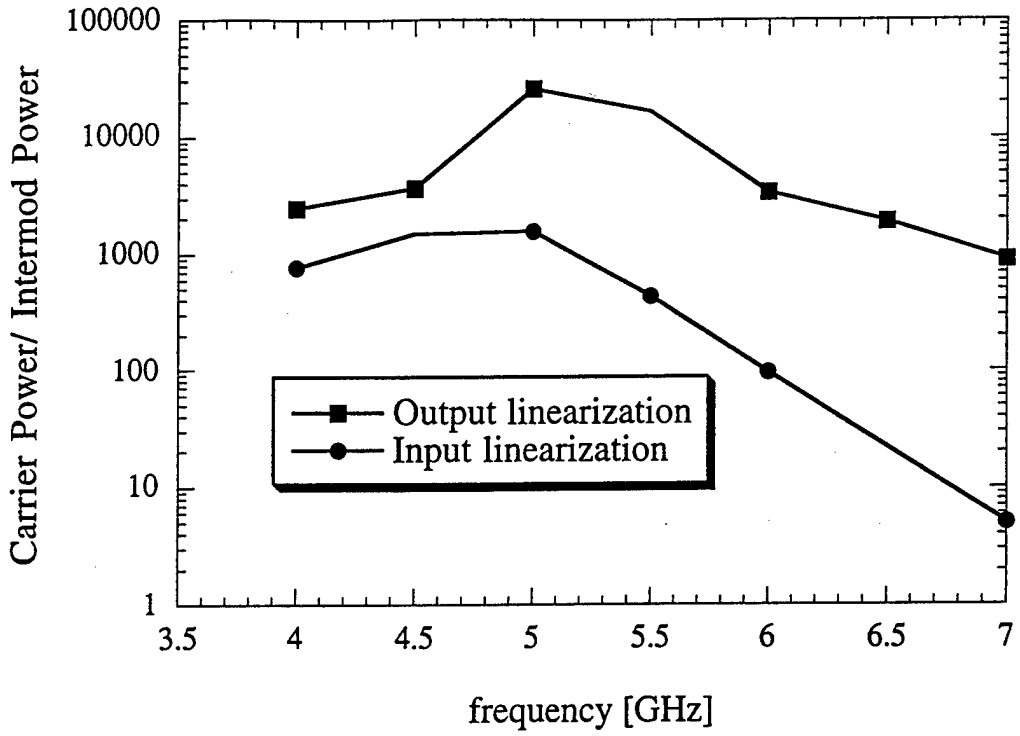

Fig. 11 Comparison of carrier to intermodulation power as a function of frequency for the case s of input and output linearization.

III Electronic Tuning of Gain

In this section we consider the possibility of tuning the frequency response of the TWT transfer function by electrically varying the dielectric constant of the rods which support the helix. The basic idea is that these rods could be made of or coated with a ferroelectric material (operating in the paraelectric phase). A DC voltage applied to the rods would then change their dielectric constant and alter both the phase velocity and coupling impedance of the helix structure. We imagine that relatively modest changes, ± 20 %, are realizable and seek to determine the effect on the TWT transfer function. The bandwidth of Helix TWTs is determined by both the dispersion of the structure as well as the frequency dependence of its coupling impedance. For this reason we can not employ the formulation of Sec. IIC to calculate the effect of a small change in dielectric constant on the transfer function. This formulation calculates only the change in dispersion (specifically, axial wavenumber) due to a given change in dielectric constant. Instead, we use the solutions of the sheath helix dispersion relation (25) and vary the dielectric constant of the outer region.

We begin this study by calculating the linear gain as a function of frequency for the untapered structure considered in the previous section. The parameters of this structure are shown in table 1. Figure 12 shows the gain versus frequency for this structure when the effective dielectric constant is varied.

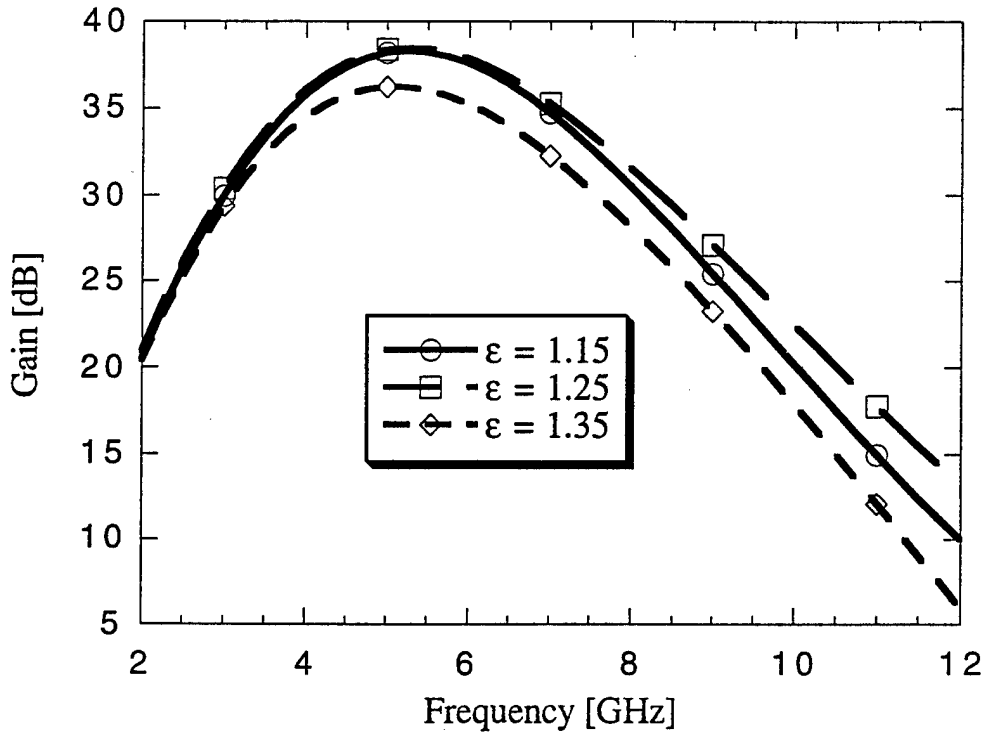

Fig. 12 Gain versus frequency for the low dispersion structure of table 1.

As can be seen, the main effect of varying the dielectric constant is to vary the magnitude of the gain but not to vary the frequency of maximum gain. This is because the structure has low dispersion. Thus, varying the dielectric constant mainly moves the phase velocity on and off synchronism with the beam across the entire frequency range. Further, since the effective dielectric constant is rather low, $\varepsilon = 1.25$ the variation in susceptibility , $(\varepsilon - 1)$, implied by fig. 12 is rather large.

To achieve tuning requires a dispersive phase velocity. Additionally, the gain at higher frequencies tends to be limited by the decrease in coupling impedance. Thus a

means must be found to increase coupling impedance at higher frequency. The structure whose parameters are given in table 2 has these properties.

Table 2

High Dispersion Structure Parameters

Helix period, λ_H	0.0802 cm
Helix radius, r_H	0.12446 cm
Wall radius, r_w	0.18 cm
Vane radius, r_v	0.2794 cm
Effective dielectric constant, ε	1.75
Beam voltage, V_B	3.0 kV
Beam current, I	0.17 A
Beam radius, r_{bo} (r_{bi} = 0.)	0.05 cm

Note that for this structure the vane radius is greater than the wall radius. This implies that the interaction waveguide needs to be loaded with conducting discs. Future studies which

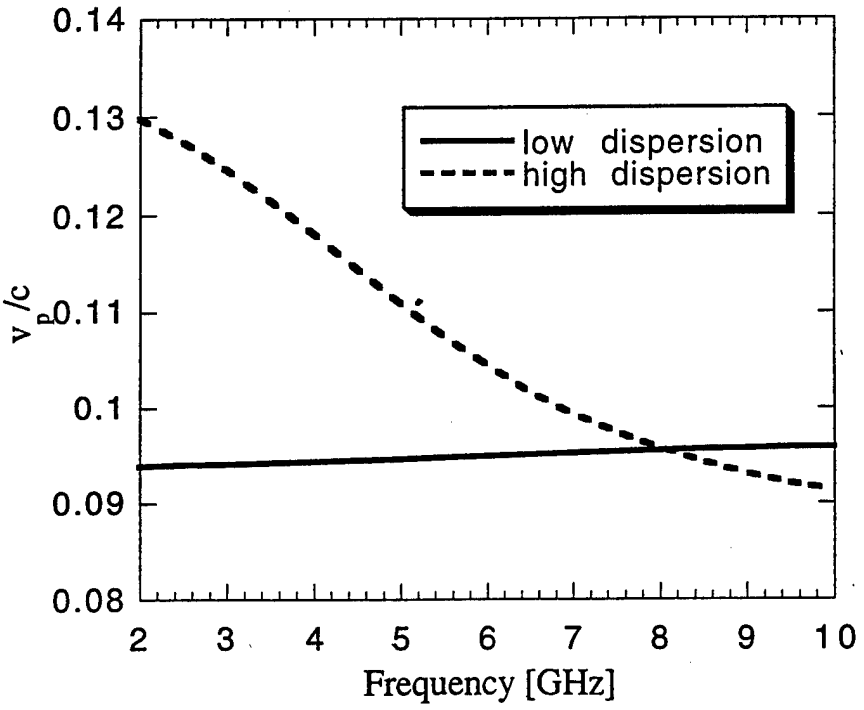

Fig. 13 Comparison of phase velocities for low and high dispersion structures. Parameters are given in Tables 1 and 2.

go beyond the sheath helix model will address the issue of the structure geometry in more detail.

The dispersion and coupling impedance versus frequency for the two structures is shown in figs 13 and 14.

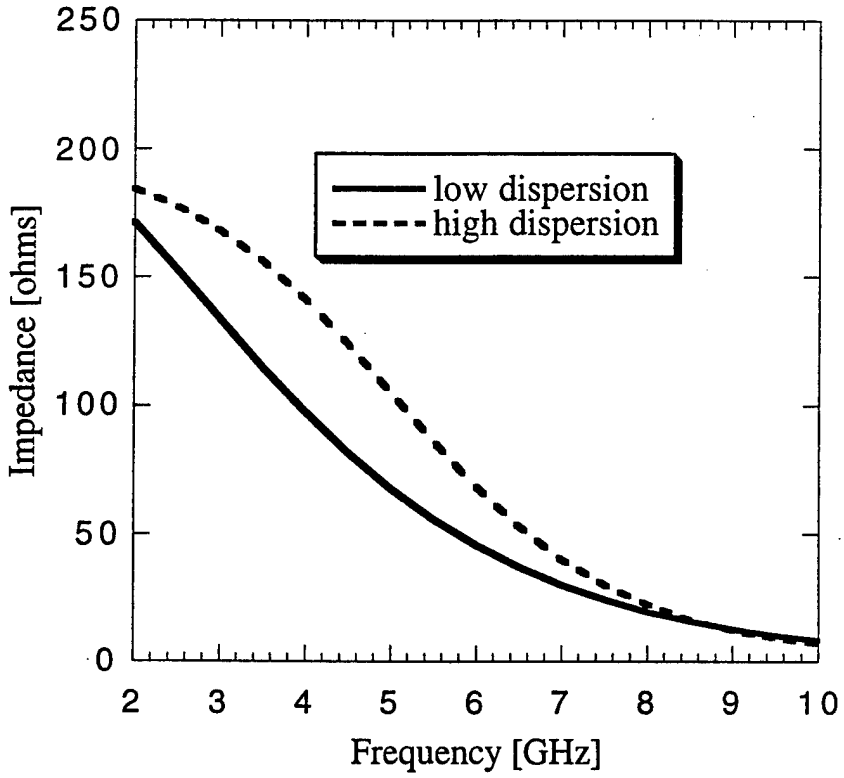

Fig. 14 Comparison of coupling impedance for low and high dispersion structures. Parameters are given in Tables 1 and 2.

As can be seen the phase velocity for the high dispersion structure varies across the frequency band, and the coupling impedance for frequencies between 5 and 7 GHz is 30 to 50% larger than that of the low dispersion structure.

The gain versus frequency for the high dispersion structure is shown for several values of dielectric constant in fig. 15.

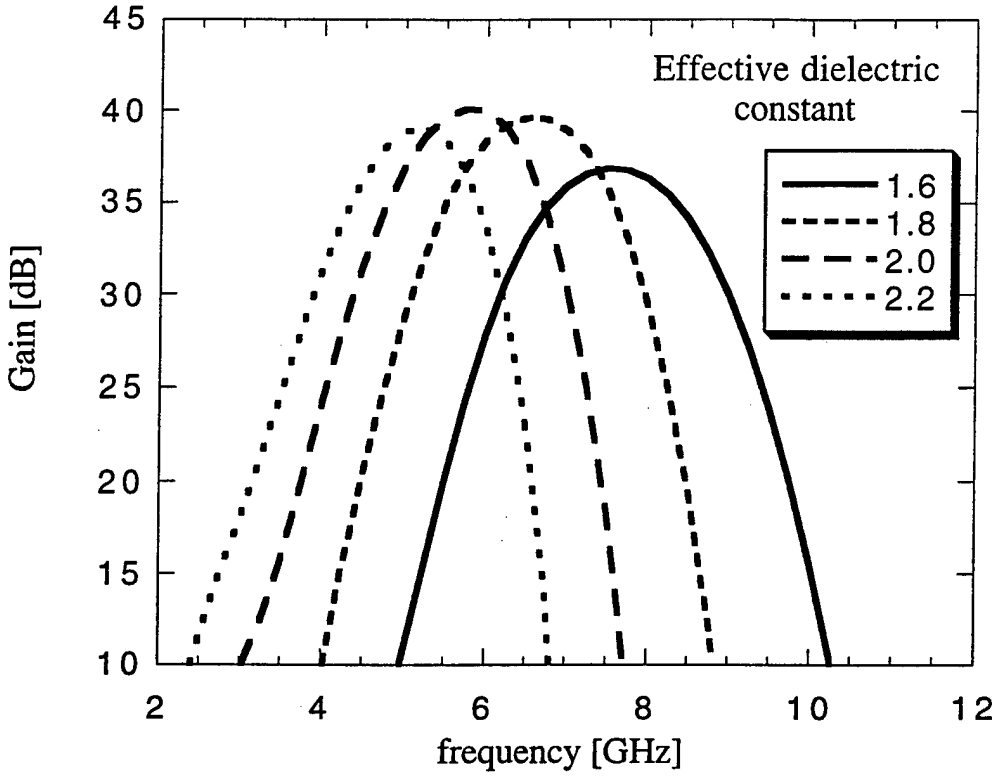

Fig. 15 Gain versus frequency for t several values of dielectric constant for the structure whose parameters are given in table 2.

In the case of fig. 15, variation of the dielectric constant has tuned the frequency of peak gain from 5 to 8 GHz. Further, the overall bandwidth has been improved over the low dispersion structure. While the improvement in bandwidth over the low case dispersion case is marginal, it must be remembered that a helix TWT is an inherently high bandwidth device. Thus, it is difficult to improve the bandwidth by a large margin. The concept of electronic tuning of gain to increase bandwidth might be more attractive if applied to low bandwidth amplifiers, such as coupled cavity TWTs.

III Conclusions

In this manuscript we have examined two possible uses for nonlinear dielectric elements in traveling wave tube amplifiers. The realization of these depends in large part on finding appropriate dielectric materials. The two schemes require materials for which

the dielectric constant depends on the strength of the applied electric field. In the case of intermodulation distortion reduction what is required is a material with a negative coefficient of third order dielectric constant $\delta\varepsilon_0^{(3)}$. While in the case of electronically tuning of amplifier gain what is required is a material whose first order dielectric constant can be varied by applying a bias voltage.

A possible candidate material fulfilling both requirements is a ferroelectric operating above the Curie temperature. These materials have a dielectric constant which depends on applied electric field. For small electric fields the dielectric constant depends quadratically on the field strength and decreases with increasing field strength giving the required negative third order dielectric constant [Vendik]. Additionally, the dielectric constant can be changed over a relatively large range by varying a DC bias electric field, this feature is required for the concept of electronically tuning the gain of a TWT. Recent advances in the development of Barium Strontium Titanate composites [ ] have allowed significant progress in the design of phase shifters for phased array antennas [ ]. The proper composition of Barium and Strontium with additives allows one to operate the phase shifter in the para-electric regime, thus reducing possible losses and hysteresis effects. For example, these material improvements have resulted in voltage controlled phase shifts greater than 360 degrees with less than 6 dB insertion loss [ ]. The phase shift variation is proportional to the tunability of a material $[\varepsilon'(0) - \varepsilon'(V_{app})] / \varepsilon'(0)$, where $\varepsilon'(0)$ is the dielectric constant without applied electric field and $\varepsilon'(V_{app})$ is the dielectric constant after some electric field is applied. Depending on the material composition the tunability can be between 1% to 40% [ ] when electric field on the order of few volts/mm is applied . The dielectric constant of these materials can be as high as few thousand. The loss tangent also has significant variation as a function of compositions as well as a function of frequency. For example, at 10 GHz $Ba_{.50}\ Sr_{.50}\ TiO_3$ with sixty percent by weight added oxide has a relative permitivity 84.5 and loss tangent 6.55×10^{-3} [ ]

As mentioned, an important consideration for such materials is the amount of loss caused by their introduction into the circuit. For example, in the case of output linearization, since the phase compensation is applied at the output of the amplifier it is critical that the loss be small. An order of magnitude estimate of these losses can be obtained as follows. Examination of fig. 5b shows that the nonlinear dielectric element must provide a nonlinear phase shift of about .4 radians to be effective. This number is obtained by comparing the phase shift at 100 W output power in the taper optimized circuit with that in the fully linearized circuit. This phase shift would be realized by passing the

signal through a section of circuit of length L_ε which had a nonlinear wave number shift of the form given by Eq. (30). Using the same reasoning that lead to Eq. (33) we can write this phase shift $\delta\phi = \delta\varepsilon_{nl}(\partial k_{zn}/\partial\varepsilon)L_\varepsilon$ where $\delta\varepsilon_{nl}$ is the nonlinear shift in the dielectric. The attenuation Γ in dB realized in passing through this dielectric, assuming perfect matching, can be expressed in terms of the loss tangent and the real part of the dielectric constant, $\Gamma = 8.69\,(tan\delta)\varepsilon'(\partial k_{zn}/\partial\varepsilon)L_\varepsilon$. Thus, for a phase shift of .4 radians the attenuation can be estimated as

$$\Gamma = 3.48\,(tan\delta)\,(\varepsilon'/\delta\varepsilon_{nl})\,. \tag{38}$$

This attenuation will be small provided the loss tangent is much smaller than the tunability of the material $\delta\varepsilon_{nl}/\varepsilon'$. For example, it is reasonable to assume 10% tunability and 1% loss tangent is achievable in practice. This will result only in 0.348 dB attenuation. The above estimate, however, assumed perfect matching. The dielectric constant of ferroelectric materials operating in this regime tends to be very large. Thus, there is the problem, which is solvable with proper matching design, of coupling the field into the dielectric without inducing large reflections.

The electronic tuning of gain can be implemented, for example, by incorporating the ferroelectric material in the dielectric structures which are used in the TWT circuit to support the helix. If the amplifier is of the coupled cavity type the ferroelectric material would be added to the individual cavities of the structure. The dielectric constant of the ferroelectric material is typically measured in thousands, while the dielectric constant of BeO, the material of which the helix support structures is made, is about 6. The high dielectric constant will again raise the issue of coupling the fields into the material. One approach would be to deposit a very thin layer of the ferroelectric material on to another dielectric substrate. Electrical conductors would have to be attached so that a DC electric field would be applied to the ferroelectric material. If the dimension of the ferroelectric is small enough it would only require a small voltage to achieve the desired tunability. In future studies we will address more specifically the optimum geometry and effective implementation of the adaptive TWT circuit with tunable a ferroelectric for gain control.

What we have shown here is that nonlinear dielectric elements have, in principle, the capability of enhancing the performance of traveling wave tube amplifiers. The next step is to attempt to implement these ideas in a real amplifier.

Acknowledgment

This work was supported by the ?????

References

1. A. S. Gilmour "Principles of Traveling Wave Tubes", Artech House, 1994
2. H. Seidel "A Microwave Feed-Forward Experiment", The Bell System Technical Journal", vol. 50, #9, p. 2879-2916 (1971)
3. S. Narahashi, T. Nojima "Extremely Low Distortion Multi Carrier Amplifier -Self Adjusting Feed Forward Amplifier", CH2984-3/91/0000-1991, IEEE, pp. 1485-1490
4. H. G. Kosmahl "Modern multistage depressed collectors -A review", Proc. IEEE, vol. 70, pp. 1325-1334 (1982)
5. A. Katz, R. Sudarsanam and D. Aubert " Areflective Diode Linearizer for Spacecraft Applications", IEEE MTT-S International Microwave Symposium Digest, pp. 661-664, June 1985
6. J. Maynard, B. Cogo, M. Pouysegur "Fully MMIC Ku-band and C-band CAMP/Linearizers for TWTs", European Space Agency WPP-072, Space TWTAs Workshop, 18-20 May, 1994, Noordwijk, The Netherlands
7. T. Antonsen, Jr. and B. Levush "CHRISTINE: A Multifrequency Parametric Simulation Code for Traveling Wave Tube Amplifiers", NRL/FR/6840-97-9845
8. J. E. Rowe, Nonlinear Electron-Wave Interaction Phenomena (Academic Press, New York, 1965).
9. A.J. Giarola, "A Theoretical Description for the Multiple-Signal Operation of a TWT", IEEE Trans. Electron Dev. **ED15**, 381 (1968).
10. N.J. Dionne, "Harmonic Generation in Octave Bandwidth Traveling-Wave Tubes" IEEE Trans. Electron Dev **ED 4**, 365 (1970).
11. Sven Wallander, "Non-linear Multi-signal Traveling Wave Tube Theory", Int. J. Electronics **29**, 201 (1970).
12. H. Kosmahl and J. Peterson "A TWT Amplifier with a linear power transfer characteristic and improved efficiency", NASA Technical Memorandum 83590, presented at 10th Communications Satellite Systems Conference sponsored by the AIAA, Orlando, Florida< March 18-22, 1984
13. R. G. Geyer, J. Krupka, L. Sengupta, S. Sengupta " Microwave properties of composite ceramic phase shifter materials" IEEE Proc of the International Symposium of the Application of Ferroelectrics, 96 CH-35948, p. 851-854, 1996
14. R. Babbitt, T. Koscica, W. Drach and L. Didomenico " Ferroelectric phase shifters and their performance in microwave phased array antennas", Integrated Ferroelectrics, vol. 8 , pp. 65-76 (1995)

15. L. Sengupta, E. Ngo, S. Stowell, M. O'Day and R. Lancto " Processing, Packaging, and Characterization of Electroceramic Materials for Phased Array Antennas", ARL-TR-448, May 1994

16. O. Vendik " Dielectric Nonlinearity of the dispacive ferroelectrics at UHF", Ferroelectrics, vo. 12, pp. 85-90, (1976)

APPENDIX XIX

Shot Noise in Gyroklystrons

T.M. Antonsen, Jr. and W.M. Manheimer
Work in Progress

SHOT NOISE IN GYROKLYSTRONS

Thomas M. Antonsen Jr.[a] and Wallace Manheimer[b]

Vacuum Electronics Branch
Code 6841
Electronics Science and Technology Division
Naval Research Laboratory
Washington DC 20375-5320

Abstract

Expressions for the shot noise generated in the input cavity of a Gyroklystron are calculated. Results are given for noise amplitude, noise temperature, and phase noise. For a beam of uncorrelated electrons the noise temperature scales as the beam energy. An estimate of the role of collective effects on the noise properties is given. These might either decrease or increase the noise level. It is expected that the shot noise in an actual device will depend in a sensitive way on the profile of magnetic field in the compression region preceding the input cavity.

a. Science Applications International Corporation, 1710 Goodrich Drive McLean VA, and Departments of Electrical Engineering and Physics, University of Maryland, College Park, MD 20742

b. Code 6707, Plasma Physics Division, NRL, Washington, DC 20375

I Introduction

A high power 94 GHz Gyroklystron is now being developed at NRL, ultimately for application in a millimeter wave radar system [1]. In modern radar systems, it is important to keep the transmitter noise as low as possible. For the gyroklystron, which is a multiple cavity amplifier, this means minimizing the noise in the input cavity, since this is the noise which is amplified as it progresses through the various cavities. There are a number of sources of noise which can effect electron beam devices [2]. These may be classified as intrinsic or extrinsic depending on their source. Intrinsic noise results from processes directly associated with the formation and transport of the electron beam. Examples include shot noise which is associated with the discreteness of the electronic charge, flicker noise which is associated with imperfections in the emmision process, and ion oscillation noise which is associated with the unstable interaction between the electron beam and ions trapped in the beam region. Extrinsic source noise results from fluctuations in the external power supplies attached to the device. The effect of these has been examined for gyroklystrons in in ref. 3. This paper will be concerned exclusively with shot noise.

As a result of the discreteness of the electronic charge, the beam current entering the first cavity is not steady in time, but has a high frequency fluctuation spectrum which excites a signal in the cavity. The level of the signal depends on the spectrum and amplitude of the current fluctuations as well as the mean parameters of the electron beam and those of the cavity. As we shall see these latter parameters serve to define an effective resistance which along with the fluctuating part of the beam current determines the noise power in the cavity. The effective resistance, given in Eq. (15), depends on the geometry of the cavity, the coupling between the cavity mode and the beam, and the velocity pitch ratio of the spiraling electron beam. A typical value is about $100Q$ Ohms.

The level of current fluctuations depends on the degree of correlation of the electrons as they enter the cavity. The simplest expression for 'bare' shot noise assumes that all of the particles in the electron beam are uncorrelated with one another. In this sense, the 'bare' shot noise is a very fundamental quantity to calculate. It is certainly a useful quantity to know as one starts to do noise measurements on the input cavity. Under the assumption of uncorrelated electrons we shall find that the noise power spectrum in the cavity corresponds to a noise temperature of the order of the beam energy. Various physical processes can increase or decrease the shot noise level by inducing correlations among the electrons. It could be decreased by electrostatic shielding of long wavelength fluctuations (dependent on beam temperature and geometry) or by some active beam conditioning. It could be increased by electrostatic instabilities in the beam tunnel. The

possibility of these effects will also be discussed in this paper. Calculation of the 'bare' shot noise is thus the point of departure for more refined theories which take into account dielectric shielding and beam instabilities. We hope this work will prove useful in interpreting initial noise experiments and in stimulating future theoretical studies.

II. Calculation of Shot Noise in the Input Cavity of a Gyroklystron

The input of a gyroklystron is coupled to the microwave source through a combination of waveguides and coupling cavities. This excites a signal in the bunching cavity of some strength which is amplified from cavity to cavity. However, there is also noise (current fluctuations) on the electron beam. These fluctuations also excite a signal in the bunching cavity which will compete with the desired signal. One cause of the noise is that the electron beam is not a continuous stream of charge, but rather, a random stream of electrons which enter the input cavity at some rate. This is the shot noise. The purpose here is to calculate the shot noise under a variety of assumptions.

We now sketch out a derivation of the basic equations. The cavity fields are governed by Maxwell's equations which we write in the Fourier domain

$$\nabla \times \hat{\boldsymbol{B}} = \frac{4\pi}{c}\hat{\boldsymbol{J}} - i\frac{\omega}{c}\hat{\boldsymbol{E}} \tag{1a}$$

$$\nabla \times \hat{\boldsymbol{E}} = i\frac{\omega}{c}\hat{\boldsymbol{B}} \tag{1b}$$

where the hatted variables are the Fourier transforms with frequency ω of the real time dependent fields. We now assume that the fields in the cavity are dominantly those of a single mode of the cavity. The mode eigenfunction satisfies Eqs (1a) and (1b) with $\hat{\boldsymbol{J}} = 0$, and satisfies the boundary condition that tangential components of electric field and normal components of magnetic field vanish on the cavity walls. This eigenfunction is denoted by $\boldsymbol{E_n}$, and $\boldsymbol{B_n}$, where the eigenfrequency is ω_n, and we choose the normalization of the electric and magnetic fields to be given by

$$\int d^3x \, |\boldsymbol{E_n}|^2 = \int d^3x \, |\boldsymbol{B_n}|^2 = V \tag{2}$$

where V is the volume of the cavity. Thus, $\boldsymbol{E_n}$ and $\boldsymbol{B_n}$ are dimensionless. Further, we have used the fact that the electric and magnetic fields of a resonant cavity mode have the same stored energy.

The actual, time dependent field in the cavity is given approximately by

$$\boldsymbol{B}(x,t) = \int_0^\infty \frac{d\omega}{2\pi} A(\omega)\, \boldsymbol{B_n}(x)\, e^{-i\omega t} + c.c. , \tag{3a}$$

and

$$E(x,t) = \int_0^\infty \frac{d\omega}{2\pi} A(\omega)\, E_n(x)\, e^{-i\omega t} + c.c.\,, \tag{3b}$$

where $A(\omega)$ is a complex scalar amplitude to be determined. Here we have introduced the single sided Fourier integral, which when added to its complex conjugate is equivalent to the normal Fourier integral for the real functions $E(x,t)$ and $B(x,t)$. This step is taken so that in subsequent operations only positive values of frequency need to be considered.

Inserting $\hat{E} = A\,E_n$ and $\hat{B} = A\,B_n$ into Eqs. (1a) and (1b) and using a few standard vector manipulations gives [4,5],

$$A(\omega) = -\frac{2\pi i \int d^3x\, E_n^* \cdot \hat{J}}{V(\omega - \omega_n + i\omega_n/2Q)} \tag{4}$$

where we have lumped all dissipation and frequency shifts due to, for instance, coupling holes, beam tunnels, wall resistivity, etc. into the value of Q and adjusted the resonant frequency ω_n. The average energy stored in the cavity can be expressed in terms of A,

$$U = \frac{V}{4\pi} \int_0^\infty \frac{d\omega\, d\omega'}{(2\pi)^2} A(\omega) A^*(\omega')\, e^{-i(\omega-\omega')t} + c.c. \tag{5}$$

where we have assumed, according to Eq. (4), that $A(\omega)$ is peaked near ω_n and averaged over time corresponding to $2\pi/\omega_n$ eliminating terms with approximate frequency $2\omega_n$. The average power dissipated in the cavity is given in terms of the energy stored, the frequency, and the quality factor,

$$P = \frac{\omega_n U}{Q}.$$

The next step of the calculation is to evaluate the numerator in Eq. (4). To do this we first write the time dependent current density in terms of the trajectory followed by individual increments of charge,

$$J(x,t) = \sum_{\delta Q} \delta Q\; v_o(t)\; \delta(x - x_o(t)) \tag{6}$$

where δQ represents an increment of charge which follows the trajectory $[x_o(t), v_o(t)]$. For the case of shot noise δQ will represent the charge of an individual electron and the summation will include all electrons passing through the cavity. However, at this point we will allow flexibility in our treatment and leave the specification of δQ for later. The trajectory will be calculated assuming that the high frequency fields in the cavity are weak and that the trajectory is unaffected by them. In this case trajectories for particles with

identical entrance momenta and coordinates are distinguished only by their entrance time. The current density can then be written

$$J(x,t) = \sum_{\delta Q} \frac{\delta Q(t_e)}{v_z(z)} \, v_o(z) \, \delta(x_\perp - x_{\perp o}(z)) \, \delta(t - \tau(z) - t_e) , \qquad (7)$$

where we now express the orbit with z as the independent variable and $\tau(z)$ represents the time to reach the point z (measured from some reference surface, $z=0$). The variable t_e is the time of entrance of the increment of charge δQ. This increment of charge can be related to the beam current entering at a particular time $I(t_e)$,

$$\sum_{\delta Q} \delta Q(t_e) = \int dt_e \, I(t_e) .$$

That is, we replace the sum over increments of charge by an integral over the time dependent beam current. Various temporal forms for this beam current can be assumed. For example, bare shot noise is calculated if one takes the beam current to consist of a train of delta functions with weight e, the electron charge, and random entrance times. Alternatively one could take the beam current to vary coherently in time. Both these and more will be considered subsequently.

We now take the Fourier transform with respect to time of Eq. (7), and insert it in the numerator of Eq.(4) to obtain for $A(\omega)$,

$$A(\omega) = - \frac{2\pi i c \, \hat{I}(\omega) \, F(\omega)}{V(\omega - \omega_n + i\omega_n/2Q)} , \qquad (8)$$

where $\hat{I}(\omega)$ is the Fourier transform of the time dependent beam current. The quantity $F(\omega)$ in Eq. (8),

$$F(\omega) = \int d\tau \; E_n^*[x_0(\tau)] \cdot \beta(\tau) \; e^{i\omega\tau} , \qquad (9)$$

is an integral over time along the orbit. It represents the Fourier transform of the product of the relativistic factor, $\beta(\tau) = v_o(\tau)/c$, and the cavity electric field eigenfunction. A similar quantity appears in the expression for the power radiatied per unit frequency and per unit solid angle into free space [6]. Generally, the quantity F will have a peak value which scales as the product of the perpendicular component of β times the time of flight through the cavity. Due to the oscillatory nature of $\beta_\perp$, this peak will occur for frequencies near the cyclotron frequency. Additionally, the value of F will reflect how well the particles couple to the fields in the cavity. This time integral can be evaluated for a TE_{npl} mode in a

circularly symmetric cavity of radius r_w and length L_c. We take the axial profile of the electric field to be Gaussian with a full width at 1/e of the maximum to be L_c ($E_n \sim exp\,(-4z^2/L_c^2)$). The resulting value of $F(\omega)$ is

$$F(\omega) = \left(\frac{\pi}{2}\right)^{1/4} \frac{L_c \beta_\perp h}{2v_z} exp\,(-\delta^2/4) \qquad (10)$$

where

$$h = \frac{J_{n+1}(j'_{np} r_b / r_w)}{\left(1 - n^2/j'^2_{np}\right)^{1/2} J_n(j'_{np})}$$

is the coupling coefficient, with J_n the ordinary Bessel function, r_b the annular beam radius, and j'_{np} the zero of the derivative of the Bessel function. The frequency dependence of F enters through the dimensionless detuning parameter δ,

$$\delta = (\omega - \Omega_c/\gamma)\frac{L_c}{2v_z}, \qquad (11)$$

where Ω_c/γ is the relativistic cyclotron frequency. The quantity F is, thus, peaked in frequency at the cyclotron frequency with a width in frequency determined by the particle transit time through the cavity.

We are now at a point where we can compare the power dissipated in the cavity for the case of a beam which is premodulated at a specified frequency and an unmodulated beam consisting of a stream of uncorrelated electrons. In the first case the time dependent beam current is given by $I(t) = I_0 + \delta I\, cos\omega_0 t$. The Fourier transform for $\omega>0$ is thus, $\hat{I}(\omega) = \pi\ \delta I\ \delta(\omega - \omega_0)$. The resulting power dissipated in the cavity is given by,

$$P = \frac{\pi F^2 c^2}{2V} \frac{\omega_n/Q}{|\omega_0 - \omega_n + i\omega_n/2Q|^2} (\delta I)^2 . \qquad (12)$$

In circuit theory this formula corresponds to the power dissipated in the parallel combination of a resistor, capacitor, and inductor driven by an ideal current source δI. The equivalent shunt resistance is given by,

$$R(\omega_0) = \frac{4\pi F^2 c^2}{V \omega_n / Q}, \qquad (13)$$

and the power dissipated at the resonance is $P = (1/2)\, R(\omega_n)\, (\delta I)^2$. The values of the equivalent inductance and capacitance can then be determined by the relations $\omega_n = 1/(LC)^{1/2}$ and $Q = R\,(C/L)^{1/2}$.

The shunt resistance is frequency dependent through its dependence on F. In this sense, the simple circuit analogy doesn't quite apply. However, the concept of a shunt

resistance, which is used to characterize cavities in accelerators and klystrons [7], is useful anyway as we shall see. In the electrostatic system of units (ESU), which we have used so far, resistance has the units of inverse velocity. To convert to ohms (SI) one multiplies by $c/4\pi$ and the impedance of free space, $(\mu_0/\varepsilon_0)^{1/2} = 377$ ohms,

$$R_\Omega = 377 \frac{F^2 c^3}{V \omega_n / Q} \text{ [ohms]} . \qquad (14)$$

For a TE_{np1} mode in a cylindrical cavity we can use expressions (10) and (14) to write the resistance,

$$R_\Omega = 236\, Q \frac{L_c}{\lambda} (1 - \frac{\lambda^2}{4L_c^2}) \frac{\alpha^2 h^2}{j'^2_{np}} exp\,(-\delta^2/2) \quad \text{[ohms]}, \qquad (15)$$

where $\alpha = v_\perp / v_z$ is the beam pitch factor and λ is the wavelength based on the cavity resonance frequency. Thus, for typical parameters the shunt resistance is on the order of 100 Q ohms. For example, for a TE_{011} mode, with the beam placed on the maximum of the coupling coefficient, $\alpha = 1$, $\delta = 0$, and $L_c/\lambda = 3$ we find $R_\Omega = 97\, Q$ ohms. An electron beam with a 2A modulation injected into a cavity with a quality factor of 150 would then dissipate about 29 kW in the cavity. This number is comparable to the expected saturated power that would be extracted in the output cavity. This follows from the observation that in a good design the beam current is nearly fully modulated when it reaches the output cavity.

For the case of random electrons we need to compute the expected value of the product $I(\omega)\, I^*(\omega')$. This we do by first representing the current by a train of delta functions, $I(t) = e\sum_i \delta(t - t_i)$. This leads to the Fourier transform $\hat{I}(\omega) = e\sum_i exp\,(i\omega t_i)$. We then form the expected value of the product of two Fourier transforms,

$$\langle \hat{I}(\omega)\hat{I}^*(\omega') \rangle = e^2 \sum_{i,j} \langle exp\,[i(\omega t_i - \omega' t_j)] \rangle .$$

We now assume that the entrance times are uncorrelated, and as a result, only terms with i=j contribute to the sum. Then, assuming entrance times are uniformly distributed, we replace the sum and average with an integral over entrance time,

$$\sum_i \langle exp\,[i(\omega - \omega')t_i] \rangle = \int_{-\infty}^{\infty} \frac{dt_i}{\Delta t} exp\,[i(\omega - \omega')t_i] = \frac{2\pi}{\Delta t} \delta(\omega - \omega')$$

where $\Delta t = e/I_0$ is the mean time between electron arrivals, and I_0 is the average current (taken here to be positive). The result is the well known 'white noise' power spectrum for a beam of uncorrelated electrons

$$\left\langle \hat{I}(\omega)\hat{I}^{*}(\omega')\right\rangle = 2\pi e I_0\, \delta(\omega-\omega') \ . \qquad (16)$$

This expression, when inserted in Eqs (8) and (5), gives the following for the power dissipated in the cavity,

$$P = \frac{eI_0}{2}\int \frac{d\omega}{2\pi} R(\omega) \frac{(\omega_n/Q)^2}{|\omega-\omega_n+i\omega_n/2Q|^2} \ . \qquad (17)$$

The shape of the spectral density of the power is thus determined by both the cavity resonance and the shunt resistance. We recall from (15) that the shunt resistance is peaked in frequency at the cyclotron frequency. The width of the shunt resistance resonance is v_z/L_c while the width of the cavity resonance is ω_n/Q. Thus, the detailed shape of the spectral density of the power will vary depending on the widths and central frequencies of the two resonance functions.

The total amount of noise power (integrated over frequency) will now be estimated in two limiting cases. In the first case we assume that the cyclotron resonance is much broader than the cavity resonance. This requires $Q\, L_c\, \omega_n/v_z >> 1$. In this case, carrying out the integral in the above gives,

$$P = \frac{1}{2} R(\omega_n)\,(e\omega_n/Q)\, I_0 \, . \qquad (18)$$

From (17) it is clear that in this case the noise power is spread out over a range of frequencies corresponding to the Q width of the input cavity.

The power given by (18) can be compared with the form that applies in the case of coherent excitation by noting, $e\omega_n/Q = I_0/N$, where N is the number of electrons that pass through the cavity in a cavity decay time Q/ω_n. A typical vale of N is 10^{10}. Thus, the noise power is about ten orders of magnitude smaller than the amount of power that could be driven by a coherently modulated beam. Since the later power corresponds roughly to the saturated output power in the device and since noise is amplified as the signal proceeds through the device, a very rough rule for the signal to noise ratio measured in dB is,

$$Signal/Noise \ = \ 10\, log_{10} N \ - \ G \ [dB] \qquad (19)$$

where G is the gain of the amplifier. Equation (19) is really only approximate as the parameters of the input and output cavities might be quite different. Also, it compares the signal power which may be in a very narrow band to the noise power which will be spread out over the resonance width of the cavity. More properly the signal to noise ratio is found by comparing Eq. (18) with drive power coupled into the first cavity.

In the second case of a narrow cyclotron resonance, $Q\, L_c\, \omega_n/v_z << 1$, the noise power can be estimated using the form (15) for the shunt resistance, one obtains

$$P = \frac{1}{2}\left(\frac{\pi}{2}\right)^{1/2} R(0)\, \frac{(\omega_n / Q)^2}{|\Omega_c/\gamma - \omega_n + i\omega_n/2Q|^2}\, (eL_c / v_z)\, I_0 \,. \qquad (20)$$

In this case the detuning between the cyclotron frequency and cavity frequency is introduced into the cavity resonance function and the noise power is spread out over a range of frequencies corresponding to the inverse of the particle transit time, v_z/L_c . Further, one can introduce a dimensionless number of electrons N based on the transit time $eL_c/v_z = I_0/N$. Generally, the smaller of (18) and (20) is applicable.

An alternate way of characterizing the noise is in terms of the noise temperature. According to the definition, the noise temperature is the power per unit frequency [in Hz] dissipated in the cavity. From (17) this is seen to be

$$T(\omega) = \frac{1}{2} R(\omega)\, eI_0\, \frac{(\omega_n / Q)^2}{|\omega_0 - \omega_n + i\omega_n/2Q|^2} \,. \qquad (21)$$

At resonance the temperature $T(\omega_n)$ is given by,

$$T(\omega_n) = 2R(\omega_n)\, eI_0 = 4\,(e/I_0) \times \frac{1}{2} R(\omega_n)\, I_0^2 \,. \qquad (22)$$

According to our previous discussions, the last factor on the right hand side, $1/2\ R\ I_o^2$ (with R replaced by the resistance of the output cavity), is essentially the maximum output power the beam could deliver. This is a good fraction of the beam power $V_0 I_0$. The temperature, therefore, corresponds roughly to the energy of the electron beam. This may seem surprising at first since our beam is cold, but a spiraling electron beam is far from thermodynamic equilibrium and has an available free energy which for $\alpha \sim 1$ scales as the beam energy. This interpretation is enforced by noting that the resistance R is proportional to α^2, and thus vanishes if the free energy of the beam is removed.

For pulsed Doppler radar applications the phase of the returning signal is detected. Over a period of many pulses this phase will change reflecting the motion of the target relative to the source and detector. To estimate the pulse to pulse fluctuations due to shot noise in the detected phase we assume the phase is determined after integrating the beating the signal with the carrier and integrating over the pulse duration τ_p

$$A_s = A_0 + \int_{-\tau_p/2}^{+\tau_p/2} \frac{dt}{\tau_p} \int_0^{\infty} \frac{d\omega}{2\pi} A(\omega)\, e^{i(\omega_0 - \omega)t} \,.$$

Here, A_s is the complex amplitude of the total signal, A_0 is the complex amplitude of the coherent signal and $A(\omega)$ is the Fourier transform of the noise. The phase error is then given by $\delta\Phi = arg\{A_s A_0 *\}$. For low levels of noise this gives,

$$\delta\Phi = Im \{ \int_0^\infty \frac{d\omega}{2\pi} \frac{A(\omega) A_0^*}{|A_0|^2} sn(\omega - \omega_0) \} ,$$

where

$$sn(\omega - \omega_0) = \frac{sin [(\omega - \omega_0) \tau_p / 2]}{[(\omega - \omega_0) \tau_p / 2]}$$

represents a filter function describing the integrating process.

Each pulse will have a phase error. The mean phase error will be zero, and the variance will be given by,

$$\langle \delta\Phi^2 \rangle = \int_0^\infty \frac{d\omega\, d\omega'}{(2\pi)^2} \left\langle \frac{A(\omega) A^*(\omega') + c.c.}{4 |A_0|^2} \right\rangle sn(\omega - \omega_0) sn(\omega' - \omega_0) .$$

Using the expression (5) for the energy density in the cavity, along with the definition of the noise temperature, and the expression the coherent power coupled into the cavity $P_0 = \omega_n V|A_0|^2/(2\pi Q_\Omega)$ where Q_Ω is the ohmic Q value (not including the coupling hole) it is possible to express the variance of the phase error,

$$\langle \delta\Phi^2 \rangle = \frac{Q}{2Q_\Omega} \int_0^\infty \frac{d\omega}{2\pi} sn^2(\omega - \omega_0) \frac{T(\omega)}{P_0} .$$

Basically, the variance of the phase errors is proportional to the noise power in a band of frequencies of width τ_p^{-1} and centered at the drive frequency.

III Collective Effects

Expression (17) for the power spectrum of the beam current was derived assuming that the electrons entering the cavity are uncorrelated with one another. This is an assumption which most likely is not valid. Experience with sources of microwaves driven by linear beams has shown that the electrons can become highly correlated and this reduces substantially the noise in the beam. An excellent review of the early studies of shot noise in devices with linear beams can be found in Refs. 2 and 8. We will review here some important results, but presented from an alternate point of view. Within the framework of plasma kinetic theory the correlations occur because of the dielectric shielding of the

discrete electron charges by the beam itself. We can consider this effect by analogy to the case of electrostatic plasma waves treated in text books [9]. By working in either the spatial or Fourier domain one can show that the shot noise is generated by shielded rather than bare electrons. The end result is that the power spectrum of the noise is modified by a term representing the dielectric shielding. For example, we modify expression (21) by noting that the shunt resistance depends on the velocity space coordinates of the electron beam. Thus, if the beam has a distribution of velocities we expect that the shunt resistance $R(\omega)$ should be redefined as follows,

$$R(\omega) \rightarrow \int d^3v \, \frac{v_z}{v_0} f(v) \frac{R(\omega,v)}{|1+\chi(\omega,k_d)|^2} \tag{23}$$

where $f(v)$ is the velocity space distribution function for the beam, v_0 is the average axial velocity of the beam, $\chi(\omega,k)$ is the beam susceptibility (we assume a one dimensional model of the self fields), and $k_d(v) = \omega/v_z$, is the Doppler wave number for electrons of velocity v interacting with fields of frequency ω. The factor v_z/v_0 accounts for the fact the product I_0R is what enters expression (17). Thus, if we were to consider the beam to be composed of many beamlets the distribution function should be weighted by the axial velocity.

The shielding effect occurs when the beam susceptibility χ is large. Generally, this requires a combination of sufficiently high beam density and sufficiently low beam temperature. To illustrate this we consider for the moment the case of a linear beam. We ignore the velocity dependence of the shunt resistance and calculate a reduction factor $H(\omega)$,

$$H(\omega) = \int d^3v \, \frac{v_z}{v_0} \frac{f(v)}{|1+\chi(\omega,k_d)|^2} \tag{24}$$

where we have used $k_d = \omega/v_z$ for the Doppler wave number. Let us further take the beam distribution function to be Maxwellian with mean velocity v_0 and temperature $T_b = (1/2) mv_t^2$,

$$f(v_z) = \left(\frac{m}{2\pi T_b}\right)^{1/2} exp\left[-\frac{m(v_z-v_0)^2}{2T_b}\right] \tag{25}$$

For this distribution the beam susceptibility can be expressed in terms of the plasma dispersion function $Z(\zeta)$,

$$\chi(\omega,k) = \frac{2\omega_p^2}{k^2v_t^2}\left[1 + \frac{\omega - kv_0}{|k|v_t} Z\left(\frac{\omega - kv_0}{|k|v_t}\right)\right] \tag{26}$$

We emphasize again that we are using a one dimensional model of the self fields. Thus, the quantity ω_p represents the reduced plasma frequency which accounts for the transverse structure of the space charge fields.

The integral in Eq. (24) can be evaluated approximately in the limit of low beam temperature. That is, $k^2 v_t^2 = \omega^2 v_t^2 / v_0^2 << 2\omega_p^2$. There are two types of contribution to the integral. First, for velocities v_z which are in the thermal distribution, $|v_z - v_0| \approx v_t$, the susceptibility is large, $\chi >> 1$, and the contribution to the reduction factor scales as

$$H \approx \left(\frac{\omega^2 v_t^2}{2\omega_p^2 v_0^2} \right)^2 \approx \frac{\omega^4}{\omega_p^4} \frac{T_b^2}{E_b^2} \quad , \tag{27}$$

Where $E_b = (1/2) m v_0^2$ is the beam energy. For a cold dense beam, this is a large reduction. A second contribution comes from velocities for which $1 + \chi \cong 0$; in other words, from velocities which resonantly interact with beam space charge waves. For a relatively cold beam these velocities are in the tail of the distribution function so the numerator in the integral is very small. However, the imaginary part of the susceptibility is also very small and the contribution to the integral is nonnegligible. This contribution can be found by expanding the denominator around the two velocities corresponding to excitation of the slow and fast space charge waves. The result for the contribution to the reduction factor is,

$$H(\omega) = \frac{n \omega T_b}{2 \omega_p E_b} , \tag{28}$$

where n = 1 or 2 depending on whether there are one or two forward propagating space charge modes where the denominator in Eq. (24) becomes very small. This contribution dominates that of the thermal particles if $T_b/E_b < (\omega_p/\omega)^3$. In this limit the noise temperature at resonance (22) is given by

$$T(\omega_n) = n \frac{R(\omega_n)}{Z_0} T_b , \tag{29}$$

where $Z_0 = 2(\omega_p/\omega) E_b/(eI_o)$ is a characteristic impedance. In fact, one can show that Z_0 is the characteristic impedance of the space charge modes [8]. That is, a beam that supports a small space charge wave will have fluctuations in both voltage and current. The ratio of the voltage fluctuation to the current fluctuation is Z_0. In the case in which the cavity and space charge waves have comparable impedances the noise temperature is equal to the beam temperature. Further, the dominant current fluctuations are in the form of weakly damped space charge modes as opposed to ballistic perturbations associated directly with the motion

of individual particles. In linear beam devices these fluctuations are imposed near the cathode where the beam is dense and the mean speed is comparable to the thermal speed. That is the, the damping Landau damping of plasma waves is sufficiently weak once the beam has been accelerated that the waves and beam are not strongly coupled. That is the temperature T_b is determined by the cathode temperature and the linear propagation of plasma waves on the accelerating beam as they travel from the cathode to the interaction region.

In the preceding discussion we evaluated the susceptibility for a one dimensional, linear beam. The dominant collective effect in this case is the excitation of beam space charge modes: i.e. plasma waves. The beam in a magnetron injection gun (MIG) is spiraling about the magnetic field lines and a more appropriate susceptibility takes into account the possibility of cyclotron resonance. For example, the susceptibility of a warm beam, responding to transverse electrostatic fields with frequencies near the cyclotron resonance can be found in ref. [10],

$$\chi(\omega,k) = \frac{\beta_{\perp 0}^2 \gamma_0^3 \omega_p^2}{4\gamma_{z0}^2 \Omega_c^2} \left(\omega^2 - k^2 c^2\right) \int \frac{d\gamma du_z f(\gamma,u_z)}{\left(\gamma\omega - ku_z - \Omega_c\right)^2} \tag{30}$$

where γ_0 = is the mean relativistic factor, $\gamma_{z0} = (1-(v_0/c)^2)^{-1/2}$ where v_0 is the mean axial velocity of the beam and $\beta_{\perp 0}$ is the mean transverse relativistic factor for the beams perpendicular velocity. This expression assumes k is the axial wave number, and that the perturbations also have a perpendicular wave number which is much greater than k. However, in this approximation, the value of the perpendicular wavenumber does not appear in the expression for the susceptibility (See ref. 10 for details). The function $f(\gamma,u_z)$ describes the beam's distribution of energy and axial momentum. In principle, one should include the variations of perpendicular momentum under the integral. However, when the spread in the various momenta is small, as assumed here, only the variation of quantities which appear in the resonant denominator needs to be taken into account. Let us now assume that the beam is monoenergetic but with a distribution that depends on axial momentum. For ease of integration we take the distribution of axial momenta to be Loretzian with mean velocity v_0 and thermal velocity v_t

$$f(\gamma,u_z) = \frac{v_t \, \delta(\gamma - \gamma_0)}{\pi\gamma_0 \left[\left(u_z/\gamma_0 - v_0\right)^2 + v_t^2\right]} \tag{31}$$

In this case the susceptibility can be evaluated in terms of simple functions,

$$\chi(\omega,k) = \frac{\beta_{\perp 0}^2 \gamma_0 \omega_p^2}{4\gamma_{z0}^2 \Omega_c^2} \frac{(\omega^2 - k^2c^2)}{(\omega - \Omega_c/\gamma_0 - kv_0 + ikv_t)^2} \tag{32}$$

The sign of the term $\omega^2 - k^2c^2$ in the numerator of the expression for χ is of significance. The factor ω^2 can be attributed to gyrophase bunching of the beam while the term k^2c^2 is attributable to axial bunching. If $\omega^2 > k^2c^2$ gyrophase bunching dominates and electrostatic cyclotron modes can be unstable. The axial wavenumber of the cyclotron mode with frequency ω is determined by setting $1 + \chi = 0$. It can be written as the Doppler wavenumber based on the mean velocity of the beam plus a correction,

$$k = \frac{\omega - \Omega_c/\gamma_0}{v_0} + \delta k \tag{33}$$

In the limit of a tenuous beam, $\beta_{\perp 0}^2 \gamma_0 \omega_p^2 << 4\gamma_{z0}^2 \Omega_c^2$,the small wave number shift δk is given by,

$$\delta k = \pm ik_I + ik_t \tag{34}$$

where

$$k_I^2 = \frac{\gamma_0 \omega_p^2 \alpha^2}{4\gamma_{z0}^2 \Omega_c^2} \left[\frac{\omega^2}{c^2} - \frac{(\omega - \Omega_c/\gamma_0)^2}{v_0^2} \right] \tag{35a}$$

and

$$k_t = \frac{|\omega - \Omega_c/\gamma_0| \nu_t}{v_0^2} \tag{35b}$$

The quantity k_I represents the spatial growth rate of the instability for a cold beam, while k_t represents a damping rate due to axial velocity spread. We note that the spatial growth rate is maximum at cyclotron resonance where k_I reaches its maximum value and k_t vanishes. The maximum growth rate occurs at cyclotron resonance because the Doppler wave number vanishes. Consequently, axial bunching is negligible and the resonant denominator in (30) is insensitive to the spread in axial velocities.

In a MIG the magnetic field typically varies by a factor of 10 to 30 in the drift region between the cathode and the cavity. This has a large effect on the amount of spatial amplification a fluctuation with fixed frequency will experience. Fluctuations with frequencies close to the cyclotron frequency in the input cavity, where the magnetic field is near its maximum, will be damped in the drift region up to a point where the magnetic field is close to its value in the cavity. At this point the fluctuations become unstable and grow exponentially. Thus the amount of noise will be largely affected by the amount of growth that occurs in these last few centimeters [10]. The growth length of the instability is also

on the order of a few centimeters. Therefore, large enhancements in the noise level are possible. For example, fig. 1 [11] shows the expected amount of noise power amplification due to the electrostatic cyclotron instability for the beam parameters of the NRL gyroklystron [1]. Plotted is the number of decibels of growth versus frequency for a several different beam currents. For these calculations the beam was assumed to have a 'top hat' dependence on axial velocity as opposed to Lorenzian. The resulting expression for the wavenumber is given by Eq. (27) of Ref. (10). As can be seen, for the highest currents nearly 50 dB of amplification is expected.

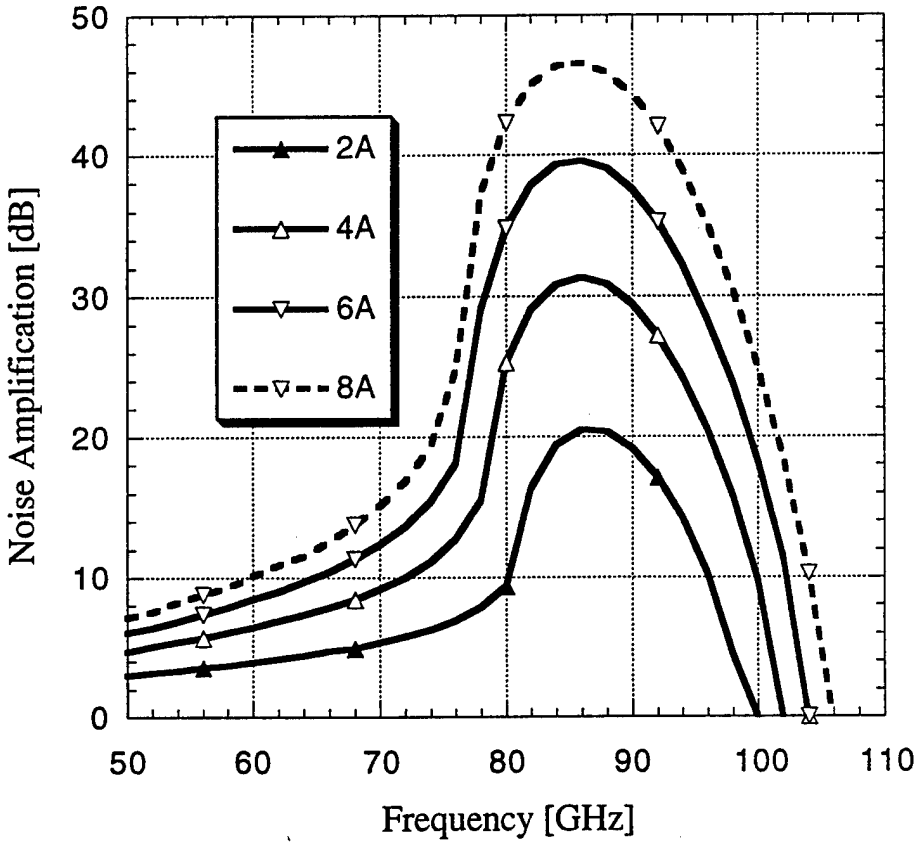

Fig. 1 Noise amplification [11] versus frequency for the parameters of the NRL 94 GHz gyroklystron.

Formula (23) for the effect of dielectric shielding assumes that the plasma is stable, and can not be applied for cases in which the instability is present. A more refined theory

is required to describe the growth of current fluctuations on the beam as it passes from a region where the beam is stable to one where the beam is unstable. Presumably fluctuations start at a level given by (23) and then grow exponentially after the beam becomes unstable. At the point where the beam becomes unstable the susceptibility is of order unity, since $1 + \chi = 0$. Thus the noise may grow from a level for which the dielectric shielding is unimportant. This was the situation assumed in ref. [10]. However, a more precise prediction awaits the development of a theory which treats the evolution of noise fluctuations on an inhomogeneous beam.

An additional collective effect which is easily incorporated in the present theory is the coherent response of the electron beam to the fields in the cavity. In particular, we have calculated the fields in the cavity assuming the current perturbation is prescribed. These fields will produce a coherent response in the beam which is nonnegligible if the beam is close to the value required to start oscillations in the cavity. The result is that all the resonant denominators appearing in Eqs (4), (8), (12), (17), (20), and (21) need to be modified to include the complex frequency shift induced by the beam. That is the following replacement should be made [5],

$$\omega - \omega_n + i\omega_n/2Q \;\rightarrow\; \omega_0 - \omega_n + i\omega_n/2Q - \Delta\omega\,, \tag{36}$$

where after a small calculation the frequency shift is written

$$\Delta\omega = -\frac{2\pi i Ie}{mV}\int d^3v\, f \frac{\partial}{\beta_\perp \partial\beta_\perp}\left(\int_{-\infty}^{\tau} d\tau F_\tau \frac{d}{d\tau}F_\tau^*\right). \tag{37}$$

The integral over d^3vf in (37) is an average over initial particle momenta, while the integral over τ is carried out along the unperturbed particle orbit. The quantity F_τ is defined

$$F_\tau(\omega,\beta_\perp) = \int_{-\infty}^{\tau} d\tau'\; E_n^*[x_0(\tau')]\cdot\beta(\tau')\; e^{i\omega\tau'}\,. \tag{38}$$

Thus, according to Eq.(9) $F_\infty = F(\omega)$. Using Eq. (38) the imaginary part of the frequency shift can be expressed in terms of the shunt resistance.

$$Im\,\{\Delta\omega\} = -\frac{\omega_n}{2Q}\frac{Ie}{mc^2}\int d^3v\, f \frac{\partial R(\omega,\beta_\perp)}{2\beta_\perp\partial\beta_\perp}\,. \tag{39}$$

Expression (39) reiterates the known relation between the linear gain and the spontaneous emission rate. In the case of free electron lasers this is known as Madey's theorem. It has been derived previously for gyrotrons by Latham [12].

Conclusions

The excitation of noise in the input of a gyroklystron cavity can be expressed in terms of the excitation of a resonant circuit, with an equivalent frequency dependent shunt resistance, by the random fluctuations of the beam current. A typical value of the shunt resistance is 100 Q ohms where Q is the quality factor of the cavity. For the case of spontaneous emission, which neglects correlations in the entrance times of particles, the noise spectrum has two peaks, one at the cyclotron resonance and one at the cavity resonance. The noise temperature in the case of spontaneous emission scales as the beam energy. Collective effects tend to reduce the noise level in linear beams to a value dependent on the beam temperature. However, in the case of a spiraling beam such as that produced by a MIG the noise can be enhanced by many dB due to the presence of unstable electrostatic cyclotron modes on the beam.

Acknowledgment:

This work was supported by the Office of Naval Research.

References:

1. NRL gyroklystron

2. *Noise in Electron Devices*, L. D. Smullin and H. A. Haus editors, The Technology Press of the Massachusetts Institute of Technology, and John Wiley and Sons, 1959.

3. G. S. Nusinovich and O Dumbrajs, "Technichal Noise in Gyroklystrons and Phase-locked Gyrotron Oscillators", Phys Plasmas **4**, 1424-1433 (1997).

4. Robert E. Collin, *Foundation for Microwave Engineering*, second edition, Chapter 7, McGraw Hill, 1992

5. M. Garven, W. Manheimer, and M. Blank, *Simple Theory of the Input Couplers for Gyroklystron* Amplifiers, Submitted to IEEE Transactions on Plasma Science 1997.

6. J.D. Jackson, *Classical Electromagnetic Theory*, second edition, Chapters 8 and 9, J. Wiley and sons, New York, 1975

7. G. A. Loew and R. Talman, "Lectures on the Elementary Principles of Linear Accelerators", in *Physics of High Energy Particle Accelerators*, AIP Conference Proceedings No. 105, M. Month Editor, American Institute of Physics, New York 1983, p.15.

8. J. R. Whinnery, "History and Problems of Microwave Tube Noise", Scienta Electra, **5**, 133-150 (1959).

9. N. A. Krall and A. W. Trivelpiece, *Principles of Plasma Physics*, San Francisco Press Inc. San Francisco CA, 1986, pp. 556-567.

10. H. Li and T. M. Antonsen Jr., "Space Charge Instabilities in Gyrotron Beams", Phys. Plasmas, **1**, 714-729 (1994).

11. Simon Cooke, private communication.

12. Peter Latham, private communication.

APPENDIX XX

Amplifier Performance of the NRL Ubitron

D.E. Pershing, R.D. Seeley, R.H. Jackson, and H.P. Freund

Nucl. Instrum. Meth. **A358**, 104 (1995).

Nuclear Instruments and Methods in Physics Research A 358 (1995) 104–107

NUCLEAR INSTRUMENTS & METHODS IN PHYSICS RESEARCH Section A

ELSEVIER

Amplifier performance of the NRL ubitron ☆

D.E. Pershing *,[1], R.D. Seeley [1], R.H. Jackson, H.P. Freund [2]

Naval Research Laboratory, Washington, DC 20375, USA

Abstract

Operation of the Naval Research Laboratory K_u-band ubitron has successfully demonstrated a high power/efficiency and broad bandwidth. This device employs a helical wiggler/axial guide field configuration. Performance levels achieved at 16.6 GHz can be summarized as a peak power of 4.2 MW for an efficiency of 17.5% and a gain of 29 dB, and an instantaneous bandwidth of 22%. Substantial beam loss was observed. The specific loss rate was correlated with output power, and reached a level of 50% beam loss at the 4.2 MW level. Nonlinear simulations of the experiment are in good agreement with these observations.

1. Introduction

The NRL ubitron [1] has demonstrated operation as a high power, broad band, and efficient amplifier with a maximum output power of 4.2 MW for an efficiency of 18%, a 29 dB gain, and a large signal bandwidth (not saturated) greater than 22%. The experiment met the performance goals for the fundamental mode amplifier; specifically, an output power of 1–5 MW, an efficiency greater than 15%, a large-signal gain of 25–30 dB, and a large-signal bandwidth greater than 20%. Experimental results are in good agreement with theoretical predictions using the 3-D nonlinear code ARACHNE [2–4]. It is important to note in this regard that, in contrast to earlier devices operating in the Raman regime [3], the DC self-fields of the beam played an important role in the interaction.

2. Experimental results

An extensive description of the experiment is given in Ref. [1]. The wiggler is a pulsed bifilar helix with a period of 2.54 cm and a length of 33 wiggler periods. The first five and the last three periods represent an adiabatic entrance and exit. Amplification was measured over the following parameter ranges: wiggler amplitude $\approx$ 175–320 G, axial field $\approx$ 1.75–2.54 kG, beam voltage $\approx$ 212–254 kV, and beam current $\approx$ 67–100 A. The beam radius upon wiggler entry is $\approx$ 0.4 cm and the waveguide radius is 0.815 cm. The FWHM of the beam pulse is $\approx$ 2.4 μs, with a flat top of $\approx$ 1 μs. Operation is largely in the TE_{11} mode at K_u band (12.4–18 GHz). The experimental configuration is shown in Fig. 1. Note that the solenoid is split to accommodate a gate valve separating the gun and the interaction/diagnostics sections which necessitated additional solenoid coils to maintain the field profile.

Amplification has been measured over a wide parameter range. Although the nominal beam and axial field values are 250 kV/100 A and 2.2 kG, these do not necessarily represent the optimal parameter range, and equivalent output power has been obtained for several different parameter sets. The maximum power measured is 4.2–4.5 MW at 16.6 GHz. Typical waveforms showing the essential characteristics of ubitron operation are given in Fig. 2. In this case, an output power of $\approx$ 4.5 MW (4.2 MW from calorimeter) was measured for a 245 kV/94 A beam, with axial guide field and wiggler field amplitudes of 2.47 kG and 270 G, respectively. This represents a gain of 29 dB and an efficiency of 18%.

It is important to observe the beam loss on the rising and falling edges of the pulse at the voltage resulting in gyroresonance for the fixed magnetic fields, as well as the high beam loss during the interaction. The ripples on the two beam current traces are due to current monitor ringing. It should also be noted that the output power shown does not represent saturation. Indeed, for most parameters we have been unable to drive the system to saturation.

The ubitron has also demonstrated a wide instantaneous bandwidth. However, there are two factors which render this measurement difficult. Specifically 1) the modulator

☆ This work is supported by the Office of Naval Research.

* Corresponding author. Tel. +1 703 339 6500, fax +1 703 339 6953.

[1] Permanent address: Mission Research Corp., Newington, VA 22122, USA.

[2] Permanent address: Science Applications International Corp., McLean, VA 22102, USA.

SSDI 0168-9002(94)01581-3

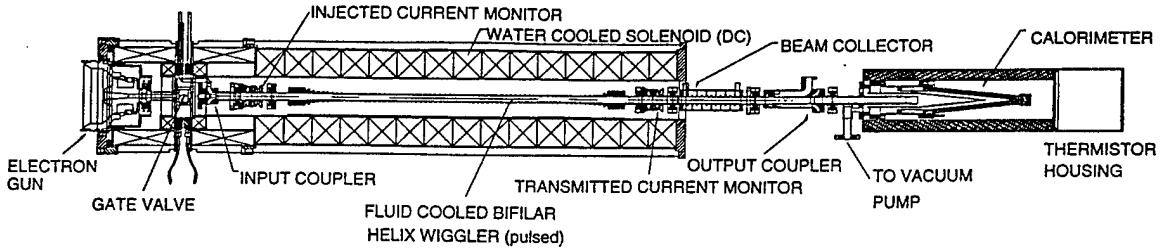

Fig. 1. Experimental configuration.

exhibits a slow time scale voltage drift, and 2) in order to accommodate high input power, the phase splitting circuitry utilizes two sets of short slot hybrids to cover most of the K_u band and several hours are required to switch between them. Hence, the bandwidth measurements are not always made with the identical parameters, but are indicative of ubitron bandwidth potential. Fig. 3 shows the bandwidth characteristics for a case in which the output power exceeds 600 kW. This represents a bandwidth in excess of 22%.

The NRL ubitron exhibits is highly sensitive to variations in the beam voltage and the axial and wiggler magnetic fields. An example of the output power sensitivity to beam voltage is shown in Fig. 4. Output power is seen to reach a maximum in excess of 4 MW at of 245 kV, and to increase from 2–4 MW as the voltage increases about 4.5% from 234–245 kV. This sensitivity points to the need for very tight modulator voltage control. Similar sensitivity to variations in the axial and wiggler magnetic fields has also been observed. In order to illustrate the sensitivity of the interaction to variations in the axial magnetic field, we consider a 250 kV/83 A beam with a wiggler field amplitude of 275 G. Experimentally, the output power varies from 2–4.4 MW at 16.6 GHz as the axial magnetic field increases from 2.4–2.54 kG. Observe that the output power nearly doubles for an axial field increase of 5.5%. Somewhat less sensitivity is measured for wiggler field variations. With a 247 kV/83 A beam and an axial magnetic field of 7.6 kG, the output power increases from 0.4 to 2.6 MW at 16.6 GHz as the wiggler field increases from 160–280 G (i.e., a field increase of $\approx 25\%$ is required to double the output power). Part of this parametric sensitivity arises because the system is not driven to saturation; hence, small changes in the growth rate can result in relatively large variations in the output power.

3. Comparison with theory

A key feature of the NRL ubitron program is the integration of theoretical and experimental efforts which leads to the development and validation of a design and simulation capability. To demonstrate this capability, we compare experimental measurements with theory. We use the 3-D nonlinear simulation code ARACHNE, which in its latest version [3,4] includes both RF and DC beam space charge effects, under the assumption of an initial axial energy spread of 1.5%. It is also important to, the inclusion of the DC space-charge fields is important for the current experiment.

In general, experimental performance follows theoretical predictions as far as trends with wiggler field, axial field, beam voltage, and beam transmission are concerned. However, we usually measure a somewhat higher power than predicted. Typically, we find that a 5% increase in both the wiggler and axial fields in ARACHNE, over the experimental calibration, results in good agreement with

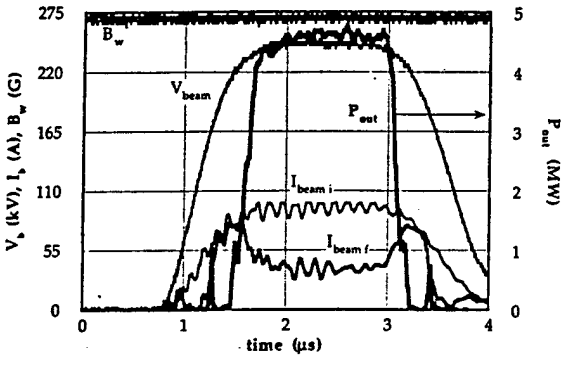

Fig. 2. Typical waveforms.

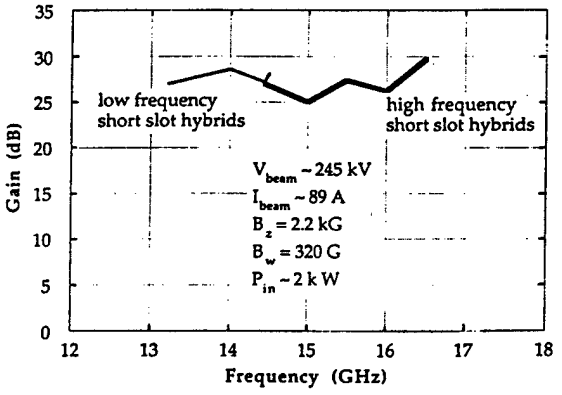

Fig. 3. Ubitron bandwidth characteristics.

the experiment. This is slightly outside our estimated 2–3% experimental uncertainty. Although this is not a large discrepancy, it is an issue that is still under investigation, and there are several possible contributory factors. On the theoretical side, possible reasons for the discrepancy include unavoidable differences between the experimental implementation and theoretical model, such as mechanical and field misalignments or actual injected beam conditions. Although these factors normally have a deleterious affect on output power, they cannot be ruled out. Experimentally, the presence of internal reflections could increase the effective input power, and thereby increase the output power over that expected for a single pass amplifier. In addition, although the solenoid and wiggler fields were carefully measured with calibrated diagnostics and compared with simulations prior to assembly, a final confirmation of the field calibrations must await the ultimate dismantling of the apparatus.

The first comparison between theory and experiment deals with the dependence of output power on input power. Power measurements are typically higher than predicted by ARACHNE for single-pass amplification with no reflections and for the nominal experimental parameters. To explain the discrepancy, we first assume the presence of a small amount of internal reflections. Note that the beam flat top is about 1 μs wide and more than 100 round trips of the radiation are possible. Hence, even a small degree of reflection can substantially alter the output power. In order to describe the effect of internal reflections using ARACHNE we adopt the following procedure. A single-pass drive curve is first computed to obtain a gain function $P_{out} = G(P_{in})$. Using this gain function, we define a repetitive map for the output power over each roundtrip of the radiation through the cavity, i.e. $P_{n+1} = G(P_{inj} + \varepsilon P_n)$, where P_{inj} is the injected power and ε is the roundtrip reflection coefficient. As expected, the output power over the total pulse time increases with the reflection coefficient, and good agreement can be found with the experiment for an effective reflection coefficient of 0.65%. This is illustrated in Fig. 5 showing drive curves obtained from the experiment and from the above-mentioned procedure for a 244 kV/82 A beam and for wiggler and guide magnetic fields of 231 G and 2.47 kG at 16.6 GHz. However, based on cold tests and measurements of reflected power during operation, we expect round trip reflections of the order of 0.1–0.3%.

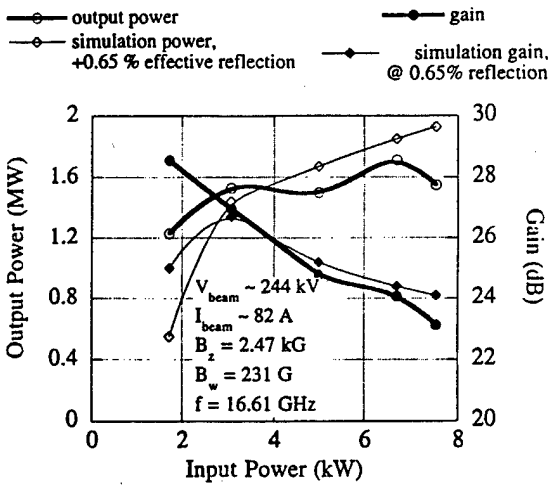

Fig. 5. Drive curve showing the output power and gain as a function of the input power.

It is also possible that the actual injected power is underestimated. However, the uncertainty in the injected power is thought to be $< 20\%$ and this is not sufficient to explain the discrepancy over a single-pass; internal reflections affect output power much more strongly. Therefore, we expect that other factors must be involved.

A second possible explanation for the discrepancy between the theory and experiment is in the diagnostic calibration accuracy of 2–3%. The strong dependence of the output power on beam voltage for several values of the

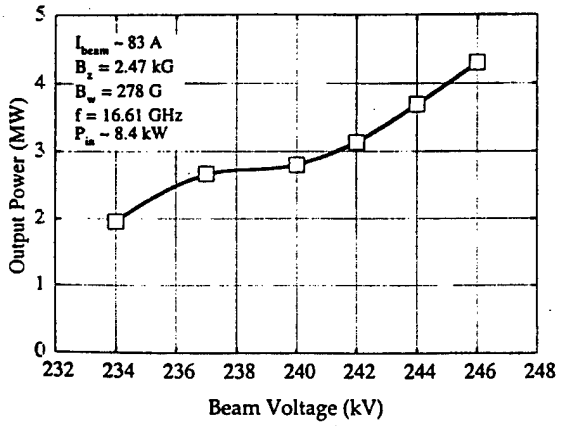

Fig. 4. Variation in the output power with beam voltage.

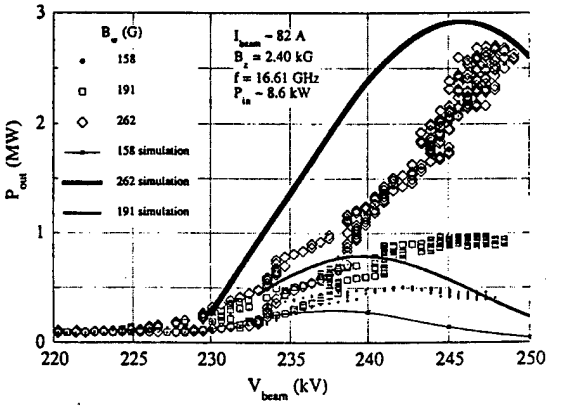

Fig. 6. Variation in the output power with beam voltage for several values of wiggler amplitude.

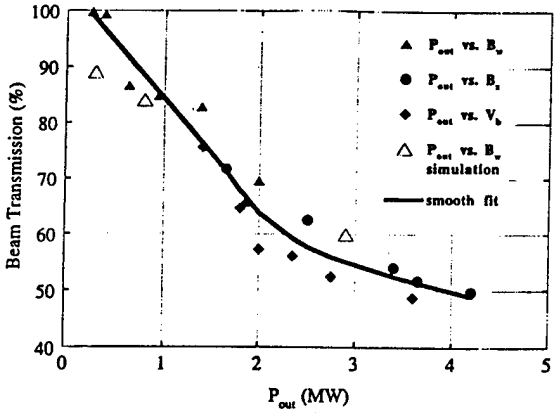

Fig. 7. Variation in beam loss with output power.

wiggler field is shown in Fig. 6. The data for this figure are presented as output power vs. beam voltage. The simulation results from ARACHNE are shown with the solid curves, with the curve thickness matching the corresponding point thickness of the experimental measurement. Reasonable agreement is shown in the voltage where the peak power occurs and in the overall voltage dependence, although the output power peaks as predicted by ARACHNE are at voltages 2–3% less than observed. However, both the wiggler and axial magnetic field values used in ARACHNE were 5% higher than the nominal experimental values.

In view of these comparisons, we expect that the bulk of the discrepancy between theory and experiment is accounted for by the assumptions of 1) a small degree of internal reflections, and 2) small changes from the nominal values of the magnetic fields and beam voltage.

One final issue important for a production device is beam loss. Both simulation and experiment show high beam loss in the interaction region at multimegawatt power levels. This is demonstrated in Fig. 7 in which we plot the variation in beam loss with output power for a variety of different beam, wiggler and axial field parameters. The solid triangles in the figure represent data collected from experimental runs in which the variation in output power versus wiggler amplitude was studied. Similarly, the solid circles (diamonds) represent data collected from studies of the variation in the output power versus the axial guide field (beam voltage). The hollow triangles represent ARACHNE simulations of output power dependencies on wiggler and axial guide fields. The solid line is simply a smooth fit to all of these points. It is evident that the fraction of transmitted beam falls fairly uniformly with output power and reaches about 50% transmission at a 4 MW power level. Observe that all the points from both the experiment and the simulation cluster fairly closely about the fitted curve, and represent good agreement between the theory and the experiment. Two factors contribute to the high beam loss: operation near gyroresonance, and large beam orbits at high output power. Note that gyroresonant beam loss begins at a voltage reduction of $\sim 20\%$, which is comparable to the measured 18% efficiency.

Although this degree of beam loss is clearly undesirable for high duty factor operation, it does not necessarily result in tube damage. The NRL ubitron was disassembled after many hours of operation at 6 pps and examined for damage. For this experiment it was found that the beam loss is sufficiently distributed axially to result in little or no tube damage. This effect could probably be reduced by simply reducing the initial beam diameter, or operation further from gyroresonance.

4. Summary

In conclusion, results from the NRL ubitron experiment demonstrate that the performance potential of the ubitron/FEL has been realized. A configuration using a fundamental mode circularly polarized rf wave and a helical wiggler results in a relatively compact, high power, and efficient amplifier with wide instantaneous bandwidth and without the necessity of wiggler field tapering. Performance levels compare quite favorably with those from other pulsed, high power microwave amplifier designs.

In general, there is good agreement between theory and experiment. Both theory and experiment show a high degree of output power sensitivity to beam voltage and axial magnetic field. Some differences exist, with the experimental power levels typically higher than predicted. We are examining the questions of internal reflections, magnetic field calibrations, and beam modeling as sources of the discrepancy. Further attention to the beam loss issue is required for higher duty factor operation. Future work will include more extensive measurements of noise and phase characteristics, as well as utilization of our theory/design capability for designs at higher frequency and lower voltage regimes.

References

[1] D.E. Pershing, R.H. Jackson, H. Bluem and H.P. Freund, Nucl. Instr. and Meth. A 304 (1991) 127.
[2] A.K. Ganguly and H.P. Freund, Phys. Fluids 31 (1988) 387.
[3] H.P. Freund, R.H. Jackson and D.E. Pershing, Phys. Fluids B 5 (1993) 2318.
[4] H.P. Freund and T.M. Antonsen, Jr., Principles of Free-electron Lasers (Chapman & Hall, London, 1992) Chap. 5.

APPENDIX XXI

Design and Performance Calculations for a Ka-Band CHI Wiggler Ubitron Amplifier

J.M. Taccetti, R.H. Jackson, H.P. Freund, D.E. Pershing,
M. Blank and V.L. Granatstein
Nucl. Instrum. Meth. **A358**, 193 (1995).

Nuclear Instruments and Methods in Physics Research A 358 (1995) 193–196

NUCLEAR INSTRUMENTS & METHODS IN PHYSICS RESEARCH Section A

ELSEVIER

Design and performance calculations for a K_a-band CHI wiggler ubitron amplifier

J.M. Taccetti [1], R.H. Jackson, H.P. Freund [2,*], D.E. Pershing [3], M. Blank, V.L. Granatstein [1]

Naval Research Laboratory, Washington, DC 20375, USA

Abstract

Design and performance calculations for a coaxial hybrid iron (CHI) wiggler free-electron laser configuration are presented. The capability of generating high fields at short periods, as well as good beam focusing properties, make it a desirable configuration for high power coherent radiation sources in relatively compact systems. In addition to a description of the geometry, numerical calculations detailing the magnetostatic wiggler fields, the beam dynamics, and the interaction of the beam with the electromagnetic waves in the K_a-band (26–40 GHz) will be presented. Key considerations for the experimental design will be outlined and discussed.

1. Introduction

Fast-wave interaction devices, i.e. gyrotrons and FEL/ubitrons, have many attractive properties for the generation of high power, high frequency microwaves. However, practical devices have been elusive because of magnetic field, voltage, and size requirements. For FELs/ubitrons the disadvantage can be partially overcome by the utilization of short period ($\lambda_w < 5$ mm) magnetic wigglers. Several micro-wiggler configurations have been investigated, each having its own advantages and disadvantages in the areas of achievable field strength and uniformity, ease and cost of fabrication, control, tuning, and beam acceptance and focusing.

The coaxial hybrid iron (CHI) wiggler is a short-period compatible configuration which offers several advantages relative to the above issues. The CHI wiggler is a coaxial configuration constructed by insertion of ferromagnetic and non-ferromagnetic elements into a solenoidal field [1,2]. Other wiggler configurations derived from a solenoidal field have also been discussed in the literature [3–6]. This paper will present design and performance calculations for a CHI wiggler based K_a-band FEL amplifier under development at the Naval Research Laboratory. The goal is an output power of 100 kW at 35 GHz while reducing the voltage to approximately 150 kV. A companion paper appearing in this issue discusses the application of the CHI wiggler to a high power FEL designed for the cyclotron resonant heating of fusion plasmas [7].

2. CHI wiggler configuration

The CHI wiggler consists of alternating rings of ferro- and nonferromagnetic materials, surrounding a central rod consisting of cylinders of the same materials as the rings but shifted axially by half a period. As shown in Fig. 1, a wiggler period consists of only two ferromagnetic pieces (an inner cylinder and an outer ring) along with their respective non-ferromagnetic spacers. The width of the two ferromagnetic pieces need not be the same, as long as the combined length is the same for both inner and outer sections. This entire structure is placed inside a solenoid (the axes of the solenoid and the wiggler are coincident) and causes a deformation of the solenoidal field into a combination of periodic radial and axial components. Having the magnetic field source external to the wiggler offers advantages for coil cooling and field tapering. Large wiggler fields are possible while maintaining a relatively simple and low-cost design.

The electron beam is annular and travels down the gap

* Corresponding author. Tel. +1 703 734 5840, fax +1 703 821 1134, e-mail freund@mmace.nrl.navy.mil.

[1] Permanent address: University of Maryland, College Park, MD 20742, USA.

[2] Permanent address: Science Applications International Corp., McLean, VA 22102, USA.

[3] Permanent address: Mission Research Corp., Newington, VA 22122, USA

SSDI 0168-9002(94)01424-8

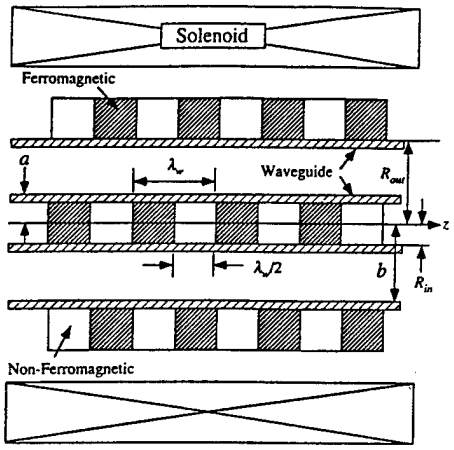

Fig. 1. CHI wiggler geometry.

between the outer rings and the central piece. The radially undulating magnetic fields cause this annular beam to wiggle azimuthally. The electrons may then exchange energy with coaxial modes which contain an azimuthal electric field component, for example the TE_{01} mode. Note that for the experiment under construction the primary interaction is with this mode. Simulations using the formulation described in Ref. [2] indicate that the interaction with the TEM and TM modes is much weaker at the frequencies of interest.

The magnetic fields in the gap can be found analytically by solving Laplace's equation with the boundary conditions that the axial component of the magnetic field be zero along the faces of the ferromagnetic pieces and some constant value B_z along the faces of the non-ferromagnetic ones. The resulting equations for both the axial and radial components of the field (and accompanying figures) are described in earlier publications [1,2]. In essence, the radial component varies sinusoidally along the axial direction and has a minimum at the center of the gap. The axial component consists of a constant term and oscillating terms which are small at the gap center.

3. Magnetostatic wiggler analysis

The magnetic field profile of a CHI wiggler may be modified by changing or tapering several parameters of the basic configuration. Multiple variations of the basic CHI wiggler geometry were studied in order to optimize the configuration for the highest periodic field. This search also detailed ways in which the field may be tailored by varying the parameters of the geometry. These parametric variations were performed using the POISSON simulation codes. The ferromagnetic material was assumed to be low-carbon steel, and the B–H table provided with the codes was used. Only one quarter of the actual wiggler is input because the codes take advantage of cylindi symmetry. The configuration used in POISSON also lows the study of the entrance fields. Parameters varie the standard configuration include: gap height; inner p height, width, taper angle; outer pole height, width, ta angle; and axial phase offset of inner and outer pieces.

The ultimate field strength of the periodic componen limited by the saturation of the ferromagnetic material. ' variation in the maximum radial field at saturation been studied in Ref. [1] as a function of gap height. shown in Fig. 5 in that paper, the maximum radial field saturation decreases monotonically with increasing g spacing. Fig. 2 shows how varying the height of the ou rings can also be used to change the value of the pe radial field. These and other results show that variations pole shapes increased the peak radial field by only a fe percent, and also show various ways to taper the field.

4. Beam dynamics

The dynamics of electrons in the CHI fields we studied both analytically and computationally. For th analytic solution, it was assumed that the particle did no stray far from the gap center – its original position (i.e $\delta r \ll \lambda_w$); hence an idealized field model is used for th analytic orbit treatment. The simplified form used for th field is:

$$B_r = B_w \sin k_w z, \qquad B_z = B_0, \tag{1}$$

In the above equations $k_w = 2\pi/\lambda_w$ and B_w and B_0 ar constants. Assuming a constant bulk axial velocity $v_\parallel$ an solving the equations of motion to lowest order in wiggle amplitude, one obtains the quasi-steady-state solutions:

$$v_\theta = \left[\frac{B_w(\beta_z/\beta_0)B_T}{B_0^2 - (\beta_z/\beta_0)^2 B_T^2}\right] v_\parallel \cos k_w z, \tag{2}$$

$$v_r = \left[\frac{B_0 B_w}{B_0^2 - (\beta_z/\beta_0)^2 B_T^2}\right] v_\parallel \sin k_w z, \tag{3}$$

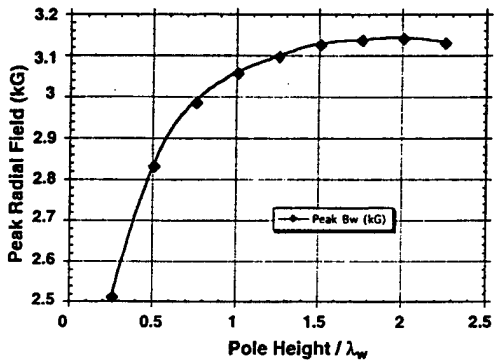

Fig. 2. Peak radial field versus the height of the outer rings.

where $\beta_z = v_\parallel/c$ and B_T is a constant field in the axial direction, called the transition field, and is given by:

$$B_T = \frac{mc^2}{e}\gamma\beta_0 k_w, \tag{4}$$

where γ is the relativistic factor and β_0 is the magnitude of the total particle velocity (a constant) in units of c. The transition field is a constant value of the axial field which delineates the transition from group I orbits to group II orbits as B_z is increased. These equations describe an electron performing an elliptical orbit in the $r-\theta$ plane (with a period equal to the wiggler period) while streaming at a constant axial velocity. These results are analogous to those of a simplified planar wiggler field with a constant axial guide field [8].

Using energy conservation and the quasi-steady state solutions for v_θ and v_r obtained above, one may obtain a quartic polynomial in $v_\parallel$, which may be solved numerically. The existence of a constant field in the axial direction causes the transverse velocities to increase about a certain resonant value of the axial field. The azimuthal component of the velocity (Eq. (2)) (as well as the radial component) is seen to depend strongly on this gyroresonance effect, from the fact that the fields are squared in the denominator.

A figure of merit of the strength of the wiggler is α (the ratio of azimuthal to axial velocity). A plot of α against the applied field is given in Fig. 3 showing the gyroresonant gap. Notice that orbits below B_T (Group I) are more sensitive as B_z approaches B_T than those above B_T (Group II). This sensitivity indicates that tapering of parameters will be very important for achieving maximum performance. It also shows the enhancement possible in the interaction due to the existence of the axial field. In preparing this figure, single and multi-particle three-dimensional orbits were simulated using the TRACK-3 code to integrate trajectories using the realistic three-dimensional field model described in Refs. [1,2]. Results of the simulations agree very well with simplified analytic values

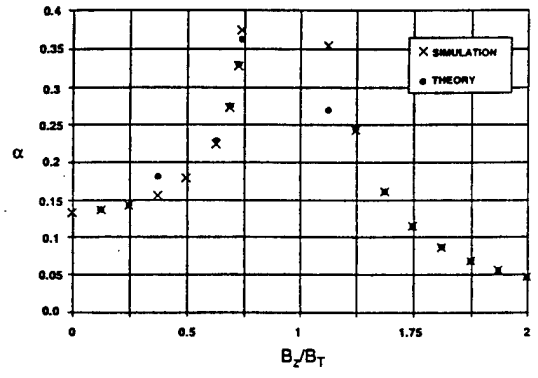

Fig. 3. Variation of α versus the applied field for $B_w/B_T = 0.135$ (comparison of theory and TRACK-3 simulation results).

away from the gyroresonant gap, as the electron remains very near the wiggler gap center.

An examination of the trajectories shows a drift in the θ-direction, but this is acceptable in the CHI FEL case since it remains in the interaction region due to the cylindrical geometry. Calculations have shown that this drift can be explained using Busch's theorem and depends on the entrance conditions used in the simulation. Actual CHI wiggler axial fields decrease in magnitude at the entrance into the wiggler (due to the iron pieces), and may partially cancel out this drift. Future plans include running simulations with PIC (particle in cell) codes utilizing 2-D simulations of the CHI wiggler field including entrance conditions.

5. The experimental design

The experiment to be built at the Naval Research Lab will be a CHI-wiggler FEL operating as an amplifier at a frequency of 35 GHz in the K_a-band. The principal goal of the experiment is to operate at lower voltages while still generating high power, high frequency microwaves. Current plans call for operation at approximately 150 kV with an output power of 100 kW.

The major components of the FEL are the gun, the wiggler section (including the solenoid and the waveguide), the beam collector, and the input and output couplers. The gun will operate at around 150 kV and produce a 10 A annular beam for the CHI wiggler. The wiggler assembly will be placed horizontally within the bore of an existing superconducting magnet. The central rod of the wiggler will be supported by radial struts located near the gun and the collector. The coaxial waveguide consists of the (electroplated) faces of the inner and outer pieces of the wiggler. This waveguide will contain a central sever to reduce rf reflections. The diameter of the wiggler, and therefore of the waveguide, is limited by the bore of the magnet, 6.4 cm, and places a lower bound on our operating frequency. The wiggler will have a period of about 1 cm and will be about 60 periods in length.

A SLAC klystron gun will be modified to produce the necessary annular beam. The superconducting magnet, with an axial field of up to 30 kG, will permit an extensive study of the full performance range of the CHI FEL. The bore size of the magnet is 6.4 cm and its total length is 78.3 cm.

Preliminary calculations using untapered configurations (using a previously described nonlinear three-dimensional slow-time-scale formulation [2]) have shown gains on the order of 0.3 dB/cm and efficiencies in excess of 10% in this frequency range. Studies are currently under way to lower the voltage required while still retaining performance. Fig. 4 shows the gain profile for a specific set of parameters, for which a saturated gain of about 30 dB (0.26 dB/cm) with a gain bandwidth of around 20% was

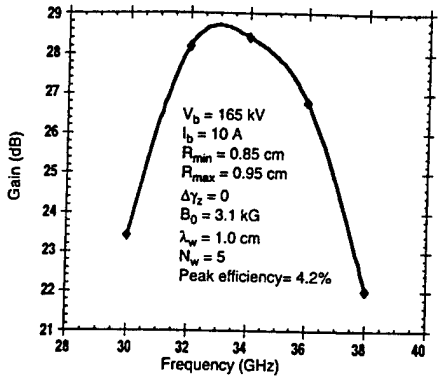

Fig. 4. Preliminary simulation results for a K_a-band amplifier utilizing a coaxial TE_{01} mode.

achieved. In this figure, R_{min} and R_{max} are the inner and outer radii of the coaxial waveguide (i.e. the wiggler gap), and N_w is the number of adiabatic entrance periods. It must again be stressed that these results are very preliminary since optimization of parameters was not performed.

6. Summary and conclusions

The above results indicate interesting potential for high frequency amplifiers based on the CHI wiggler configuration. Work is in progress on the design of a CHI wiggler ubitron amplifier in the K_a-band. A Pierce-type electron gun is being modified to produce a hollow beam for the device, which will have a period of about 1 cm and wil consist of about sixty periods with a central sever. Ai existing superconducting magnet ($B_z \leq 30$ kG) will b used to produce the axial field in order to allow explo ration of the full performance range of the CHI wiggler.

Acknowledgement

This work was supported by the Office of Naval Re search.

References

[1] R.H. Jackson, H.P. Freund, D.E. Pershing and J.M. Taccetti Nucl. Instr. and Meth. A 341 (1994) 454.
[2] H.P. Freund, R.H. Jackson, D.E. Pershing and J.M. Taccetti Phys. Plasmas 1 (1994) 1046.
[3] K.D. Jacobs, G. Bekefi and J.R. Freeman, J. Appl. Phys. 52 (1981) 4977.
[4] A.H. Ho, R.H. Pantell, J. Feinstein and Y.C. Huang, IEEE J Quantum Electron. QE-27 (1991) 2650.
[5] A.A. Varfolomeev, S.N. Ivanchenkov, A.S. Khlebnikov and N.S. Osmanov, Nucl. Instr. and Meth. A 318 (1992) 809.
[6] H. Golombek, E. Agmon and E. Jerby, Nucl. Instr. and Meth. A 331 (1993) 775.
[7] H.P. Freund, M.E. Read, R.H. Jackson, D.E. Pershing and J.M. Taccetti, these Proceedings (16th Int. Free Electron Laser Conf., Stanford, CA, USA, 1994) Nucl. Instr. and Meth. A. 358 (1995) 163.
[8] H.P. Freund and T.M. Antonsen, Jr., Principles of Free Electron Lasers (Chapman & Hall, London, 1992).

APPENDIX XXII

A CHI Wiggler Ubitron Amplifier Experiment: Wiggler Characterization

J.M. Taccetti, R.H. Jackson, H.P. Freund, D.E. Pershing,
M. Blank and V.L. Granatstein
Nucl. Instrum. Meth. **A375**, 496 (1996).

Nuclear Instruments and Methods in Physics Research A 375 (1996) 496–499

NUCLEAR INSTRUMENTS & METHODS IN PHYSICS RESEARCH Section A

ELSEVIER

A CHI wiggler ubitron amplifier experiment: wiggler characterization

J.M. Taccetti[1], R.H. Jackson[2], H.P. Freund[3,*], D.E. Pershing[4], M. Blank, V.L. Granatstein[1]

Naval Research Laboratory, Washington, DC 20375-5347, USA

Abstract

A Ka-band (26–40 GHz) coaxial hybrid iron (CHI) wiggler ubitron amplifier experiment under construction at the Naval Research Laboratory is described. The principal goal of the experiment is to investigate the performance tradeoffs involved in the CHI configuration for high frequency amplifiers operating at low voltages with small wiggler periods. The nominal design parameters are a center frequency of 35 GHz, wiggler period of 0.75 cm, and beam voltage of approximately 150 kV. Nonlinear simulations of the interaction are presented, along with the results of magnetic field measurements performed on a prototype version of the CHI wiggler.

1. Introduction

Free Electron Lasers (FELs) are an attractive alternative as generators of high power, high frequency microwaves. Their strong points include a wide instantaneous operating bandwidth, frequency tunability, high power, and component physical dimensions which can be large compared to the operating wavelength. One of the major obstacles to practical devices is the high voltage necessary for operation. The higher the voltage, the larger the system becomes. One would like to lower the voltage requirement, allowing for a more compact system, while maintaining a strong enough magnetic field to sustain a high gain.

An FEL being designed and built at the Naval Research Laboratory, addresses some of these issues by utilizing a coaxial hybrid iron (CHI) wiggler [2]. Its simple design enables scaling to smaller periods while maintaining high magnetic fields. The CHI wiggler consists of rings of ferromagnetic and non-ferromagnetic materials stacked together by alternating between each type. A central rod of similar alternating design is radially concentric with the annual stack, but is shifted along the axis by half a period. The rf waveguide, which doubles as the vacuum envelope, consists of two non-ferromagnetic stainless steel cylindrical tubes: the outer tube fits inside the outer CHI rings; the inner tube contains the inner CHI pieces inside it. A lateral cross-section of the wiggler, along with the waveguide, is shown in Fig. 1. Once inserted in a solenoidal magnetic field, the CHI structure deforms the axial field to create a radial field oscillating with the same periodicity as the rings. An annular electron beam propagates along the axis through the coaxial gap, where the oscillating radial magnetic field imparts an aximuthal wiggle motion to it.

An analytic approximation to the CHI wiggler magnetic fields has been calculated and can be found in Refs. [1,2]. Two major points which distinguish these fields are the constant presence of the axial field and the good focusing quality of the field due to the increase in field amplitude towards the gap edges. Harmonics are also present, since the fields are formed from a discrete set of pole pieces. Up

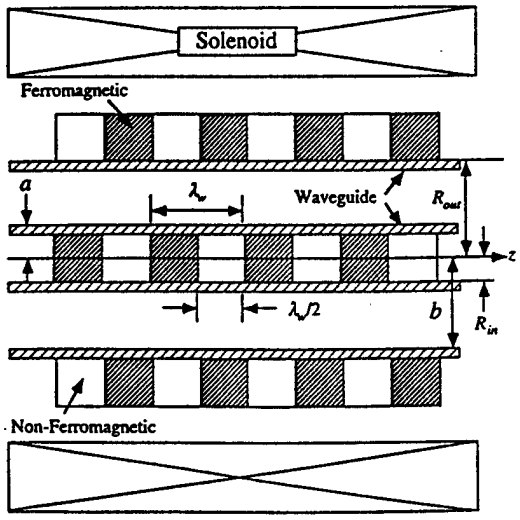

Fig. 1. CHI wiggler geometry.

* Corresponding author. Tel. +1 703 734 5840, fax +1 703 821 1134, e-mail freund@mmace.nrl.navy.mil.

[1] Permanent address: University of Maryland, College Park, MD 20742, USA.

[2] Presently on sabbatical, Culham Laboratory, Abingdon, United Kingdom.

[3] Permanent address: SAIC, McLean, VA 22102.

[4] Permanent address: MRC, Newington, VA 22122.

0168-9002/96/$15.00
SDI 0168-9002(95)01230-3

to the third harmonic component is visible in both the analytic and simulation field plots [1,2].

Issues regarding the design of the CHI experiment have been published previously [3]. Related work shows the CHI wiggler in a G-band amplifier configuration also has great potential for cyclotron resonant heating in magnetic fusion reactors [4].

2. Wiggler construction and characterization

A CHI wiggler prototype has been fabricated and its performance characteristics investigated. This prototype is to scale but consists of only twenty periods instead of the full length of about sixty periods to be used in the final version. The purpose of this exercise was to study the fabrication techniques and the uniformity of the resulting fields and to compare them to those expected from theory and simulations. Both the pulsed wire [5] and the Hall probe methods were used to measure the magnetic fields. The Hall probe method is not sufficient on its own due to the small dimensions of the gap and the restricted motion allowed within it due to the struts supporting the central rod. It is useful, though, as a check of the pulsed wire method.

The inner and outer pole pieces were made out of Consummate iron (a ferromagnetic material with a high saturation field). Aluminum was used for the non-ferromagnetic spacers. The outer rings had an outer diameter of 5.09 cm and an inner diameter of 1.75 cm. Both iron and aluminum pieces were $0.5\lambda_w$ thick (λ_w = wiggler period). These fit over a 304 stainless steel (non-ferromagnetic) tube, which makes up the outer cylinder of the coaxial waveguide. To hold the outer rings together, four equally spaced holes were drilled into their faces and stainless steel rods were run through them. This method causes an asymmetry in the field in the azimuthal direction, and will not be used in the final version of the wiggler, but it was thought to be acceptable for an axial measurement. A measurement in the azimuthal direction would also show the magnitude of the symmetry. Minor imperfections in the machining of the parts and misalignments of the holes, however, can also cause an asymmetry in the axial direction, either directly or indirectly by making it hard to assemble the pieces together. In the final version, the aluminum spacers will be replaced by copper spacers and will be held together with the iron pieces by brazing.

The inner pieces were manufactured of the same materials as the outer pieces. They were made with a hole in their center also, to decrease the weight of the inner rod and to allow a stiffer rod through them to hold them together if necessary. Studies of this configuration showed that the resulting wiggler field would still be adequate in amplitude. These inner pieces had an outer diameter of 0.58 cm and an inner diameter of 0.3 cm. The thickness of the iron pieces was $0.55\lambda_w$, while that of the spacers was $0.45\lambda_w$. They fit inside another stainless steel tube, which became the inner cylinder of the coaxial waveguide.

Two sets of three equally spaced struts, one at either end, support the central rod horizontally. The struts used for the prototype consist of small screws which connect two indexing pieces, an inner one and an outer one, each butting up against the respective wiggler pieces (see Fig. 2). The outer indexing piece slips on the outer waveguide tube, while the inner indexing piece fits partly inside the inner waveguide. This method is not acceptable for the final version since it necessitates that the struts go through the vacuum envelope. The final design for the struts to be used in the experiment is therefore still under development. The struts nearest the gun may in fact be done away with by attaching the central rod to the central focusing electrode in the gun.

As stated above, both pulsed wire and Hall probe methods were used to measure the magnetic fields. The pulsed wire system consisted of a 25 μm diameter tungsten wire stretched from one end of the structure to the other, held taut by a small mass hung at one end. Short electrical pulses were sent down this wire, causing the wire to respond to the wiggler fields as a free electron would. The deflections were detected outside the wiggler, at one end of the structure, by using a laser detector–photodetector pair for each orthogonal direction of motion. The deflections recorded are proportional to the integral of the magnetic field.

The Hall probe used was a miniature transverse field probe mounted on an annular piece which fit in the gap spacing of the wiggler and moved in the axial direction indexed on the outer diameter of the coaxial waveguide. The motion of the index piece was very limited, and the wires were frayed after only two full measurements of the field along the axis. The probe holder is being redesigned for a new set of measurements.

A sample of measurements performed using the pulsed wire method is shown in Fig. 3. This figure shows a measurement done using the pulsed wire method at B_z = 6.25 kG (below saturation) at a radius close to the inner rod. The initial and final periods have higher amplitudes,

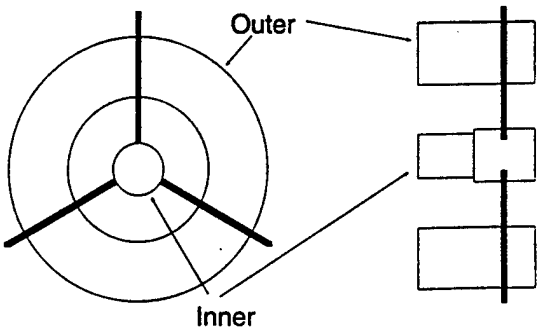

Fig. 2. Inner rod support system.

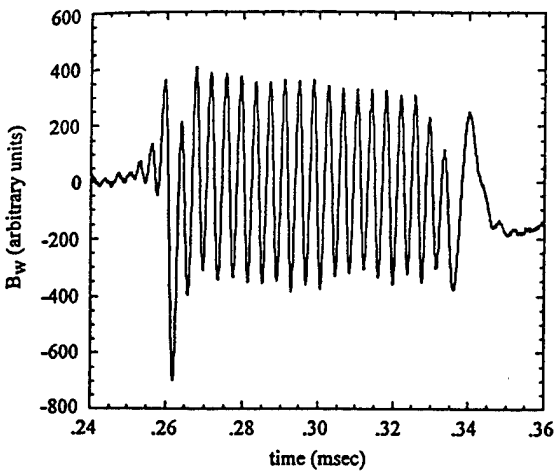

Fig. 3. Wiggler field measured by pulsed wire method.

as expected. This sudden jump in the field is taken care of in the final version by adding a five period adiabatic entry taper in the field. A comparison of the Hall probe and pulsed wire methods was done and the two agree very well. Such agreement corroborates the pulsed wire measurement technique, although it does not say why it is nonuniform. The nonuniformity is believed to be due to the method in which the prototype was assembled. The tightness of the outer pole pieces and spacers on the waveguide did not allow much freedom of motion and restricted them to certain positions which resulted in the nonconcentricity of the pieces with respect to each other. Due to the tight fit of the pieces, it is impossible to reassemble the prototype and check if this is the cause. For this reason, an improved method was developed for putting the prototype together and will be tested shortly.

3. Device simulation

The experiment being built will be a CHI wiggler FEL operating as an amplifier at a frequency of 35 GHz in the Ka-band (26.5–40 GHz). The principal goal of the experiment is to test the CHI concept and achieve operation at lower voltages than normal while still generating high power, high frequency microwaves. Current plans call for operation in the neighborhood of 150 kV with an output power of 100 kW for an input power of 100 W. The inner and outer waveguide radii are 0.317 cm and 0.843 cm, respectively, the wiggler period is 0.75 cm, and the axial field used has an amplitude of 6.2 kG.

The major components of the FEL (the gun, the wiggler, the beam collector, and the input and output rf couplers) are being designed or modified specifically for the experiment. The gun to be used is a modified version of a SLAC

Table 1
Experimental parameters for the 35 GHz CHI wiggler FEL

Beam voltage	150 kV
Beam current	10 A
Inner waveguide radius	0.317 cm
Outer waveguide radius	0.843 cm
Wiggler period	0.75 cm
Axial guide field amplitude	6.2 kG
Center frequency	35 GHz
Input power	100 W

klystron gun which will be modified in-house. The cathode is being redesigned to produce an annular beam at the appropriate voltage and radii. The wiggler will be placed horizontally within the bore of an existing superconducting magnet. The magnet, having a maximum field amplitude of 30 kG, will permit a study of the performance of the FEL over an extensive range of parameters. A central sever will be used in the wiggler section to reduce rf reflections and prevent oscillations at high gain.

Calculations using untapered configurations (using a previously described nonlinear three-dimensional slow-time-scale formulation [3]) and the parameters of Table 1 yield the gain curve shown in Fig. 4. In this figure, R_{bmin} and R_{bmax} are the inner and outer beam radii, and N_w is the number of wiggler adiabatic entrance periods. A 28 dB gain was obtained. The bandwidth is so wide (greater than 25%) because the interaction between the uncoupled dispersion curves of the TE_{01} mode and the beam line occurs at grazing incidence. The upper part of it falls outside the range of the Ka band, but the entire range could be utilized with custom sized waveguides. The saturation length was 53 cm at 35 GHz (72 cm at 42 GHz). Fig. 5 shows a plot of the efficiency versus the beam's axial energy spread. According to the figure, the efficiency only decreases by 35% for a relizable axial energy spread of 0.2%. Better efficiencies, on the order of 9% (at zero energy spread), were found by raising the current, but for the current experiment it is desired to keep the current at

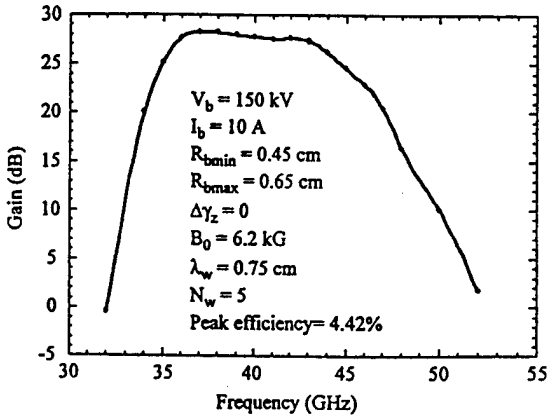

Fig. 4. Gain curve.

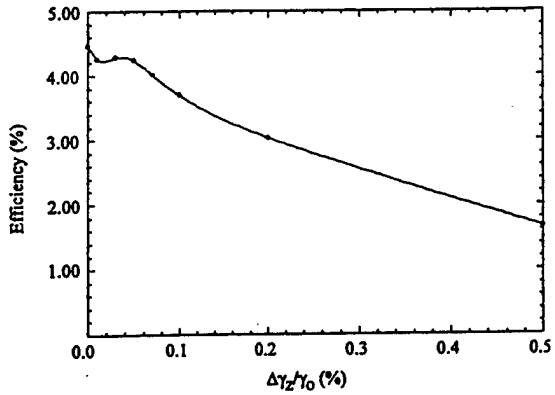

Fig. 5. Effect of energy spread on efficiency.

10 A. Work is still in progress to raise the efficiency, by wiggler field tapering or other methods.

4. Conclusion

The simulation results show very interesting potential for high frequency amplifiers based on the CHI wiggler configuration. Work is still ongoing to increase the efficiency of the wiggler. A new prototype, with a more precise method of assembly, is being fabricated and new measurements will be performed.

We note that the gain and efficiency are similar to those realized in a recent experiment [6] using a sheet electron beam (gain = 24 dB, $\eta = = 3.3\%$). However, the annular configuration of the present study is easier to fabricate and may be more practical, as well as allowing for smaller realizable values of λ_w.

Acknowledgement

This work was supported by the Office of Naval Research.

References

[1] J.M. Taccetti, R.H. Jackson, H.P. Freund, D.E. Pershing, M. Blank and V.L. Granatstein, Nucl. Instr. and Meth. A 358 (1995) 193.
[2] R.H. Jackson, H.P. Freund, D.E. Pershing and J.M. Taccetti, Nucl. Instr. and Meth. A 341 (1994) 454.
[3] H.P. Freund, R.H. Jackson, D.E. Pershing and J.M. Taccetti, Phys. Plasmas 1 (1994) 1046.
[4] H.P. Freund, M.E. Read, R.H. Jackson, D.E. Pershing and J.M. Taccetti, Nucl. Instr. and Meth. A 358 (1995) 163.
[5] R.W. Warren, B.E. Newnam, J.G. Winston, W.E. Stein, L.M. Young and C.A. Brau, IEEE J. Quantum Electron. QE-19 (1983) 391.
[6] S. Cheng, V.L. Granatstein, W.W. Destler, J. Rodgers and T.M. Antonsen, Jr., these Proceedings (17th Int. Free Electron Laser Conf., New York, NY, 1995) Nucl. Instr. and Meth. A. 375 (1996) 160.

APPENDIX XXIII

60% Efficient Miniature C-Band Vacuum Power Booster for the Microwave Power Module

D.R. Whaley, C.M. Armstrong, B. Gannon, G. Groshart, E. Hurt. J. Hutchins, M. Roscoe, T.M. Antonsen, Jr. and B. Levush

IEEE Transactions on Plasma Science
submitted to the special issue on high power electronics

60% EFFICIENT MINIATURE C-BAND VACUUM POWER BOOSTER FOR THE MICROWAVE POWER MODULE

D. R. Whaley, *Member, IEEE*, C. M. Armstrong, *Member, IEEE*, B. Gannon, G. Groshart, *Member, IEEE*, E. Hurt, J. Hutchins, M. Roscoe

Northrop Grumman Corporation, Electronics & Systems Integration Division
600 Hicks Rd., M/S H6402, Rolling Meadows, IL 60008

T. M. Antonsen, Jr., *Member, IEEE*

Institute for Plasma Research and Departments of Electrical Engineering and Physics
University of Maryland, College Park, MD 20742

Baruch Levush, *Member, IEEE*

Naval Research Laboratory, 4555 Overlook Avenue SW, Washington, D.C. 20375

ABSTRACT

Results from a high efficiency miniaturized C-Band vacuum power booster (VPB) development program have resulted in the development of a miniature C-Band traveling wave tube (TWT) operating at 32% circuit efficiency and 61% total efficiency at an output power in excess of 170 W. When combined with a microwave power module (MPM) this VPB results in a module DC-to-RF conversion efficiency of 51%. This high efficiency power amplifier is particularly well suited for space and airborne applications where small size, light weight and low thermal dissipation is required. Other parallel development of VPBs operating at lower perveance and higher power has also been pursued and has resulted in nearly identical performance of 32% circuit efficiency and 61% total efficiency at power levels in excess of 240 W. A new TWT interaction code CHRISTINE is benchmarked with experimental data from several of these VPBs. Simulated performance is seen to accurately predict experimental data.

I. INTRODUCTION

The development of the Microwave Power Module (MPM) is the result of the need for an efficient compact lightweight microwave power source which possesses both high

power, high gain, and low noise characteristics. Northrop Grumman Corporation's development of microwave power modules provides microwave power at various power levels, frequencies, and bandwidths for a variety of applications including communications, radar, and electronic countermeasures (ECM). The MPM combines an integrated power conditioner (IPC), solid state amplifier (SSA), and a vacuum power booster traveling wave tube within a single module resulting in a small, lightweight device for efficient DC-to-RF energy conversion. This unique combination of both solid state and vacuum electronic technologies results in significant reduction in size and weight over conventional transmitters as well as increasing overall efficiency, decreasing thermal dissipation and prime power requirements, and reducing noise.

Many airborne and space applications require high RF conversion efficiencies due to limitations on size and weight of available system power supplies. The MPM subcomponent which most limits the overall MPM efficiency is the miniaturized TWT which serves as the module power booster. As current requirements for these VPBs become more and more difficult to achieve in practice, accurate modeling of the device is required as well as effective design and testing optimization methods. Several advances have been realized in methodology, modeling, and testing which have substantially improved VPB and MPM performance while maintaining the original miniature size and light weight. The resulting VPBs, and MPMs incorporating them, are the smallest and lightest of their kind operating at such efficiency and power levels.

II. GENERAL VPB/MPM DESIGN

A photograph of the C-Band MPM is shown in Fig. 1 and a table of general MPM specifications is shown in Table 1. The components shown include the high voltage IPC, SSA, modulator, and VPB. The C-Band VPB shown at the bottom of the photograph includes, from left to right, the electron gun, pole piece-magnet structure, RF vacuum windows, and collector. The length and weight of the VPB are 18.5 cm (7.3 in) and 0.2 kg (0.44 lb), respectively. VPB fabrication uses high temperature precision brazed metal and ceramic parts. The major sub-assemblies - the electron gun, input line, output line and collector - are joined together via laser welded flanges. The electron gun is of Pierce type using a focus electrode designed to provide beam cutoff at approximately 1 kV. The low perveance design, at 0.51 μP produces a 0.130 A beam at 4.0 kV using an M-type dispenser cathode with a current density of 1.2 A/cm^2. The gun assembly incorporates an adjustable gun housing which allows for in situ change of the relative anode-cathode spacing and therefore of gun perveance for the space charge limited

operation. This permits empirical perveance correction required due to build tolerance and assures tube-to-tube reproducibility. The interaction circuit consists of two helix sections supported in a barrel assembly by three BeO rods. The rod ends are sputtered with graphite which serve as attenuators of the RF wave near the sever. The collector is a graphite four-stage depressed collector required for high total efficiency under saturated conditions and low thermal dissipation under low drive conditions. The RF chain starts at the RF input to the MPM followed by the SSA which provides 30-35 dB gain under saturated and small signal VPB drive conditions, respectively. The SSA output feeds the VPB which further amplifies the power by 23-33 dB. The output window connects to a multipaction-free connector designed for low loss and high power transmission. The total 270 V DC-to-RF conversion efficiency of the MPM shown here is in excess of 50%, with the VPB conversion efficiency exceeding 60%.

III. MODELING AND TESTING

The miniaturized vacuum power booster performance has been increased substantially during a C-Band efficiency enhancement program. During the program, 14 VPBs have been designed and tested and the progression of the VPB efficiency during the program is shown in Figure 2. The total efficiency of the device is seen to increase from ~40% at the start of the program to over 60% at its conclusion. Advances include accurate modeling and optimization of the VPB magnetic field structure and beam entrance conditions, enhanced accuracy of design codes, new hybrid circuit design methodology for high efficiency interaction including harmonic power growth, electron gun perveance reduction, and development of a real-time automated system for parameter optimization.

A. Magnetic Field Optimization

The magnetic field used to focus and confine the beam of a VPB takes the form shown in Fig. 3. The field shown is that of a periodic permanent magnet (PPM) structure and is seen to oscillate in 'z' with a period equal to two magnet cells of the periodic magnet structure. The magnetic field labeled 'stack field' can be designed to any value greater than the Brillioun value and determines the confinement factor and consequently the stiffness of the electron beam under the influence of RF forces. The electrons are not born in the PPM stack but in the fringe field at the entrance to the stack before they are accelerated though the full cathode potential into the oscillating magnetic field. Laminar flow can be achieved in this field only if the electrons possess the correct angular rotation frequency when they reach the first peak of the full stack field. For confined flow

conditions at fields greater than the Brillioun value, this matching of the angular rotation frequency requires the cathode threading shown in Fig. 3. The non-zero field at the cathode increases the canonical angular momentum of the electrons to the value necessary for laminar flow once the beam is fully transported into the PPM stack. To achieve laminar flow, not only must the angular rotation frequency of the electrons be correct at the first maximum of the full stack field, but at the same location the beam must experience no expansion or contraction i.e. $dr_b/dz = 0$. This requirement implies proper tailoring of the magnetic field entrance profile of the first few cells of the PPM structure. This is seen in Fig. 3 as the increasing stack field at the entrance to the structure before the full field is attained. Much care has been taken during this program to properly model and optimize the entrance magnetic field profile to produce the desired laminar beam. Difficulty with simulation and optimization arises due to cell-to-cell coupling of the PPM stack magnetic cells as well as the computation time required to generate accurate solutions of the inherent high-gradient fields. A method has been developed to rapidly and very accurately compute the actual vector potential fields generated by the PPM stack magnets which are required to produce an arbitrary user-defined PPM stack profile. In this way precise magnetic profile optimizations can be rapidly performed which result in highly laminar electron beams. An example of a beam immersed in an optimized PPM stack magnetic field is shown in Fig. 4.

The highly laminar beams produced using this method have several advantages. Such beams have good transmission characteristics and require essentially no empirical optimization of the magnetic field during test. This is the case for these C-Band VPBs which exhibit essentially 100% transmission (<0.1 mA helix current) at turn-on with no tuning or shimming of the original field required. The shimless design of the VPB is clearly seen in Fig. 1. With the collector lenses biased, the backstreaming helix current from the collector also remains low, typically less than 1%. This increased beam laminarity also allows for an increased fill factor and therefore higher beam/circuit coupling without sacrificing the good helix current characteristics of the device. Laminarity also favors fundamental over harmonic power growth as the γa values for harmonic excitation are significantly greater than that of the fundamental. The electric field, and therefore coupling of large γa circuit waves, increases more rapidly with radius than low γa circuit waves. A scalloping beam will therefore experience a greater increase in coupling and consequently a more rapid growth of harmonic power.

This simulation method resulting in the shimless design of the C-Band VPBs has to date resulted in fabrication of over 10 consecutive C-Band VPBs, spanning three different design programs, all exhibiting the same beam focus and transport characteristics. Experimental console test time has been significantly reduced for each of these tubes and effects of azimuthal field asymmetries which in itself induces scalloping are no longer

observed in the VPBs. The method for calculation of vector potential fields in the gun region is also applied to the collector region to determine the optimum refocusing cell field profile for maximum collector efficiency.

B. Circuit Design

The RF interaction circuit of the VPB is of helix type and has been optimized for high fundamental circuit efficiency. The circuit design is the result of a compromise between several factors. The VPB must exhibit signal amplification adequate to produce saturated output power at an input drive value not exceeding the maximum drive produced by the module SSA. Excessive amplification will however degrade the module noise figure, increase small signal gain variation, group delay and may cause the VPB to oscillate. For high efficiency operation the circuit must also generate maximum fundamental RF current in the output section of the VPB before final energy extraction while maintaining low harmonic RF current levels. Proper phasing of the circuit phase velocity and beam velocity in the large signal region of the output circuit is also crucial for high efficiency interaction. Proper gain partitioning between input and output circuits is also found to be important for efficient operation. The input and output are decoupled along the circuit through implementation of a circuit sever. Ballistic debunching of the tightening electron packets can occur in the sever if excessive signal amplification and bunching is allowed in the input section of the VPB. In contrast, if insufficient amplification occurs in the input section, the RF modulation of the electron beam is not adequate to excite the circuit wave at the output of the sever. These considerations have resulted in a methodology used to determine the proper circuit profile for high fundamental interaction efficiency and has now been used on the two of the three C-Band programs mentioned above. All seven of these VPBs have performed at over 30% interaction efficiency.

C. Automated Testing

To achieve maximum total VPB efficiency, many parameters must be optimized during test. The total efficiency of the device is a function of 11 measured parameters (cathode voltage, cathode current, RF power, four collector stage voltages, and four corresponding collector stage currents), six of which are independently variable during test and five of which are dependent on the first six. This optimization is by nature extremely labor intensive and for this reason, an automated efficiency optimization system has been developed and implemented which acquires from the laboratory measurement equipment, in real time, all experimental data necessary to compute DC-to-RF VPB conversion efficiency. The data is acquired and displayed on the computer control monitor as well as computed quantities such as circuit efficiency, collector efficiency, total efficiency, beam

power, recovered power, etc. Real time plots are displayed for each time-changing quantity.

The most difficult optimization to perform is the collector optimization where the kinetic energy in the spent beam of the VPB must be efficiently recovered. During the design process, the geometry of the four stages of the VPB collector is optimized as is the predicted bias voltages for maximum beam energy recovery. This design process relies on the computed energy distribution of the beam exiting the interaction region of the VPB helix and therefore these optimized voltages must again be determined empirically during test. The automated efficiency optimization system allows for real-time evaluation of the total efficiency of the device as a function of the four collector bias voltages and corresponding dependent currents. Full collector optimizations have proven to be rapid and not only has the collector voltage optimization time for the VPB been reduced to ~15 minutes, one can be sure to have completely optimized the collector voltages for maximum efficiency. Typical collector efficiency for the C-Band collectors have reached 73% under full RF drive conditions. Optimizations of cathode voltage and current are also easily performed along with the corresponding collector optimizations.

The voltages supplied to the VPB by the IPC can vary from those specified during VPB tests. With real-time feedback of the VPB efficiency to cathode and collector voltages, the sensitivity to variation in these voltages can also be easily determined. This performance sensitivity is important for IPC design. The efficiency optimization system is now used on all VPBs and TWTs developed in the C-Band program.

IV. EXPERIMENTAL RESULTS AND SIMULATION

A. C-Band VPB performance

The performance of the C-Band VPB shown in this section was attained using the methods previously described. Power and efficiency data for the VPB and the MPM operating at 100% duty factor is shown in Figs. 5(a) and (b). Figure 5(a) shows an output power of 170 W with a bandwidth at 1 dB power points of approximately 1.6 GHz. Figure 5(b) shows the corresponding efficiency of the optimized VPB with a 61% total conversion efficiency centerband. Here the 92% efficient IPC allows for a maximum total MPM DC-to-RF conversion efficiency of 51%. The VPB and MPM are operated at any duty factor between 0% and 100%.

The prime power requirements for the VPB are shown in Fig. 6 as well as resulting dissipated power along the VPB drive curve. For a saturated output power of 170 W, the high voltage prime power increases from 125 W in the small signal regime to ~275 W at saturation. Due to the four stage collector, the dissipated power remains approximately

constant over the entire drive curve, the current being collected on the highly efficient back stages under small signal conditions and on the lower voltage front stages under full drive conditions. This low thermal dissipation, independent of drive, reduces MPM cooling requirements and increases reliability of the device regardless of whether the operating point is chosen near saturation or far into the small signal regime.

The drive curve for fundamental and harmonic power is shown in Fig. 7. This figure shows evidence of the good electron bunching and harmonic control of these high efficiency circuits. The minimum harmonic separation over the drive curve is 11 dB and over 20 dB separation is seen at saturation. The good electron phase bunching manifests itself in the n=2 drive curve where the electron bunch is seen to fall in and out of phase with the second harmonic circuit wave as the electron bunch is progressively slowed by the fundamental interaction as saturation is approached with increasing input drive power.

One remark that should be made is that after testing and optimizing the total VPB efficiency at many points in the drive curves for several tubes in each of the three C-Band programs, it is found that maximum total VPB efficiency with this design always corresponds to maximum circuit efficiency. No conditions were found in which one can optimize the collector at a backed off point in the drive curve and with the increased collector efficiency achievable, exceed the total efficiency achieved when the VPB is optimized at saturation.

Other high efficiency C-Band VPBs were developed as a parallel effort for applications requiring powers in excess of 170 W using the same methods of design and test as the original 170 W version. These VPBs operates at higher voltage and current, and lower perveance than the original C-Band VPB and has a lower gain per unit length and a modified circuit profile. The experimental results are essentially identical as shown in Fig. 8 with an output power of 240 W at an efficiency of 61% and a 1 dB power bandwidth of 1.6 GHz. This VPB can also operated at a duty factor between 0% and 100%. General operating parameters of both VPBs are summarized in Table 2.

Since the development of the High Efficiency C-Band VPBs, several tubes have been fabricated and tested of both the 170 W or 240 W version. Tube-to-tube reproducibility is important for production build of these devices to insure repeatable performance for a system comprised of many MPMs or VPBs. Figure 9 shows the peak efficiency and power performance of the seven high efficiency VPBs produced in the past several months. Reproducibility is seen to be good from device to device for both efficiency and output power.

B. CHRISTINE Simulation of C-Band VPBs

The performance of these C-Band VPBs has been simulated by a recently developed TWT interaction simulation code, CHRISTINE, developed at (politically correct location).

(description of CHRISTINE by Tom and Baruch with reference to NRL report)

These VPBs are a good vehicle with which to compare computed results to experimental data since these devices produce a scallop-free laminar electron beam similar to an ideal one dimensional beam. The electron beam is also mildly confined and stiffer under the influence of RF forces than a Brillioun focused beam. In the following figures, computed and measured data is shown for two types of curves - drive curves showing fundamental and harmonic power as a function of input power for a single frequency and saturated output power as a function of frequency. In the latter plots, each point has been optimized in input drive power both experimentally and during simulation to maximize output power.

The simulations with CHRISTINE are rapid and require ~10 s of execution time for each operating point on a 133 MHz IBM-compatible machine with a Pentium based processor. The code has the ability to compute coupling impedance and phase velocity of the helix circuit based on a helix sheath model for given input geometry or experimental data can be input in tabular form. The sheath helix model assumes a smeared dielectric between the helix and TWT backwall. The code includes a model for annular beams as well as pencil beams and DC space charge, shot noise, and thermal spread can also be included. Interaction with gated beams can be computed as well as interaction with several input frequencies at arbitrary relative input powers and phase. For the case of multiple input frequencies, intermodulation products are also computed. For the C-Band simulations, CW beams with single frequency injection has been used. Attenuation profiles can also be input and typically values resulting from measurement are used. Frequency scaling of attenuation is included with the scaling factor allowed as an input parameter. Severs are modeled as regions of high attenuation which appears to be a good model provided the equivalent profile is chosen with care. Variable pitch helices can be input and are modeled in 'z' as a piecewise continuous pitch function. Continuously varying profiles can be modeled by defining several points along the variable pitch section. The code also will include an arbitrary number of harmonic frequencies in the calculation, the desired number specified in the input.

Output includes values of interaction efficiency, output power, axial power profiles, axial beam energy profiles, and phase space plots as a function of axial position. The code has scanning capabilities as well which is useful when performing optimizations or determining parameter sensitivities. The code will scan in beam current, beam voltage, energy spread, beam size, input frequency, input power, input phase. One or two dimensional scans can be performed with either linear or logarithmic step sizes and the output is tabulated in convenient output files.

Two approximations have been made in the simulations presented here. Since CHRISTINE uses a sheath helix model to compute beam/helix coupling impedance, an impedance reduction factor is used, reducing the coupling factor to account for the tape geometry of the actual helix. A typical reduction factor used is $R_{red} = Z_{actual} / Z_{sheath} = 0.9$. Also since the code uses a one dimensional beam in its formulation, it does not account for the increased size of the beam under near saturated conditions in the latter part of the output circuit of the VPB. For this reason, the equivalent one dimensional beam fill factor, r_b / r_{helix}, has been increased by 10% from the actual design value for these simulations. In all of the simulations shown here for each of the C-Band VPB types, a consistent impedance reduction factor of $R=0.9$ and an increase in equivalent fill factor of 10% are used.

Inclusion of the harmonic interaction in the interaction calculation is found to be important in reproducing experimental data. Even if one is interested only in fundamental power, the presence at the second harmonic frequency is seen to significantly alter fundamental output performance and should be included in the calculation. This is illustrated in Fig. 10 where the calculated drive curves for the 170 W VPB is shown where only the fundamental interaction is calculated and where both fundamental and first harmonic power growth is included. It is clear that even though the second harmonic power is relatively low as seen later, the qualitative appearance of the fundamental drive curve is significantly altered by the presence of the second harmonic wave. The shape of fundamental drive curve including the second harmonic calculation is quite distinctive and is in fact that which is measured experimentally. One sees two linear sections in the fundamental drive curve, the turnover point occurring approximately 10 dB below saturation. The fundamental-only drive curve is more classic with a linear rise to just below saturation and a corresponding lower input drive power required to achieve saturation. This type of fundamental-only drive curve has never been measured on the C-Band VPBs and therefore exemplifies the need for inclusion of harmonic power growth in the interaction calculation. Including higher harmonics in the CHRISTINE calculation significantly increases run times but simulations show that only second harmonic power is necessary to properly simulate the C-Band interaction.

Figure 11 illustrates the good agreement that has been observed between experimental data from the C-Band VPBs and CHRISTINE results. The distinctive qualitative shape of the fundamental and second harmonic drive curves are reproduced. The small signal gain at the lower end of the curve is correct for both frequencies, the turnover point between the two linear regimes of the fundamental curve is correctly predicted, minimum separation between fundamental and second harmonic curves are correct as are the minimums in the second harmonic drive curve. These minimums are due to premature saturation of second harmonic power along 'z' and subsequent re-extraction of this

power by the well formed electron bunch as the it falls into the acceleration region of the second harmonic circuit wave.

These distinctive drive curves change in shape with frequency and between the 170 W and 240 W C-Band VPB. Figures 12(a) and (b) show similar harmonic drive curves for the 240 W VPB at 4.5 and 5.0 GHz respectively. Using the same impedance reduction factor and beam fill factor as for the curves of Fig. 11, CHRISTINE is seen to accurately predict the unique drive curves for each of the cases shown.

The response of the VPBs with frequency can also be computed. Again choosing consistent simulation values for the impedance reduction and fill factors as for the drive curve simulations, the experimental and simulation results for the two different C-Band programs are shown in Figs. 13 and 14. Here the saturated power for each frequency is shown, each point optimized in input drive power, and the agreement is seen to be good. The CHRISTINE code accurately predicts the shapes of these curves, the band center easily predicted by the code as well as the rolloff characteristics on each side of band center. Output powers are typically computed to be slightly higher than measured but this is most likely due to the one dimensional nature of the code, not allowing for PPM transport along the helix, axial beam shear inherent in PPM structures, and helix interception in the large signal region. One VPB has been built and tested incorporating an output helix circuit taper defined by CHRISTINE. Predicted circuit efficiency was within 1% of the existing 170 W VPBs. Within measurement error, this VPB did perform at expected output power and bandwidth.

V. CONCLUSIONS

The development program and results of high efficiency C-Band VPBs and MPMs have been presented. These miniaturized devices are particularly suited for space and airborne applications where lightweight highly efficient power amplifiers of small size and low thermal dissipation are required. The performance presented in this paper is a result of improvements in beam quality through magnetic modeling, effective circuit design methodology, and development of a real-time automated parameter optimization system. Two different programs have resulted in VPBs operating at 170 W and 240 W both at over 30% circuit efficiency and over 60% total efficiency. The resulting MPM incorporating the 170 W VPB operates at over 50% DC-to-RF conversion efficiency with a total weight and volume of only 1.2 kg and 770 cm^3 respectively. The TWT interaction code CHRISTINE has been shown to accurately predict performance of the C-Band VPBs for both the 170 W and 240 W versions which exhibit distinctly different experimental drive and frequency dependence.